Silicon Detector Development for Future Lepton Colliders & Quality Control of the ATLAS Strip Tracker Production

Dissertation
zur
Erlangung des Doktorgrades (Dr. rer. nat.)
der
Mathematisch-Naturwissenschaftlichen Fakultät
der
Rheinischen Friedrich-Wilhelms-Universität Bonn

vorgelegt von
Sara Ruiz Daza
aus
Santander, Spain

Bonn 2026

Angefertigt mit Genehmigung der Mathematisch-Naturwissenschaftlichen Fakultät der Rheinischen Friedrich-Wilhelms-Universität Bonn

Gutachterin/Betreuerin: Prof. Dr. Ingrid-Maria Gregor
Gutachter: Prof. Dr. Jochen Dingfelder

Tag der Promotion: 25.06.2026
Erscheinungsjahr: 2026

Some results presented in this thesis have been published previously in:

[103] R. Ballabriga et al., *Characterization of the H2M Monolithic CMOS Sensor*, Nuclear Instruments and Methods in Physics Research Section A: Accelerators, Spectrometers, Detectors and Associated Equipment (2026) 171353, `https://doi.org/10.1016/j.nima.2026.171353`.

[148] S. Ruiz Daza et al., *The H2M Monolithic Active Pixel Sensor — characterizing non-uniform in-pixel response in a 65 nm CMOS imaging technology*, Journal of Instrumentation **20** (2025) C06037, `https://doi.org/10.1088/1748-0221/20/06/C06037`.

[161] A. Boebel et al., *The End-of-Substructure (EoS) card for the ATLAS Strip Tracker upgrade — from design to production*, Journal of Instrumentation **19** (2024) C02067, `https://doi.org/10.1088/1748-0221/19/02/C02067`.

Abstract

Future high energy physics aims to probe the Standard Model with unprecedented precision, through upgrades of existing collider experiments and the development of future collider facilities. Achieving the ambitious physics goals requires detector instrumentation with a performance beyond the current state of the art. This challenge motivates dedicated studies of detector technologies for future upgrades and the next generation of collider experiments. In this context, this thesis is divided into two parts.

In the first part, the H2M (Hybrid-to-Monolithic) test chip, developed envisioning tracking applications at a future lepton collider, is characterised through sensor simulations and laboratory and test beam measurements. The H2M is a monolithic pixel sensor designed and fabricated in a modified 65 nm CMOS imaging process with a small collection electrode. The chip matrix consists of 64×16 square pixels with a pitch of 35 µm. Each pixel includes an analog front-end and digital logic with an 8-bit pulse-processing counter. A minimum ionising particle detection efficiency of 99% has been achieved at a threshold of approximately 205 electrons, demonstrating that the sensor modifications maintain a high efficiency at relatively large pixel pitches, which are beneficial for large-area tracking applications. The spatial resolution has been measured to be (9.3 ± 0.1) µm at a threshold of 178 electrons, consistent with the sensor design and large pitch. A non-uniform in-pixel response has been observed in the measurements, which has been attributed to the formation of local potential wells in regions with low electric field and interpreted further with the aid of simulation. The timing resolution, limited by this effect, has been determined to be (28.4 ± 0.2) ns. Furthermore, single-die chips have been thinned to a total chip thickness of 21 µm without performance degradation, proving that the technology is suitable for ultra-low material budget applications.

The second part of the thesis presents the quality assurance and quality control of the End-of-Substrature (EoS) cards. These cards will be installed in the Inner Tracker detector, the upgrade of the current Inner Detector of the ATLAS experiment at the Large Hadron Collider (LHC) for the High-Luminosity LHC. Acting as the interface between the on- and off-detector systems, the EoS cards are a critical component. Therefore, all the 1 552 cards that will be placed in the detector are undergoing strict non-destructive testing. In particular, a card flatness tolerance of 300 µm has been set to ensure proper gluing to the detector's carbon-fiber core and effective heat dissipation. To verify this, a capacitive sensor setup has been developed to perform fast flatness measurements of all cards, demonstrating results consistent with those obtained using a smartscope.

Contents

Introduction

The Standard Model has proven to be a successful theory, capable of describing the elementary particles and their interactions [1, 2]. However, several fundamental questions remain unanswered, such as the nature of dark matter [3] or the origin of neutrino masses [2]. Addressing these questions requires higher experimental precision and sensitivity to rare or previously inaccessible processes.

In high energy physics, the Large Hadron Collider (LHC) [4] will start its High Luminosity program (HL-LHC) around 2030 [5]. With an increase in the luminosity by a factor of ten above its design value, the physics goals cover precision measurements of known observables (e.g., particle masses), as well as the extension of the reach for discovery of new physics [6]. In the long-term future, the European Strategy for Particle Physics identifies a lepton collider as the highest-priority next collider after the LHC [7].

Achieving the physics programs of the HL-LHC and future lepton colliders critically depends on the performance of their tracking detectors, whose primary task is to reconstruct the primary and secondary vertices, as well as the trajectories, of the charged particles created in the collisions [8]. These tracking systems are planned to rely on silicon detectors [9–11]. While the tracking detectors for the experiments at the HL-LHC are already under construction, general research and development is ongoing for tracking systems at future lepton colliders. This thesis explores these two topics. Accordingly, Chapter 1 presents the physics programs at the HL-LHC and future lepton colliders, deriving their tracking requirements, and Chapter 2 reviews the fundamentals of silicon pixel detectors.

The first part of the thesis focuses on the development of silicon detectors for a tracking detector at a future lepton collider, where an excellent spatial resolution, low material budget, high efficiency, and precise timing are required [12]. For this application, monolithic active pixel sensors (MAPS) with a small collection electrode manufactured in an advanced CMOS imaging process are a promising technology. The H2M (Hybrid-to-Monolithic) is a monolithic pixel sensor designed and fabricated in a 65 nm CMOS imaging technology, recently made accessible to the high energy physics community. This technology enables a higher in-pixel logic density in MAPS compared to earlier explored processes with larger feature sizes [13]. The H2M test chip is introduced in Chapter 3.

Simulations are a powerful tool for accelerating the detector development by reducing the number of chip prototype iterations, thereby also lowering overall costs [14]. For this reason, Monte Carlo simulations of the H2M sensor are performed and presented in Chapter 4.

With the H2M chip in hand, laboratory measurements are carried out, as presented in Chapter 5. The chip particle detection performance is characterised through test beams, whose methodology and results are described in Chapter 6 and Chapter 7, respectively. Chapter 8 shows the comparison between the simulations and measurements.

The second part of the thesis describes contributions to the construction of the new strip Inner Tracker (ITk) [15] of the ATLAS detector [16], one of the experiments at the LHC, which will upgrade its tracking system in order to maintain the performance in the HL-LHC phase. The ITk is made of substructures (staves and petals) where the silicon modules are mounted. At the end of each substructure, a pair of End-of-Substructure (EoS) cards is placed, being the physical interface between the on- and off-detector systems [17]. This work presents the quality assurance and quality control tests performed on the EoS cards that will be installed in the detector, as well as the development of one of the testing setups. Chapter 9 describes the ITk detector and Chapter 10 presents the measurements performed on the EoS cards.

CHAPTER 1

Prospects for High Energy Physics

Particle physics is a branch of physics that studies the fundamental particles and forces that constitute matter and radiation. It addresses the mysteries of the universe, such as its origin and composition, through both theoretical and experimental approaches. From a theoretical perspective, the Standard Model serves as the primary framework, capable of providing an accurate description of particles and forces, as well as making predictions that can be tested in experiments. Those experiments typically involve high energy particle collisions, like those carried out at the circular Large Hadron Collider (LHC) — currently the largest particle accelerator in the world — which is being prepared for its High Luminosity phase (HL-LHC).

This chapter reviews the Standard Model, with an emphasis on the open questions that motivate the need for a collider beyond the LHC. In particular, it summarises the high energy physics (HEP) programs of the HL-LHC and of proposed future lepton colliders. For the latter, the stringent tracking detector requirements are derived.

1.1 The Standard Model and Beyond

The *Standard Model* (SM) of particle physics [1, 2] describes all known elementary particles and three out of the four fundamental interactions among them: the electromagnetic, the weak and the strong interaction, while failing to include a description of gravity. The fundamental particles of the SM are classified into *fermions* (constituents of matter) and *bosons* (mediators of the interactions). They are illustrated in Figure 1.1.

The twelve fermions, with spin 1/2, are split into two families: six *leptons* and six *quarks* [19]. Each family has three generations of doublets with increasing masses. While the first generation of fermions constitutes the ordinary matter, fermions in the second and third generations are unstable — they are only generated at high energies and decay into fermions of the first generation.

A lepton doublet consists of a negatively charged lepton and an electrically neutral neutrino. The lightest charged lepton is the *electron* (e^-). *Muons* (μ) have a lifetime of 2.2 µs [20], which is sufficiently long that they can be observed in the collisions produced at the LHC [4]. *Taus* (τ) have a shorter lifetime of 0.3 ps [20], making their direct detection only possible through their decay products. *Neutrinos* (ν_e, ν_μ, and ν_τ) are very light (but not massless, as derived from the

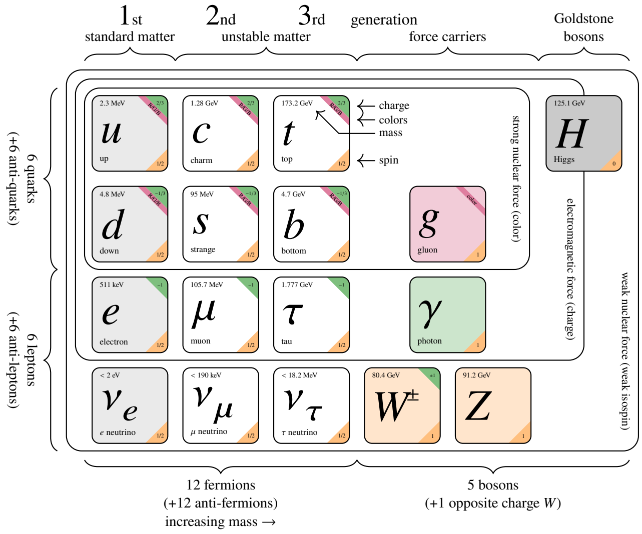

Figure 1.1: Illustration of the fundamental particles of the Standard Model and their properties. Taken from [18].

observed neutrino oscillations [21]). Charged leptons interact via the electromagnetic and weak interactions, whereas neutrinos only through the weak interaction.

In contrast to leptons, quarks do not exist freely and form bound states called *hadrons*. Quarks have an additional quantum number compared to leptons, the *color charge*, which allows them to also interact via the strong force. Depending on the number of constituent quarks, hadrons are classified as *mesons*, composed of two quarks, and *baryons*, made of three quarks. Protons and neutrons are baryons made of up (u) and down (d) quarks, and form the nuclei of the atoms of ordinary matter. More exotic bound states with four and five quarks, known as *tetraquarks* [22] and *pentaquarks* [23], have been found in the last years. Further, hadrons containing *bottom quarks* (b) have a long lifetime of about 1.5 ps [24]. At high energies, they can travel a few millimeters in the detector before decaying, producing a secondary vertex displaced from the primary collision point. Similarly, hadrons containing *charm quarks* (c) also have a long enough lifetime to travel a few hundred micrometers before decaying. Particles originating from b and c quarks are identified using *b-tagging* and *c-tagging* algorithms [25]. The *top quark* (t) has a lifetime shorter than the hadronization time [26], meaning that, unlike all other quarks, it decays before forming hadrons and thus it can be observed directly. It is the heaviest fundamental particle observed (172.3 GeV), and thanks to its large mass, it couples very strongly to the Higgs field, playing a fundamental role in the electroweak symmetry breaking mechanism [27, 28]. Its mass also affects the shape of the Higgs potential, influencing the stability of the universe [29].

Additionally, each fermion has its corresponding antiparticle (antifermion) with the same mass and spin, but opposite charge. For example, *positrons* are the antiparticle of electrons.

Bosons can be classified into two categories: *force carrier bosons* and the *Higgs boson*. The force carriers are the gauge bosons, with integer spin, and act as the force propagators. The gluons (g) mediate the *strong interaction*, coupling to quarks and to themselves. The *electromagnetic interaction* is carried by the photon (γ), which is massless and neutral. Three massive bosons (W^+, Z^0 and W^-) mediate the *weak force*, and couple with leptons, quarks, and among themselves. The Higgs boson has a spin of zero. It provides mass to the W^+, Z^0, and W^- bosons and fermions, via the spontaneous electroweak symmetry breaking mechanism [27, 28].

With an accurate description and prediction of particles and interactions — such as the discovery of the Higgs boson [30, 31] and the unification of the electromagnetic and weak forces into a single electroweak interaction [2] — the SM has been proven to be a successful theory, capable of making precise predictions that have been validated by experimental results. However, there are still open questions and discrepancies between the SM predictions and measurements. Among these shortcomings are the absence of gravity within the model [32], the hierarchy problem [33], the origin of particle masses [2], the description of dark matter [3] and dark energy [34], and the explanation for the observed matter-antimatter asymmetry in the universe [35]. These limitations make the SM an incomplete model, both from a theoretical and experimental perspective, and motivate the search for new physics *beyond the Standard Model* (BSM) at future particle colliders.

1.1.1 Experimental Tests of New Physics

In the experimental search for physics BSM, two strategies can be followed: *direct searches* and *indirect searches*.

Direct searches aim to discover new heavy particles produced in high energy collisions. Their production requires sufficient center-of-mass energy (at least the rest mass of the new particle). These particles are then identified through the detection of their decay products. An example of this approach is the discovery of the Higgs boson by the CMS [30] and ATLAS [31] experiments, achieved by reconstructing its decay products.

Alternatively, indirect searches look for derivations from the SM predictions through precision measurements of known processes. Since such derivations are very small, precise theories and high resolution measurements are required. The main advantages of this approach is its sensitivity to higher energy scales than those achieved in direct searches. This is possible by exploring observables through loop diagrams or couplings, involving virtual particles that do not appear in the final state, and therefore, do not require large production energies. For instance, at lepton colliders, the electroweak couplings of the top quark can be measured with high precision [36].

1.2 Physics at the HL-LHC

Two of the most important parameters for a collider experiment are the *centre-of-mass energy* and *event rate*.

The centre-of-mass energy ($\sqrt{s}$) of a collider determines the heaviest particle produced, and therefore it limits the reach of the physics programs based on direct searches. In a particle collider with symmetric beam energy E_{beam} the centre-of-mass energy is:

$$\sqrt{s} = 2E_{beam} . \tag{1.1}$$

Given a determined process with cross section σ, the event rate R is:

$$R = \mathcal{L} \cdot \sigma \tag{1.2}$$

where $\mathcal{L}$ is the *instantaneous luminosity*, which is defined as the total number of collisions per unit area and time. Therefore, in order to be sensitive to rare processes that have a small cross section, a high luminosity is needed. The integration of the instantaneous luminosity over time is the *integrated luminosity*, which is the total number of collisions per unit area in a data sample, and it is especially useful when referring to physics studies since it determines the total amount of data available.

With an unprecedented integrated luminosity of 3 000 fb^{-1}, the $\sqrt{s} = 14$ TeV proton-proton collisions program at the HL-LHC [5] aims to probe the SM and physics BSM with high precision. Its physics projections have been documented in great detail in the 2020 update of the European Strategy for Particle Physics [37] and 2022 Snowmass report [38]. Based on those publications, a few examples of key physics goals projected to be achieved during the HL-LHC program are mentioned below.

The increase in statistics will enable precision measurements and enhance sensitivity to low probability processes, improving the ability to search for new physics in rare SM processes. In the Higgs sector, one of the most important measurements planned in the HL-LHC is the precise determination of couplings that are currently statistically limited at the LHC, such as the up to now unobserved $H \rightarrow \mu^+\mu^-$ and $H \rightarrow Z\gamma$, with expected percent-level uncertainty. Di-Higgs production is expected to be observed with a significance better than 7σ, allowing the measurement of the Higgs boson trilinear self-coupling λ_3 with a precision better than 30 % [6]. The top-quark sector will also greatly benefit from the HL-LHC data. For example, measurements of simultaneous four-top production ($t\bar{t}t\bar{t}$) are projected to be measured with a precision of around 6 % [39]. In particular, studies of the $t\bar{t}t\bar{t}$ channel result in an effective search for new physics, where any deviation from the SM prediction (such as a slightly different top-Yukawa coupling) could point to new particles. More generally, particle properties like their masses, couplings and branching ratios will be measured with smaller uncertainties [6]. Furthermore, uncertainties on the Parton Distribution Function (PDF) will also be reduced [40], allowing more accurate measurements such as the W boson mass, which is currently limited by PDF uncertainties. In addition to the improvement of the W boson mass, precision electroweak physics at the HL-LHC also includes the improved measurement of the electroweak mixing angle $\sin\theta_W$ [41].

BSM searches at the HL-LHC will extend the kinematic reach for supersymmetry, dark matter and dark sectors, while improving the sensitivity for heavier resonances (e.g., Z' or W') and long-lived particles [42].

Additionally, when colliding heavy ions (p-Pb and Pb-Pb) large data samples will be collected in the HL-LHC program. This will allow precision measurements of the quark-gluon plasma and other nuclear effects, such as nuclear PDFs and parton energy [42].

The luminosity increase will not be the only advantage of the HL-LHC era: the experiments will undergo major detector upgrades, pushing the technology research and development (R&D) further. In the case of the ATLAS experiment [16], for example, the improved lepton acceptance at high $|\eta|$ of the Inner Tracker detector (see Chapter 9) will improve the measurement of the W boson mass and studies of vector-boson scattering, which are characterised by high p_T forward jets [43].

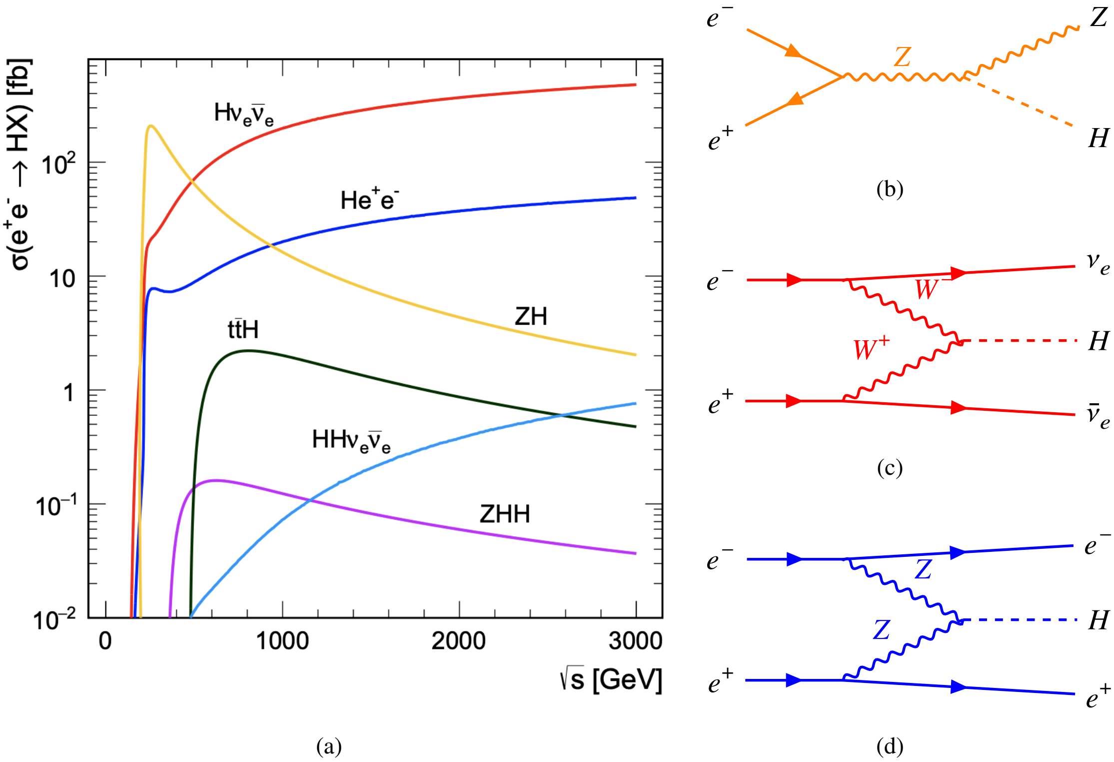

Figure 1.2: (a) Cross sections for the main Higgs production processes at an e^+e^- collider. Taken from [44]. Feynman diagrams of the three highest cross sections: (a) $e^+e^- \rightarrow ZH$, (b) $e^+e^- \rightarrow H\nu_e\bar{\nu}_e$, and (c) $e^+e^- \rightarrow He^+e^-$.

1.3 Physics at Future Lepton Colliders

In contrast to hadrons that are composite particles dominated by strong interaction, charged leptons are point-like particles whose interactions are governed by the electroweak force. As a result, lepton collisions provide a clean environment where the initial state is well defined (i.e., the quantum numbers and energies of the colliding leptons are known). This allows for high precision measurements. Additionally, as a consequence of the clean environment, free from strong-interaction backgrounds and pile-up effects [1], detectors can operate with a triggerless readout system and significantly lower radiation levels than hadron colliders.

Lepton colliders are considered Higgs-Electroweak-Top factories due to their strong focus on precision measurements of the Higgs boson, electroweak sector, and the top quark. In terms of Higgs physics, the primary advantage of a lepton collider lies in its ability to measure Higgs couplings in a model-independent way, which is not possible at hadron colliders. In particular, the Higgs decay width can be determined regardless of its decay modes, which is explained below. Top quark studies in lepton colliders allow for precise determinations of its properties, such as the mass and electroweak couplings [36]. Due to its high mass, the top quark is also considered “a

[1] For backgrounds at linear lepton colliders see Section 1.4.1.

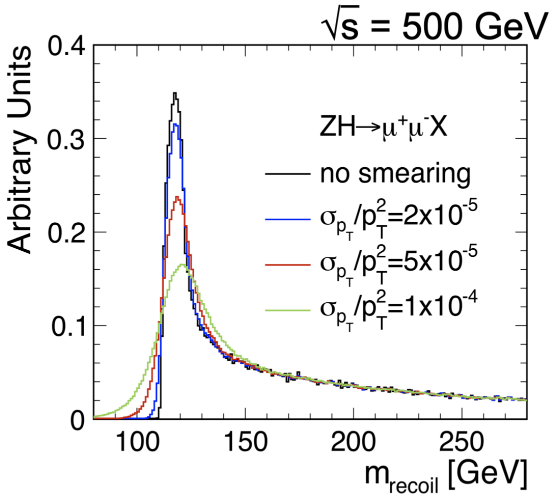

Figure 1.3: Simulation of the Higgs recoil mass distribution in ZH events where the Z decays into two muons. The center-of-mass energy is 500 GeV. Results are shown for different momentum resolutions. Taken from [48].

window" for new physics. Additionally, lepton colliders provide a clean environment for flavour physics. Weakly coupled particles can also be explored through precision measurements of W and Z bosons.

Given this physics potential, the 2022 update of the European Strategy for Particle Physics has identified that "*an electron-positron Higgs factory is the highest-priority next collider*" [7]. Several lepton colliders have been proposed as successors to the LHC. Some have a circular design, as the Future Circular e^+e^- Collider (FCCee) [11] or the Circular Electron Positron Collider (CEPC) [45], while others have a linear design, such as the Compact Linear Collider (CLIC) [10] or the International Linear Collider (ILC) [46]. Their physics programs and detector constraints are similar, and the most important points are summarised below. A more detailed description can be found in the Briefing Book [47].

Figure 1.2(a) shows the cross sections for the main Higgs production processes at an electron-positron (e^+e^-) collider. At an center-of-mass energy, $\sqrt{s}$, of about 240 – 250 GeV, the cross-section of the Higgsstrahlung process, $e^+e^- \rightarrow ZH$, reaches its maximum. This channel, whose Feynman diagram is illustrated in Figure 1.2(b), gives access to the total Higgs decay width and to its coupling with the Z boson in a model-independent manner. By reconstructing the Z boson four-momentum in $Z \rightarrow \mu^+\mu^-$ events and applying the energy-momentum conservation principle, the Higgs recoil mass is calculated. This measurement is shown in Figure 1.3, where a peak corresponding to the Higgs boson mass is visible. Note that the track-momentum resolution of the measurement strongly affects the measured width of the recoil mass peak, thereby imposing stringent constraints on the tracker detector (see Section 1.4).

According to Figure 1.2(a), Higgsstrahlung is the dominant production process up to a center-of-mass energy of approximately 350 – 380 GeV, above which the WW fusion-production process, $e^+e^- \rightarrow H\nu_e\bar{\nu}_e$ (Figure 1.2(c)), becomes dominant. This production channel gives access to couplings of the Higgs boson to fermions and to gauge bosons.

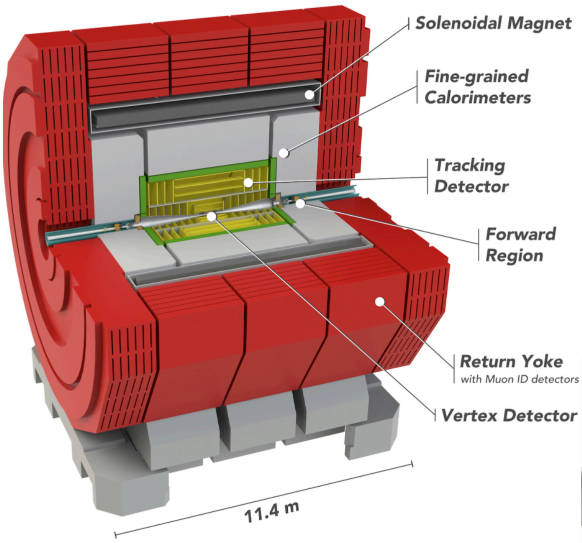

(a) CLIC detector

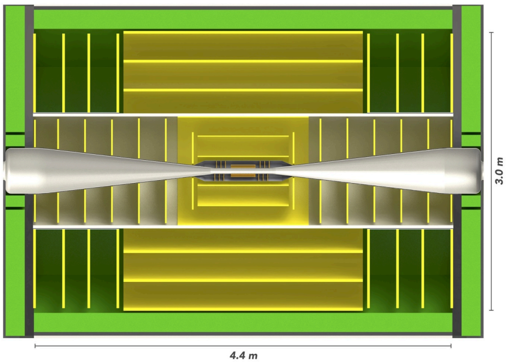

(b) Tracking detector

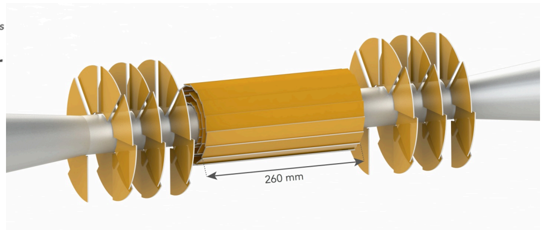

(c) Vertex detector

Figure 1.4: (a) Schematic of the CLIC detector design, (b) its tracking detector, and (c) its vertex detector. Taken from [49].

At higher energies, around 500 – 550 GeV, the production process $e^+e^- \rightarrow t\bar{t}H$ reaches its maximum cross section, giving direct access for measurements of the top-Yukawa coupling. Higgs self-coupling studies through the rare $e^+e^- \rightarrow ZHH$ production channel can also be explored at this energy range. Above 1 TeV, the Higgs trilinear self-coupling can be probed further via the $e^+e^- \rightarrow HH\nu_e\bar{\nu}_e$ process, and the ZZ fusion-production process $e^+e^- \rightarrow He^+e^-$ (Figure 1.2(d)) also becomes significant. Towards higher energies, rare Higgs decay modes can also be investigated, benefiting from the improved statistical uncertainties of the other production channels.

All these physics processes define the center-of-mass energy needed for the production of the particles under study. Taking advantage of this, lepton colliders adopt the so-called staged running programs, where the accelerator operates at different center-of-mass energies, each optimised for a specific set of physics goals [44]. These specific physics goals, in turn, drive the corresponding detector requirements introduced below.

1.4 Detector Requirements at Lepton Colliders

Regardless of a circular or linear lepton collider, the physics requirements for their particle detectors are similar, and thus, their design concepts are alike. All the detector designs have layers of subdetectors, as shown in Figure 1.4(a) for the CLIC detector concept. The innermost layer consists of the tracking system, with a tracker (see Figure 1.4(b)) and a vertex (see Figure 1.4(c)) detector. The *vertex detector* is the central part of the detector and reconstructs the primary and secondary vertices, while the *tracker detector* reconstructs the trajectory of the charged particles in the presence of a magnetic field to determine the momentum of the particle. They can also perform particle identification (PID), e.g., using time-of-flight information. Surrounding the tracking system, an *electromagnetic calorimeter* (ECAL) is placed to measure the energy of electrons and photons, and a *hadron calorimeter* (HCAL) for the hadrons. The outermost layer consists of a *muon detector*.

Since the main topic of this thesis is the technology development for tracking detectors for future lepton colliders, the main requirements derived from the physics goals are highlighted in the next section.

1.4.1 Tracking Systems

Both circular and linear lepton colliders require excellent vertex and momentum resolution. However, differences in their experimental conditions (e.g., accelerator design, center-of-mass energies, backgrounds, and beam structures) lead them to focus on different design aspects explained below [50].

Circular colliders are characterized by a continuous beam and very high luminosity, especially at low-energy stages[2]. This sets the focus on minimising the material budget to reduce multiple scattering of the dominant low-momentum tracks. Particle identification (PID) using dE/dx, cluster counting (dN/dx) or Time-of-Flight (ToF) also becomes essential for precise studies of quark flavour physics [51].

On the other hand, linear colliders have a very low duty cycle. The *duty cycle*, defined as the time of the collisions divided by the time between the collisions, is below 0.001 % for CLIC [10], where 156 ns bunch trains are collided every 20 ms. This allows for triggerless readout of all the subdetectors, and enables power pulsing, i.e., over the majority of time between particle collisions, the front-end electronics can be set in a low-power mode to reduce the power consumption [52, 53]. To guarantee sufficient heat removal with forced air flow cooling, the average power dissipation of the front-end electronics is limited to a maximum 50 mW/cm^2 in the vertex detector [50]. The strong beam focusing of lepton colliders generates beam-induced background. Beamstrahlung photons are created when the e^- (e^+) particle beam interacts with the electric field of the opposing e^+ (e^-) beam [54]. These photons can produce high instantaneous (simultaneously with the collisions) hit rates of electron-positron pairs and hadrons. To distinguish the beam-induced background from the actual particles produced during the collision, timing cuts can be applied, requiring a hit time tagging with a precision of a few nanoseconds in the tracking region [55]. Additionally, to exploit the high momentum tracks produced in collisions at high center-of-mass energies, achieving an excellent position resolution is the design focus of the tracking system of lepton colliders.

[2] Circular e^+e^- colliders achieve very high luminosities at low center-of-mass energies (ZH and WW production). At higher energies, synchrotron radiation becomes the limiting factor, preventing their operation with significant luminosities. In contrast, linear colliders increase their luminosity with the center-of-mass energy, as they are not limited by synchrotron-radiation losses. At ZH production energies, both collider types reach comparable luminosities.

Table 1.1: Comparison of vertex and tracker requirements for a hadron and a lepton collider, using as an example the ATLAS ITk at the HL-LHC and the CLIC detector concept. Data from [12, 15, 56].

	HL-LHC (ATLAS ITk)		Lepton Collider (CLIC)	
	Vertex	Tracker	Vertex	Tracker
Single-point resolution	~10 µm	~20 µm	~3 µm	~7 µm
Efficiency (after irradiation)	>97 %	>99 %	>99.7 %	>99.7 %
Material budget per layer	$\sim 2\,\%X_0$	$< 2.3\,\%X_0$	$< 0.2\,\%X_0$	$< 1-2\,\%X_0$
Power consumption	$<10^3$ mW/cm^2	<10 mW/cm^2	<50 mW/cm^2	<150 mW/cm^2
Radiation tolerance TID [Gy/year] NIEL[n_{eq}/cm^2/year]	 $<10^6$ $<2\times10^{15}$	 $<2\times10^3$ $<1.6\times10^{14}$	 $<10^3$ $<10^{11}$	 <1 $<10^{10}$

Despite the differences in experimental conditions, linear and circular colliders share common requirements. These include precise vertex resolution and track-momentum resolution, and are driven by the physics goals. The requirements are listed and compared to those of the Inner Tracker Detector upgrade for ATLAS (see Chapter 9) in Table 1.1.

First, an impact parameter resolution of $\sigma(d_0) = 5 \oplus 15/(p[\mathrm{GeV}]\sin^{3/2}\theta)$ µm is required for accurate vertex reconstruction and efficient identification of secondary vertices from b and c quark decays. This can be achieved with a vertex detector with a single-point resolution of 3 µm and a material budget below 0.2 %X_0 per layer [57, 58].

A track-momentum resolution of $\sigma_{p_T}/p_T^2 \leq 2\times10^{-5}\,\mathrm{GeV}^{-1}$ is required for precise momentum measurement of the leptonic final states, for example, for the Higgs recoil analysis in the $Z \rightarrow \mu^+\mu^-$ channel (see Figure 1.3). Full Monte Carlo simulations of the CLIC tracker concept have shown that this performance can be achieved with a combination of a single-point resolution of 7 µm in the direction perpendicular to a 4 T magnetic field, limited granularity along the longitudinal direction to the magnetic field between 1 and 10 mm based on the detector occupancy, hit detection efficiency above 99.7 %, and a material budget below 1-2 %X_0 per layer [57, 58]. Additionally, the low material budget imposes constraints on the low-mass supports and services for active cooling and, consequently, limits the power dissipation to 150 mW/cm^2 in the tracker detector [50].

In the CLIC vertex detector, the expected Non-Ionising Energy Loss (NIEL) is below 10^{11} n_{eq}/cm^2/year and the Total Ionising Dose (TID) is lower than 10^3 Gy/year [12]. Note that these values are several orders of magnitude lower than those at the LHC experiments. Therefore, radiation tolerance is not a major concern for lepton colliders.

Finally, a low-angle coverage, particularly in the forward region, is needed for lepton identification, photon tagging and precise measurement of missing energy.

All vertex detector concepts for future colliders rely on silicon pixels [50]. However, with the current state-of-the-art, no pixel detector can meet all the listed requirements simultaneously. Thus, R&D efforts are ongoing in projects such as TANGERINE [59, 60] or OCTOPUS [61], in which context this thesis has been developed. Furthermore, the investigated chip in this work, H2M, does not aim to target any specific requirement of a vertex detector. Instead, it explores novel design approaches such as the porting of a hybrid detector technology into a monolithic chip to reduce the material budget, the use of a large pixel pitch to explore limitations of charge collection in the recently accessible 65 nm CMOS imaging process, the design of a complex analog front end, or the limitations of backside thinning for further reducing the material budget. The goal is that all lessons learned during the design, simulations, and characterisation of H2M can be applied in the development of a future vertex and tracker detector for a lepton collider.

CHAPTER 2

Fundamentals of Silicon Pixel Detectors

Silicon pixel detectors are solid state devices widely used in many large HEP experiments, such as ATLAS [16], CMS [62], LHCb [63] and ALICE [64], as well as in smaller-scale experiments like Mu3e [65] or test beam setups like the ADENIUM beam telescope [66]. Their use is also foreseen in future detector upgrades, including the ATLAS ITk [15, 56], and in proposals for detectors at future particle colliders, such as FCC-ee [11] and CLIC [12], as already hinted at in Chapter 1.

Although the specific pixel detector design varies depending on the physics goals of the experiment, their working principle is similar and governed by semiconductor physics. This chapter provides a brief introduction to the theoretical aspects relevant to understanding the simulations and measurements presented in this work. A more detailed description of silicon pixel detectors can be found in [8, 67, 68].

2.1 Silicon Detector Properties

This section provides an overview of the most important properties of silicon in the context of particle physics and how it has to be modified to be used as a particle detector.

2.1.1 Basic Properties of Silicon

Silicon atoms form a periodic crystal structure, where each atom is covalently bound to four nearest neighbors in a tetrahedral pattern. The interaction of neighboring atoms in the crystal results in the splitting of discrete energy levels. Since these discrete energy levels of individual atoms are energetically so dense ($\mathcal{O}$(meV)), they merge into a continuous *band* of allowed energies, where weakly-bound electrons can move through the crystal [69].

The *valence band* (VB) is defined as the highest band fully filled with electrons, and the *conduction band* (CB) is the next higher energy band not fully filled with electrons at temperature T = 0 K. These two bands are separated by a *band gap* of forbidden energies. Depending on the band gap size (E_g), materials can be classified as *conductors* ($E_g \approx 0$ eV), *semiconductors* ($E_g \approx 1$ eV) and *insulators* ($E_g \approx 1$ eV) [8].

In semiconductor materials, thermal excitations at room temperature are enough for electrons to overcome the band gap and to be promoted from the VB to the CB, where they can move freely through the crystal. When this happens, a vacant state (a *hole*) is left in the VB. The motion of electrons in the CB, as well as electrons in the VB hopping into these vacant states (hole motion), contributes to the electrical conductivity.

Silicon is a semiconductor with $E_g = 1.12\,eV$ [8]. However, the average energy required to create an electron-hole pair in silicon is approximately 3.66 eV [67]. The reason for this higher value is that silicon is an indirect semiconductor. Thus, the transition of an electron from the VB to the CB involves a change in momentum, which is facilitated by a phonon (lattice vibration).

In addition to the promotion of electrons from the VB to the CB, electrons can also *recombine* with holes in the VB. In this way, in thermal equilibrium, the electron concentration in the conduction band (n) and the hole concentration in the valence band (p) satisfy:

$$n = p = n_i \tag{2.1}$$

where n_i is the intrinsic concentration of charge carriers (i.e., number of electrons and holes in a pure semiconductor). The intrinsic carrier concentration of silicon is approximately $n_i \simeq 1 \times 10^{10}\,cm^{-3}$ [8]. It should be noted that this concentration of charge carriers is orders of magnitude higher than the number of electron-hole pairs generated by the interaction of a MIP with silicon (see Section 2.2.1). Therefore, the number of free charge carriers has to be reduced in order to use silicon as a particle detector at room temperature. This is achieved by doping the silicon and enabling the formation of a pn-junction, as explained below.

2.1.2 Doping of Silicon

The conduction properties of intrinsic semiconductors can be modified by introducing impurity atoms in the crystal structure [8, 69]. This process of adding impurities in a controlled manner is known as *doping*, and it changes the concentrations of electrons in the conduction band and holes in the valence band (while the crystal stays neutral). A doped semiconductor is called *extrinsic semiconductor*.

When silicon is doped with donor atoms, it results in an *n-type semiconductor*. Donor atoms have more valence electrons than silicon, providing free electrons that become the majority charge carriers. Since silicon has four valence electrons, typical n-type dopants are elements from group XV of the periodic table (with five valence electrons, such as phosphorus or arsenic).

Conversely, if silicon is doped with acceptor atoms, it becomes an *p-type semiconductor*. Acceptor atoms have fewer valence electrons than silicon, creating vacancies in the VB, thus holes become the majority charge carriers. Typical p-type dopants in silicon belong to group XIII of the periodic table (with three valence electrons, such as boron or gallium).

A silicon substrate can not only be uniformly doped, but also locally modified through implantation to create different doped regions. Highly n-type or p-type doped regions are referred to as n^+ or p^+, respectively.

2.1.3 Silicon pn-junction for Particle Detection

When an n-type and p-type silicon are brought together, a *pn junction* forms at the interface (see Figure 2.1). Electrons from the n-type region diffuse towards the p-type region and recombine

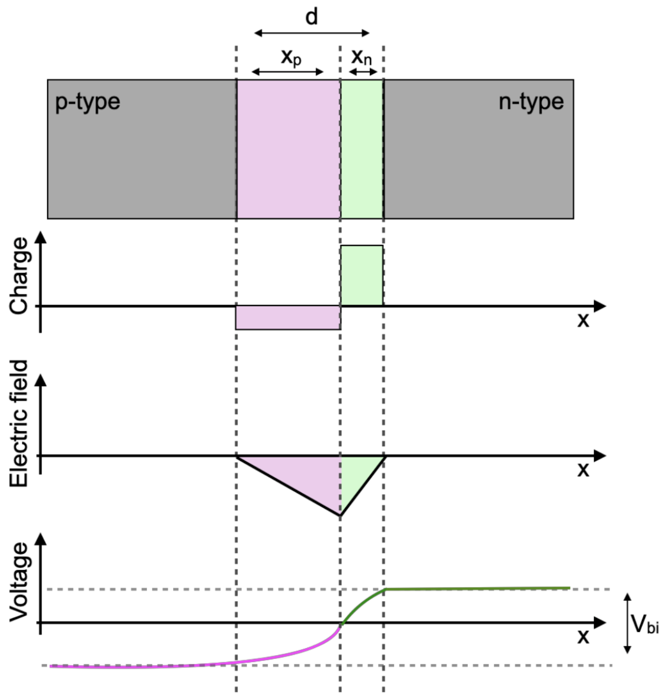

Figure 2.1: Sketch of the depleted region at the pn-junction, together with the charge density, generated electric field, and built-in potential. Adapted from [8].

with holes, while holes from the n-type region diffuse into the n-side and recombine with electrons. This process creates a region without mobile charge carriers, called *depleted region*.

The immobile dopant atoms in the depleted region create a space charge region, positively charged in the n-type region and negatively charged in the p-type region. As a result, an electric field is generated and a built-in potential is created, counteracting the diffusion of charge carriers until thermal equilibrium is reached and the condition

$$N_A x_p = N_D x_n \tag{2.2}$$

holds, with N_D and N_A the donor and acceptor concentrations, and x_n and x_p the widths of the depleted region in the n-type and p-type regions, respectively. This neutrality condition implies that the depletion region extends deeper towards the more weakly doped region. The built-in potential across the junction V_{bi} can be calculated as

$$V_{bi} = \frac{k_B T}{e} \ln\left(\frac{N_D N_A}{n_i^2}\right) \tag{2.3}$$

where T is the temperature, e is the elementary charge and k_B is the Boltzmann constant [8]. For typical doping concentrations in silicon at room temperature (T= 300 K), the built-in potential corresponds to approximately V_{bi} = 0.6 V [8].

If an external reverse bias V_{ext} is applied (the n-side is connected with the positive terminal and the p-side is connected with the negative terminal of a voltage source), electrons on the n-side and holes on the p-side are pulled away from the pn boundary, and the width of the depletion region grows. Assuming $N_A \gg N_D$, as it is the case of the studied sensor in this work, the depletion width ($d = x_n + x_p \approx x_p$) can be approximated by

$$d \approx \sqrt{\frac{2\epsilon_s}{e} (V_{bi} + V_{ext}) \frac{1}{N_{eff}}} \tag{2.4}$$

with ϵ_s and $N_{eff} = |N_D - N_A|$ the permittivity of silicon and the *effective doping concentration*, respectively. The effective doping concentration is inversely proportional to the resistivity ρ,

$$\rho = \frac{1}{e\mu N_{eff}} \tag{2.5}$$

where μ is the mobility (see Section 2.3.1). For typical detector operation, $V_{ext} \gg V_{bi}$, the depleted width is proportional to $\sqrt{\rho\, V_{ext}}$ [8]. Thus, larger bias voltages and silicon resistivity increase the volume of the depleted region.

Electrical Properties of the pn-junction

The maximum electric field occurs at the pn-junction boundary, as sketched in Figure 2.1. It is proportional to $\sqrt{V_{ext}/\rho}$ [8] and decreases linearly at the edges of the depletion region, as illustrated in Figure 2.1. Therefore, higher electric fields are achieved in the boundary at larger bias voltages and higher doping concentrations (or lower silicon resistivity).

The *detector capacitance* is an important parameter because it has influence on other properties such as noise, signal-to-noise ratio, or power consumption. Assuming a planar pn-junction with area A, the capacitance C can be calculated as

$$C = A \sqrt{\frac{\epsilon_s}{2} \frac{N_{eff}}{V_{bi} + V_{ext}}} . \tag{2.6}$$

Consequently, a larger bias voltage, a lower effective doping concentration, and a smaller pn-junction lead to a smaller capacitance. The size of the pn-junction is determined by the detector design, as discussed in Section 2.5.2.

Ideally, no net current flows across the pn-junction. However, thermal excitations generate charge carriers in the depleted region, causing a small *leakage current* [67].

NMOS, PMOS, CMOS

One of the most important structures built from silicon by allowing the formation of pn-junctions, and that are the most common transistors for digital circuits, are Metal-Oxide-Semiconductor Field-Effect Transistors (MOSFETs) [8]. Two types of MOSFETs exist: n-type MOSFET (NMOS) and p-type MOSFET (PMOS). Complementary MOS (CMOS) technology combines both types on the same *substrate* or *bulk*. A schematic of their cross sections is shown in Figure 2.2.

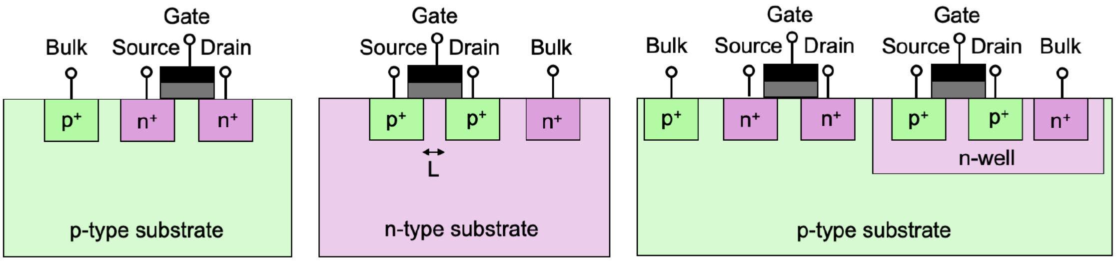

Figure 2.2: Schematic cross sections of NMOS (left), PMOS (middle), and CMOS (right) transistors. The thin insulating layer between the gate and the substrate is shown in gray. The minimum gate length (L) is indicated in the PMOS device. Adapted from [8].

NMOS (PMOS) transistors are created by implanting two highly doped n^+ (p^+) regions in a p-type (n-type) substrate. These two regions are called *source* and *drain*. Between them, a *gate* is placed on the surface, separated from the substrate by a thin layer of silicon dioxide (SiO_2) which insulates the gate from the substrate. Thus, the gate and the substrate behave as two parallel conductive plates. When a voltage is applied to the gate, an electric field is induced across the SiO_2, which controls the charge distribution in the substrate. Specifically, in an NMOS (PMOS) transistor, a positive (negative) bias voltage at the gate attracts electrons (holes) beneath the SiO_2 while repelling holes (electrons). In this way, a conductive *channel* between the source and drain is formed. Depending on the applied bias voltages, MOSFETs can operate in different modes [8, 68], which are briefly explained below for an NMOS transistor.

If the voltage applied between the gate and source is smaller than the threshold voltage, $V_{GS} < T_{THL}$, the transistor operates in the *cut-off mode*. The device is turned off, but a small drain current I_D still flows through the channel, known as *weak-inversion current*. In the *ohmic or linear mode*, $V_{GS} > T_{THL}$ and the applied voltage between drain and source $V_{DS} < V_{GS} - T_{THL}$. The device is turned on and I_D flows through the channel, which can be controlled by varying V_{DS}. If $V_{GS} > T_{THL}$ and $V_{DS} \geq V_{GS} - T_{THL}$, the device operates in *saturation mode*. In this mode, the channel does not fully extend to the drain (*pinch-off channel*), but I_D continues to flow due to the strong electric field created. The current can be controlled by varying V_{GS}. Commonly, digital circuits exploit the cut-off (OFF state) and saturation (ON state), where MOSFETs act as switches. In contrast, in analog circuits, MOSFETs are usually operated in the saturation regime, and they behave as controlled current sources or amplifiers.

The combination of NMOS and PMOS in a CMOS device is possible via the implantation of an additional large doped well (see Figure 2.2). This arrangement is explained in Section 3.1, using the investigated sensor in this work as an example. In the steady state, CMOS devices have no net current flowing, reducing the power consumption and heat dissipation. This makes CMOS an attractive transistor in circuit design.

An important characteristic of CMOS devices (as well as NMOS and PMOS) is the distance between the source and the drain, L. It is known as the *gate length*, and the minimum gate length quantifies the density of the CMOS logic. Reducing L allows for a higher logic density on the same substrate.

Basic Concepts of Silicon Detectors

Silicon detectors are used for the detection of charged particles and photons, as introduced in Section 2.2. They consist of a *sensor*, where a signal is generated (see Section 2.3), and the readout electronics, which are often implemented using CMOS circuitry (see Section 2.4). The side where the electronics are located is referred to as the *frontside*, while the opposite side is called the *backside*.

In a standard n-type (p-type) doped sensor, a p^+(n^+) *collection electrode* is implanted, such that the depletion region begins at the boundary of the collection electrode and extends into the n-type (p-type) bulk. The depleted volume is increased by applying a reverse bias voltage on the sensor frontside or backside. A silicon detector with a p-type (n-type) bulk and n^+ (p^+) collection electrode receives the name of n-in-p (p-in-n). The collection electrode collects charge carriers generated by particle interaction.

Silicon pixel detectors are segmented imaging devices formed through the creation of an array of pn-junctions. Each segmented part is called a *pixel*, and an array of pixels constitutes a *pixel matrix*. If the segmentation is performed only in one direction, the device is referred to as a *silicon strip detector*, where each segment is called *strip*. The distance between collection electrodes is called *pitch*, and defines the granularity of the detector. Vertex detectors, which require precise spatial resolution and high granularity, are often made of silicon pixel detectors, while tracker detectors, that require less spatial precision and granularity, typically consist of silicon strip detectors as they allow large areas to be covered at relatively low cost. An example of this approach is presented in Chapter 9, where the ITk detector for the ATLAS experiment is described.

2.2 Interaction of Particles with Silicon

Particles are detected through their interaction with matter. These interactions depend on the particle type, its energy, and the detector material.

In this work, an electron beam with an energy of about 5 GeV is used to characterize the performance of a silicon detector, with a total thickness from 21 to 50 µm and a depletion region of approximately 10 µm. For calibration purposes, an iron (^{55}Fe) source emitting X-rays, with an energy of approximately 5.9 keV is employed. Additionally, a 1 064 nm pulsed infrared laser, corresponding to a photon energy of about 1.2 eV, is used to study the sensor response. This section provides a brief review of the theory of particle interactions in silicon, which is necessary to understand the results. A more detailed description can be found in [8, 67].

2.2.1 Charged Particles

Charged particles interact with silicon through many interactions with individual atoms. Interaction with the electrons of the atoms results in ionisation or excitation, whereas the interaction with the atomic nuclei results in multiple Coulomb scattering or radiation emission (such as bremsstrahlung). In the following, these dominant interactions are described — ionisation, excitation, Coulomb scattering, and bremsstrahlung.

Ionisation and Excitation

Charged heavy particles, such as protons and heavy ions, lose energy when they pass through silicon via interactions with the electrons in the silicon atoms. These interactions can lead to the excitation of an electron to a higher bound energy level (excitation), or to its ejection from the atom (ionization).

Because energy loss results from many single interactions, it is expressed as the average energy loss per unit path length. It is described by the Bethe-Bloch formula [70] and depends on the particle mass and momentum. It is often parametrised as a function of the $\beta\gamma$[1], allowing the identification of different regions for all charge particles. At non-relativistic energies ($\beta\gamma \ll 3$), particles are highly ionising, depositing a large amount of energy in the material. At $\beta\gamma \approx 3$, the Bethe–Bloch formula reaches a global minimum, corresponding to the smallest energy deposition. A particle around this global minimum is called *Minimum Ionising Particle* (MIP). Towards larger $\beta\gamma$ values, the energy loss is dominated by radiative processes, and the energy deposition increases again.

Typical values of the mean energy deposition per unit thickness in silicon for MIPs are $\sim$388 eV μm^{-1} [20]. For a 50 µm sensor, this corresponds to an energy deposition of about 19.4 keV. MIPs are commonly used for detector characterization because their minimal energy losses provide the “worst-case” scenario for charge deposition (producing the lowest amount of signal).

Corrections to the Bethe Bloch formula are necessary for electrons (and positrons) due to their low mass, the fact that they are indistinguishable from the electrons in the outer shells of the silicon atoms, and because their energy loss is dominated by bremsstrahlung [20].

Energy Loss Fluctuations The Bethe Bloch formula describes the mean energy loss of charged particles passing through matter, while the actual loss fluctuates from event to event because the process is stochastic, meaning the number of interactions, as well as the energy loss in each interaction, varies. For example, if a charged particle collides head-on with an electron of an atom, it can transfer enough energy to eject the electron from its bound state. The emitted electron is called δ-electron, and it is ejected in a direction different from the original trajectory of the incoming charged particle. This δ-electron produces secondary ionisations, resulting in a large amount of energy deposited. As a consequence of these kinds of events, the statistical fluctuations of energy loss around the mean are significant and non-Gaussian. They can be parametrised by a Landau-Vavilov distribution [71, 72] with a maximum (representing the majority of collisions with little energy loss) and a long tail towards higher energy loss (representing the few collisions with large energy loss due to δ-electrons). Thus, the *most probable value* (MPV) of energy loss is lower than the average value.

In the case of a thin sensor, like the one investigated in this thesis, this fluctuation in the energy loss becomes more pronounced due to the smaller number of interactions between the charged particle and the material atoms compared to a thicker sensor [73]. This means that fewer interactions occur, but some of them involve high energy loss. As a consequence, the MPV shifts

[1] The ratio of the particle's velocity (v) to the speed of light in vacuum (c) is given by $\beta = v/c$. The Lorentz factor, γ, is defined as $\frac{1}{\sqrt{1-/\beta^2}}$.

towards lower energies for thinner materials. The Bichsel straggling calculations account for this effect and provide an accurate description of experimental data [74]. The theoretical Photon Absorption Ionisation (PAI) model [75] also describes the energy loss of charged particles in thin sensors and is widely used in simulations due to its flexibility in handling parameters such as the sensor thickness. In particular, the PAI model is applied in the simulations presented in this work.

For a detector with a finite energy resolution, effects like electronic noise in the readout or non-uniform charge collection (e.g., recombination or trapping) can be described as an additional Gaussian contribution. Consequently, a Landau-Gaussian convolution is commonly used to model the charge collection in a silicon detector.

Bremsstrahlung

For charged light particles, such as electrons or positrons, bremsstrahlung is the dominant energy loss mechanism at high energies. It is the electromagnetic radiation (photon emission) produced when a particle is deflected in the Coulomb field of an atomic nucleus. At low energies, the contribution from bremsstrahlung is still quite significant; however, ionisation losses dominate. The energy at which the energy losses from ionisation and bremsstrahlung are equal is called the *critical energy*. In silicon, the critical energy for electrons is 40.2 MeV [20].

The average distance traveled by an electron through a material before it loses all but $1/e$ (≈37%) of its initial energy via bremsstrahlung is called *radiation length* (X_0). In silicon, the radiation length is 9.36 cm [20]. Therefore, for a 4.6 GeV electron beam, the energy loss through bremsstrahlung in a 50 µm sensor is approximately 2.5 MeV. Although this value is much higher than the energy loss of a MIP (~19.4 keV), the photons emitted through bremsstrahlung have a low probability of being absorbed in thin silicon (see Section 2.2.2), and thus, they do not deposit significant energy within the sensor. As a result, the energy deposited by charged particles in thin silicon sensors is dominated by ionization.

Multiple Coulomb Scattering

Charged particles crossing a material are scattered multiple times, mainly due to interactions with the Coulomb fields of the nuclei of the material [76]. These small-angle scatterings lead to a net scattering angle, θ, with respect to the incoming particle trajectory.

For small deflection angles, the scattering angle distribution θ_{rm} follows a Gaussian distribution with mean $\langle\theta_{rm}\rangle = 0$. Its Root Mean Square (RMS) value, θ_{rm}^{RMS}, depends on the particle momentum p, velocity β, and charge z, and on the thickness of the traversed material in units of the radiation length x/X_0. It is defined by the Highland Formula [77]:

$$\theta_{rm}^{RMS} \approx \frac{13.6\,\mathrm{MeV}}{\beta c p}\, z \sqrt{\frac{x}{X_0}} \left[1 + 0.038 \ln\left(\frac{x}{X_0}\right)\right]. \tag{2.7}$$

This interaction, known as *Multiple Coulomb Scattering*, is undesired in tracking applications because it changes the particle trajectory, degrading the spatial and momentum resolution. According to Equation 2.7, higher particle momentum and velocity, as well as smaller material budget, reduce the RMS of the scattering angle distribution.

2.2.2 Photons

In contrast to charged particles, neutral particles, such as photons, interact with matter through localized processes. According to the Lambert-Beer's law [78], as photons traverse a medium, their number decreases exponentially as a function of the depth, and the attenuation rate depends on the material and photon energy [78]. The three main mechanisms of interaction of photons with matter in HEP are: photoelectric effect, Compton scattering, and pair production.

Photoelectric effect Photoelectric effect occurs when an incoming photon is absorbed by an atom, causing the emission of one of its bound electrons. The energy of the ejected electron is equal to the difference between the photon's energy and the electron's binding energy. When an inner-shell electron is ejected, a vacancy is created that can be filled by an electron from a higher-energy shell. This transition emits a photon with a characteristic energy equal to the energy difference between the shells, known as a fluorescence X-ray.

In order to eject the electron, the photon's energy must be greater than the electron's binding energy. Additionally, this effect is more likely to occur at photon energies just above the electron's binding energy, and becomes less probable as the photon's energy increases. This makes the photoelectric effect the dominant mechanism for photon interactions with silicon up to 100 keV. This range includes the typical X-rays used for silicon sensor calibration, such as those emitted by the iron (^{55}Fe) source introduced below and utilised in this work.

Compton scattering Compton scattering occurs when an incoming photon interacts with a free or weakly bound electron in an atom, transferring part of its energy to the electron [79]. The electron is ejected, and the incoming photon scatters with an angle related to the energy transferred. In silicon, the Compton effect dominates for photon energies between 100 keV and 1 MeV.

Pair production Above twice the electron rest mass ($2m_ec^2 \approx 1.022$ MeV), pair production becomes relevant. In this process, a high-energy photon interacts with the electric field of a nucleus and is converted into an electron-positron pair. Given the high photon energy required for this interaction, pair production is not relevant for the measurements performed in this work with the investigated sensor. However, it plays an important role in the context of calorimeters [8] and in the DESY II test beam generation (see Section 6.1).

Radioactive source

The energy deposited in the sensor creates electron-hole pairs, as will be explained in the following sections. The motion of these charge carriers induces a current on the collection electrode, which is then converted into a voltage signal by the readout electronics. In order to express the signal in physical units (number of electrons), calibration of the detector is required. Expressing the measured signal in this unit allows for direct comparison among different chips and with simulations.

Due to its availability, energy range, and emission of monochromatic X-ray photons with discrete energies, the ^{55}Fe radioactive source is commonly used for MAPS calibration. By measuring these monochromatic X-ray photons with well-known energies, the detector response can be calibrated — i.e., the signal amplitude can be converted into an equivalent number of electrons.

The ^{55}Fe isotope, with a half-life of 2.737 years, decays into ^{55}Mn via electron capture. This process results in the emission of Auger electrons, γ-photons, and X-rays [2]. Due to their low energy (below 0.6 keV), Auger electrons are absorbed within the source enclosure, and γ-photons are emitted with a very low probability (1.3×10^{-7} %) and can therefore be neglected. Consequently, the most relevant emissions for detector calibration are the X-ray photons at $K_{\alpha_1} = 5.9$ keV, $K_{\alpha_2} = 5.89$ keV, and $K_\beta = 6.49$ keV, with a probability of 16.57 %, 8.45 % and 3.4 %, respectively [80]. Given the energies, these photons interact with silicon primarily through the photoelectric effect. Since the K_{α_1} and K_{α_2} peaks are too close to each other in energy, and the energy resolution of the detector is typically not high enough for their separation, they are both referred to K_{α_1} in the following.

When a target foil is placed in front of the ^{55}Fe source, the emitted ^{55}Fe K_{α_1} can ionise the target atoms (if their binding energy is smaller than 5.89 keV), creating a vacancy in its inner shell. This vacancy is then filled by an electron from a higher-energy shell, releasing fluorescence X-rays, as explained above. In this work, a 75 µm thick titanium (Ti) foil is used, with the most relevant emissions being the $K_{\alpha_1} = 4.51$ keV and $K_\beta = 4.93$ keV [20]. The intensity of the fluorescence Ti X-rays depends on the original X-ray intensity, as well as the thickness of the Ti foil.

2.3 Charge Carrier Transport and Signal Formation in Silicon

When a charged particle passes through the silicon sensor, or a photon is absorbed within it, energy is deposited in the silicon and charge carriers are generated. As explained in Section 2.2, charged particles produce electron-hole pairs along the trajectory of the particle through ionisation, whereas a photon interaction generates charge carriers in a more localised region. Assuming that a mean energy of about 3.66 eV is required to produce an electron-hole pair in silicon at room temperature [67], the mean number of electron-hole pairs $\langle n_{eh} \rangle$ created is given by

$$\langle n_{eh} \rangle = \frac{\langle E_{deposited} \rangle}{3.66\,\text{eV}} \tag{2.8}$$

where $E_{deposited}$ is the energy deposited by the incoming particle. The *Fano factor* (F) describes fluctuations in the n_{eh} at constant energy deposition, which are smaller than those predicted by Poisson statistics because part of the $E_{deposited}$ goes into phonon excitations. Thus, $\langle \sigma^2_{n_{eh}} \rangle = F \cdot \langle n_{eh} \rangle$, with $F \approx 0.1$ for silicon [8].

In a partially depleted sensor, charge carriers generated in the non-depleted region move by diffusion until they recombine or reach the depleted region. In the depleted region, the electric field separates electrons and holes (see Section 2.1.3) and causes them to drift in opposite directions. The movement of the charge carriers — through *drift* and *diffusion* — induces a current on the collection electrode. The macroscopic motion of charge carriers is defined as a current density,

[2] γ-photons are produced by nuclear transitions, while X-rays are generated by atomic transitions.

J_{eh}, with the two motion components

$$J_{eh} = J_{eh}^{drift} + J_{eh}^{diff} \tag{2.9}$$

where the macroscopic current J_{eh}^{drift} and J_{eh}^{diff} are created by drift and diffusion, respectively.

During transport, electrons and holes can recombine to maintain equilibrium, reducing the total number of charge carriers that contribute to signal formation. Additionally, both drift and diffusion are governed by the *charge-carrier mobility*. This section introduces the concepts of mobility, drift, diffusion, recombination and signal formation.

2.3.1 Mobility

Charge carrier motion in silicon is influenced by scattering processes with phonons (lattice vibrations), impurities, and other imperfections [81]. To account for these microscopic effects, the mobility (μ) is introduced in the transport equations. It depends on macroscopic parameters, such as the temperature, the doping concentrations, and the type of charge carrier (electron or hole).

Several models exist that parametrise the charge carrier mobility in silicon. For the simulations in this work, the *extended Canali model* [82] is used, which combines the Jacoboni-Canali [83] and Masetti [84] models. In this way, the mobility (and thus the transport equations) accounts for the electric field (and its saturation, see Section 2.3.2) and temperature dependence from the Jacoboni-Canali, while incorporating the doping concentration dependence from the Masetti model. Simulation studies testing different models in sensors similar to the one investigated in this work can be found in [85, 86].

Typical values for the low-field electron and hole mobilities in silicon at room temperature are approximately [8]:

$$\mu_e = 1\,450\,\mathrm{cm^2/Vs} \qquad\qquad \mu_h = 500\,\mathrm{cm^2/Vs}. \tag{2.10}$$

2.3.2 Drift

In the presence of an electric field, charge carriers move under its influence via drift. The drift velocity, v_{drift}, is given by,

$$v_{drift} = \mu \cdot E. \tag{2.11}$$

Here, μ is the mobility (depending on the charger carrier type and accounting for scattering processes, as explained above) and E is the electric field magnitude. At low electric field magnitudes (below 1×10^3 V/cm), the mobility is approximately constant, and the drift velocity increases linearly with the electric field. However, at higher fields, the drift velocity saturates (mainly due to the increased scattering with phonons) and the effective mobility decreases [87].

The macroscopic current created by drift (J_{eh}^{diff} in Equation 2.9) can be expressed as,

$$J_{eh}^{drift} = q \cdot \mu \cdot n_{eh} \cdot E \tag{2.12}$$

with q the charge of the electron or hole, and n_{eh} the number of electron-hole pairs.

2.3.3 Diffusion

In the absence of an electric field, charge carriers move only by diffusion. Diffusion is characterised by a random thermal movement of charge carriers, causing charge clouds that slowly and isotropically expand. The charge cloud can be modeled as a function of time t by a Gaussian distribution with width σ_{diff} given by:

$$\sigma_{diff} = \sqrt{2Dt} = \sqrt{2 \cdot \frac{k_B \cdot T}{q} \cdot \mu \cdot t}, \tag{2.13}$$

D is the diffusion constant (related to the mobility μ through the Einstein equation), and k_B and T are the Boltzmann constant and the temperature, respectively. Using the values in Equation 2.10, typical diffusion constants at room temperature [8], in silicon for electrons and holes are

$$D_e = 37.5\,\mathrm{cm^2/s} \qquad D_h = 11.6\,\mathrm{cm^2/s}. \tag{2.14}$$

This means that, for example, a charge collection time of 10 ns leads to a diffusive expansion of electrons of approximately 8.7 µm.

Finally, the macroscopic current created by diffusion (J_{eh}^{diff} in Equation 2.9) can be expressed as,

$$J_{eh}^{diff} = q \cdot D \cdot n_{eh}. \tag{2.15}$$

2.3.4 Recombination

Charge carriers are continuously generated and recombined to maintain a thermal state of equilibrium. When electron-hole pairs are created by particle ionisation in silicon, the minority carrier concentration is perturbed and the generation rate temporarily increases. To restore the state of equilibrium, the recombination rate increases. This net recombination strongly depends on the temperature and doping concentration [81]. Several models describe the recombination mechanisms. In the simulations in this work, the Shockley-Read-Hall (SRH) [88] and Auger [89] recombination models are employed, which are briefly introduced below.

In the Shockley-Read-Hall model, recombination centers are typically located near the middle of the silicon band gap. These centers arise from defects in the lattice that create intermediate energy levels between the valence and conduction bands. They act as trapping centers, capturing mobile charge carriers (electrons from the conduction band and holes from the valence band), and facilitating pair recombination. In this process, the energy released is transferred to the lattice in the form of vibrations (phonons). The average time that a free charge carriers exist before recombination is called *carrier lifetime*. If the carrier lifetime is shorter than the charge collection time, charge carriers will not fully contribute to the signal.

For heavily doped silicon (above $5 \times 10^{18}\,\mathrm{cm^{-3}}$), the Auger [89] recombination becomes significant. In contrast to the SRH model, the released energy in an electron-hole recombination is transferred to another free carrier, which is excited to a higher energy state.

For the sensor investigated in this work, a doping above $5 \times 10^{18}\,\mathrm{cm^{-3}}$ is present in the substrate. Under such conditions, accurate modeling of the recombination processes is essential for realistic simulations. A combination of the two statistical models introduced, known as the Shockley-Read-Hall-Auger model [82] is used in the simulations performed in Chapter 4.

2.3.5 Signal Formation

The movement of charge carriers induces a current, I, on the collection electrode described by the Shockley-Ramo theorem,

$$\mathrm{I} = \mathrm{q} \cdot \mathrm{E_w} \cdot \mathrm{v} \tag{2.16}$$

where q is the charge of the moving charge carrier with velocity v, and E_w denotes the weighting field [90, 91]. The weighting field is a mathematical construct that quantifies the contribution of the movement of a charge carrier at a given position to the induced current on the collection electrode. For the sensor investigated in this work, the weighting field is strongest around the collection electrode and gradually decreases with increasing distance from the collection electrode [86].

Finally, the total charge Q induced on a collection electrode over a given time interval (t_1, t_2) is given by,

$$\mathrm{Q} = \int_{t_1}^{t_2} \mathrm{I(t)}\, \mathrm{dt}\,. \tag{2.17}$$

where I(t) is the instantaneous current induced on the electrode.

2.4 Signal Readout in a Silicon Pixel Detector

The readout electronics process the induced signal at the collection electrode. Figure 2.3(a) illustrates a typical readout chain for a pixel detector in HEP. First, the induced signal is fed into a preamplifier. A capacitive feedback loop is usually connected in parallel to the preamplifier, integrating the input current over time so that a voltage step (V = Q/C) proportional to the collected charge is obtained. The signal passes through a shaper, which returns the voltage step to baseline and suppresses high- and low-frequency noise. At this stage, the output signal has an amplitude and/or duration ideally proportional to the input charge.

A discriminator is used to reject low-amplitude noise and digitise the signal. It compares the input signal to a reference voltage, known as the *threshold*. Signals below the threshold are ignored, while those above it are processed by the digital logic. A typical form of digital processing consists of measuring the *Time-of-Arrival (ToA)* and *Time-over-Threshold (ToT)* of the signal. The ToA is defined as the time the signal crosses the threshold, while the ToT is the time that the signal stays above the threshold. If the ToT is proportional to the deposited charge, it serves as an energy measurement after calibration. Figure 2.3(b) illustrates the ToT and ToA for two different signal amplitudes. In addition, smaller signals also cross the threshold later than larger ones — an effect known as a *timewalk*.

The digitalised signal needs to be transmitted off the detector. Hence, a readout system is required. Different readout schemes exist for particle physics detectors. Among the most common are *data-driven*, *frame-based* and *triggered* modes [92]. In the data-driven scheme, the detector is acquiring and reading out data continuously. Since this scheme generates a large volume of data,

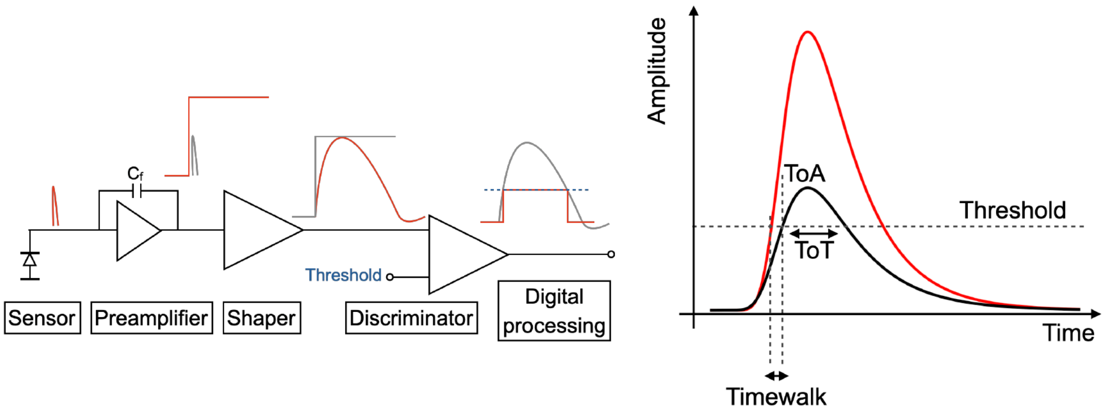

(a) (b)

Figure 2.3: Typical readout scheme for a silicon pixel detector in HEP. Adapted from [8]. (b) Sketch of two signals with different amplitudes and timewalk. For the smallest signal, the ToT and ToA are indicated.

zero suppression is usually implemented, meaning that only signals above threshold are read out. This is particularly useful in experiments with a low occupancy, where most of the pixels do not fire. In the frame-based (or shutter-based) scheme, the detector collects data only during a defined duration. This duration, known as the *shutter window*, defines the *frame* duration. Outside the shutter window, the readout can be performed. The frame-based readout scheme is often used in experiments with pulsed beams, when the readout can be performed during the intervals between beam pulses. In the triggered acquisition scheme, the readout is initialised by an external trigger decision. During the waiting time for the trigger decision, hit information is temporarily stored in internal buffers. This approach (followed, for example, at the LHC [93]) allows the detector to record only events of interest, thereby reducing the data volume. The detector investigated in this work supports both the frame-based and triggered schemes. In the frame-based scheme, the ToT or ToA values can be measured, as explained in detail in Section 3.3.

2.5 Hybrid and Monolithic Technologies

Depending on how the sensor and readout electronics are integrated, a silicon pixel detector can be classified as *hybrid* or *monolithic*.

2.5.1 Hybrid Pixel Detectors

A schematic cross-section of a hybrid pixel detector is shown in Figure 2.4(a). They separate the sensor (particle sensing element) from the readout chip (front-end electronics). This separation enables the independent development, optimisation and manufacturing of both components. As a result, novel sensor designs and advanced industry readout processes can be investigated. After manufacturing, these two parts are connected, typically using flip-chip and bump-bonding techniques. However, this interconnection step is one of the main disadvantages of the technology,

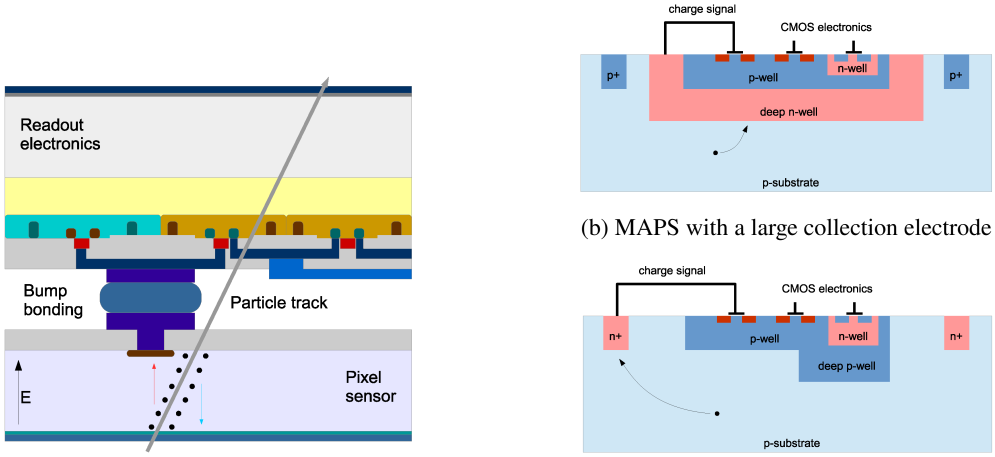

(a) Hybrid

(b) MAPS with a large collection electrode

(c) MAPS with a small collection electrode

Figure 2.4: Schematic of the cross section of a hybrid (a), MAPS with a small collection electrode (b), and MAPS with a large collection electrode (c) pixel detector. Taken from [94].

as it increases fabrication costs and the bump size limits the achievable pixel pitch. The overall material budget, consisting of several layers (sensor, bump bond, and readout chip), is also higher compared to monolithic technologies, potentially degrading the precision of particle trajectory reconstruction through multiple Coulomb scattering, as explained in Section 2.2.1.

This technology is employed in the ITk detector described in Chapter 9.

2.5.2 Monolithic Pixel Detectors

Monolithic Active Pixel Sensors (MAPS) integrate the sensor and front-end electronics into a single silicon bulk. The interconnection step required for hybrid detectors is no longer needed, reducing the material budget and enabling smaller pixel sizes. MAPS are manufactured using commercially available CMOS processes, which potentially lowers the cost of large-scale production. Depending on the size of the collection electrode, two design concepts can be distinguished: *MAPS with a large collection electrode* [95] and *MAPS with a small collection electrode* [96].

Large collection electrode MAPS In MAPS with a large collection electrode, the in-pixel electronics are inside the collection electrode, as illustrated in Figure 2.4(b). Generally, large depleted regions can be achieved with homogeneous field configurations when large bias voltages are applied to the sensor. Charge collection is fast and dominated by drift, resulting in a good timing resolution. The vertex detector at the Mu3e experiment currently being assembled is using MuPix11 sensors [97], which are MAPS featuring a large collection electrode design.

The main disadvantage of this technology is the high sensor capacitance (hundreds of fF [94]), which leads to high noise and large power consumption, as derived below.

Small collection electrode MAPS MAPS with a small collection electrode host the electronics outside the collection electrode, in dedicated wells, as shown in Figure 2.4(c). In the case of a p-type substrate, the bias voltage applied to the sensor is limited by the breakdown of the NMOS transistors, which are located directly in the biased p-well. This fact, combined with the small pn-junction from which the depletion region starts growing (small collection electrode), means that the sensor have a large undepleted area with complex field configurations. Sensor modifications [13, 96] have been developed during the last years to enhance the depletion region, increasing the amount of collected charge by drift.

The main advantage of this technology is the small detector capacitance, which is a direct consequence of the small area of the collection electrode. A lower sensor capacitance reduces the thermal and 1/f noise contributions at the output of the shaper [96], resulting a lower noise level and allowing the operation of the pixel detector at small thresholds. Additionally, since the signal amplitude voltage is inversely proportional to the capacitance ($V = Q/C$), MAPS with small collection electrode features large signals. The combination of reduced noise and increased signal amplitude results in a greater signal-to-noise ratio (SNR) compared to MAPS with larger collection electrodes. Besides, the analog front-end power consumption ($P_{analogue}$) scales proportionally with the capacitance (C) and inversely with the collected charge (Q) [96]:

$$P_{analogue} \propto \left(\frac{Q}{C}\right)^{-m} \qquad \text{with } 2 \leq m \leq 4. \tag{2.18}$$

Hence, minimising the detector capacitance not only improves the SNR but also reduces the analogue power consumption, and thus the heat dissipation and the material budget through cables and cooling (passive material). All these reasons make small collection electrode MAPS an attractive technology for tracking detectors.

An example of a large-scale detector using MAPS with a small collection electrode is the currently installed vertex detector at ALICE composed of ALPIDE sensors [98]. Future upgrades of this experiment — ALICE ITS3 scheduled for 2030 [99] and ALICE3 for 2036 [100] — also plan to employ this technology.

Part I

Characterization of the Hybrid-to-Monolithic Technology Demonstrator

CHAPTER 3

The Hybrid-to-Monolithic Technology Demonstrator

The Hybrid-to-Monolithic (H2M) technology demonstrator is a MAPS that has been developed to explore the capabilities of the 65 nm CMOS imaging process in tracking applications for future high-energy lepton collider experiments such as CLIC [10] or FCCee [11].

The chip architecture is based on a hybrid readout chip from the Medipix/Timepix family [101, 102], with the goal of learning about the challenges and opportunities involved in porting this hybrid readout architecture to a monolithic chip. This transition combines the advantages of a monolithic design (see Section 2.5.2) with an advanced and well-tested hybrid architecture, reducing the design effort.

The chip design has been carried out using a digital-on-top design workflow. In this approach, the analog front-end blocks are implemented first, and then the digital logic is synthesized and automatically placed around the predefined analog cells. This results in a compact layout and a more automatised design procedure. A dedicated digital cell library has also been developed and tested, which is approximately 25 % smaller than standard cell libraries, reducing the space needed for the digital logic. Compact and fast in-pixel readout circuits, described below, have also been designed.

The H2M test chip features a matrix of 64×16 square pixels, with a pitch of 35 µm, resulting in a total sensitive area of $2.24{\times}0.56\,\text{mm}^2$. Including the periphery, differential-to-CMOS receivers/drivers, and I/O connectors at the bottom of the pixel matrix, the total chip size is $3{\times}1.5\,\text{mm}^2$. Each pixel comprises a small collection electrode, an analog front-end, and digital logic that allows for 8-bit pulse processing. The relatively large pixel size, compared to other chips in the same technology, is necessary to fit the complex readout circuitry within each pixel. Additionally, outer tracker detectors for future lepton collider proposals such as CLIC need to cover a large surface (around $100\,\text{m}^2$), while achieving a single-point resolution of approximately 7 µm. Therefore, the investigation of a large pixel size and optimised sensor layout is of interest to enable coverage of large areas while reducing costs.

The following chapter covers the sensor design, including the analog front-end and digital logic, chip periphery components, readout architecture, and a description of the samples investigated in this work.

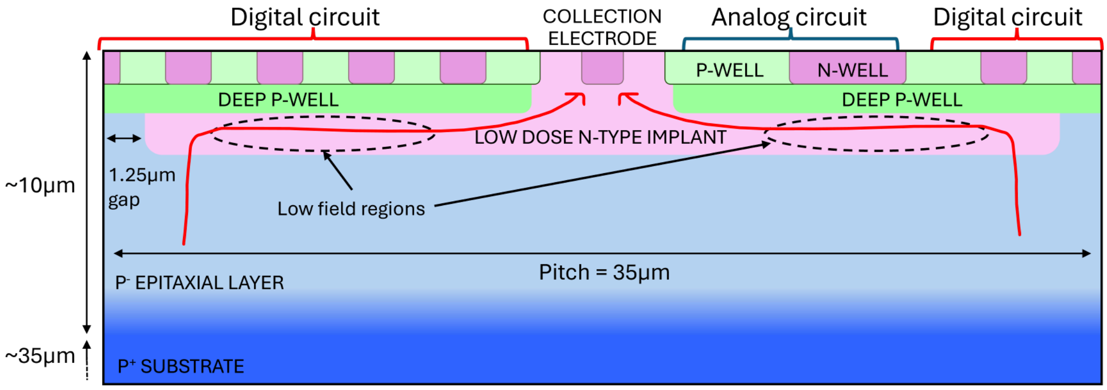

Figure 3.1: H2M cross section sketch of one pixel. The low field regions, located far from the n-gap and the collection electrode, are indicated. The drift paths of electrons are depicted as red arrows. The metal interconnection layers placed on frontside are not shown. Taken from [103].

3.1 Sensor Design

The H2M sensor is fabricated in a modified TPSCo 65 nm CIS (Tower Partner Semiconductor Co., Ltd. 65 nm Image Sensor CMOS) process [13], and has been wafer-thinned to a total chip thickness of approximately 50 μm.

The total chip thickness includes approximately 5 μm of metal interconnection layers, a 10 μm p-type epitaxial layer, and a 35 μm highly-doped p-type substrate. Since the substrate is highly doped, charge carriers in that region have a short lifetime and recombine before they can contribute to signal formation. As a result, mainly the ~10 μm epitaxial layer serves as the active volume.

The H2M sensor layout is known as *n-gap* layout [13], where a low-dose n-type implant with a 2.5 μm gap at the pixel boundaries is introduced, as illustrated in Figure 3.1. Compared to the *standard* layout [13], which lacks this implant, the depletion region within the epitaxial layer is enlarged, improving the charge collection efficiency. The gap at the pixel boundaries forms a horizontal doping gradient, introducing a lateral electric field component, improving the efficiency and timing performance of the sensor [104]. This is visible in the simulations of Chapter 4. A small n-type collection electrode is located at the top center of the pixel, acting as the only charge collection implant.

Each pixel has its own analog front-end and digital logic, integrating CMOS circuitry with both NMOS and PMOS transistors, using the quadruple well technology [105]. This allows NMOS transistors to be placed in p-wells and PMOS transistors in n-wells, shielded by a deep p-well that prevents unwanted charge collection by these n-wells. A simplified cross-sectional view of the n-wells and p-wells within the deep p-well, hosting the analog and digital circuits, is sketched in Figure 3.1, and a top view of four pixels is illustrated in Figure 3.2. In the analog front-end, the PMOS transistors are placed in a ~4 μm wide n-well, while those for the digital logic can be placed in narrower n-wells, distributed uniformly within the deep p-wells. The reason for this is that digital logic uses standard cells with fixed n-well sizes, which are stacked together to form long and thin stripes. The compact digital cell library of H2M makes these stripes even thinner. For the analog front-end, there is more freedom in the arrangement of the PMOS transistors,

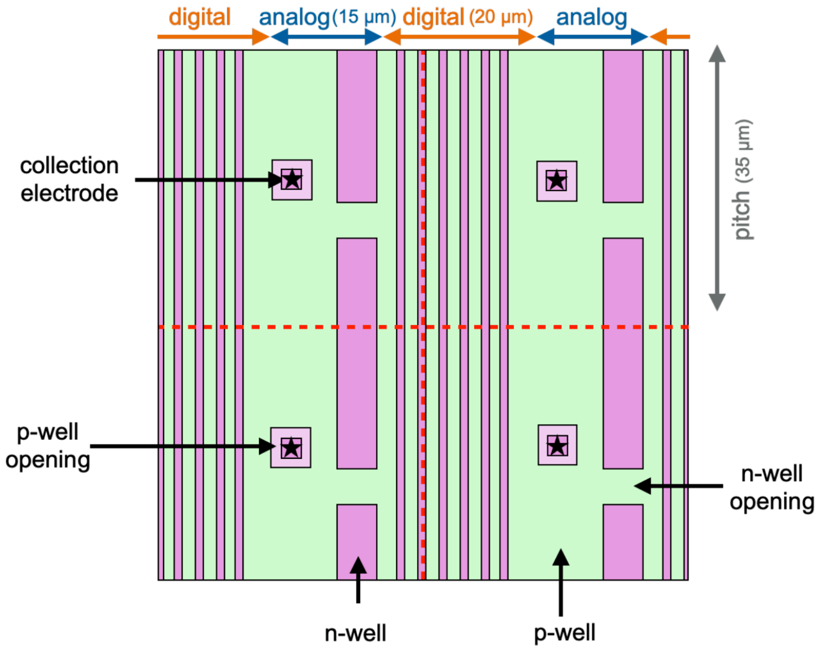

Figure 3.2: Simplified layout of the n-well and p-well positions within the deep p-well in four pixels. The position of the collection electrode, analog front-end, and digital logic is also indicated. The pixel boundary is marked with a red dashed line.

and usually only one n-well is preferred. Additionally, larger transistors generally improve the chip performance (e.g., lower noise) and adding circuitry complexity further increases the n-well size. In the case of H2M, this results in a wide n-well for its analog front end. This n-well is not continuous and has a cut (see Figure 3.2), referred to as the *n-well opening*. The distance between the deep p-well and the collection electrode is called *p-well opening*.

The sensor is reverse-biased from the front side through a contact placed outside the pixel matrix, connecting the deep p-well and p-substrate to the same potential. The negative bias voltage applied is limited by the voltage tolerance of the NMOS transistors inside the p-wells. Since there is no junction between the p-well and the p-substrate in the gap region of the deep n-type implant, current flows through this gap when the p-well is biased differently from the p-substrate. This prevents the sensor from operating with different p-well and p-substrate bias voltages. The n-type collection electrode is held at a positive potential of 0.8 V, and the negative bias applied at the p-well and p-substrate is referred to as the *sensor bias voltage*.

3.2 Analog Front-end

The current pulse induced on the collection electrode by the movement of charge carriers in the sensor is first processed by the in-pixel analog front-end. A schematic of the main components of the analog circuitry within each pixel is shown in Figure 3.3, and described in this section.

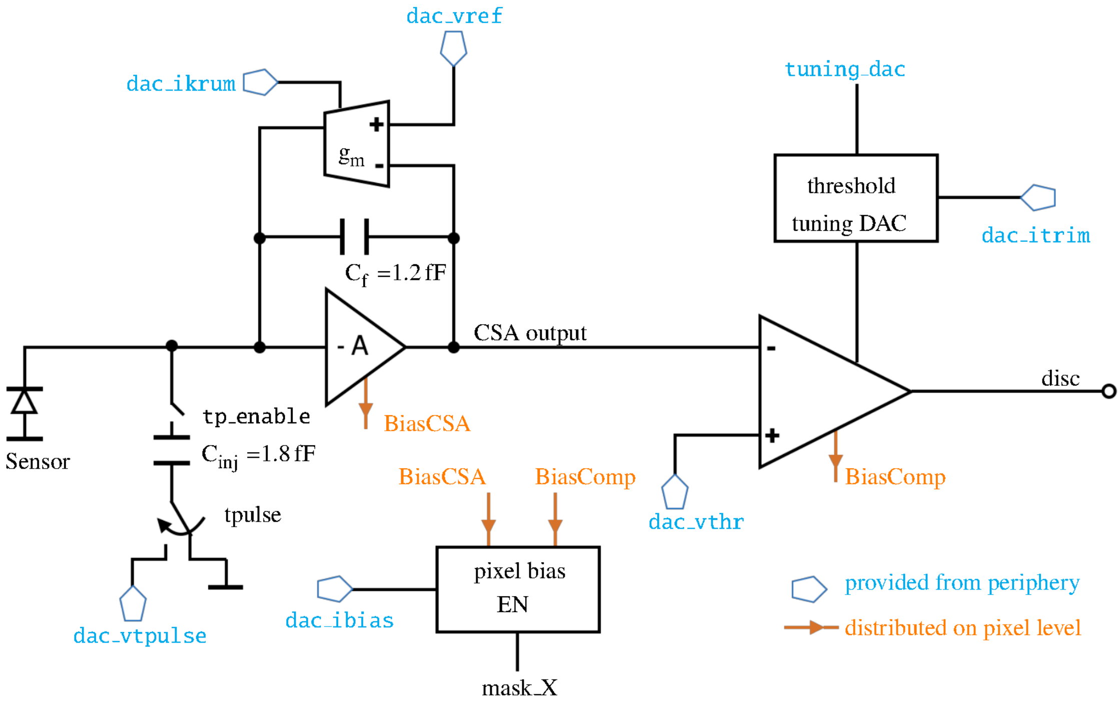

Figure 3.3: Simplified schematic of the in-pixel analog front-end.

3.2.1 Charge Sensitive Amplifier with a Krummenacher Feedback

The first stage of the analog in-pixel front-end is a charge-sensitive amplifier (CSA) [67] with Krummenacher feedback [106]. The inverter amplifier has been designed with a gain of approximately 120 mV/ke$^-$. Therefore, negative and small current pulses, resulting from the collection of electrons in the thin p-epitaxial layer, are amplified and inverted. The CSA integrates the input current over time using a feedback capacitor, C_f, which has a design value of 1.2 fF. Ideally, the output voltage V_{out} of the CSA is then proportional to the input charge $Q = \int I(t)dt$, and is given by

$$V_{out} = -\frac{Q}{C_f}. \tag{3.1}$$

The output voltage is reset (discharge of C_f) with a Krummenacher feedback. It consists of a linear discharge controlled by a feedback current (*ikrum*), which is provided by dac_ikrum, an 8-bit DAC (digital-to-analog converter) in the chip periphery. This feedback current is supplied to all pixels globally. According to front-end simulations, variations of about 12 % in the effective dac_ikrum applied are expected between pixels due to manufacturing processes [107].

The feedback current determines the speed at which the signal returns to baseline: a higher *ikrum* results in a steeper descent, meaning that the signal returns to baseline faster. This concept is illustrated in Figure 3.5 (top) with a triangular signal shape for two different *ikrum* settings. The continuous discharge of the C_f with the applied feedback current also reduces the leakage current at the CSA input, maintaining the baseline stable over time, and reducing the noise. Since the signal decay is linear and always has the same slope, the time it stays above the threshold is proportional to the input charge, enabling energy measurements in the Time-over-Threshold acquisition mode (see Section 3.3).

Two additional 8-bit DACs, `dac_ibias` and `dac_vref`, set the CSA current bias and the Krummenacher reference voltage, respectively.

3.2.2 Threshold Comparator

The CSA with a Krummenacher feedback is followed by a continuous-time threshold comparator, where the CSA output voltage signal is compared to a reference voltage. The global reference voltage (or threshold) is defined by an 8-bit DAC, located in the chip periphery and provided to all the pixels (`dac_vthr`). Local fine-tuning per pixel is achieved through an additional 4-bit DAC, `tuning_dac`. The granularity of this fine adjustment are set by an additional 8-bit DAC in the chip periphery (`dac_itrim`), which controls the current for the tuning DACs. A higher value of `dac_itrim` results in a larger tuning step size, and thus covers a wider dynamic range, with the cost of losing precision.

3.2.3 Test Pulse Injection

The analog front-end also offers test pulse injection through a dedicated 1.8 fF capacitor connected to the CSA input. A step voltage can be injected for each pixel by enabling the `tp_enable` DAC. If this setting is disabled, the injector capacitor is electrically disconnected.

Test pulses can be configured via dedicated registers and DACs, allowing control over polarity (`tp_polarity`), amplitude (`dac_vtpulse`), duration (`tp_on` and `tp_off`), and timing relative to the shutter opening (`shutter_tp_lat`). Injection after the shutter is opened ensures the recording of the entire test pulse. Frame data acquisition employing a shutter window is explained in Section 3.3.

A sketch of a test pulse with a positive polarity is shown in Figure 3.4. A test pulse of one polarity has its corresponding pulse with opposite polarity, with the same absolute amplitude, due to charge conservation (discharge of C_{inj}). Additionally, overshoots or undershoots become visible, especially at higher amplitudes. By setting the same duration to the shutter window and `tp_on`, the pulse with inverted polarity is not acquired.

3.2.4 Pixel Masking

During data taking, pixels that do not meet the requirements of the equalisation procedure (see Section 5.2) are masked. This is done individually by switching off their digital logic and setting the analog front-end to a low-power state.

3.3 Digital Logic and Acquisition Modes

This section describes the digital logic of the H2M test chip, which processes the output of the analog front-end.

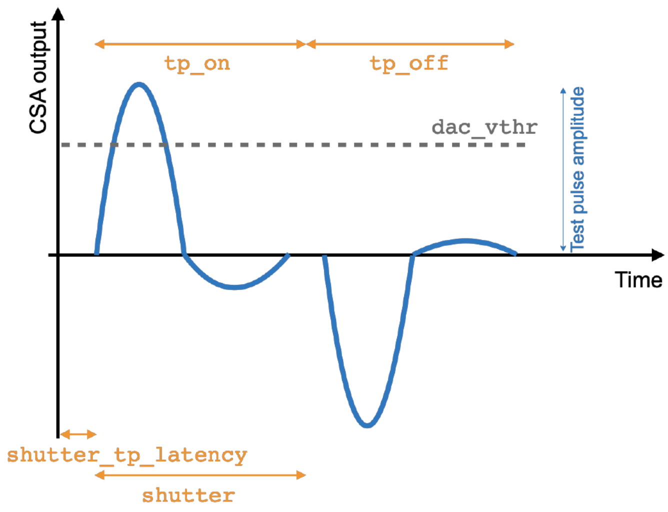

Figure 3.4: Simplified schematic of a test pulse injection with positive polarity.

The chip supports operation in four acquisition modes: Time-over-Threshold (ToT), Time-of-Arrival (ToA), photon counting, and triggered. For this purpose, each pixel contains a configurable 8-bit counter, which is used differently depending on the selected acquisition mode. These acquisition modes are mutually exclusive, such that, e.g., ToT and ToA cannot be measured at the same time.

In ToA and ToT acquisition modes, each pixel records when the time of the first threshold crossing in the corresponding frame/shutter and the accumulated time above threshold, respectively. In ToA mode, the measured value corresponds to the number of clock cycles from the threshold crossing to the closing of the shutter. For a ToT measurement, the number of clock cycles between the rising and falling threshold crossings is counted. If several hits occur (several threshold crossings) within the same shutter window, their individual ToT values are summed for each pixel. This is known as integrated ToT measurement.

The acquisition clock operates at 100 MHz, meaning that each clock cycle has a duration of 10 ns. This sets a lower limit on the time resolution in ToA mode of $10\,\text{ns}/\sqrt{12} \approx 2.9\,\text{ns}$. As the chip cannot measure ToT and ToA simultaneously, timewalk corrections cannot be applied (see Section 2.4).

In photon counting mode, each pixel counts the number of times the signal crosses the threshold within a shutter window.

In triggered mode, hits are validated using an external trigger signal before being read out. The on-pixel 8-bit counter is initially configured with a preset value that corresponds to the trigger latency. This trigger latency is a fixed delay between the particle crossing H2M and the arrival of the trigger signal at H2M, including the logic processing time. When a pixel detects a signal, the 8-bit counter begins counting from the preset value and produces a one-clock-cycle carry signal when it reaches its maximum value (at 256 counts). An external strobe signal derived from the trigger defines a configurable coincidence window, which should be large enough to accommodate the H2M time walk. This strobe signal is sent through the same line used for the shutter in the

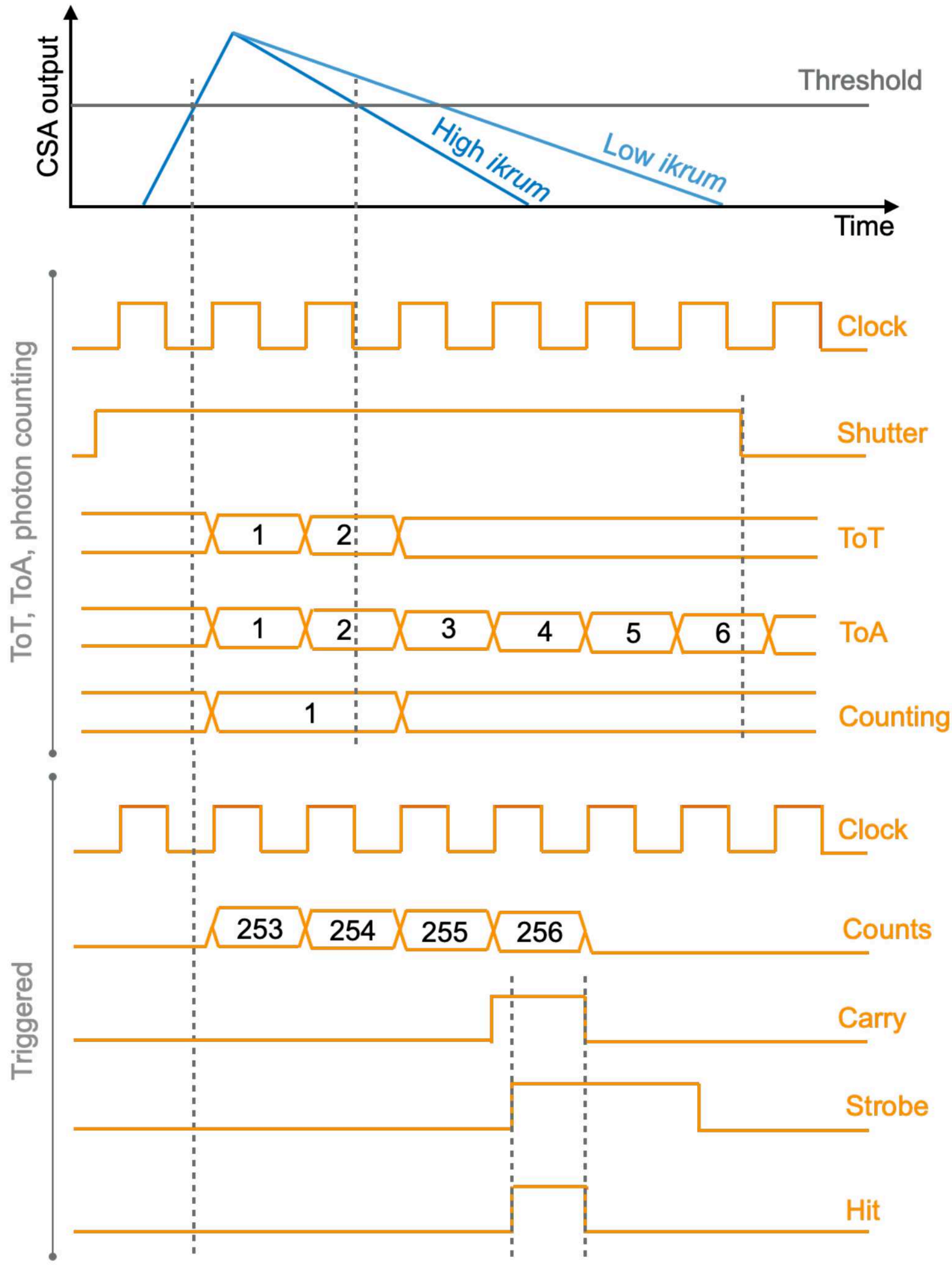

Figure 3.5: Schematic layout of the four acquisition modes. On top, the CSA output signal is represented with a triangular shape, whose return-to-baseline slope depends on the *ikrum* setting. In the middle, for the high *ikrum*, the signal is compared to a reference voltage (threshold), and the corresponding measured counts in ToT, ToA, and photon counting modes are indicated. At the bottom, a readout in triggered mode is depicted.

other three acquisition modes. If the carry signal lies within the strobe window, the hit is valid. As the in-pixel counter is used for the latency, only binary information (hit or no hit) is available.

A schematic layout of the four acquisition modes is shown in Figure 3.5. In this example, two clock cycles are recorded in ToT mode, six clock cycles in ToA mode, and one count in photon counting mode. For the triggered mode, the counter is preset to 253, and the strobe window is equal to two clock cycles.

3.4 Configuration and Readout

The chip is configured via a slow control interface based on the Medipix4/Timepix4 protocol [101, 102], which uses a serial communication bus (sends data one bit at a time) featuring dedicated data and clock signals. Configuration signals are applied either globally or locally. Global configuration signals affect the entire pixel matrix, controlling settings such as the threshold, shutter window, acquisition mode selection, or trigger latency. Local signals are applied to individual pixels, enabling features like test pulse injection, pixel masking, and tuning DAC.

While the clock frequency of the slow control is 40 MHz, the readout operates using a 100 MHz clock (10 ns per clock cycle). Due to the small chip matrix size, the clock is generated externally and distributed directly to the pixel matrix. During readout, the 8-bit pixel counters in each pixel are connected as a shift register, and their data are shifted sequentially from the top to the bottom of each column across the entire matrix. The readout is performed without zero suppression, meaning that the whole pixel matrix is read out, even if no hits are recorded in some pixels.

3.5 The Caribou DAQ System

Powering, slow control, and readout of the H2M chip are performed using the Caribou DAQ system [108, 109]. The Caribou DAQ is a versatile and modular system designed to support rapid, cost-effective, and easy integration and testing of various detector prototypes. Its hardware consists of three main blocks: the System-on-Chip (SoC) platform, the Control and Readout (CaR) board, and the chip board. Figure 3.6(a) shows a picture of the setup with an H2M sample.

The SoC platform is implemented on a ZC706 evaluation board (ZYNQ board) [110]. The board combines a Kintex-7 FPGA with a dual-core ARM Cortex-A9 processor. They communicate through an AXI bus, which allows the software (Peary) to access and control hardware registers. The ARM processor runs a lightweight Yocto-based Linux distribution (Poky) and can be accessed remotely with an Ethernet connection. The FPGA acts as an interface between the software and the detector. Both the software and firmware are detector-specific and are stored on an SD card.

The ZC706 board interfaces with the CaR board with an FPGA Mezzanine Card (FMC) connector. The CaR board provides all the necessary infrastructure to operate a wide range of detector prototypes, including the H2M test chip. It includes 8-input 12-bit analogue-to-digital converters (ADCs), programmable voltage and current supplies, and an I^2C bus for chip communication. It can also receive external clock and trigger signals from systems, such as the Trigger Logic Unit (TLU). The entire setup is powered by a 12 V DC external supply, and can be connected to an Ethernet network and accessed remotely via Secure Shell (SSH) [111].

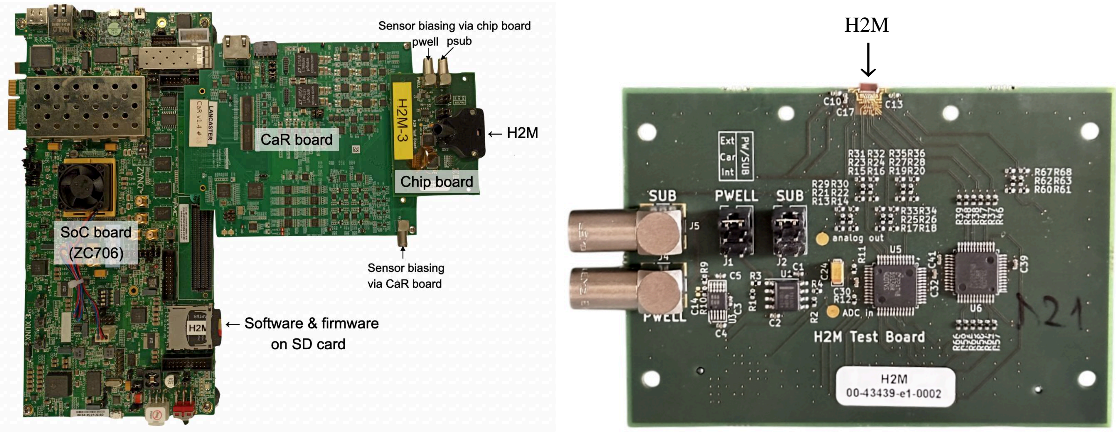

(a) (b)

Figure 3.6: (a) Picture of the Caribou DAQ system with an H2M sample. (b) H2M chip board.

The H2M chip is mounted on a chip board, which is connected to the CaR board via a 320-pin SEARAY connector. This custom-designed PCB is designed explicitly for each detector prototype.

3.5.1 The H2M Chip Board

The H2M chip board provides a mechanical and electrical interface between the chip and the CaR board. It only contains passive components and serves to route signals and supply lines to the sensor. Debugging of some signals is possible through access to bias lines via surface-mounted connectors. Additionally, it also includes a three-jumper-configurable connection, enabling flexible routing of the sensor bias voltages. The sensor bias voltage can then be supplied via LEMO connectors either on the chip board or on the CaR board, or internally generated by the CaR board. For precise biasing and independent control of the p-well and p-substrate voltages, in this work, the sensor is biased through the two mounted LEMO connectors on the chip board, which are connected to a Keithley 2410 source measure unit (SMU). A picture of the chip board is shown in Figure 3.6(b).

The H2M chip is glued and wire-bonded at the edge of the chip board, as shown in Figure 3.7, with the active area staying outside to reduce the material budget and allow for backside illumination. A conductive glue is used for both mechanical attachment and contribution to a uniform distribution of the p-substrate bias sensor across the pixel matrix. Communication with the chip board (clock and data transmission, ground, and power supply) is handled via wire bonding to the Input/Output (I/O) pads. Some of them, such as the p-well and p-substrate biasing, are duplicated.

3.6 Backside Thinning of H2M Samples

The H2M chip is thinned at wafer level to a nominal total thickness of 50 µm. After thinning, wafers are diced and the individual chips are tested on a probe station to detect failures in the

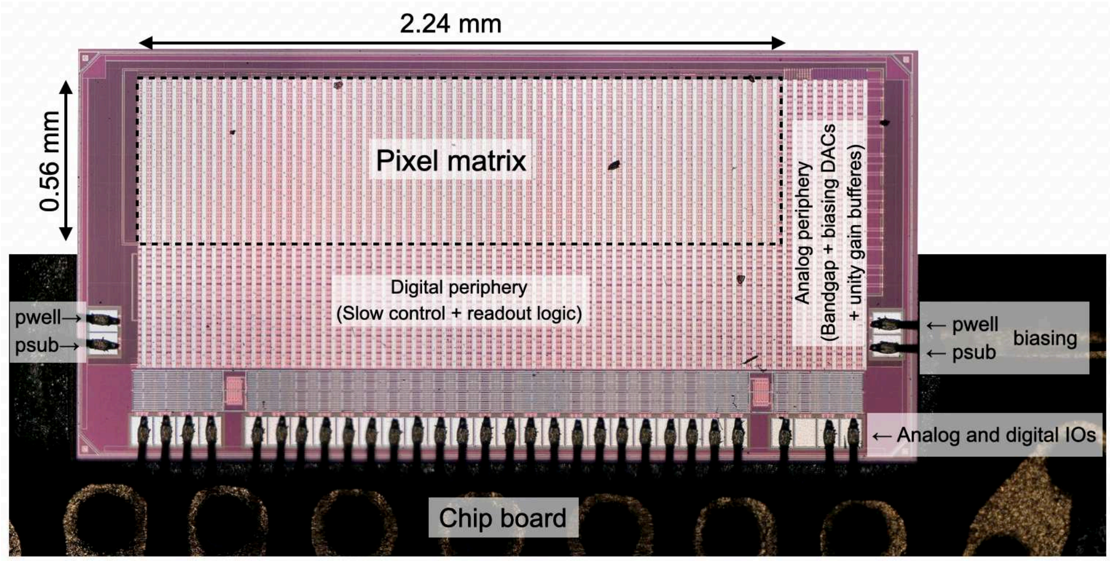

Figure 3.7: Picture of an H2M chip glue and bonded onto a chipboard. The locations of the pixel matrix, the analog and digital periphery, and biasing and IO pads are indicated.

powering of the analog front-end and digital logic. Chips that pass this initial test are then glued and wire-bonded onto the chipboards and tested in the laboratory and in test beam campaigns. A picture of an H2M chip is shown in Figure 3.7.

The thickness of the epitaxial layer in this technology is about 10 µm [13], while the highly-doped p-substrate (which does not significantly contribute to the signal formation) adds around 35 µm. Therefore, thinning the substrate is an attractive way to reduce the material budget without reducing the signal amplitude. To investigate this, individual chips that had already been diced were further thinned down to 21 µm by OPTIM Wafer Services [112].

In this work, four samples are tested in the laboratory and test beam campaigns, and are listed in Table 3.1. Two of them have the nominal thickness of 50 µm, while the other two have been thinned to 25 µm and 21 µm, respectively. These are the thinnest samples tested in the technology so far.

A second motivation for thinning of the substrate is the possibility of detecting soft X-rays (X-rays with low energies), which have a short absorption length, via backside incidence. In the case of a top-side incidence, the soft X-rays could be stopped in the interconnection metal layers and do not reach the sensor, so they cannot be detected. For backside incidence, soft X-rays will reach the active region only if the substrate is thin enough. Otherwise, the charge will be deposited and recombined in the highly doped thick substrate before being collected. These studies on backside illumination with low-energy X-rays are planned and are not included in this thesis.

Table 3.1: Samples and their total chip thicknesses investigated in this work.

Sample	Physical chip thickness [µm]
H2M-2 (50 µm)	50
H2M-3 (50 µm)	50
H2M-8 (25 µm)	25
H2M-10 (21 µm)	21

CHAPTER 4

Monte Carlo Simulations of H2M

Sensor simulations are a valuable tool for studying sensor behavior, accelerating the design process, as prototype chip submissions are expensive and require a long time from design to testing.

Using a commercial 65 nm process enables relatively low-cost large-scale production. However, it restricts access to manufacturing process information that is not publicly available. This lack of detailed process information, combined with the complex electric field configuration in sensors with small collection electrodes, makes sensor simulations challenging.

In this context, the Tangerine project [59, 60, 113] in collaboration with the CERN EP R&D programme on technologies for future experiments [114] has developed a technology-independent approach using generic doping profiles for the simulation of MAPS [14].

Section 4.1 summarises the simulation workflow and explains the adaptations made for simulating the H2M sensor in order to understand and predict its response to MIP detection. A focus is set on discussing the limitations of the method. Section 4.2 presents the simulation results. The comparison between data and simulations is provided in Chapter 8.

4.1 Technology-Independent Approach Using Generic Doping Profiles

Generic doping profiles are used in 3D TCAD simulations of pixel cells to model the field within the sensor. These generic doping profiles, derived from semiconductor sensor physics assumptions, do not contain any proprietary information and do not include any structures within the deep p-wells.

The simulated electric fields and doping profiles with TCAD [115] are imported into the Allpix^2 framework [116]. Although TCAD can also be used to simulate the sensor response to incident particles, such simulations are computationally intense. Therefore, the Allpix^2 framework is employed to carry out high statistical simulations, including stochastic fluctuations stemming from the physics processes, using less computational power — while TCAD recalculates the electric field in every step of the simulation, Allpix^2 does not. This combined use of TCAD and Allpix^2 has been proven to significantly reduce simulation time without compromising precision compared to using TCAD alone [86].

The approach has been shown to reproduce measurement results obtained from other chips manufactured in the same 65 nm CMOS imaging technology as H2M, such as APTS [14, 117, 118].

4.1.1 TCAD Simulations

A brief overview of the TCAD simulations is given below, although they were not performed in this work. Instead, the doping profiles and electric fields were provided by a colleague, whose work is summarised in [117], and used as input for the Monte Carlo simulations described in Section 4.1.2.

The first step in the simulation workflow is the simulation of the electric field from generic doping profiles. This is performed using Sentaurus TCAD (Technology Computer-Aided Design) from Synopsys [115]. After defining the doping profiles, a 3D mesh is created using tetrahedral elements. The mesh density depends on the doping gradients, with a finer mesh in the non-uniform regions where the doping changes, such as at the boundary between differently doped areas. The quasistationary simulation is then performed at the mesh vertices by computing Poisson's and carrier continuity equations, and the electric field within the sensor is obtained.

Figure 4.1 shows an example of the electric field on the left and the lateral electric field on the right obtained for a sensor bias of 0 V, −1.2 V, −3.6 V and −6 V. The white and brown lines indicate the boundaries of the depleted region and the position of the pn-junctions, respectively. At 0 V, a large volume of the pixel cell remains undepleted, increasing the sensor capacitance, and thus reducing the signal output (see Equation 3.1) and increasing the noise. As the sensor bias voltage increases, the depleted region extends and the electric field increases. The low electric field regions are located at the pixel boundaries and in the low-dose n-type implant.

Compared to −3.6 V, at a −1.2 V sensor bias, a small undepleted region and a low-field region surround the collection electrode. An effect of this is an increase in the sensor capacitance and an enhanced carrier collection through diffusion. The electric field is also weaker beneath the deep p-well, along the path that charge carriers follow. Ramping the voltage to −6 V shows no significant difference compared to a sensor bias of −3.6 V.

Charge carriers follow the electric field in the depleted region, as introduced in Section 2.3. Figure 4.2 shows the streamlines of the electric field. At every point, the tangent to the streamline indicates the direction of the electric field, and therefore, they correspond to the path that the charge carriers will follow. Electrons generated in the epitaxial layer will first drift upwards, and then move horizontally toward the collection electrode. Note that during this horizontal movement, electrons pass through a low-field region.

Since most of the signal originates from the epi layer and the highly doped p-substrate is assumed to be homogeneous, only the top 10 µm of the sensor is simulated with TCAD. The deepest simulated doping concentration value with TCAD is then extrapolated in Allpix^2 throughout the substrate to the sensor backside, and the electric field in the substrate is set to zero.

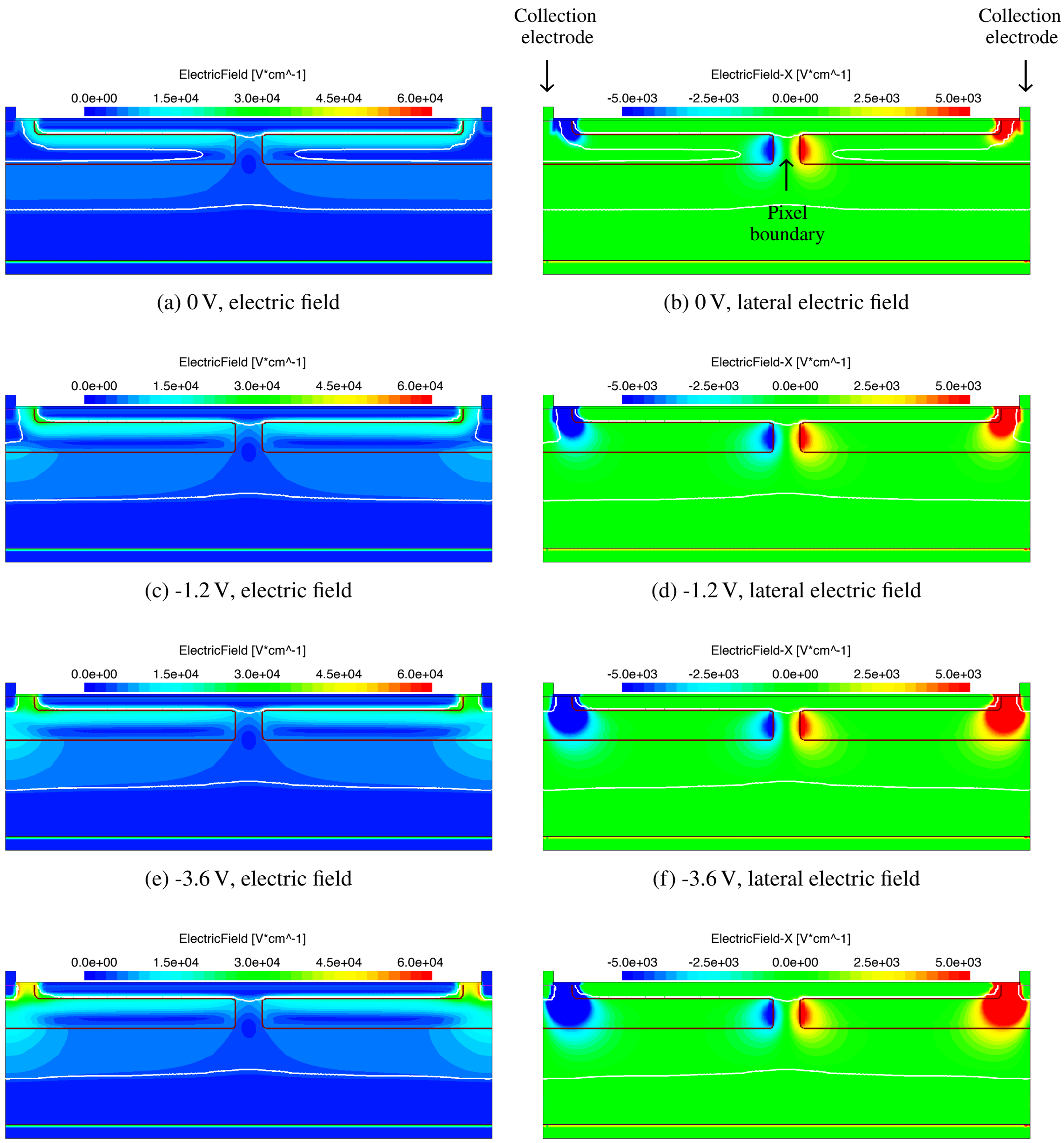

(a) 0 V, electric field

(b) 0 V, lateral electric field

(c) -1.2 V, electric field

(d) -1.2 V, lateral electric field

(e) -3.6 V, electric field

(f) -3.6 V, lateral electric field

(g) -6 V, electric field

(h) -6 V, lateral electric field

Figure 4.1: TCAD simulation of the electric field (left) and lateral electric field (right) on the epitaxial layer using generic profiles. Different sensor bias voltages are shown. The white line defines the boundary of the depleted region, and the brown lines the position of the pn-junctions. Data from [119].

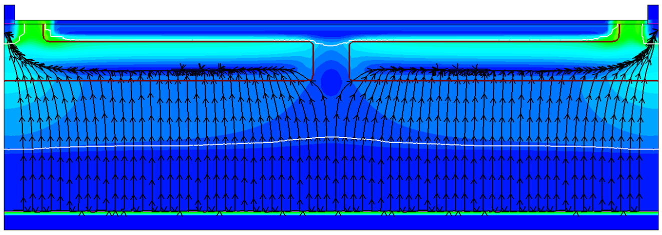

Figure 4.2: TCAD simulation of the electric field for a sensor bias of −1.2 V using generic profiles. The white line defines the boundary of the depleted region, and the brown lines the position of the pn-junctions. The black arrows are the streamlines of the electric field. Taken from [119].

4.1.2 Allpix Squared Monte Carlo Simulations

Allpix^2 is a modular, open-source framework for the simulation of solid state detectors [116]. The configuration files used in this work are provided in Appendix A. A detailed discussion of the parameter choices can be found in [14, 86, 120].

The Allpix^2 framework interfaces with the Geant4 simulation toolkit [121] through the `[GeometryBuilderGeant4]` and `[DepositionGeant4]` modules, which are used to simulate the particle source and the corresponding energy deposition, taking physical effects and statistical fluctuations into account. In this work, a 5 GeV single-electron Gaussian spread (DESY-like) beam is simulated. The width of the Gaussian beam profile is 100 µm and strikes the sensor surface perpendicularly (along the z-direction).

The deposited energy is converted into charge carriers using Equation 2.8, with fluctuations modeled using the Fano factor [122]. The maximum step length allowed for energy deposition is 0.5 µm. This means that the maximum step that can happen before a Geant4 calculation is performed is 0.5 µm along the trajectory of the particle, although the actual steps are often smaller. The physics list `FTFP_BERT_EMZ` is used together with the photo-absorption ionisation model to provide a more accurate description of the ionisation energy loss in the thin sensor [75], as introduced in Section 2.2.

The doping profiles and electric fields generated with TCAD are imported into Allpix^2 . This is handled by the `[DopingProfileReader]` and `[ElectricFieldReader]` modules. For that, the vertex coordinates and values obtained from the quasistationary simulation of TCAD are mapped onto a regularly spaced grid with 525×525×100 divisions (in x, y, and depth) using a barycentric interpolation. This corresponds to 15×15×10 divisions per µm — a mesh granularity that has been optimised in previous studies [120]. The TCAD simulation covers only the top 10 µm of the sensor, and the deepest calculated values for the doping concentrations are extrapolated throughout the substrate to the backside of the sensor, while the electric field is set to zero in the substrate. In total, a 50 µm-thick sensor is simulated. A pixel matrix of 20×20 pixels is created by replicating the individual pixel structure, surrounded by an additional 200 µm of sensor material to account for edge effects.

The generated charge carriers are propagated, using the [GenericPropagation] module, in groups of maximum five throughout the sensor. This maximum number of charge carriers per group has been optimised in [120]. A fourth-order Runge-Kutta-Fehlberg method [123] is employed to compute the particle equations of motion in the defined electric field. After each Runge-Kutta step, random diffusion is accounted for by applying an offset derived from Equation 2.13. The timestep size used for the Runge-Kutta-Fehlberg integration is between 0.05 ps and 0.5 ps, and changes dynamically in the simulation to maintain precision. The charge carrier mobility (see Section 2.3.1) is computed using the extended Canali model [83] and recombination (see Section 2.3.4) is described by the combined Shockley-Read-Hall-Auger model [88], which depend on the doping concentrations. The integration time is set to 25 ns, meaning that after 25 ns from the start of the event, charge carrier propagation is stopped.

The propagation of charge carriers stops when they reach any surface of the sensor (or the implant, after version 3.0.0 of the framework [116]). Charges within the defined implant at the end of integration time are transferred to the readout. This is done through the [PulseTransfer] module, which also creates approximately pulses using the charge arrival times. The size of this implant, 2.2×2.2×1.3 μm^3 (in x, y, and depth), is larger than the n-well collection electrode to account for the diffusion of charges during the last propagation steps. Charges located outside the implant are effectively lost and do not contribute to the signal formation.

Finally, the signal is digitized using a simple model with a fixed threshold employing the [DefaultDigitizer] module. The noise level and threshold smearing applied come from the laboratory measurements presented in Section 5.3, while the track resolution is derived from the test beam studies discussed in Section 6.5.4. For a sensor bias of −1.2 V, a noise level of 40 electrons is used, and the threshold is applied with a 17 electron dispersion. A track resolution of 3.7 µm is used to smear the Monte Carlo truth. The threshold, noise, and track resolution smearings are drawn from a Gaussian distribution with the specified widths.

For each chip parameter (such as sensor bias or threshold), 500 000 events are simulated, and the statistical uncertainties are calculated.

4.1.3 Observables from Simulation

From the simulations, the efficiency, clustering, spatial resolution, and collected charge distributions are evaluated. These are typical parameters used to characterise the performance of the chip in particle detection, and are directly linked to the detector requirements derived in Chapter 1. This section defines and explains how these observables are calculated.

Efficiency The H2M simulated efficiency is defined as the ratio of events detected by H2M to the total number of events hitting the sensitive area of the detector. For that, the Monte Carlo truth for the hit position (smeared by 3.7 µm) is used, and an event is considered "detected" if the collected charge is above the defined threshold.

Clustering Charge carriers generated by a single perpendicularly-incident charged particle, even in the absence of an external magnetic field, can be collected by multiple pixels due to charge sharing between neighboring pixels. Adjacent pixels firing in the same event are grouped into a cluster, and the cluster size is defined as the number of pixels it contains.

Spatial resolution The spatial residuals are defined as the difference between the reconstructed cluster center and the true Monte Carlo particle position. The width of the residuals ($RMS_{97.7\%}$) is calculated as the RMS of the central 99.7% of the distribution, and defines the spatial resolution. Since the collected charge (q) is available for each pixel, the cluster center ($x_{cluster}, y_{cluster}$) is reconstructed using a charge-weighted reconstruction algorithm,

$$x_{cluster} = \frac{\sum_{i \in C} \omega_i \cdot x_i}{\sum_{i \in C} \omega_i} \quad , \quad y_{cluster} = \frac{\sum_{i \in C} \omega_i \cdot y_i}{\sum_{i \in C} \omega_i} \tag{4.1}$$

with C the set of pixels in the cluster, (x_i, y_i) the pixel center coordinates, and $\omega_i = q_i$ the weights given by the charge collected in each pixel. For two-pixel clusters, the η-correction algorithm [124] is applied to account for non-uniform charge sharing within the pixel cell. This is done using the Corryvreckan framework [125], as explained in Section 6.4.2, after exporting the simulated data from Allpix^2 into the Corryvreckan. Exporting simulated data from Allpix^2 is done using the `[CorryvreckanWriter]` module. The data are then read in Corryvreckan using the `[FileReader]` module.

For the spatial resolution study, the track resolution in the simulation is set to zero. Appendix C.4 illustrates the change in spatial residuals resulting from the addition of a track resolution smearing.

Signal For each cluster, the seed pixel is defined as the one with the highest amount of charge carriers collected exceeding the threshold. Thus, the seed pixel charge refers to the charge collected by the seed pixel. The cluster charge is given by the sum of the charges in all pixels within the cluster.

4.1.4 Limitations of the Simulation Approach

In this work, the simulations consider an idealised sensor with doping profiles based on basic semiconductor physics assumptions. The deep p-wells, that host both the analog front-end and the digital logic, are represented in TCAD as flat profiles, without internal structures such as the n-wells of the PMOS transistors. The H2M analog front-end, including the CSA with Krummenacher feedback, is not simulated. Additionally, only quasistationary simulations have been carried out in TCAD to obtain the electric field. Transient simulations, which can be used to study the signal response to a traversing charged particle, have not been performed, and signal pulse-shape and timing studies are not included here.

More complex simulations, relying on proprietary information, including the entire sensor layout (with internal structures in the deep p-wells), as well as readout electronics and TCAD transient simulations, have been performed at CERN. The results are published in [103, 126]. Chapter 8 highlights the differences between the simulation methods when they are compared to test beam data.

4.2 Simulation Results

The following section presents the simulation results obtained. More detailed quantitative discussions are given when discussing the same observables measured in the test beam in Chapter 7.

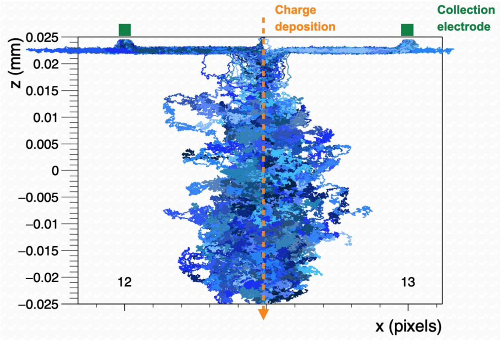

(a)

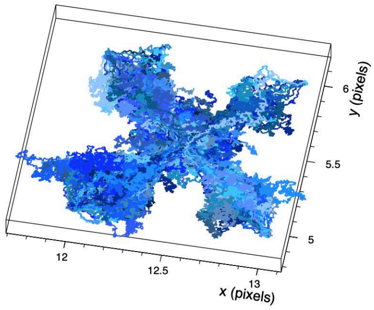

(b)

Figure 4.3: Blue linegraphs representing the paths of the collected electrons from a lateral (a) and top (b) view. The vertical axis shows the sensor depth, and the x-and y-axes use "pixel pitches" as units. The position of the collection electrodes is indicated by green boxes at integer number positions. The trajectory of the incoming charged particle near the pixel corners is sketched in orange. The sensor is biased at −1.2 V.

4.2.1 Charge Collection

Figure 4.3 shows a linegraph, indicating the path followed by the collected electrons. In the example, the charge carriers are generated after the interaction of a charged particle with the sensor near a pixel boundary. For charge deposition close to the pixel boundary, most electrons are collected by the neighboring pixels via lateral drift in the epitaxial layer. In particular, charge carriers first drift nearly vertically and then horizontally beneath a region approximately 1 µm thick under the p-wells. A small portion of electrons is collected mainly via diffusion from the sensor substrate.

In the region of the gap in the deep n-type implant, charge collection via diffusion is more pronounced, as expected from the movement of electrons in this low-field lateral region.

4.2.2 Efficiency

The simulated efficiency is shown as a function of the threshold for different sensor bias voltages in Figure 4.4. An efficiency above 99% is observed up to a threshold of 250 electrons. As expected from the sensor design, the behavior is similar across different sensor bias voltages (from −1.2 V to −6 V), with the small differences attributed to the undepleted region around the collection electrode at low bias voltages (see Figure 4.1). At a sensor bias of 0 V, the large undepleted region, visible in Figure 4.1(b), leads to low efficiency even at low thresholds.

At higher thresholds (above 250 electrons), the efficiency begins to drop, in particular at the corners and edges of the pixel. At the pixel boundaries, charge sharing becomes more likely, leading to the collected charge being divided among adjacent pixels. As the threshold increases, the probability of collecting enough charge carriers to exceed the threshold decreases, resulting in a large number of inefficient events. This effect is illustrated in Figure 4.5, which shows the in-pixel efficiency map projected onto four pixels for two different thresholds. The relatively high threshold values of 224 and 300 electrons have been chosen to match those discussed during the test measurements in Chapter 7.

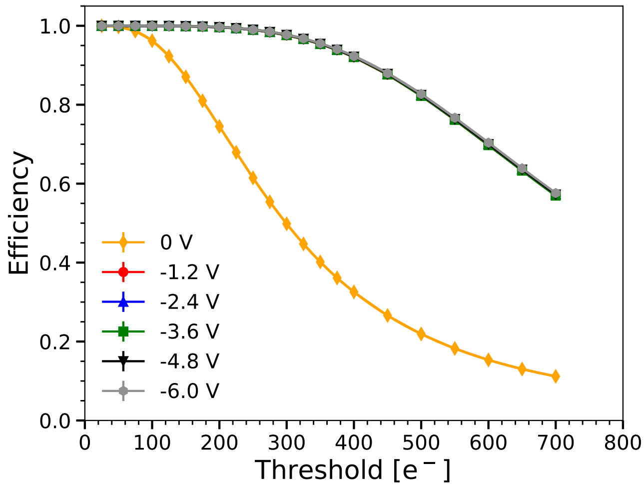

Figure 4.4: Simulated efficiency as a function of the threshold for different sensor bias voltages.

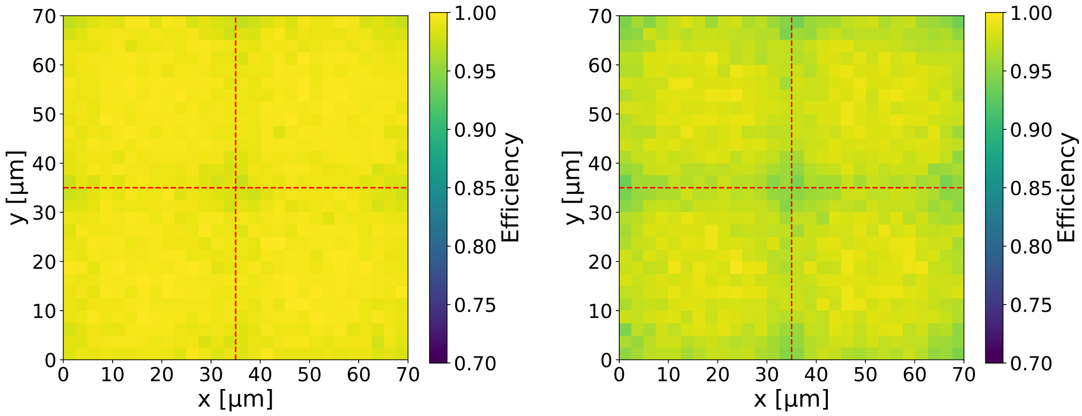

(a) 224 electrons

(b) 300 electrons

Figure 4.5: Simulated in-pixel efficiency projected onto four pixels for a threshold of 200 (a) and 300 (b) electrons. The sensor is biased at $-1.2\,\mathrm{V}$. The pixel cell boundary is marked with a dashed red line.

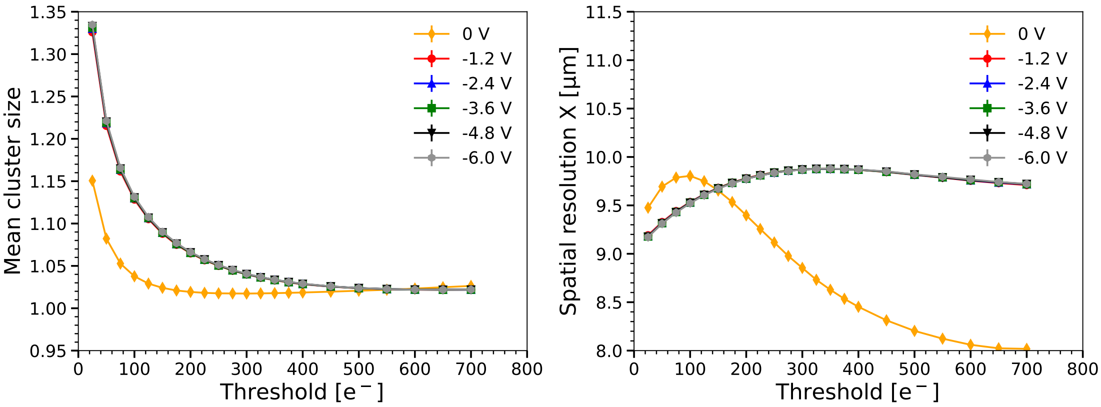

(a) Cluster size

(b) Spatial resolution in X

Figure 4.6: Simulated cluster size (a) and spatial resolution in X (b) as a function of the threshold for different sensor bias voltages.

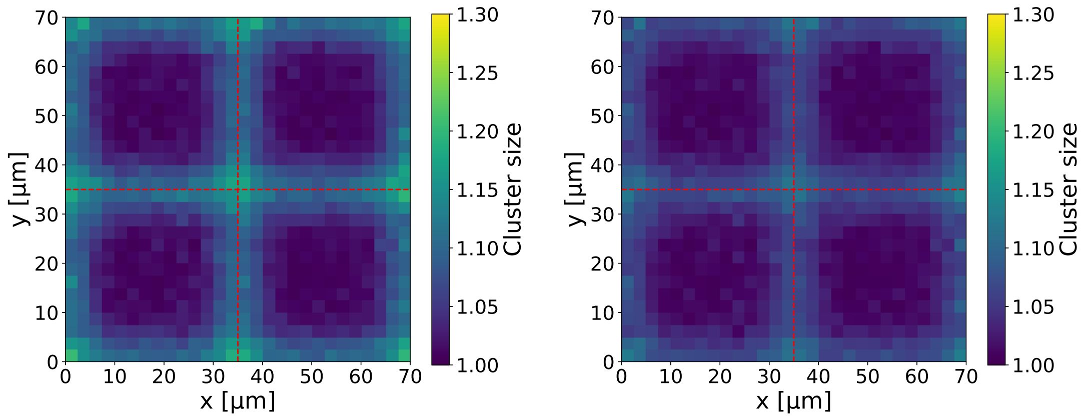

(a) 224 electrons

(b) 300 electrons

Figure 4.7: Simulated in-pixel cluster size projected onto four pixels for a threshold of 200 (a) and 300 (b) electrons. The sensor is biased at -1.2 V.

4.2.3 Cluster Size and Spatial Resolution

Figure 4.6(a) shows the mean cluster size as a function of the threshold for different sensor bias voltages. The minimal charge sharing between adjacent pixels leads to a majority of single-pixel clusters, resulting in a spatial resolution close to the binary resolution, which is limited by the pixel pitch ($35/\sqrt{12} \approx 10.1$ µm). The spatial resolution in X (same in Y due to the square geometry of the pixel) is shown in Figure 4.6(b) as a function of the threshold.

Only in the edges and corners of the pixel cells, a sufficient amount of charge is shared with neighboring pixels to overcome the detection threshold. This can be seen in Figure 4.7, where the

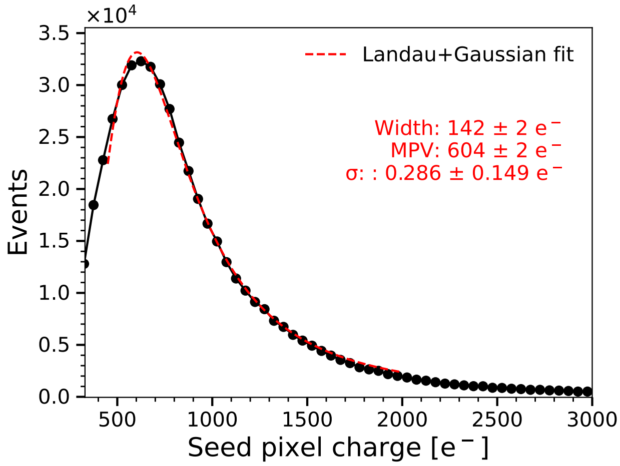

Figure 4.8: Simulated seed pixel charge distribution. The sensor is biased at −1.2 V, and a threshold of 300 electrons is used. A Landau-Gaussian convolution is used for fitting. The fit parameters of the width and MPV of the Landau distribution, and the standard deviation of the Gaussian component, are displayed.

in-pixel cluster size map is dominated by clusters of size one, with larger clusters appearing only at edges and corners, particularly at lower thresholds.

At larger thresholds, efficiency decreases, and charge collection is limited to particle incidences around the collection electrode. Consequently, the effective pixel size shrinks, leading to an improved spatial resolution. This effect is visible above 400 electrons in Figure 4.6.

A similar effect is observed at a sensor bias of 0 V, where the efficiency drops sharply with increasing threshold. Above 100 electrons, the low efficiency at 0 V is limited to a small region, resulting in an improved spatial resolution. Below 100 electrons, the simulated noise and the highly non-uniform field with a large undepleted bubble around the collection electrode (see Figure 4.1(b)) result in degraded spatial resolution compared to larger bias voltages. Since most of the events have a cluster size of one, the reconstructed hit position (deteriorated by the non-uniform field) cannot be corrected by the η-algorithm.

4.2.4 Signal Distribution

Figure 4.8 shows the seed pixel charge distribution for a threshold of 300 electrons. It follows the expected Landau convolved with a Gaussian shape described in Section 2.2.1. This function is fitted, and an MPV of (604 ± 2) electrons is obtained at a sensor bias voltage of −1.2 V. This value is consistent with the expected charge collected in the ~10 µm epitaxial layer [8].

Furthermore, no significant differences have been observed at higher bias voltages. Since the depleted region does not change and the cluster size remains constant, the collected charge is similar.

4.2.5 Integration Time Studies

Due to the large pixel pitch, low-field regions appear along the path of charge carrier collection. The lateral component of the electric field, strongest at the vertical pn-junction, loses strength as it gets further from it (increasing again close to the collection electrode). Consequently, the generated electrons travel longer distances in low field regions, and charge collection is slower compared to other sensors with smaller pixels. To illustrate this effect, the integration time is reduced from 25 ns to 12 ns. This integration time corresponds to the propagation time of charge carriers in the simulation. When the propagation time ends, charges that arrived at the collection implant are processed by digitisation, and the simulated observables are computed.

Figure 4.9(a) shows the efficiency as a function of the threshold for two integration times (25 ns and 12 ns) and sensor bias voltages (−1.2 V and −6 V). After 12 ns, not all the charges have reached the collection electrode, and thus, the efficiency is lower compared to the 25 ns integration time. At higher bias voltage, the stronger electric field speeds up charge collection and reduces diffusion, so the difference in efficiency between the two integration times becomes smaller.

Although a larger bias voltage in principle leads to reduced charge sharing and smaller mean cluster size, Figure 4.9(b) shows the opposite trend: at −6 V, the cluster size is larger than at −1.2 V for the 12 ns integration time. This is explained by the reduced efficiency at −1.2 V, where carriers diffusing at the pixel edges (giving rise to larger cluster sizes) are not collected with a short integration time, resulting in a smaller cluster size. With an integration time of 25 ns, no significant differences are observed between the sensor bias voltages.

Figure 4.9(c) shows the spatial resolution in X as a function of the threshold. The smaller cluster size for a shorter integration time worsens the spatial resolution. At larger thresholds, however, the reduced efficiency for the 12 ns integration at −1.2 V, caused by the losses of diffused charges at the pixel boundaries, leads to an improvement in the spatial resolution.

This study highlights the relatively slow charge collection in a large-pixel-pitch sensor of H2M, characterized by non-uniform charge collection times. It also suggests the need for a sufficiently long integration time in the analog front-end to record the full signal.

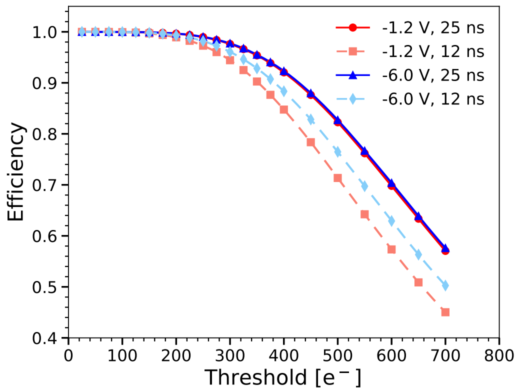

(a) Efficiency

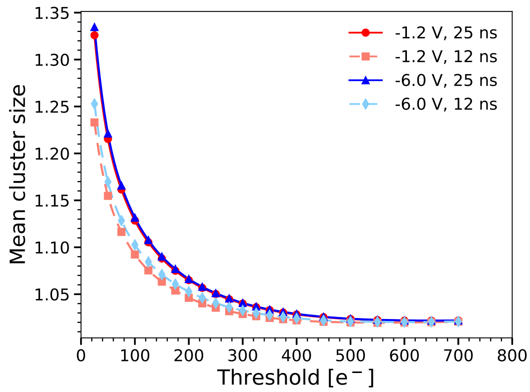

(b) Cluster size

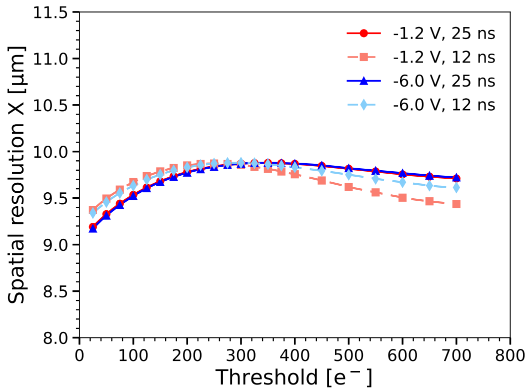

(c) Spatial resolution in X

Figure 4.9: Simulated efficiency, cluster size, and spatial resolution for two different integration times and sensor bias voltages.

CHAPTER 5

Performance in Laboratory Measurements

This chapter presents the results of the H2M chip characterisation conducted in the laboratory. It includes the first electrical test, optimisation of operational parameters, a description of the equalisation procedure for the pixel matrix, noise determination, calibration with radioactive sources and analog test pulses, power consumption studies, and measurements with a laser setup. The discussion also includes a comparison with the analog front-end simulations based on the chip design, as well as comparisons among different samples and chip settings.

5.1 Current-Voltage Characteristic

Once the chips are glued and bonded to the chip boards, the first electrical test consists of the current-voltage (IV) measurement. The p-well and p-substrate bias voltages (corresponding to the reverse bias of the sensor diode) are simultaneously increased in steps of 0.02 V, and the total chip p-well and p-substrate bias currents are recorded. The n-well collection electrode is fixed at +0.8 V.

The scans are performed on a configured chip, kept in the dark at room temperature, and a Keithley 2410 SMU is used for both voltage biasing and current measurement. After each voltage step, a 1.5 s delay is added to allow for stabilisation, after which 20 current measurements are taken to determine the mean and its error (RMS). The delay between each of the 20 measurements is 1 ms. The short measurement duration of the full scan (less than two minutes) ensures that variations in room temperature are negligible.

Figure 5.1(a) shows the IV characteristics for four samples with different total chip thicknesses. The thinnest sample (21 µm) presents a significantly higher current, and further systematic studies of thin samples are currently ongoing to have a better understanding of this behavior. Nevertheless, the four samples have similar noise levels (see Section 5.2). For the other three samples, punch-through current appears at an absolute bias voltage of 4.8 V. At this bias voltage, the measured current between two consecutive points exceeds 0.2 µA and starts to increase exponentially. Therefore, to ensure safe operation in laboratory and test beam measurements, the absolute sensor bias voltage is limited to 4.2 V.

When biasing the p-well and p-substrate at different voltages, current flows in the sensor through the 2.5 µm gap in the deep n-type implant (see Figure 3.1). This effect is shown in Figure 5.1(b), where the p-well is kept at a fixed value while the p-substrate voltage is varied and its current

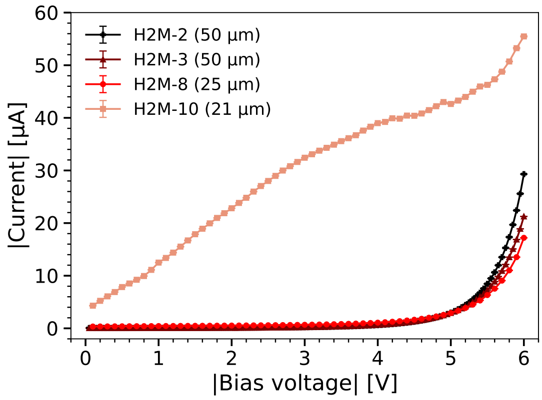

(a)

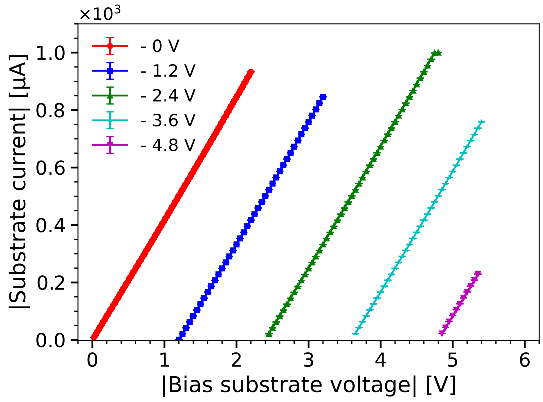

(b)

Figure 5.1: (a) IV measurements for different samples. (b) IV measurements for different p-well bias voltages with the H2M-3(50 µm) sample.

is measured. The measured p-substrate currents increase immediately and linearly, indicating that current starts to flow already at small voltage differences between the p-well and p-substrate. Consequently, all the following measurements are performed with the p-well and the p-substrate set to the same bias voltage.

5.2 Threshold Equalisation

The manufacturing process introduces pixel-to-pixel variations in the baseline position, which results in different effective thresholds among pixels [67, 127]. To correct for this, H2M features a 4-bit local threshold adjustment per pixel (see Section 3.2), allowing for 16 possible tuning DAC settings (`tuning_dac`). This process of finding the optimal `tuning_dac` setting for each pixel to achieve a uniform response across the matrix, with small threshold dispersion among pixels, is called *equalisation*. For that, a noise-based equalisation procedure, similar to the one described in [128] and explained below, is applied. The advantage of this method, compared to those based on calibration-pulse injection, is its insensitivity to gain variations, and it does not depend on the injection circuitry (e.g., pixel-to-pixel variations in the injector capacitor that can cause differences in the test pulses). In the following, the global threshold, or `dac_vthr` setting, is referred to simply as the threshold.

A threshold scan in counting mode is performed using a 10 µs shutter window for each `dac_vthr`, and the procedure is repeated ten times to reduce statistical uncertainties. All counts, corresponding to noise-induced threshold crossings, in this 100 µs window are summed and plotted per pixel as a function of the threshold. An excess of counts is expected near the baseline due to baseline fluctuations crossing the threshold multiple times and increasing the counter. This distribution is described by a Gaussian distribution, where the mean represents the baseline position of the pixel, and the width indicates the single-pixel noise in units of the threshold DAC (THL DAC). This is repeated for the 16 tuning DAC settings. The top of Figure 5.2 shows the occupancy as a function of the threshold for a pixel operated at three different tuning settings.

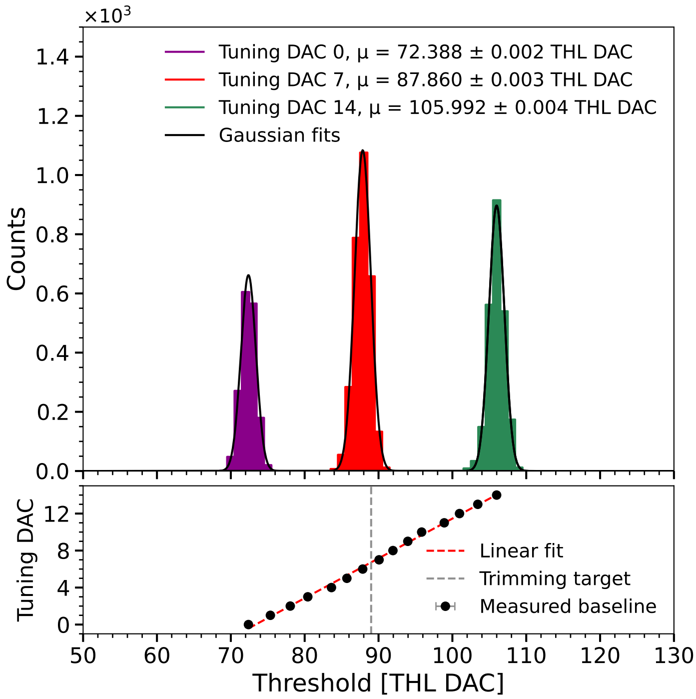

Figure 5.2: On the top: Noise occupancy as a function of the hit-detection threshold for a pixel operated at three different tuning DACs. The mean of the Gaussian fit defines the baseline position. On the bottom: the tuning DAC setting as a function of its baseline position. The sensor is biased at -1.2 V.

From the mean of the Gaussian fits, the baseline is extracted, as shown at the bottom of the figure. A straight-line fit is used to determine the relationship between the tuning DAC setting and the baseline position, and it is used to find the closest tuning DAC setting to a trimming target. For each pixel, the tuning DAC setting that is the closest to the trimming target is chosen. The global trimming target is chosen to be within the range covered by as many pixels as possible in the pixel matrix. If the Gaussian fit does not converge or the trimming target cannot be reached by any tuning DAC, the pixel is masked.

The distribution of the tuning DAC settings after equalisation, and a mapping across the matrix including masked pixels, are shown in Figure 5.3. The homogeneous map, which makes use of the entire available tuning DAC range and results in fewer than 0.3% of pixels being masked, indicates that there are no systematic effects that would lead to localised variations in the pixel baselines or thresholds. Further details on the method and systematic studies can be found in [129].

The procedure has been tested using different matrix masking patterns, including measurements of the noise-induced occupancy of individual pixels while all their direct neighbors are masked. No significant differences have been observed, indicating that there is no noise crosstalk between pixels and confirming that the equalisation procedure can be performed simultaneously for the entire pixel matrix.

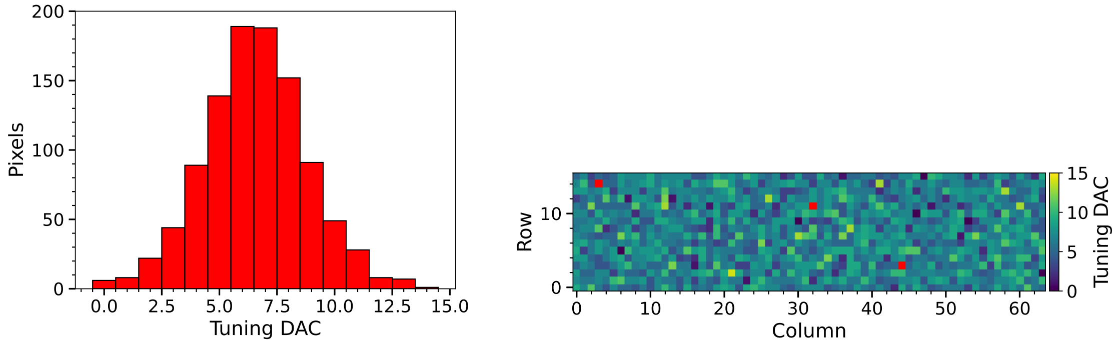

(a) (b)

Figure 5.3: Tuning DAC setting distribution (a) and map (b) after equalisation. The three masked pixels are indicated in red in the map. The sensor is biased at −1.2 V.

5.3 Threshold Dispersion and Single-Pixel Noise

The threshold dispersion and the single-pixel noise are two key performance parameters as they limit the lowest attainable threshold. The threshold dispersion, arising from pixel-to-pixel variations, is obtained from the width of the baseline distribution of all the pixels in the matrix. The single-pixel noise is determined from the width of the noise distribution of an individual pixel. These two performance parameters are discussed below.

The threshold dispersion between pixels is studied with the equalised matrix. In the same way as before, a threshold scan is performed in counting mode with no input signal present. The occupancy distribution for each pixel is fitted with a Gaussian, with mean and width representing the baseline and noise, respectively. Figure 5.4(a) shows the baseline distributions of the entire matrix when all pixels are set to the lowest and highest tuning DAC value, as well as after equalization. The mean $\mu = (94.604 \pm 0.018)$ THL DAC of the equalised distribution corresponds to the chip baseline position, and the width $\sigma = (0.564 \pm 0.015)$ THL DAC represents the threshold dispersion between pixels. This value can be converted into electrons after the threshold calibration described in Section 5.5. It results in a threshold dispersion of about 17 electrons at a sensor bias of −1.2 V.

Figure 5.4(b) shows the single-pixel noise distribution after equalization of the entire matrix, with a mean value of (1.386 ± 0.004) THL DAC, corresponding to 45 electrons at a sensor bias of −1.2 V. A mean single-pixel noise of approximately 35 electrons at −1.2 V is achieved in Section 7.2.4, at the cost of disconnecting the test pulse injection circuitry, which prevents the ToT calibration of the chip in this configuration. With the sensor biased at −3.6 V, the mean single-pixel noise is reduced to 30 electrons. Although this measured value is reduced, it is still larger than the one expected from the front-end simulations (about 28 electrons [103]). In particular, the outliers of the distribution of the single-pixel noise in Figure 5.4(b), together with ongoing measurements, suggest that Random Telegraph Noise [130] is a contributing factor. Further investigations are ongoing.

While the threshold dispersion and the single-pixel noise have been proven to be independent of

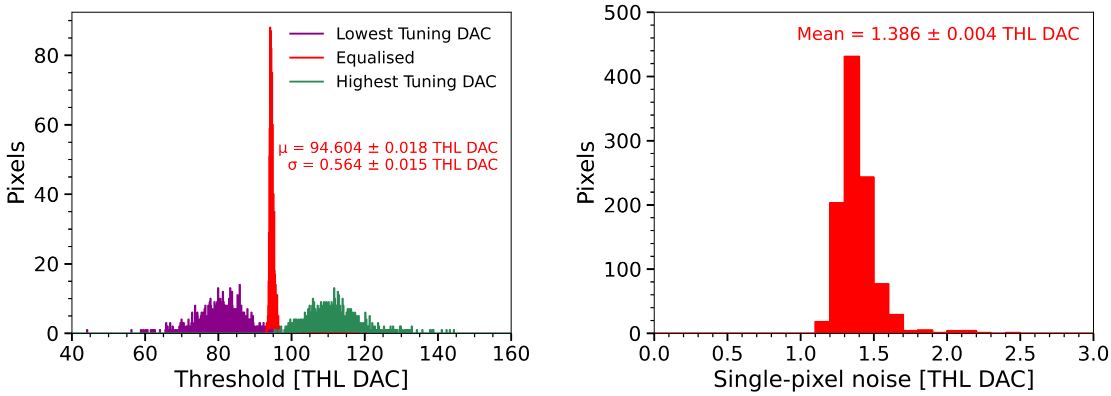

(a) (b)

Figure 5.4: (a) Baseline distribution for the equalised matrix, and the lowest and highest tuning DACs. (b) Single-pixel noise distribution of the equalised matrix. The sensor is biased at −1.2 V.

the light and temperature conditions, they strongly depend on the sensor bias voltage. Figure 5.5 shows the threshold dispersion, the mean single-pixel noise, and their quadratic sum as a function of the sensor bias voltage. The decrease in single-pixel noise up to a sensor bias of about −2 V is due to the decreasing detector capacitance. At high bias voltages, threshold dispersion increases due to the field impact on the NMOS transistors, which are hosted in the biased p-well: a higher reverse bias voltage reduces the drive current of the NMOS, slowing down digital gates, and reduces the active channel volume (see Section 2.1.3), making the transistor more sensitive to dopant fluctuations and thus increasing the threshold dispersion among pixels.

A lower value for the `dac_itrim` is used to overcome the increase in the threshold dispersion at −4.2 V. This results in a smaller step size in the tuning process, which means that pixel thresholds get closer to the trimming target, but also reduces the dynamic range, and consequently, 5 extra pixels are masked (8 out of 1024) compared to the other bias voltages.

Overall, Figure 5.5 shows that the single-pixel noise is larger than the threshold dispersion and therefore dominates the fake-hit rate, limiting the achievable lowest threshold. In addition, no significant differences are observed between samples with different total chip thicknesses. This indicates that the highly doped sensor substrate thickness has no impact on the threshold dispersion or the single-pixel noise of the chip.

Finally, the threshold dispersion between pixels has also been measured using test pulse injection, and it stays constant up to a threshold of approximately 3000 electrons (see Section 5.5.3). This range fully covers the typical operating conditions of the detector.

The equalisation process is automatised and performed before any laboratory or test beam measurement, and repeated after any modification in the chip parameters. Operating the chip at different sensor bias voltages changes the tuning DAC value by up to two units for approximately 20% of the pixels in the matrix. During a two-week test beam campaign, less than 1% of the pixels shift their tuning DAC value by one unit, ensuring stable operation.

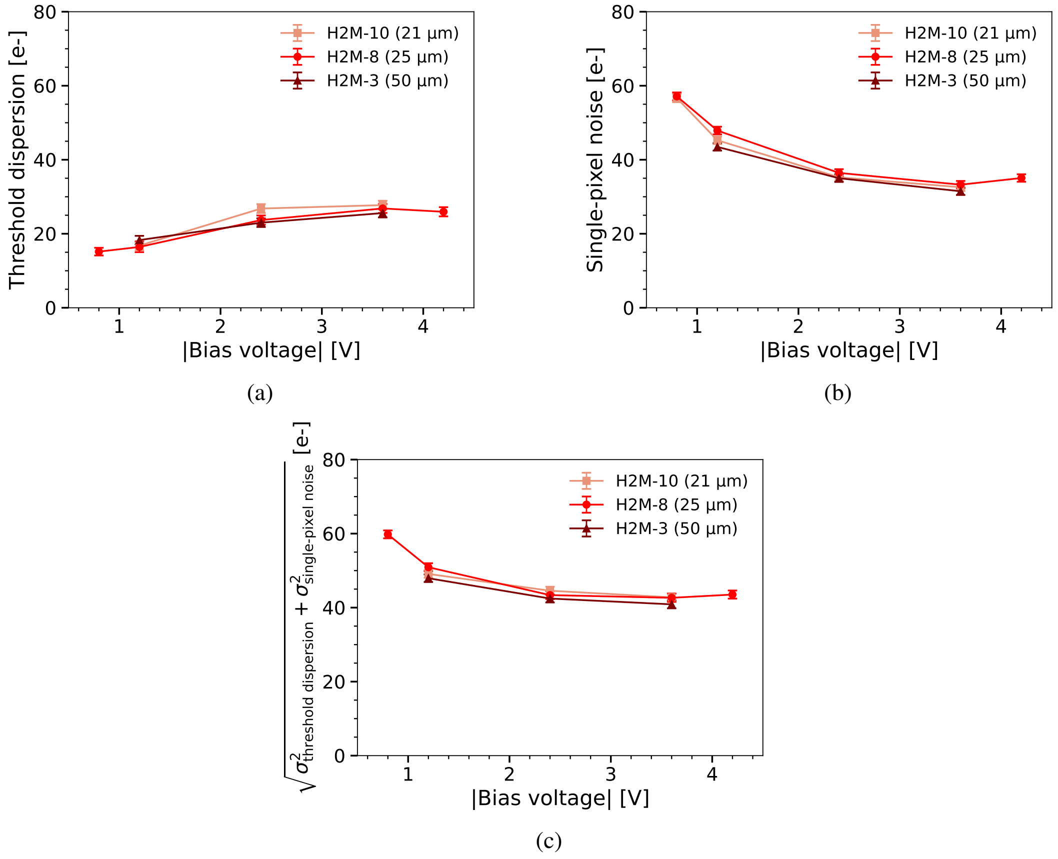

Figure 5.5: Threshold dispersion (a), mean single-pixel noise (b), and their quadratic sum (c) as a function of the bias voltage for three different chip thicknesses. The point at −4.2 V is measured at a lower `dac_itrim` setting.

5.4 Source Measurements

To evaluate the sensor performance and carry out the threshold calibration using characteristic X-rays, radioactive source measurements are performed. For this purpose, the chip is placed inside an aluminum box for radiation safety. Radioactive sources are positioned approximately 5 mm above the surface of the H2M sensor, as sketched in Figure 5.6.

The strontium (^{90}Sr) source emits high-energy beta particles with a broad energy spectrum. It is used for rapid functional testing of the sensor, such as verifying the uniformity of the pixel matrix response under new chip configurations or tuning parameters. On the contrary, the iron (^{55}Fe) source emits nearly monochromatic X-rays at known energies, which are fully absorbed by the silicon sensor via the photoelectric effect, giving well-defined peaks in the measured spectrum, as introduced in Section 2.2.2.

Figure 5.7 shows uncalibrated ToT spectra of ^{55}Fe for different sensor bias voltages and *ikrum* settings. The data have been recorded in ToT mode. The *low ikrum* setting corresponds to

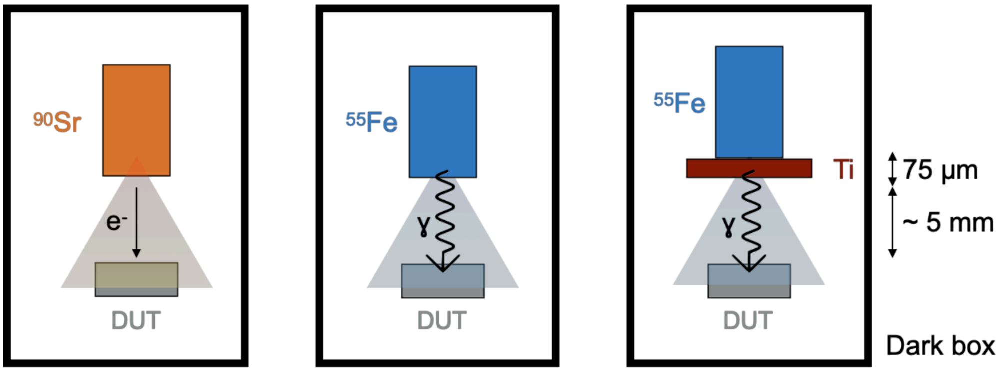

Figure 5.6: Schematic of the setup for the measurements with the ^{90}Sr, ^{55}Fe, and ^{55}Fe with Ti foil.

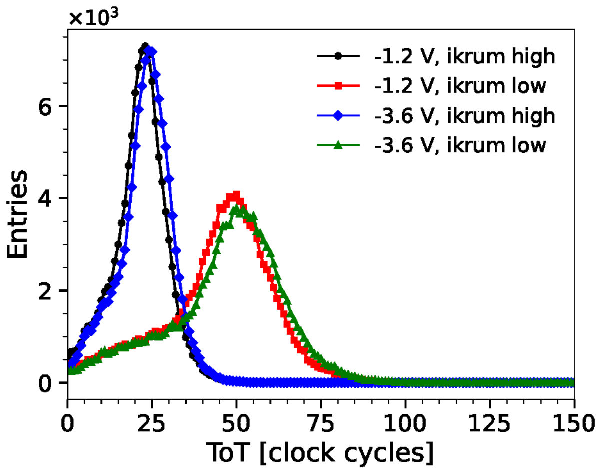

Figure 5.7: ToT spectrum recorded under exposure to an ^{55}Fe source for two different sensor bias voltages and *ikrum* settings of the whole pixel matrix. The threshold is approximately 650 electrons.

~1.65 nA (10 DACs), while the *high ikrum* setting corresponds to ~3.75 nA (21 DACs). Given the source emission rate, the shutter window duration is adjusted to 1 ms, reducing the probability of recording more than one X-ray per shutter opening, which would lead to additional ToT peaks in the spectrum. While there is no significant difference between the two bias voltages, lower *ikrum* settings result in higher measured ToT values, as expected from the slower return of pulses to the baseline. In addition, for a lower *ikrum* setting, the ToT distribution becomes wider. This is because the pixel-to-pixel spread of the effective feedback current, caused by manufacturing variations, has a larger impact. All these observations have been confirmed by analog front-end simulations presented in [103].

Additional source measurements are performed during the threshold calibration, including the use of a titanium (Ti) foil. These studies are presented in Section 5.5.2.

5.5 Chip Calibration

Calibration of the chip periphery DACs is required to compare the set values (in DACs) to physical units (Volts), which are used for comparison with analog front-end simulations and determination of the test pulse injection capacitance. The method and results are explained in Section 5.5.1.

Threshold calibration is performed to find the relation between the hit detection threshold in THL DAC units and the equivalent number of electrons. This allows for comparison with other chips and simulations. Details on the procedure and determination of the calibration factors are given in Section 5.5.2.

The ToT calibration, presented in Section 5.5.4, is necessary to convert a time measurement, in clock cycles, into electrons, enabling energy measurements in physical units. Since the ToT calibration relies on test pulse injection, calibration of their amplitude and ToT is needed, and is covered in Section 5.5.3.

5.5.1 Chip Pheriphery DACs Calibration

Six DACs in the chip periphery provide the bias voltages and currents for the analog front-end operation. Each DAC utilizes a rail-to-rail unity gain buffer, which is an amplifier that can drive its output from the lowest (0 V) to the highest (1.2 V) supply voltages without amplification. This ensures steady output bias voltages that are sent to the in-pixel front-end circuits without significant losses.

Each DAC output is selected with an internal multiplexer, routed to a dedicated pad, and measured in Figure 5.8 using the ADCs on the CaR board (see Section 3.5). The DACs that directly supply a voltage output (`dac_vthr, dac_vref, dac_vtpulse`) have a linear response, with a conversion factor of approximately 4 mV/DAC. The current-output DACs (`dac_ibias, dac_itrim, dac_ikrum`) also follow the expected behavior from simulations [107]. These three DACs define a reference current that is converted into a control voltage (which is measured) and distributed to all the pixels. In the in-pixel front-end, PMOS current mirrors regenerate the same current biases locally for the Krummenacher feedback and threshold comparator.

No significant differences have been found among samples or when operating the chip at different sensor bias voltages.

5.5.2 Threshold Calibration

For threshold calibration, the ^{55}Fe radioactive source is employed. Its characteristic peaks serve as references for converting threshold DAC values into a number of electrons (elementary charges). To obtain an additional calibration point, a 75 µm Ti foil is placed between the ^{55}Fe source and the sensor (see Figure 5.6). Some of the primary X-rays from ^{55}Fe excite the Ti atoms, and the subsequent de-excitation of Ti produces characteristic fluorescence X-rays, which also appear as a distinct peak in the spectrum. The intensity of the fluorescence Ti X-rays depends on the thickness of the Ti foil.

As introduced in Section 2.2.2, the characteristic peaks of ^{55}Fe and Ti K_{α_1} are expected to correspond to (1 609 ± 14) and (1 232 ± 10) created electrons in silicon at room temperature [131],

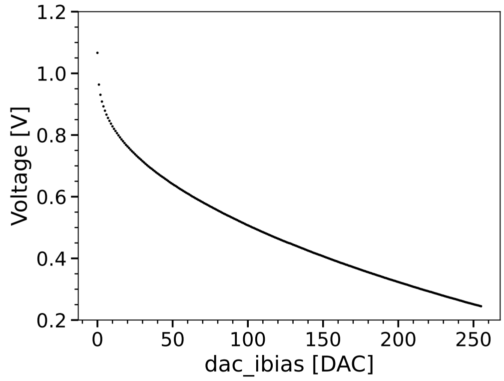

(a) CSA and comparator bias current DAC

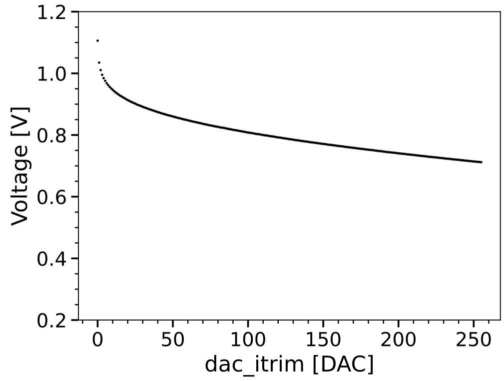

(b) Tuning bias current DAC

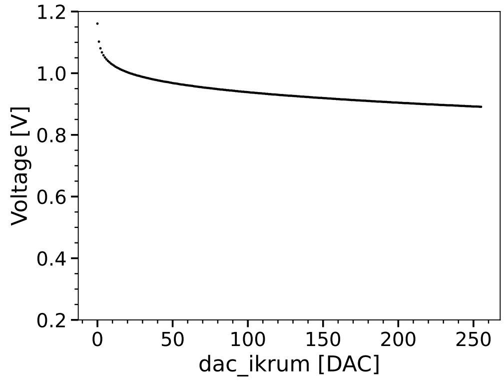

(c) Krummenacher current DAC

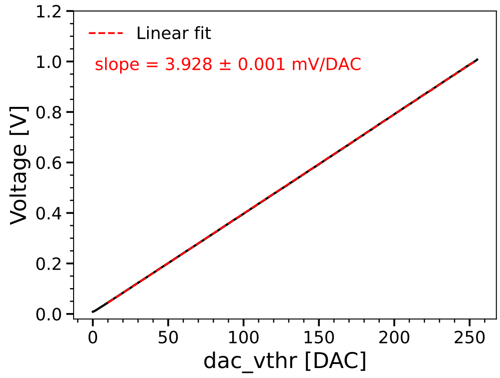

(d) Threshold voltage DAC

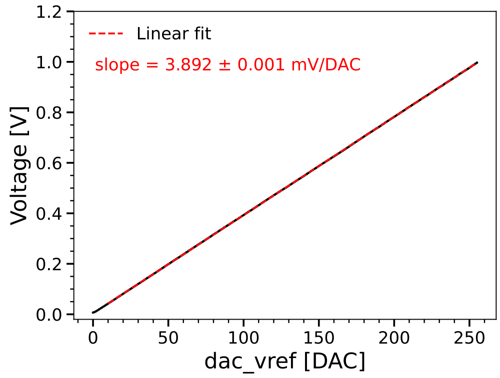

(e) Reference voltage DAC

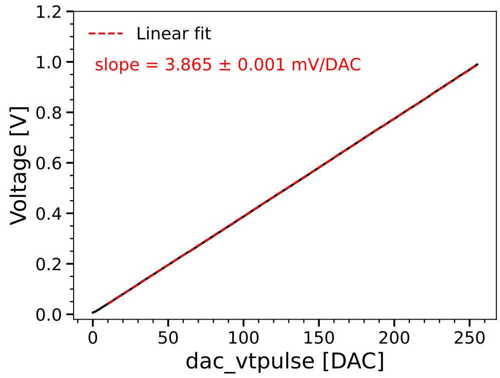

(f) Test pulse voltage DAC

Figure 5.8: Calibration of the six biasing DACs of the analog periphery. The voltage is measured using the ADCs on the CaR board, and as a function of the DAC setting.

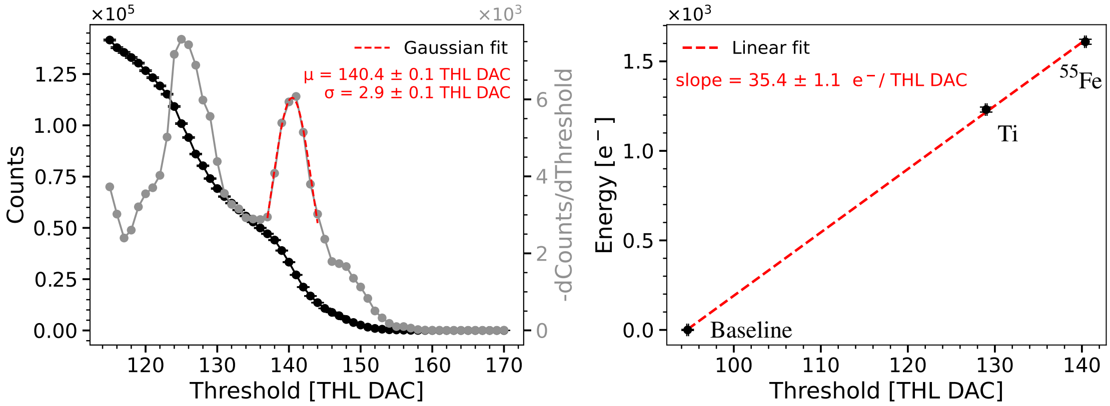

(a) (b)

Figure 5.9: (a) Occupancy (left axis) and its derivative (right axis) for the full matrix as a function of the threshold for the ^{55}Fe source. (b) Charge calibration of the threshold using the determined baseline, and the Ti K_{α_1} and ^{55}Fe K_{α_1} peaks. The sensor is biased at -1.2 V and the *high ikrum* setting is used.

respectively. With lower intensity, ^{55}Fe and Ti also emit K_β X-rays at 6.49 keV and 4.93 keV, respectively [131].

Since the chip provides no means of directly measuring the amplitude of the induced pulses, the characteristic peak amplitudes have to be obtained in an indirect way. The chosen method relies on counting the pulses above threshold for a certain threshold setting and repeating the measurement for a set of thresholds. A pixel registers one count (i.e., a threshold crossing) per deposited X-ray if the threshold lies between the baseline level and the pulse amplitude. If the threshold is lower than the baseline or higher than the pulse amplitude, the pulse is not detected (no threshold crossing), and no count is added. At the peak amplitude, the number of counts is expected to drop sharply. In this way, a cumulative spectrum is obtained using the counting acquisition mode of the chip.

For each threshold DAC, 200 frames are recorded, each with a shutter duration of 10 ms. This shutter window is longer than for the ToT measurements (see Section 5.4), as all counts are accumulated regardless of whether they are detected within the same shutter, but still short enough to avoid saturating the 8-bit counter. The measurement is repeated 400 times to reduce statistical uncertainties. Thus, the detected X-rays are recorded as a function of the threshold in THL DAC units, with a total acquisition time of 800 s per setting.

Figure 5.9(a) shows the occupancy (left axis) as a function of the threshold for the ^{55}Fe source. At the threshold corresponding to the K_{α_1} energy, the number of counts drops abruptly. This is visible as a peak in the negative derivative of the counts (right axis). The mean position, $\mu = (140.4 \pm 0.1)$ THL DAC, of the fitted Gaussian distribution corresponds to the K_{α_1} energy. A secondary peak appears at about 126 THL DAC, which does not correspond to any characteristic peak of the ^{55}Fe spectrum in silicon, and its origin is discussed below. At a threshold of approximately 148 THL DAC, a small peak is visible in the derivative, representing the K_β energy. Above 158 THL DAC, the threshold is higher than the charge deposited by X-rays, and the number

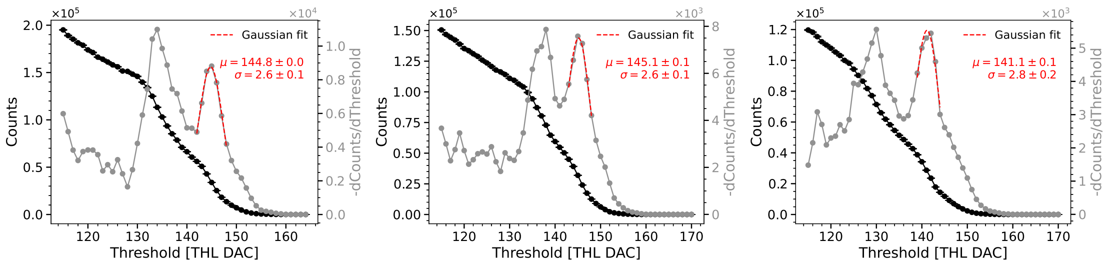

(a) -1.2 V, *low ikrum* (b) -4.2 V, *low ikrum* (c) -4.2 V, *high ikrum*

Figure 5.10: Occupancy (left axis) and derivative of the occupancy (right axis) as a function of the threshold for different sensor bias voltages and *ikrum* settings. Data recorded under exposure to an ^{55}Fe source.

of counts is zero. The same measurement is repeated with the Ti target, measuring its K_{α_1} peak at $\mu = (129.0 \pm 0.1)$ THL DAC.

The expected charge in electrons is shown as a function of the mean values from the Gaussian fits in Figure 5.9(b). The chip baseline position is also included, corresponding to a deposited charge of zero electrons. Fitting a linear function through these three points gives a slope of (35.4 ± 1.1) electrons per THL DAC, which is used as the charge calibration factor. The obtained calibration factor is consistent with the expectations from analog front-end simulations [103].

Systematic uncertainties have been studied by varying the Gaussian fit range in Figure 5.9(a) and by introducing the K_β peaks, and found to be within the quoted error of the calibration factor. Since pixel-to-pixel amplitude variations are found to be negligible (see Section 5.5.3), a single calibration factor is applied globally to the entire pixel matrix.

In Figure 5.9(a), a second peak is visible at a lower threshold of about 126 THL DAC. It indicates a loss in the signal height for a large portion of the deposited X-rays. Depending on where the X-ray energy is deposited within the pixel cell, two different signal amplitudes for the K_{α_1} characteristic peak are measured. This loss of the signal amplitude, known as ballistic deficit, affecting slow signals, is discussed in detail in Section 7.1 based on test beam measurements.

Since the left peak (at about 126 THL DAC) is affected by the ballistic deficit, only the right peak (at about 140 THL DAC) is used for the threshold calibration. The calibration procedure could be improved by applying different calibration factors to different parts of the pixel cell if spatial information of the X-ray deposition were available.

Additionally, this effect has also been observed with the X-ray measurements with the DESY ER1 test chip [132, 133], a test chip that features the same analog front end as H2M in a 2×2 pixel matrix. Its direct access to the analog signal waveforms (and thus to their amplitudes) enables a direct characterisation of this effect. A method to ensure that the calibration peak is determined without being affected by the ballistic deficit is proposed in [132, 133]. First, both the signal rise time and amplitude are computed. Then, for the determination of the calibration factor, only amplitudes associated with a fast rise time are considered. In this way, the charge calibration avoids bias from the ballistic deficit. Such an approach is not possible in H2M, as the chip has no means to measure the rise time and amplitude simultaneously.

Figure 5.9(a) and 5.10 compare the K_{α_1} peak positions for different sensor bias voltages and

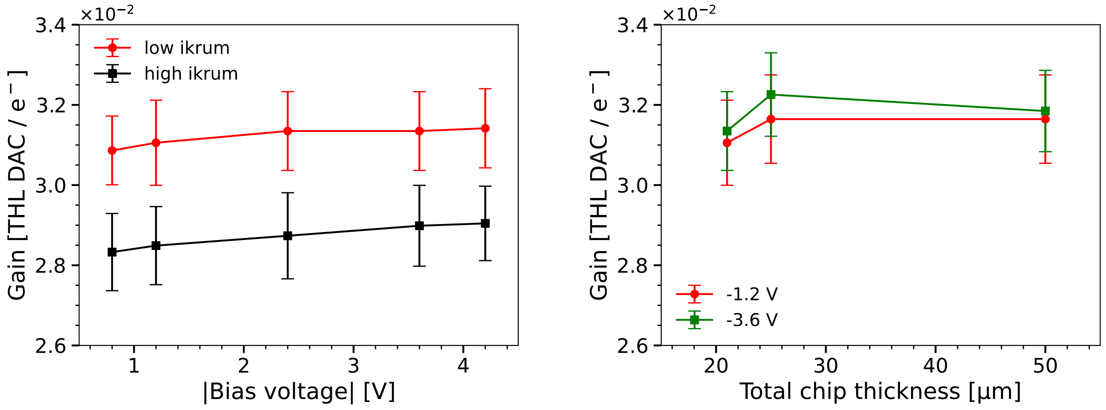

(a) (b)

Figure 5.11: (a) Gain as a function of the bias voltage for low and high Krummenacher currents. (b) Gain for three samples with different total chip thickness. The *low ikrum* setting is used, and the sensor is biased at −1.2 V and −3.6 V.

ikrum settings. Increasing the sensor bias voltage shifts the secondary peak to higher amplitudes, while the calibration peak stays at practically the same position. This chip configuration keeps the calibration factor almost constant and reduces the ballistic deficit. Similarly, lowering the *ikrum* value minimises the distance between the calibration and secondary peak, further reducing the ballistic deficit. Since in this case, the calibration peak shifts towards higher amplitudes, the calibration factor is smaller. All these observations agree with the test beam studies presented in Chapter 7.

The calibration method has been applied to several samples operated under different parameter settings. The gain is defined as the inverse of the calibration factor. It is shown in Figure 5.11(a) for different bias voltages of the sensor and Krummenacker currents. Results are consistent among samples of various thicknesses, as shown in Figure 5.11(b).

5.5.3 Test pulse Calibration

The test pulse injector circuitry is calibrated for each pixel. For an injected test pulse on the analog front end, both the amplitude and ToT are measured independently. To avoid overestimating the ToT value, the shutter is opened for 1 µs, matching the positive phase of the test pulse (`tp_on` in Figure 3.4). If the shutter duration were longer, the negative phase of the injected test pulse and its overshoot could also be recorded, increasing the ToT count (see Section 3.3).

Amplitude Calibration of Test Pulses

The test pulse amplitude is measured in a similar way as the characteristic peak amplitude of the radioactive sources in Section 5.5.2. The threshold is scanned in counting mode while injecting test pulses of a fixed positive amplitude controlled via the `dac_vtpulse`. A pixel registers one count (i.e., a threshold crossing) per injected test pulse if the threshold lies between the baseline

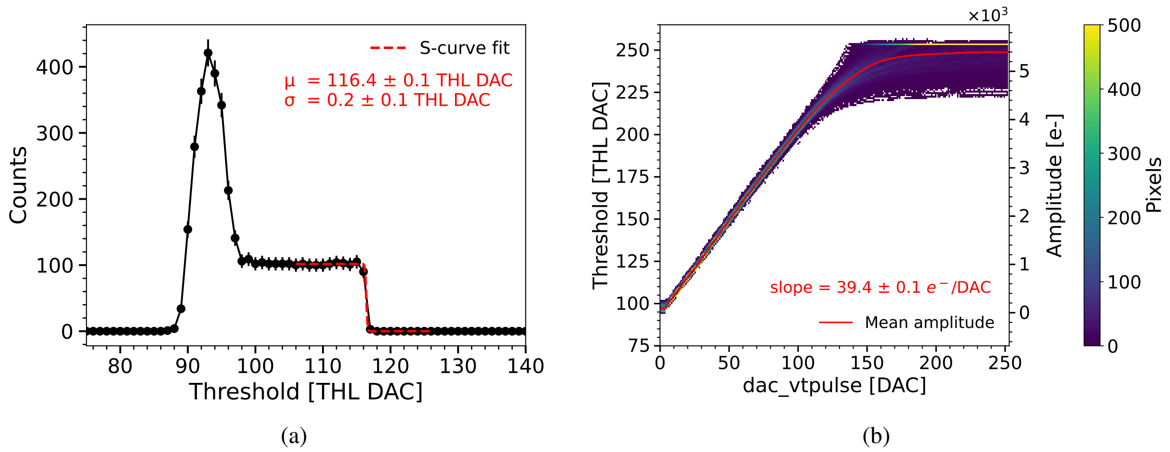

Figure 5.12: (a) Occupancy as a function of the threshold in DAC units for 100 test pulses with `dac_vtpulse` set to 20 DACs on one pixel. (b) Test pulse amplitude in DAC (left axis) and electron units (right axis) as a function of the threshold for all pixels. The mean amplitude for all pixels is shown in red. The sensor is biased at −1.2 V and the *high ikrum* setting is used.

level and the pulse amplitude. If the threshold is lower than the baseline or higher than the pulse amplitude, the pulse is not detected (no threshold crossing), and no count is added.

Figure 5.12(a) shows the occupancy as a function of the threshold for 100 test pulses with `dac_vtpulse` set to 20 DACs (corresponding to about 700 electrons) injected into a single pixel. The Gaussian part of the distribution (around 95 THL DAC) indicates the baseline. For larger thresholds, the 100 pulses are detected [1]. Once the test pulse height is reached, the occupancy drops to zero. In this region, an s-curve function is fitted, with the mean $\mu = (118.5 \pm 0.1)$ THL DAC representing the test pulse height position. The amplitude is determined by subtracting the baseline position, and converted to electrons using the threshold calibration factor obtained in Section 5.5.2.

Figure 5.12(b) shows a scan of the `dac_vtpulse` values with their corresponding height position in THL DAC units (left axis) and the amplitude in electrons (right axis) for all pixels. The slope of 39.4 e^{-}/DAC in the range from `dac_vtpulse` from 25 to 100 DAC is the amplitude calibration factor from DAC units to electrons. Pixel-to-pixel amplitude variations are small and remain constant up to injected test pulses of about 3 000 electrons, with all pixels showing a similar linear gain. The highest measured amplitude is limited by the 8-bit `dac_vthr`.

ToT Calibration of Test Pulses

The ToT value for a given test pulse amplitude is measured directly using the ToT acquisition mode. 100 pulses are injected to reduce statistical uncertainties, and the average ToT value is calculated. Figure 5.13(a) shows the ToT distribution for a single pixel with `dac_vtpulse` equals

[1] Other perturbations, such as jitter at the rising/falling edges of the test pulses, can cause the threshold to be crossed multiple times, increasing the counter.

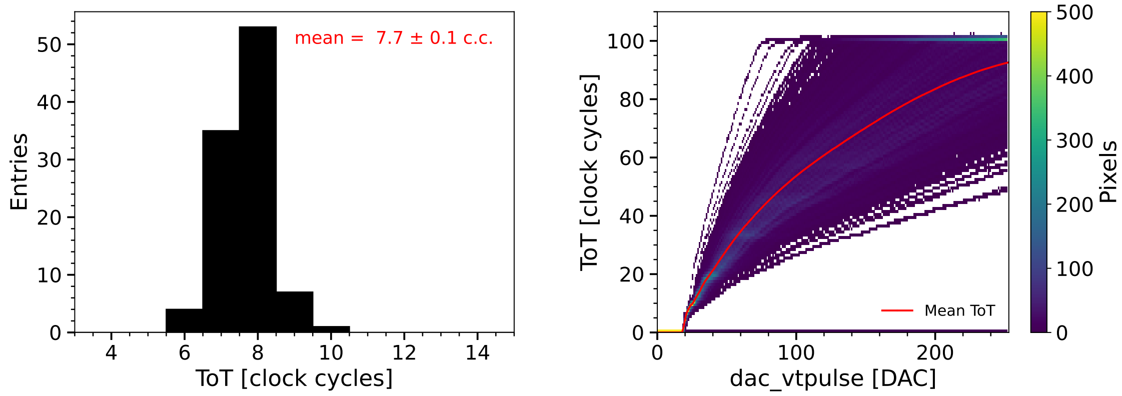

(a) (b)

Figure 5.13: (a) Distribution of the ToT for 100 injected test pulses with `dac_vtpulse` equals 20 DACs for one pixel. (b) ToT as a function of the amplitude of the injected test pulse in DAC units for all pixels. The mean ToT for all pixels is shown in red. The threshold is approximately 650 electrons. The sensor is biased at −1.2 V and the *high ikrum* setting is used.

to 20 DAC recorded at a threshold of about 650 electrons. A high threshold is used so that the results can be used later (in Section 5.5.4) to calibrate the ^{55}Fe spectrum obtained in Figure 5.7. The high threshold also ensures that fluctuations of the baseline due to noise, as well as the undershoot or overshoot of the injected test pulses, do not lead to an increase in the ToT counter.

This measurement is repeated for each pixel and all possible `dac_vtpulse` values, as shown in Figure 5.13(b). A significant pixel-to-pixel ToT variation is observed at large test pulse amplitudes (far from the expected MIP response of about 600 electrons). This effect is caused by the effective reset current between different pixels, and it motivates an individual ToT calibration for each pixel. The saturation in the ToT value is reached at 1 µs, limited by the shutter duration.

5.5.4 ToT Calibration

The ToT and amplitude measurements with test pulses, presented in Section 5.5.3, can be combined. Figure 5.14 shows the ToT as a function of the test pulse amplitude in electrons for a single pixel. A surrogate function

$$\mathrm{ToT} = \mathrm{Ax} + \mathrm{B} + \frac{\mathrm{C}}{\mathrm{x} - \mathrm{D}} \tag{5.1}$$

is used to fit each pixel, where x is the test pulse amplitude, A modulates the linear gain at higher amplitudes (above 1000 electrons according to analog front-end simulations [103]), B adjusts the ToT offset, C represents the curvature at low amplitudes, and D indicates the offset in amplitude [134]. The inverse of this function enables the conversion of measured ToT in clock cycles to signal amplitude in electrons.

Figure 5.15 shows the distribution of the fit parameters for all the pixels (on the left) and a map of their values (on the right). The mean values expected from the analog front-end simulations are included in the distributions [107]. In the simulations, test pulses are injected into a simplified

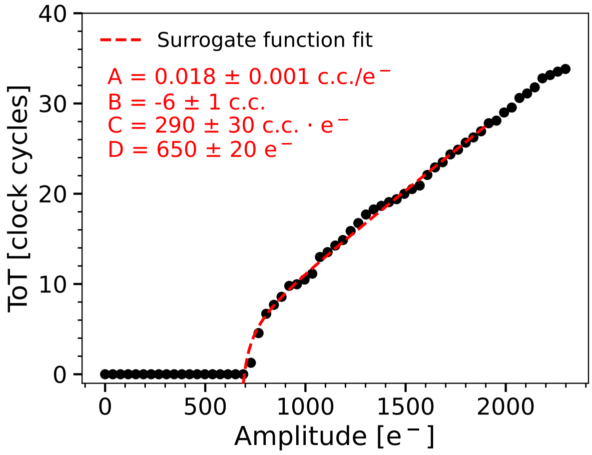

Figure 5.14: ToT as a function of the amplitude of the injected test pulse in electrons for one pixel. The sensor is biased at -1.2 V and the *high ikrum* setting is used.

circuit, and the amplitude and ToT values are computed. Similarly to the measurements, a surrogate function is fitted to the mean ToT as a function of the mean amplitude response of the pixel matrix. A good agreement is found between simulations and measurements. Since only test pulses above 600 electrons are simulated, the curvature (parameter C) is not well modeled by Equation 5.1, resulting in smaller values than in the measurements.

The well-known spectrum of the ^{55}Fe is used to validate the ToT calibration procedure. Figure 5.16(a) shows an uncalibrated ToT spectrum recorded with a threshold of approximately 650 electrons (see Section 5.4). After applying the ToT calibration, in Figure 5.16(b), the K_{α_1} peak is fitted with a Gaussian function, obtaining a mean $\mu = 1640 \pm 40$ electrons. This result deviates by about 5% from the theoretical value of $(1\,609 \pm 14)$ electrons.

Although two distinct signal amplitudes are measured (see Figure 5.9(a)), the ToT measurement remains almost unaffected by the ballistic deficit. This is evident in Figure 5.7, where no secondary peaks are observed in the uncalibrated data of the ^{55}Fe ToT spectrum, and remains true after calibration, as shown in Figure 5.13. Therefore, using a ToT-weighted average and applying the ToT calibration and η-correction is sufficient to reconstruct the particle hit position in test beam measurements (see Section 6.4).

5.5.5 Calibration and Energy Measurements Limitations

The inverse of the mean value obtained for the fit parameter A corresponds to a ToT gain of approximately 50 electrons per clock cycle. Since the ^{55}Fe K_{α_1} and K_{β} peaks are separated by about 160 electrons, the peaks are expected to appear roughly three clock cycles apart. This small separation, combined with the influence of non-uniform in-pixel response, merges the two peaks in the ToT spectrum in Figure 5.7. The separation between peaks is not even visible in single-pixel measurements. In contrast, in the amplitude measurement shown in Figure 5.9(a), the K_{β} peak is visible. The reason is that the K_{α_1} and K_{β} peak amplitudes are separated by about

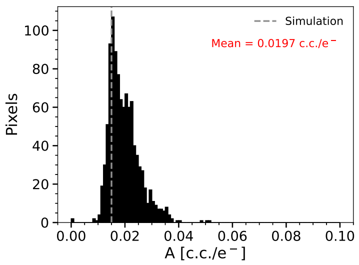

(a) Parameter A

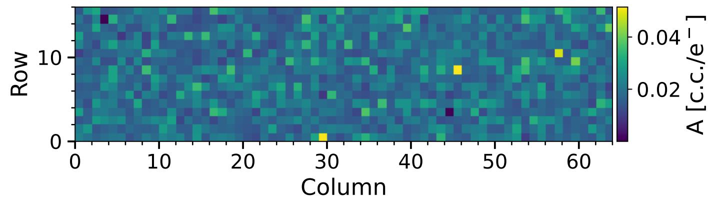

(b) Parameter A

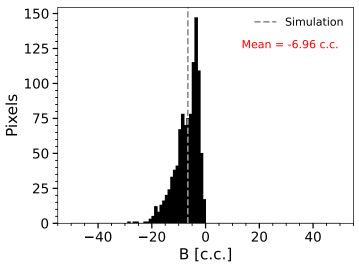

(c) Parameter B

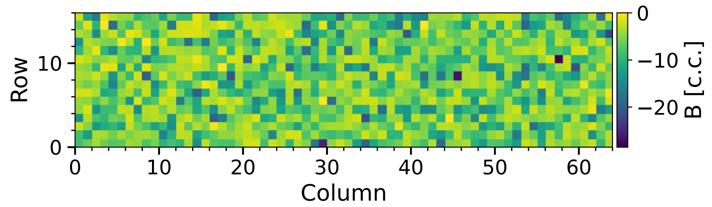

(d) Parameter B

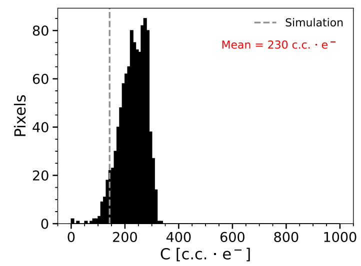

(e) Parameter C

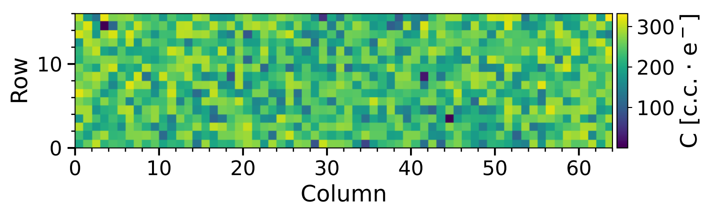

(f) Parameter C

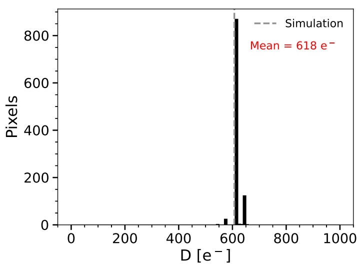

(g) Parameter D

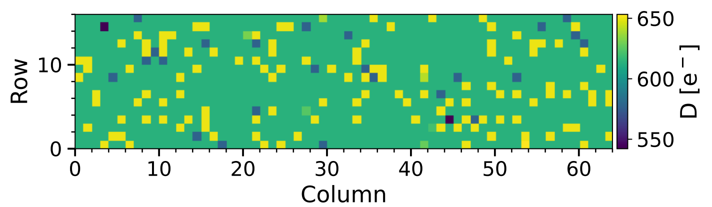

(h) Parameter D

Figure 5.15: Distribution of the fit parameters of the surrogate function across the pixel matrix. The expected value from simulations of the analog front-end is included by a dashed gray line in the distributions. The sensor is biased at -1.2 V and the *high ikrum* setting is used.

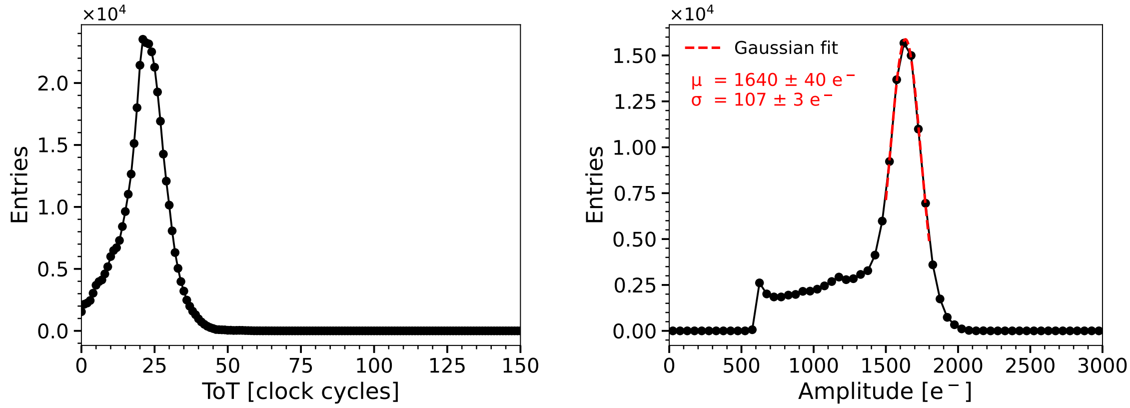

(a) Before calibration

(b) After calibration

Figure 5.16: ToT spectrum recorded under exposure to an ^{55}Fe source before (a) and after (b) calibration. The threshold is approximately 650 electrons, the sensor is biased at -1.2 V, and the *high ikrum* setting is used.

5 THL DAC, and all the pixels in the matrix have a similar amplitude gain (Figure 5.12(b)) and a small threshold dispersion of about 17 electrons.

The ToT calibration has been proven to work reliably at higher amplitudes, lower bias voltages, and different chip settings. However, in ToT mode at lower thresholds (below 300 electrons) and larger bias voltages (above 3.6 V), the noise and threshold dispersion between pixels increase (see Figure 5.5(c)), and the ToT calibration is spoiled. As a consequence, data recorded in ToT mode for thresholds below 300 electrons are not calibrated.

5.6 Injection Capacitance

The injection of test pulses is performed by charging a capacitance connected to the input of the CSA. A voltage is sent via `dac_vtpulse` (V_{TP}) to this capacitor (C_{inj}), which is translated into a charge (Q) injected into the pixel through the relation

$$Q = C_{inj} \cdot V_{TP}. \tag{5.2}$$

Therefore, the combination of DACs, threshold, and test pulse calibrations allows the estimation of the capacitance of the analog test pulse injection circuit. C_{inj} can be determined as:

$$C_{inj} = \frac{Q}{V_{TP}} = \frac{39.4\ \mathrm{e/DAC} \cdot 1.6 \cdot 10^{-19}\mathrm{C}}{3.865\mathrm{mV/DAC}} = 1.6\ \mathrm{fF} \tag{5.3}$$

where Q is obtained from the linear fit in Figure 5.12(b) multiplied by the electron charge, and V_{TP} is given by the slope of Figure 5.8(f). An injection capacitance of 1.6 fF is calculated. The measurement result is within 10% of the design value (1.8 fF).

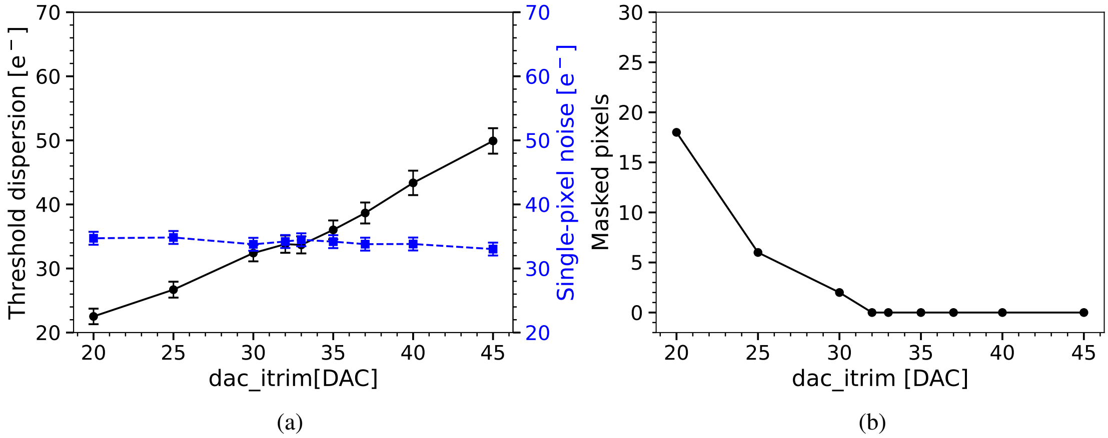

Figure 5.17: (a) Threshold dispersion (left axis) and single-pixel noise (right axis) as a function of the tuning DAC bias current (dac_itrim). (b) Number of masked pixels as a function of dac_itrim. The sensor is biased at −4.2 V.

5.7 Chip Parameters Optimisation

Each chip parameter must be adjusted to guarantee optimal operation of the analog front-end. Table 5.1 summarises the nominal and optimised values for the six biasing DACs of the analog periphery.

dac_vthr and dac_vtpulse can be freely set by the user, and therefore, do not have preferred optimised values. According to the test pulse calibration and test beam measurements, a setting of about 20 DAC for dac_vtpulse gives a signal slightly higher than the MPV of a MIP (about 700 electrons). The dac_ibias and dac_vref settings have been optimised by the chip designer through analog front-end simulations [107]. They have been chosen so that the chip baseline remains practically constant with variations in the feedback current.

The dac_itrim setting controls the bias current of the tuning DAC. At low values, the effective distance between tuning DACs levels is small, limiting the dynamic range and increasing the number of pixels that need to be masked. A minimal number of masked pixels is preferred since they increase the insensitive area in the detector. Therefore, a compromise has to be found

Table 5.1: Nominal and optimised settings for the analog periphery DACs.

Biasing DAC	Nominal value [DAC]	Optimized value [DAC]
dac_ibias	32	37
dac_itrim	32	35 (25 for −4.2 V)
dac_ikrum	21 (*high ikrum*)	10 (*low ikrum*)
dac_vthr	—	—
dac_vref	70	100
dac_vtpulse	—	—

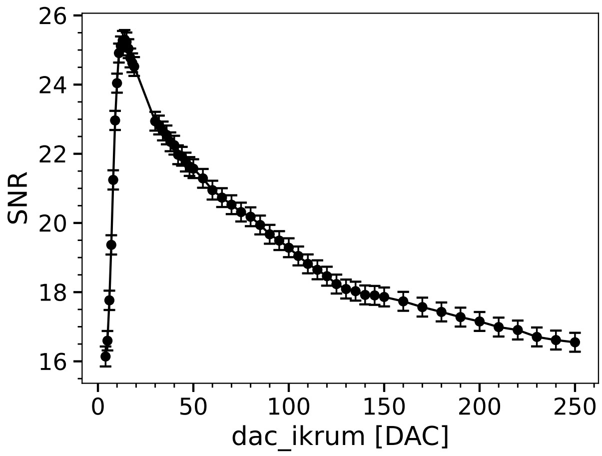

Figure 5.18: SNR as a function of the feedback current. The signal is defined as the amplitude of the injected test pulse, and the noise as the width of the baseline for each *ikrum* setting. The sensor is biased at −1.2 V.

between achieving a low threshold dispersion among pixels and keeping a low fraction of masked pixels. Since larger threshold dispersion between pixels is observed at higher bias voltages (see Figure 5.5(a)), an example of `dac_itrim` optimisation is presented in Figure 5.17 for a sensor bias of −4.2 V. Figure 5.17(a) shows the threshold dispersion and single-pixel noise as a function of the `dac_itrim`. While the single-pixel noise remains constant, the threshold dispersion increases with larger `dac_itrim` values because larger bias currents reduce the tuning DAC resolution. However, at lower `dac_itrim` settings, finer granularity improves the equalisation, but covers a smaller threshold range, causing more masked pixels as shown in Figure 5.17(b). A value of 25 DAC is selected for this sensor bias voltage, where fewer than 0.5% of the pixels are masked. For lower bias voltages, where threshold dispersion is smaller, 35 DAC is selected and less than 0.3% of the pixels are masked.

The `dac_ikrum` setting has been optimised in the laboratory employing test pulse measurements and during test beam campaigns with MIPs. The laboratory optimisation procedure and results are described below, while the test beam results are presented in Section 7.2.2. Analog front-end simulations have also been performed and can be found in [103].

For 100 test pulses injected with an amplitude corresponding to a MIP at a certain *ikrum* setting, the signal is defined as the measured amplitude (obtained as a threshold scan in counting mode, as in Figure 5.12(a)). The noise is determined as in Section 5.3, from the width of the Gaussian fit around the baseline, in the absence of any signal. Using these values, the signal-to-noise ratio (SNR) is calculated and is shown in Figure 5.18 as a function of the feedback current. A maximum SNR is achieved at 10 DACs (referred to as the *low ikrum* setting). At the nominal value of 21 DACs (referred to as the *high ikrum* setting), the SNR is still high. Below 10 DACs, noise dominates due to signal jitter, reducing the SNR. Above 10 DACs, since the gain is inversely proportional to the *ikrum*, the signal and SNR decrease. This optimal value of 10 DACs found for the feedback current agrees with the analog front-end simulations [103] and the test beam measurements (see Figure 7.7(a)).

Finally, in-pixel settings, such as the tuning DAC value and masking, are optimised using the equalisation procedure described in Section 5.2.

5.8 Power Consumption

Keeping the power consumption low is important for tracking applications, since the passive material needed for cooling increases the material budget and thereby deteriorates the spatial resolution of the detector.

In the H2M chip, in addition to the sensor biasing (p-well/p-substrate) four external voltages are applied, which contribute to the power consumption of the chip. VDDA supplies the analog in-pixel front-end, VDDD powers the digital logic (readout and clock) and switching circuitry, LVDS buffers handle data communication, and IO bias voltage defines logic levels and interfaces with external electronics. Each rail is individually supplied through the CaR board, and the currents and voltages can be monitored via ADCs.

Table 5.2 presents the current and voltage measured for VDDA and VDDD on a configured chip using the optimised chip settings listed in Table 5.1. The given statistical uncertainties correspond to the average of measurements with three different samples. Since the LVDS and IO bias currents strongly depend on the chip status (power on, configuration, or data acquisition), they are not included.

The VDDA and VDDD power consumption for the configured chip is (46 ± 1) mW, and it is dominated by the digital circuitry. Normalising this value to the active size of the pixel matrix, the total power consumption for the configured chip is $(3\,670 \pm 80)\,\mathrm{mW\,cm^{-2}}$ (about 45 µW per pixel).

Comparing this result with the values reported by other chips in the same technology, such as DPTS with a power consumption of $53\,\mathrm{mW\,cm^{-2}}$ when operating at the nominal settings [135], the measured power consumption of H2M is two orders of magnitude higher. This can be explained by the more complex in-pixel front-end and digital logic of H2M. The in-pixel front-ends increase the VDDA power consumption roughly linearly with the size of the active matrix. The digital periphery logic stays roughly the same when the pixel matrix grows, therefore, it dominates the power consumption of the comparably small H2M prototype.

Table 5.2: Contributions to the power consumption of H2M.

Contribution	Voltage [V]	Current [mA]	Power[mW]
VDDA	1.204 ± 0.001	14 ± 1	17 ± 1
VDDD	1.192 ± 0.001	24.3 ± 0.4	28.97 ± 0.5
			$P_{H2M} = 46 \pm 1$

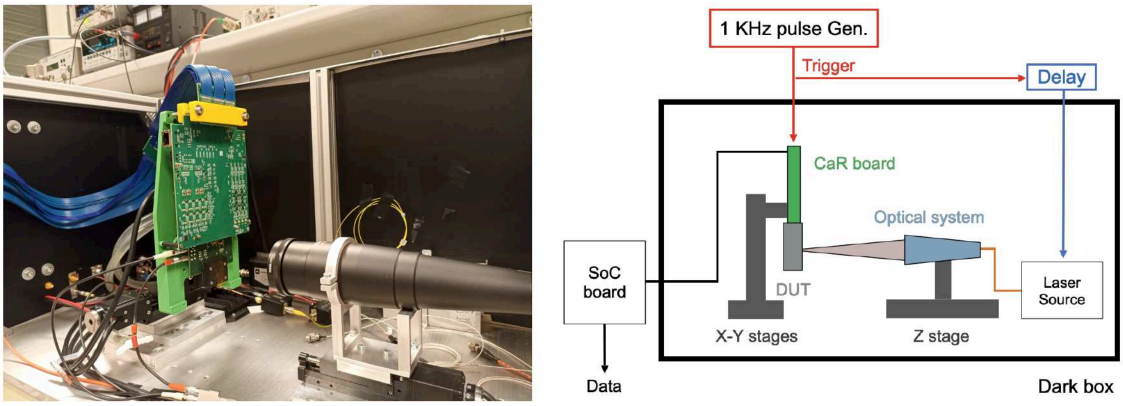

(a) (b)

Figure 5.19: Picture (a) and sketch (b) of the pulsed infrared laser setup.

5.9 Laser Measurements

Laser measurements are carried out in the laboratory to confirm the non-uniform in-pixel response observed in test beam measurements (see Section 7.1).

H2M is mounted on an x-y stage and illuminated from the back with a 1 064 nm pulsed infrared laser, which is mounted on a z-stage. Top or edge illumination of the chip is not possible due to the presence of metal interconnect layers and the unpolished edge of the sensor. The laser intensity is adjusted based on the mean ToT value measured during test beam measurements for the MPV of a MIP, and the beam is focused by performing a scan along the z-axis. The expected spatial resolution of the setup at the H2M position is defined by the width of the waist of the laser beam, and it is approximately 5 µm [136].

The chip is operated in ToT mode with a shutter duration of 150 µs. A 1 kHz pulse generator sends the trigger signal to both the laser source and H2M. While the H2M shutter opens immediately, the ~5 ns laser pulse is delayed by 150 ns to ensure it arrives within the acquisition window and the whole laser pulse can be recorded. The x-y stage is scanned in 2 µm steps. At each position, 100 frames are recorded with a waiting time of 1.5 s between steps. This ensures that the stage has moved and stabilized. A photo and a schematic of the setup are shown in Figure 5.19.

At each position, the efficiency and ToT values are determined. The efficiency is defined as the number of frames with a ToT value greater than zero, divided by the 100 acquired frames. The mean ToT value is the average of the ToT values from these 100 measurements.

Figure 5.20 shows the mean ToT value and efficiency for the top-left region of the chip matrix (the upper 12 rows and leftmost 3 columns). The observed in-pixel efficiency pattern agrees with the in-pixel test beam measurements, and is discussed in Section 7.1. The outermost parts of the top row and the left column display a different in-pixel pattern, and the reason is also investigated in Section 7.1. Sensor edge effects explain the extension of charge collection beyond the pixel matrix boundary. Some pixels show higher ToT values on the right part of the pixel cells, which is also consistent with test beam measurements (Figure 7.1).

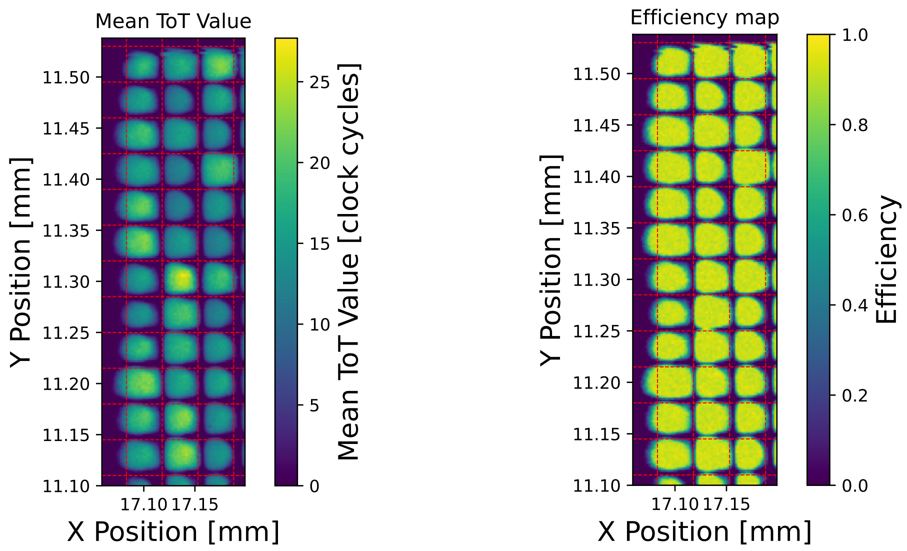

(a) (b)

Figure 5.20: Mean ToT (a) and efficiency (b) maps of the top-left part of the chip matrix measured with a pulsed infrared laser. The pixel cells are indicated with discontinuous red lines, and their positions are given using the system of reference of the x-y stage. The sensor is biased at −1.2 V and a threshold of approximately 300 electrons is used.

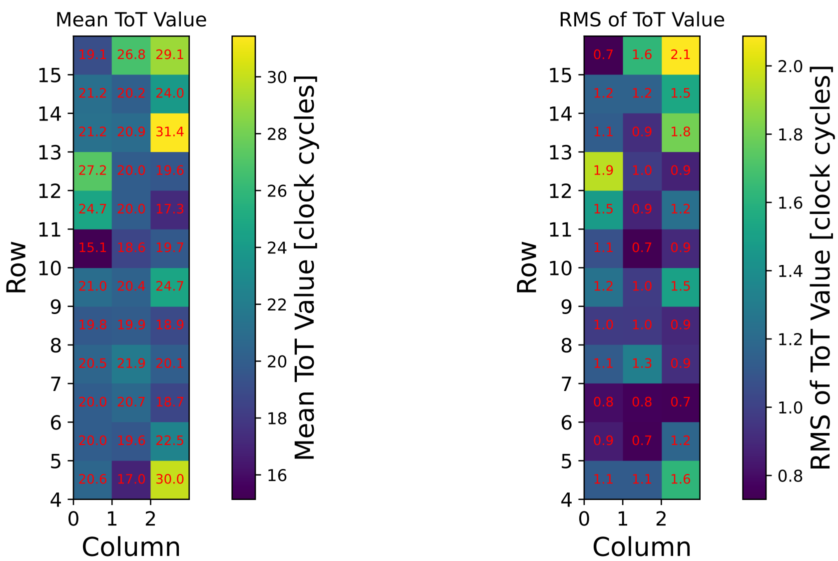

Figure 5.21: Mean (left) and RMS (right) ToT maps, measured by injecting 100 test pulses with an amplitude similar to the laser pulse on each pixel. The pixels shown correspond to the top-left part of the chip matrix, as in Figure 5.20. The numerical values are included in red in each pixel. The sensor is biased at −1.2 V and a threshold of approximately 300 electrons is used.

Additionally, the pixel-to-pixel variations in Figure 5.20(a) are reproduced using test pulse injection. Figure 5.21 shows the mean and RMS of the ToT values measured after injecting 100 test pulses, with an amplitude similar to the laser response on each pixel. Pixels with larger ToT values for test pulses also exhibit larger ToT values with the laser. These variations are attributed to differences in the effective *ikrum* setting between pixels, which originates from the manufacturing process and motivates the need for pixel-to-pixel ToT calibration (see Section 5.5.4). Pixels with larger mean ToT values also have a larger RMS. The RMS of the measured test pulses is about 5% of the mean, and is consistent with the laser measurements.

CHAPTER 6

Methodology for Test Beam Measurements

MIPs deposit charge in silicon pixel detectors as described in Chapter 2, providing a signal that is similar (or even smaller) to the one expected in a particle collider experiment. Test beam studies with MIPs are therefore essential to investigate the key performance parameters of the detector, which can be directly compared with the requirements of vertex and tracking detectors, such as the ones discussed for future lepton colliders in Chapter 1.

The charge deposition and signal formation induced by MIPs differ from those produced in the laboratory, for example using X-ray sources or lasers (see Section 2.2). Therefore, test beam studies provide a realistic and complementary validation of the detector performance with respect to the laboratory measurements presented in Chapter 5.

To study the performance of the H2M sensor in MIP detection, test beam measurements are performed. For that, an electron particle beam is used to ionise the sensor, and its response is compared to reference detectors. The particle beam utilised in this work is provided by DESY II Test Beam Facility, which is described in Section 6.1. Section 6.2 presents the reference detectors, whose arrangement forms the so-called beam telescope. Section 6.3 explains the operation of H2M during test beam measurements. The data reconstruction chain and analysis workflow are introduced in Section 6.4 and Section 6.5, and the results are discussed in Chapter 7.

6.1 The DESY II Test Beam Facility

The DESY II Test Beam Facility [137] is located at the Deutsches Elektronen-Synchrotron (DESY). Its test beams are generated through a two-step conversion process, shown in Figure 6.1. First, a carbon fiber target is inserted into the electron/positron DESY II synchrotron. When the electrons interact with the target, bremsstrahlung photons are emitted and exit the accelerator through an aluminum window. These photons hit a metal plate target, where electron-positron pairs are generated via pair production. A dipole magnet and a collimator select particles based on their charge and momentum, depending on the polarity and strength of the magnetic field. The selected particles pass through the beam shutter, and then enter one of the test beam areas (TB21, TB22, or TB24) where the beam telescope setup is located.

Based on a compromise between beam rate and reduction of multiple scattering, electrons with an energy of approximately 4.6 and 4.8 GeV in TB22 area are used in this work.

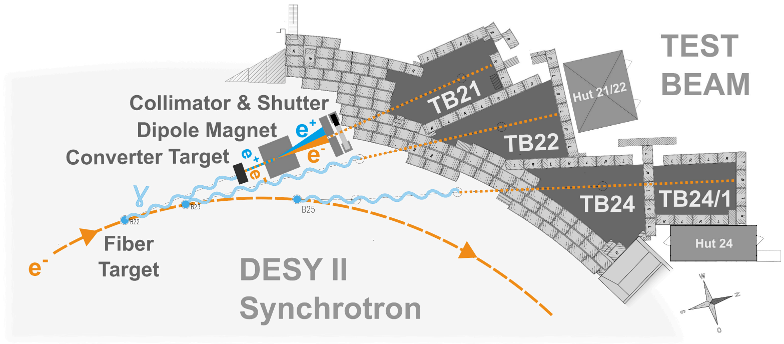

Figure 6.1: Schematic layout of the beam production and extraction at the DESY II test beam facility. Taken from [137].

6.2 Beam Telescope Setup

At the TB22 area, the ADENIUM [66] beam telescope is available for users. A picture of the setup is shown in Figure 6.2(a), with the main devices sketched in Figure 6.2(b). The ADENIUM telescope consists of six ALPIDE [138] planes. These planes are arranged to optimise the pointing resolution of the telescope at the device under test (DUT) position — three placed upstream and three downstream the DUT. All sensors are oriented perpendicular to the beam direction (z-axis), as close together as possible, with the DUT (H2M) in the middle of the setup.

The H2M chip, integrated into the Caribou DAQ system, is mounted on an x-y stage. A plastic support plate provides mechanical support to the stage, and has a cut-out at the sensor position to avoid scattering of the beam electrons. With the used configurations and electron beam energy, the track resolution at the DUT position is approximately 3.8 µm. Its determination is discussed in Section 6.5.4.

Due to the small size of H2M compared to ALPIDE detectors, many of the H2M readout frames contain no relevant particle hits, as the particles miss the sensor and only go through the telescope planes. These events are excluded from the analysis and deteriorate the data-taking efficiency. To address this, the Telepix2 HV-CMOS chip [139] is placed downstream the telescope as a region of interest (ROI) trigger. A rectangular ROI trigger size is configured to match the area of H2M, with a safety margin, and only particles that hit this ROI will cause a trigger signal, reducing the probability of reading out empty H2M frames. The trigger signal sent by Telepix2 is called Hit-OR and has a fast-rising leading edge and an amplitude of approximately 1.2 V.

The AIDA Trigger Logic Unit (AIDA-TLU) [140] ensures synchronization among all devices mentioned by distributing the time reset and global clock signal, applying the trigger logic, and handling busy signals. The Hit-OR of Telepix2 is fed into the trigger input of the AIDA-TLU, which issues a trigger signal to the telescope planes and H2M when the input signal exceeds a configured threshold.

The Hit-OR of Telepix with the TLU is also used as the time reference for ToA measurements. Its time resolution has been measured employing two scintillators and taking the time difference. It is better than 4 ns, which can be considered negligible with respect to that of H2M.

The EUDAQ2 [141] data acquisition framework is used for configuring and reading out all

(a)

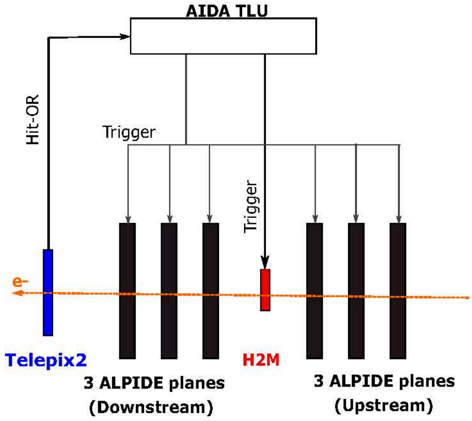

(b)

Figure 6.2: (a) Picture of the test beam setup. (b) Sketch of the test beam setup.

the devices. Remote control of the Keithley for sensor biasing and leakage current monitoring is done via the Constellation framework. A small subset of the data has also been acquired with Constellation, as one of the first applications to validate the framework functionality [142].

6.3 Operation of H2M

The ToT, ToA, and triggered acquisition modes, introduced in Section 3.3, are investigated in the test beam campaigns.

When operating the H2M chip in ToT or ToA acquisition modes, the shutter closes 100 ns after receiving the trigger signal and reopens once the readout is complete. In these acquisition modes, the shutter duration depends on the particle rate, and therefore it varies from event to event. On average, shutter durations of the order of a few microseconds are recorded.

In triggered acquisition mode, the H2M shutter (strobe window) is opened for 500 ns, starting approximately 2 µs after a hit is received, and the hits are validated with the trigger signal. Determined in Section 6.5.5, the 2 µs delay accounts for the trigger latency (dominated by the TLU signal processing), while the 500 ns shutter window accommodates the H2M time walk. The triggered acquisition modes performs a binary readout (hit or no hit).

Given the selected beam energy and small ROI trigger, the rate of recorded frames is approximately 100 Hz.

6.4 Reconstruction and Analysis

Test beam data is reconstructed and analysed using the Corryvreckan framework [125]. This section describes the analysis workflow, and Appendix B lists the configuration and geometry files used.

6.4.1 Event Building

Events are defined by the time window of each H2M frame. Data from the ADENIUM telescope are considered part of the same event if their TLU trigger timestamp falls within this window. The Corryvreckan module [EventLoaderEUDAQ2] handles the loading of H2M, ADENIUM, and TLU data, as well as the construction of events.

6.4.2 Clustering

The cluster position in each telescope plane and DUT is reconstructed using the center-of-gravity algorithm through the [Clustering4D] module, which groups neighboring pixel hits and defines cluster size as the number of pixels in the group. For single-pixel clusters (cluster size of one), the cluster position is assigned to the center of the pixel.

For multi-pixel clusters (i.e., cluster size larger than one) in ToT mode, the cluster position, $(x_{cluster}, y_{cluster})$, is calculated using a ToT-weighted average. This means following Equation 4.1.3, where the weights are given by the ToT values of individual pixels in the cluster, $\omega_i = \mathrm{ToT}_i$.

If the threshold is above 300 electrons, the ToT calibration is applied per pixel, and $\omega_i = f^{-1}(\mathrm{ToT}_i)$ with f being the surrogate function given in Equation 5.1. Below that threshold, the ToT calibration is not applied due to the reasons explained in Section 5.5.5.

For two-pixel clusters in ToT mode, the η-correction [124] is applied to account for non-uniform charge sharing within the pixel cell. This is performed with the [EtaCalculation] and [EtaCorrection] modules. More details about the η-correction algorithm are given in Section 6.5.3.

In triggered mode (binary readout), the cluster position for multi-pixel clusters is reconstructed using the arithmetic mean, with all the weights set to one ($\omega_i = 1, \forall i \in \mathcal{C}$ in Equation 4.1.3).

6.4.3 Tracking

A rectangular ROI is defined in each telescope plane by projecting the Telepix2 ROI onto it. Clusters lying outside of those ROIs are discarded. From the remaining cluster positions in the telescope planes, the particle tracks are reconstructed using the General Broken Lines (GBL) formalism [143], implemented through the [Tracking4D] module. In comparison to a straight-line track fitting, GBL allows for kinks at the telescope and DUT planes caused by multiple Coulomb scattering by constraining scattering angles based on the beam energy and material budget. The defined ROIs in the telescope planes reduce the number of multi-track events and exclude events where particles do not intercept the DUT or create clusters outside the ROI due to large scattering angles that deteriorate the track reconstruction.

A valid track is required to have one hit on each of the six ALPIDE planes and to satisfy the fit quality condition of a track χ^2 per degree of freedom (χ^2/ndof) smaller than 5. The number of degrees of freedom is the total number of measured data points minus the number of parameters estimated by the GBL tracking model.

6.4.4 Track-Hit Association for the DUT

Once tracks are reconstructed, they are matched with clusters on H2M by interpolating their trajectory to the H2M plane. A track is associated with a cluster if its interpolated position lies within a distance of 52.5 µm (1.5 pixel pitches) from the cluster center. This association is handled by the [DUTAssociation] module. The optimisation of this distance cut is explained in Section 6.5.2.

6.4.5 Measured Observables

The hit detection efficiency of H2M is determined using the [AnalysisEfficiency] module, and defined as the fraction of tracks that are associated with a cluster on H2M, relative to the total number of tracks traversing the H2M sensor. Tracks that pass through the outermost columns and rows of the pixel matrix or that intersect a masked pixel or any of its adjacent neighbors are excluded in the analysis to prevent sensor-edge effects and biases from inactive pixels, respectively. The masked pixels are identified in the equalization procedure (see Section 5.2), and are disabled during the data taking. The total percentage of masked pixels remains below 0.5% for all datasets.

The fake-hit rate is determined under test beam conditions with the beam turned off. For this measurement, the shutter is opened for 100 µs, and hits above threshold are counted. The result is normalised to the shutter duration and pixel matrix size (units of $Hz \cdot mm^2$).

The spatial residuals are the difference between the intercept track position on the H2M plane (x/y_{track}) and the cluster center position reconstructed by H2M (x/y_{hit}). The temporal residuals are calculated as the difference between the TLU trigger timestamp ($t_{trigger}$) and the hit time recorded by H2M (t_{hit}) in ToA mode. For cluster size larger than one, the pixel with the earliest timestamp among the cluster defines t_{hit}. All observables are extracted using the [AnalysisDUT]module.

6.5 Alignment, Cuts Determination and Data Corrections

This section describes some of the steps of the reconstruction and the studies conducted to define the analysis procedure. These include aligning the beam telescope and DUT, selecting the track-hit association cut, applying corrections to the data, and determining the preset and strobe durations for measurements in triggered mode.

6.5.1 Beam Telescope and DUT Alignment

Mechanical alignment of the telescope planes at the micrometer level, required to achieve good track resolution, is not possible during data-taking. Additionally, temperature variations in the test beam area lead to mechanical expansions and contractions of the setup, causing small shifts in the relative positions of the detector planes and the DUT. Therefore, the telescope planes and the DUT have to be aligned offline using the Corryvreckan software. This is performed in three steps.

First, prealignment of the telescope planes is performed along the x and y directions using the [Prealignment] module. The cluster positions on each telescope plane are compared with those in the reference detector, chosen as the telescope plane located directly downstream of the DUT. A Gaussian is fitted to the resulting spatial correlation distributions, and the mean is used to

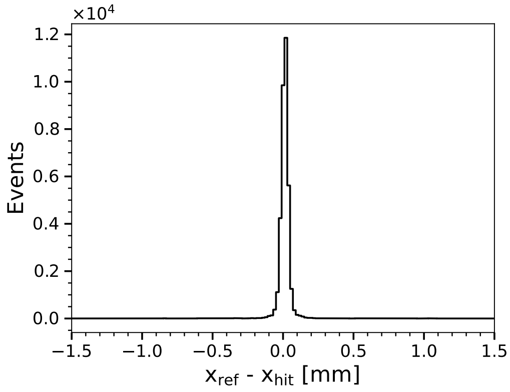

(a)

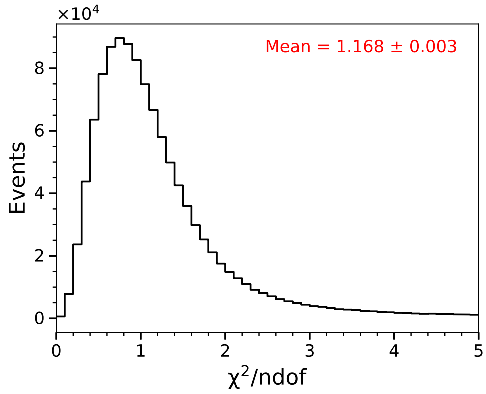

(b)

Figure 6.3: (a) Correlations in X between the reference beam telescope plane and H2M. (b) Distribution of the track χ^2 over the number of degrees of freedom after the alignment of the beam telescope.

apply the necessary shifts in x and y. After the telescope planes are prealigned, the DUT is also included and prealigned in the same way.

Figure 6.3(a) shows the spatial correlations in X between the reference detector position (x_{ref}) and the cluster position reconstructed by the H2M chip (x_{hit}). The centered distribution around zero after prealignment indicates that the applied shift in X correctly aligns the H2M sensor with respect to the reference plane. The broader (nearly flat) component of the distribution originates from uncorrelated clusters and noise. Appendix C.1 illustrates the advantages of triggering on a small ROI in Telepix2, which significantly reduces these background contributions.

In a second step, track reconstruction is enabled by the prealignment obtained in the previous stage, and the track information is then included to further align the telescope planes using the `[AlignmnentTrackChi2]` module. Translational corrections in the x and y directions, as well as rotations, are applied relative to the fixed reference plane. In each iteration, the other five telescope planes are moved, the tracks are refitted using the updated geometry, and the positions and angles are adjusted to minimize the track χ^2.

After the telescope alignment is finalised, the DUT is included in the alignment procedure. Unlike the telescope planes, the DUT is not used in the track fit to avoid biasing the reconstructed tracks. Instead, the DUT is aligned iteratively by minimising the spatial residuals between the interpolated track position at the DUT plane and the reconstructed DUT cluster. This final step is performed using the `[AlignmentDUTResidual]` module.

Each of these steps is repeated iteratively until an optimal alignment is achieved. This is the case when the final mean value of the track χ^2/nodf distribution is approximately one, as shown in Figure 6.3(b).

In Appendix C.2, the DUT position, correlated with the temperature in the test beam area, is shown as a function of time during a five-day data-taking campaign. A clear correlation between the DUT position and temperature is observed. The resulting mechanical expansions and contractions of the setup lead to relative shifts of the DUT with respect to the telescope planes. If

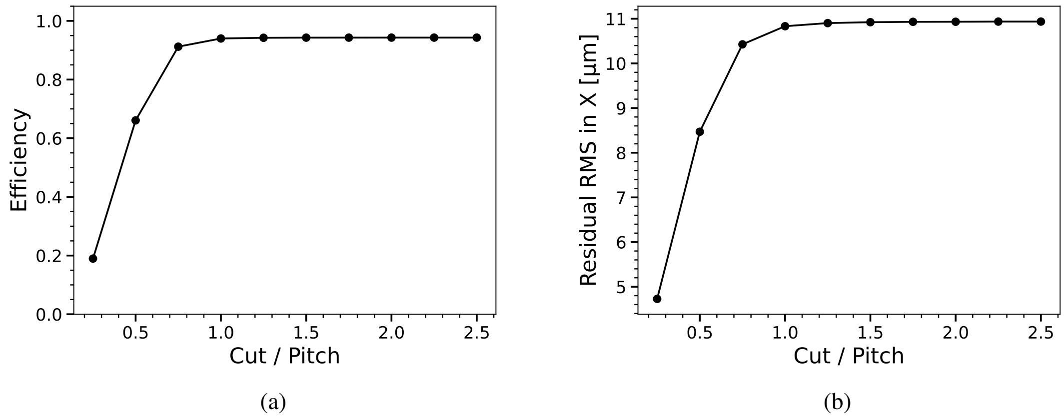

Figure 6.4: Efficiency (a) and spatial residual RMS in X (b) as a function of the association cut in pixel units. The chip is operated at a high threshold to minimise the fake-hit rate.

not corrected with the alignment procedure described above, these shifts would deteriorate the tracking resolution at the DUT position.

6.5.2 Track-Hit Association Cut of the DUT

The association cut is used to match reconstructed tracks to H2M clusters. It is determined by scanning different values and evaluating the resulting efficiency and spatial resolution of H2M. For this measurement, the chip is operated at a large threshold, where the fake-hit rate is negligible.

Figure 6.4 shows the measured efficiency and the RMS of the spatial residuals as a function of the association cut. Due to the majority of single-pixel clusters on H2M (see Section 7.3), the cluster center is typically reconstructed at the pixel center. Thus, for small association cuts (below 0.5 times the pixel pitch), only tracks passing very close to the pixel center are matched to DUT clusters, and the efficiency is underestimated. At the same time, these events have small spatial residuals, leading to an artificially low RMS of the distribution. As the association cut increases and approaches the pixel pitch, the efficiency and the RMS of the spatial residuals reach a plateau. For a cut between half and one times the pixel pitch, not all H2M clusters and tracks are still associated. The reason for that is the combination of a majority of single-pixel clusters reconstructed at the pixel center and the finite track resolution at the H2M plane. The finite track resolution, determined in Section 6.5.4, smears the reconstructed track positions, causing some of the tracks to fall outside the association cut. As a consequence, the efficiency is degraded for this small association cut.

Based on these observations, an association cut value of 52.5 µm is selected, corresponding to 1.5 times the pixel pitch.

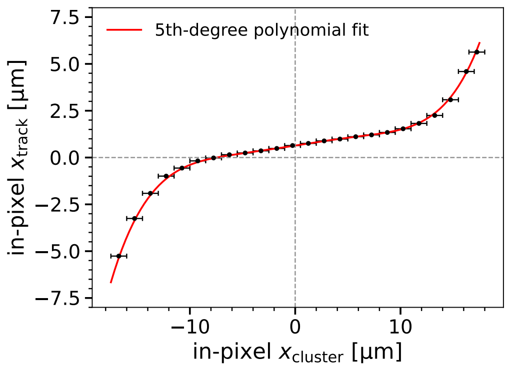

(a) x-dirention

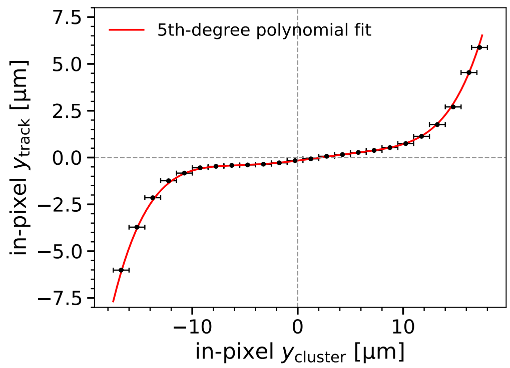

(b) y-direction

Figure 6.5: η-distribution for 2-pixel clusters in the x-direction (a) and y-direction (b). A discontinuous gray line indicates the origin axis.

6.5.3 η-correction

In the case of a linear charge sharing between pixels, the deposited charges induce a charge on each pixel that is proportional to its distance to the pixel center. In ToT mode, this induced charge is proportional to the recorded ToT value and is used to reconstruct the cluster center position via a ToT-weighted average (Equation 4.1).

However, the H2M sensor has a non-uniform charge sharing between pixels, which degrades the accuracy of this method if not corrected. This non-uniform charge sharing originates from the sensor layout, where a strong lateral electric field at the pixel boundaries pushes the charge carriers toward the closest collection electrode. As a result, the induced charge on the adjacent pixels by multi-pixel clusters is reduced, leading to a lower ToT value, and the reconstructed cluster position is biased toward the closest collection electrode.

To account for this non-uniform charge collection, the so-called η-correction algorithm [144] is applied for clusters with a projected size [1] of two in ToT mode, where the track intercept position is used to correct the reconstructed cluster position. The track intercept position is plotted as a function of the reconstructed cluster position. An example is shown in Figure 6.5 in the x and y directions. The non-linear behavior is fitted with a 5th-degree polynomial, whose parameters depend on the sensor geometry and field within it, as well as chip operational parameters (such as sensor bias voltage or threshold). This polynomial fit, obtained from a small data set, is used to correct all the reconstructed cluster positions for the chip in that configuration.

In the case of H2M, the η-correction compensates not only for the non-linear charge sharing but also for the non-uniform in-pixel response, as will be discussed in Section 7.5.1. This effect is visible in Figure 6.5(a), where the fitted polynomial is asymmetric with respect to the origin along the X direction.

[1] The *projected cluster size in X(Y)* is defined as the number of pixels that the cluster spans in the X(Y) direction.

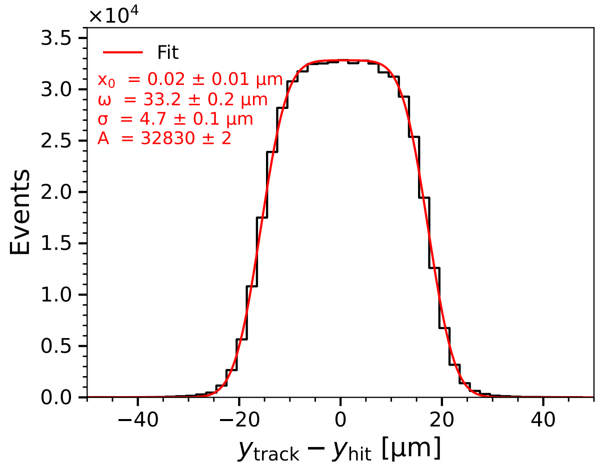

Figure 6.6: Spatial residuals in the y-direction fitted with Equation 6.2.

6.5.4 Track Resolution at the DUT Position

Several test beam campaigns have been conducted at the DESY II Test Beam facility to characterise H2M. However, the beam telescope setup was not identical across all the campaigns: the position of the telescope planes changed, the total chip thickness of H2M varied (from 21 to 50 µm), the thickness of the conductive glue, used to attach it to the chip board, might differ among samples, and the beam energy was tuned in each case (from 4.6 to 4.8 GeV) to optimise the data-taking rates. All these variations lead to different track resolutions at the DUT position (σ_{tel}), that have to be determined to extract the H2M spatial resolution (σ_{DUT}) from the measured spatial residual width (σ_{RMS}), according to the following relation

$$\sigma_{DUT}^2 = \sigma_{RMS}^2 - \sigma_{tel}^2. \tag{6.1}$$

To estimate the track resolution at the DUT position in each test beam campaign, two independent methods have been used.

The first approach employs the *GBL Track Resolution Calculator* [145], which relies on the GBL formalism to estimate the track resolution at different positions in the setup. It takes the setup geometry, the beam energy and the material budget of each detector into account. The thickness of the conductive glue layer on H2M is unknown and has therefore not been included in the estimation.

A second approach, described in [146], is used as an independent check. This technique takes advantage of the large fraction of single-pixel clusters on H2M, for which a box-shaped distribution of spatial residuals is expected. The smearing of the edges of this distribution is attributed to the resolution of the beam telescope at the DUT position. To quantify this resolution, the spatial residual distribution for single-pixel clusters is fitted with the difference of two error functions,

$$f(x) = A \cdot \left[\operatorname{erf}\left(\frac{x - x_0 + \omega_x/2}{\sqrt{2}\sigma_x} \right) - \operatorname{erf}\left(\frac{x - x_0 + \omega_x/2}{\sqrt{2}\sigma_x} \right) \right] \tag{6.2}$$

Table 6.1: Track resolution at the DUT position in three test beam campaigns, each investigating a different H2M sample. The glue thickness is not included in the *GBL Track Resolution Calculator* simulation.

Sample	*GBL Track Resolution Calculator*	Difference of error functions
H2M-3 (50 µm)	2.8 µm	3.7 µm
H2M-8 (25 µm)	3.8 µm	4.7 µm
H2M-10 (21 µm)	2.6 µm	4.1 µm

where A is the amplitude, x_0 and ω_x define the center and width of the box, and σ_x (or σ_{tel}) corresponds to the RMS of the edge smearing due to the track resolution.

Figure 6.6 shows the distribution of spatial residuals for single-pixel clusters, fitted with Equation 6.2. A track resolution of 4.7 µm is extracted from the fit. The method has been verified for different operational parameters of H2M, obtaining consistent values. It has also been verified with data obtained with the CLICdp Timepix3 beam telescope [12] at SPS [147] (see Figure 7.16(b)), and with Monte Carlo simulations (see Appendix C.4) to validate the assumption that the width of the edge is dominated by the telescope resolution.

Table 6.1 summarises the track spatial resolutions determined with the two methods across the three test beam campaigns, each investigating a different H2M sample. Although a similar beam telescope geometry is used, when studying the H2M-8 (25 µm) sample, the protection cover of the chip was not removed, adding 1 mm of extra plastic material to the beam path, and worsening the track resolution. In addition, significant differences are observed between the two approaches. In particular, the *GBL Track Resolution Calculator* yields systematically lower values, which are expected since the glue is neglected in the estimation, and the Gaussian approximation of multiple scattering, both of which lead to underestimating the actual track resolution. As a consequence, the second presented approach is chosen in this work.

6.5.5 Triggered Mode: Trigger Latency and Strobe Duration

As introduced in Section 3.3, when a hit is detected in H2M operated in triggered mode (i.e., a pulse crosses the threshold), the on-pixel 8-bit counter stars to increment from a preset value. Once the counter reaches its maximum value, it generates a carry output. In parallel, if the hit is detected in the trigger plane, a trigger signal, called a strobe, is sent to the H2M chip and distributed to the pixels. While the carry output lasts for one clock cycle, the strobe duration can be tuned, defining an adjustable coincidence window. If the carry output arrives within this strobe window, the event will be recognized as a valid hit. In this acquisition mode, the readout is binary: hit or no hit.

Two timing effects need to be considered: the trigger latency and the H2M time walk. The trigger latency is the time delay between the hit detection in the trigger plane and the arrival of the corresponding trigger signal at H2M. The H2M time walk refers to the dependence of the threshold-crossing time on the signal amplitude (see Section 2.4). Larger signals will cross the threshold earlier, while smaller signals cross it later. This causes the on-pixel counter to start at different times, broadening the distribution of when the carry output is generated. To address these two effects, the counter can be initialized with a preset value, and the strobe signal duration can be configured. To determine the optimal preset value, the hit detection efficiency is measured

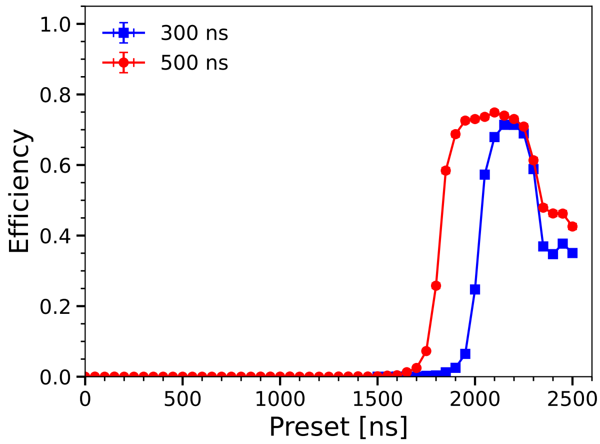

Figure 6.7: Efficiency for different strobe durations obtained in triggered mode as a function of the preset setting. The sensor is biased at −1.2 V and the threshold is 357 electrons.

as a function of the preset. Figure 6.7 shows the scan for two different strobe durations.

A lower preset value means that the counter starts far from its maximum, so the carry output is generated too late relative to the trigger signal. Thus, no coincidence is produced, and the measured efficiency is zero. As the preset value increases, the start of the coincidence window depends on the strobe duration. For longer strobes, the carry output has a higher chance of overlapping with the strobe. At that point, the efficiency rises. At a preset value corresponding to about 2 100 ns, the efficiency reaches the middle of a plateau which has a width corresponding to the strobe duration. This preset setting of 2 100 ns is chosen as the preset for the following measurements. Beyond this window, increasing further the preset value means that the counter starts closer to its maximum, so the carry output is generated too early relative to the trigger signal. This leads to a drop in efficiency. However, due to the particle rate, later hits detected by H2M will still fall in the coincidence window of a previous trigger signal, so the efficiency does not drop to zero. Besides the rate dependence, the probability of such events is proportional to the strobe duration, so longer strobes result in a higher efficiency for this secondary plateau at very high preset values. For these measurements, the threshold is set to a high value of 357 electrons to suppress threshold-related effects.

The ToA distributions are investigated to determine the optimal strobe duration. The pronounced long tail on the left, caused by time walk and the non-uniform in-pixel response discussed in Section 7.6, indicates the need for a strobe duration longer than 300 ns. This time walk impact is also visible in Figure 6.7, where the expected box-like efficiency curve is instead smeared at the edges, describing an s-curve whose width is dominated by the H2M time walk. Based on this, a conservative strobe duration of 500 ns is chosen. Longer strobe durations, up to 1 µs, have been tested and show no improvement in efficiency compared to the 500 ns setting.

CHAPTER 7

Performance in Test Beam Measurements

This chapter summarises the H2M MIP detection performance obtained in test beam measurements using the setup and methodology presented in Chapter 6. It focuses on the measured observables (efficiency, fake-hit rate, cluster size, spatial resolution, charge collection, and time resolution), covering both the global chip response and the in-pixel effects, while also discussing their limitations. The influence of different chip parameters on these observables is discussed, and results obtained in different acquisition modes are also compared.

The chapter begins with a discussion on the observed non-uniform in-pixel response, and continues with studies on the measured observables. In addition, grazing angle measurements have been conducted to extract the active thickness of the sensor.

7.1 Non-Uniform In-Pixel Response

This section discusses the non-uniform in-pixel response observed in test beam measurements, which was already hinted at by the laser and source measurements presented in Section 5.9 and Section 5.5.2, respectively. Because the effect is crucial to the interpretation of the measurement results and affects various of the presented results, it is addressed here at the beginning of the chapter. The section starts by describing the asymmetric ToA response within the pixel cell, and explains how this asymmetry leads to the non-uniform in-pixel efficiency and ToT.

The time residuals are defined as the difference between the trigger timestamp ($t_{trigger}$) and the H2M hit timestamp (t_{hit}), measured with the chip operating in ToA mode. Therefore, the time residuals distributions are often referred to as ToA distributions. For faster charge collection, t_{hit} is smaller, resulting in a larger $t_{trigger} - t_{hit}$. While the time residuals will be discussed in detail in Section 7.6, a closer look at the in-pixel response is given below.

In principle, the in-pixel ToA map of a silicon pixel detector for a chip with features similar to H2M is expected to show fast charge collection near the collection electrode, with a symmetric drop in collection speed toward the edges and corners of the pixel cell as the drift distance increases. Similarly, and according to the simulations presented in Section 4.2.2, a higher efficiency is expected in the region around the collection electrode, with a gradual drop toward the edges and corners. The in-pixel cluster size is also expected to be symmetric (see the simulations in Section 4.2.3), with larger clusters at the edges and corners.

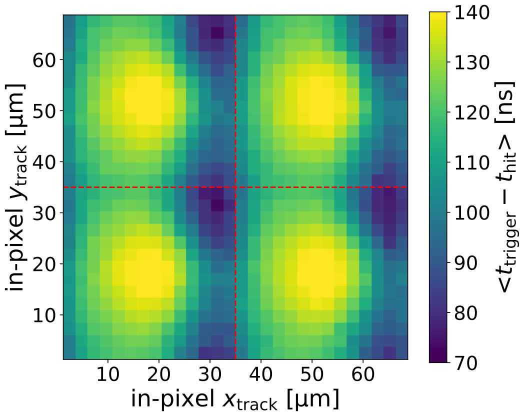

(a) ToA

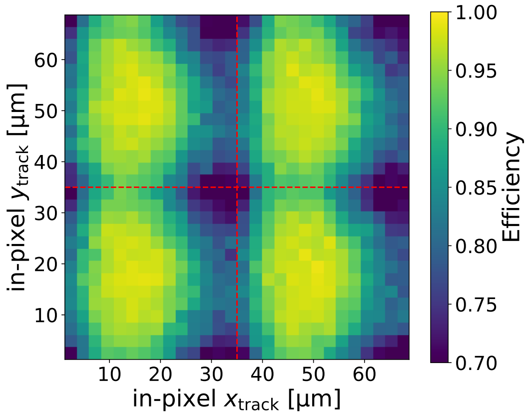

(b) Efficiency

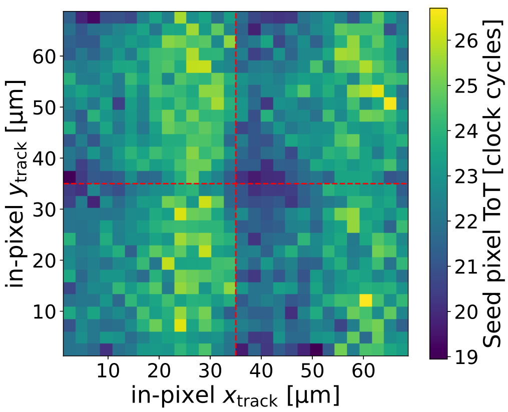

(c) ToT

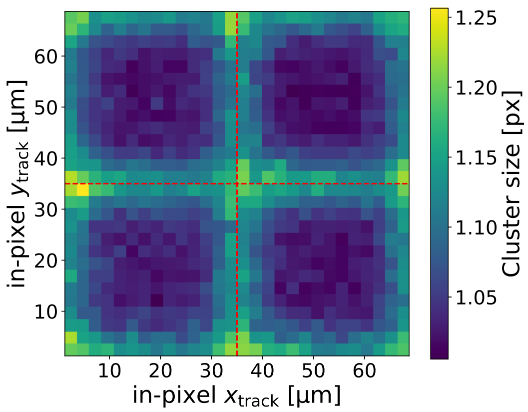

(d) Cluster size

Figure 7.1: In-pixel ToA (a), efficiency (b), ToT (c), and cluster size (d) maps projected onto four pixels. The pixel cell boundary is marked with a dashed red line. The non-uniform in-pixel response is exacerbated by employing the *high ikrum* setting, a sensor bias of -1.2 V, and a detection threshold of 300 electrons.

Figure 7.1(a) presents an in-pixel ToA map projected onto four pixels. Contrary to expectations, the response is asymmetric: the right part of the pixel shows slower charge collection compared to the rest of the cell. When comparing this map with Figure 7.2, it is possible to identify that the increase in ToA occurs at the positions of the 4 µm wide n-well of the analog front-end, which are embedded with the deep p-wells. This behavior is attributed to insufficient shielding of the n-wells within the deep p-well, leading to the formation of local potential wells at the interface between the low-dose n-implant and the deep p-well [103, 126, 148]. These local potential wells, sketched in Figure 7.2, are located in a region with a low electric field, and slow down charge collection. Furthermore, this affects not only the charge carriers generated near the interface, but also those originating close to the sensor substrate due to the drift path of charge carriers, as visible in the linegraphs (see bottom of Figure 7.2). For the same reason, it also affects all charge carriers generated on the right part of the analog n-well. In addition, because of the position of the analog n-well opening (see top of Figure 7.2), the bottom-right region of the pixel cell collects charge faster than the top-right. The mean ToA difference between the pixel center and its top-right corner is approximately 70 ns.

In contrast to the n-well of the analog front-end, the n-wells of the digital logic are relatively thin, mitigating the appearance of this effect.

One of the consequences of the slow charge collection is that it causes a mismatch with the fast response of the CSA: the CSA starts to reset before all the charge has been collected, resulting in a smaller signal amplitude. This effect is known as ballistic deficit. As a result, the reduced signal amplitude leads to a drop in efficiency. This is visible in Figure 7.1(b), where the right part of the pixel cell shows a lower efficiency compared to the left part.

The ballistic deficit effect is illustrated in Figure 7.3 for different feedback current settings (*ikrum*) and signal collection speed. The amplitude for fast signals is mostly unaffected by the *ikrum* setting, whereas the amplitude for slow signals shows a strong dependence. A lower *ikrum* slows the response of the CSA by effectively increasing its integration time, allowing more of these slow charges to be collected before reset, thereby enhancing the signal amplitude and thus the efficiency.

In Figure 7.1(a) and 7.1(b), the sensor is biased with a low voltage, −1.2 V, combined with a high threshold of 300 electrons and the *high ikrum* setting, to aggravate this non-uniform in-pixel response. Increasing the bias voltage leads to larger electric field magnitudes within the sensor (see Figure 4.1), which speeds up the charge collection beneath the deep p-well. Lowering the feedback current effectively extends the integration time of the CSA, reducing the effect of the slower charge correction. Both a large sensor bias and a low *ikrum* setting help to reduce the ballistic deficit, leading to a more uniform charge collection. Furthermore, lowering the threshold makes the efficiency less sensitive to signal amplitude losses. As a result, operating the chip with higher sensor bias and lower *ikrum* and lower threshold improves the efficiency, and a uniform in-pixel efficiency map is obtained. This is shown in Figure 7.4(b), measured with the *low ikrum* setting, a threshold of 224 electrons, and a sensor bias at −3.6 V. A high efficiency is measured around the collection electrode, decreasing towards the edges and corners of the pixel cell due to charge sharing. While the in-pixel efficiency map is symmetric when operating the chip with these settings, this is not the case for the ToA map (Figure 7.4(a)), which still keeps the asymmetry.

Differences in the signal amplitude response among pixel regions have also been observed in

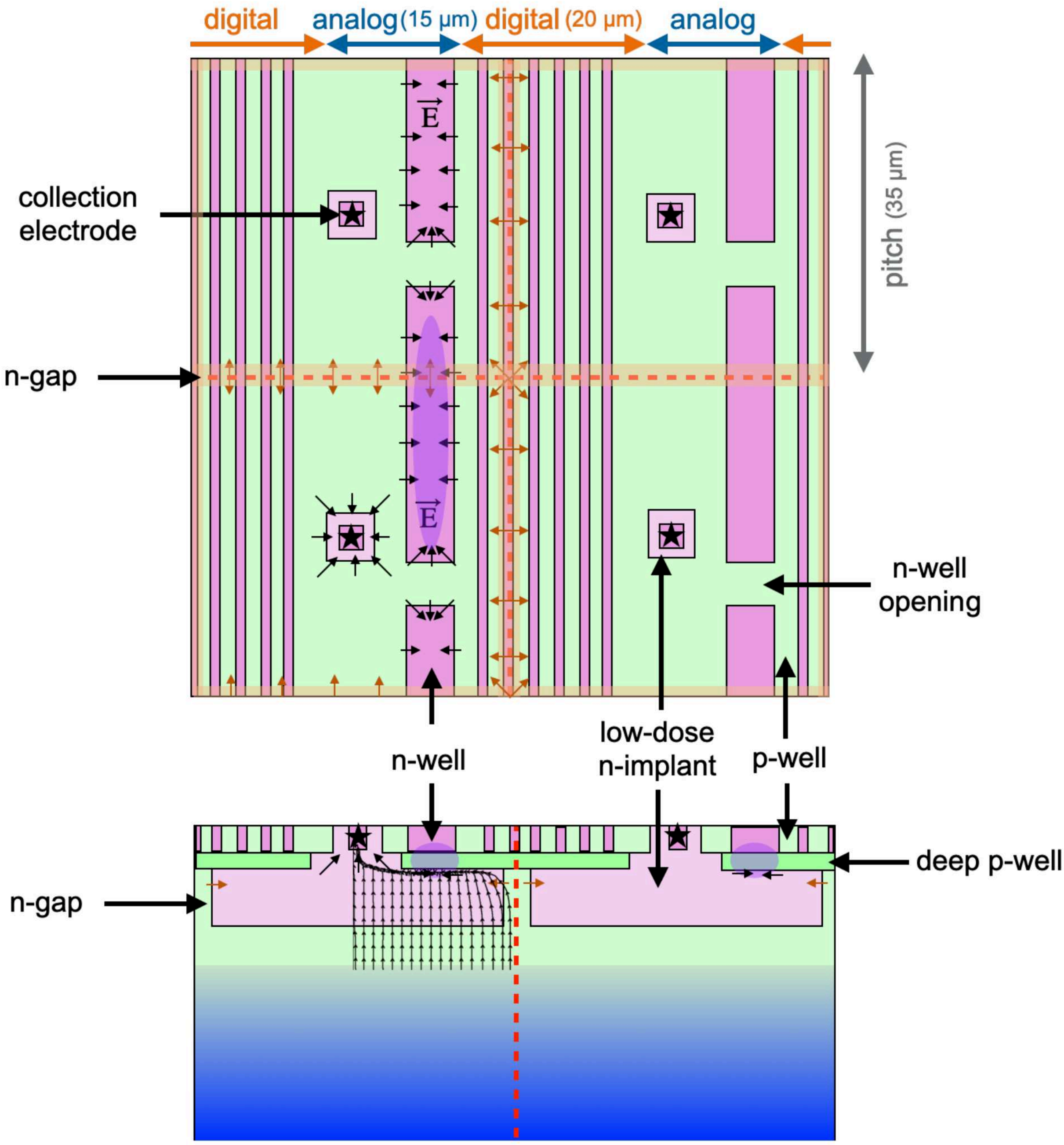

Figure 7.2: On the top: Simplified layout of the n-well and p-well positions within the deep p-well in four pixels. On the bottom: schematic cross-section of two pixels. In both figures, the position of the collection electrode, analog front-end, and digital logic is also indicated. The pixel boundary is marked with a red dashed line. The arrows sketch the direction of the electric field. The shaded regions exaggerate the positions of the generated local potential wells.

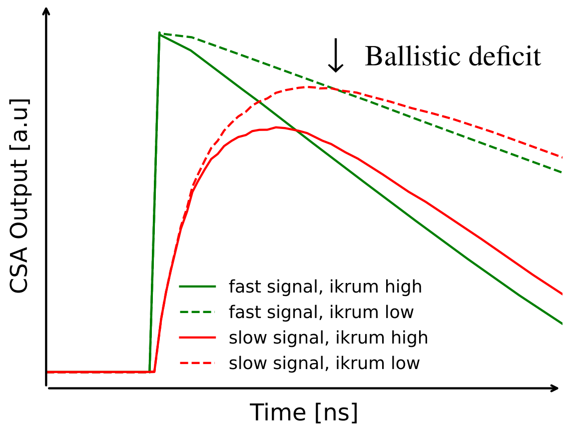

Figure 7.3: Sketch showing the different impact of the ballistic deficit on slow and fast signals. Modified from [148].

the amplitude measurements of the ^{55}Fe K_{α_1} peak described in Section 5.5.2. The smaller peak amplitude visible in Figure 5.9(a) corresponds to the X-ray deposition in the slow charge-collection region. The dependence on the sensor bias voltages and *ikrum* setting is consistent with the behavior shown in Figure 5.10, where the distance between peaks (and thus the ballistic deficit impact) decreases at higher bias voltages and lower *ikrum* settings.

Additionally, the slow charge collection in the right part of the pixel cells results in higher measured ToT values in that region, as shown in Figure 7.1(c). For a slow charge collection, the CSA feedback current is not fully saturated, and the pulse begins to discharge later and with lower effective *ikrum*, leading to an increased recorded ToT value (see Figure 7.3). This effect is more pronounced at the *low ikrum* setting, as shown in Figure 7.4(c). The ToT and efficiency in-pixel patterns are consistent with those obtained with the infrared pulse laser setup presented in Section 5.9.

Although the entire pixel matrix is projected onto the four pixels, differences between those four pixels are still visible in the ToT in-pixel maps. This is a consequence of the variations in the feedback current supplied to each pixel, resulting in different ToT values for the same input signal (see Figure 5.20(a) obtained with the laser setup and Figure 5.21 with test pulse injection).

Figure 7.1(d) displays the in-pixel cluster size map. The slower charge collection and reduced efficiency in the right part of the pixel cell do not affect the charge sharing. This means that the charge carriers are collected more slowly but without allowing for larger diffusion effects, and the in-pixel cluster size map remains symmetric. For a charge carrier generated close to the collection electrode, the resulting cluster size is one. A slight increase in cluster size occurs at the edges and corners of the pixel.

Further discussions on the efficiency, ToA, ToT, and cluster size are given in the following sections.

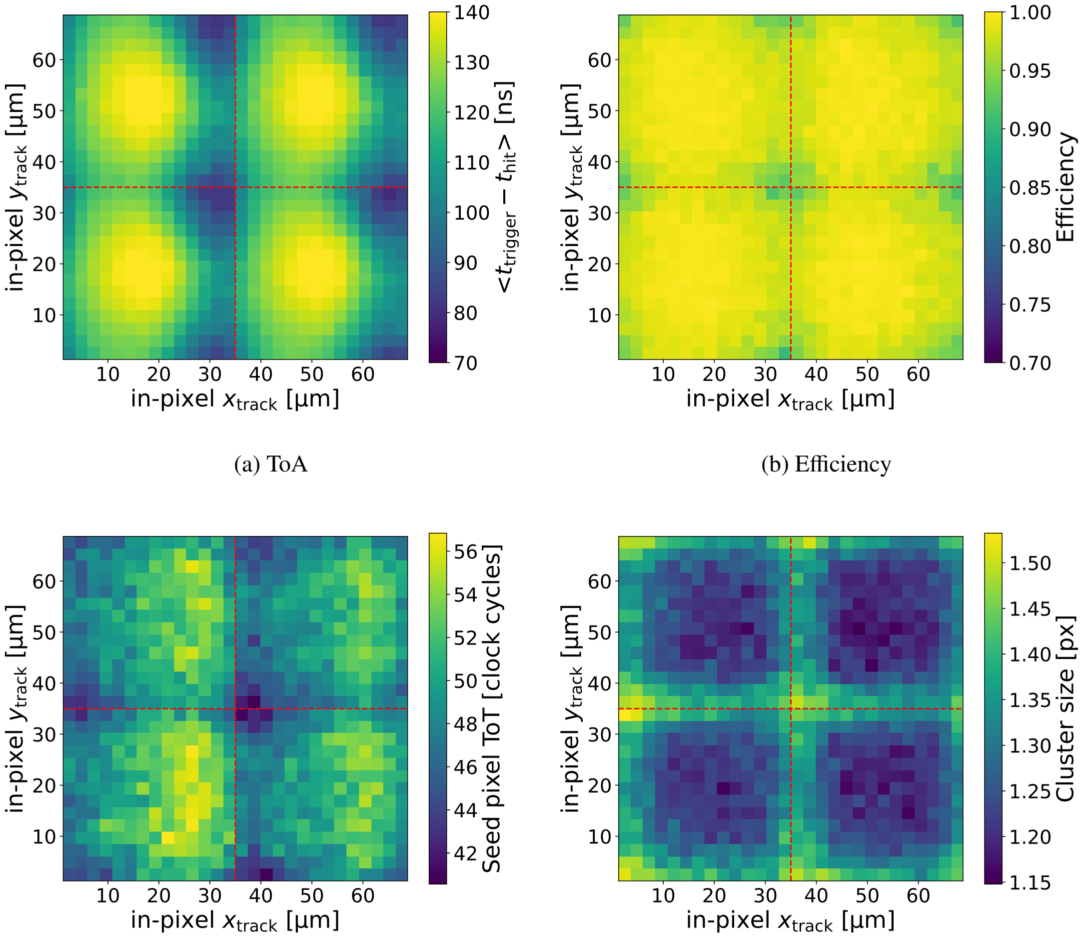

(a) ToA (b) Efficiency

(c) ToT (d) Cluster size

Figure 7.4: In-pixel efficiency (a), ToA (b), cluster size (c), and ToT (d) maps projected onto four pixels. The pixel cell boundary is marked with a dashed red line. The non-uniform in-pixel response is mitigated by employing the *low ikrum* setting, a sensor bias of −3.6 V, and a detection threshold of 224 electrons.

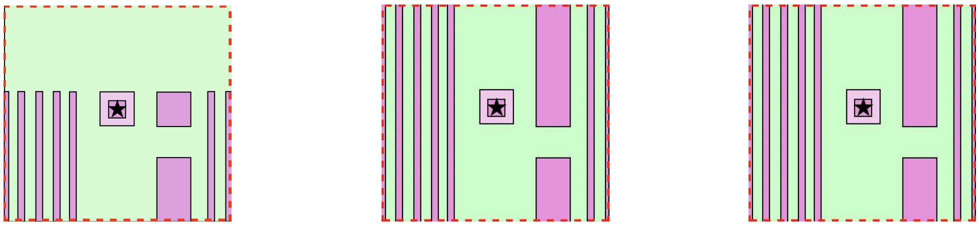

(a) N-wells sketch, top row (b) N-wells sketch, middle row (c) N-wells sketch, bottom row

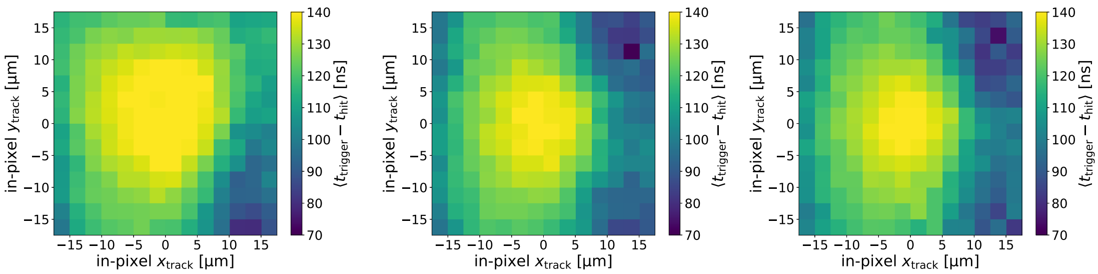

(d) ToA, top row (e) ToA, middle row (f) ToA, bottom row

Figure 7.5: On the top: sketches of the n-wells (pink) inside the deep p-wells (green) of a pixel in the top row (a), middle row (b), and bottom row (c). On the bottom: the ToA maps of the first row (d), middle row (e), and bottom row (f) projected onto one pixel. Pixels in the first and last columns are excluded.

Column and Row Dependence

Although all pixels in the matrix have the same readout circuitry, not all of them host the same structures within the deep p-well. Specifically, the upper half of the top row does not contain any n-well structure embedded in the deep p-well. Figure 7.5(a) illustrates the positions of the n-well and p-well within the deep p-well for a pixel in the top row, while Figure 7.5(b) shows the layout for a pixel in a middle row. Similarly, the left half of the left column in the pixel matrix is also free of n-well structures inside the deep p-well. This is because the circuitry of each pixel is not contained within its pixel's area, but is shifted by about half a pitch.

The in-pixel ToA map has been measured for pixels only from the top row, and compared to those from the middle rows in the pixel matrix. Figure 7.5(e) shows the ToA map of the middle row (seventh) projected onto one pixel. The in-pixel pattern is the same as the one discussed in Figure 7.1(a), where a slower charge position occurs beneath the wide n-well of the analog front end. The ToA map for a pixel on the top row, Figure 7.5(d), shows a different pattern, however. The slow charge collection is observed only in the area covered by the n-wells of the analog front-end. In the absence of electronics in the top-right part of the pixel, the ToA is reduced from approximately 70 ns to about 30 ns. To rule out sensor edge effects in the comparison, the bottom row is also studied, and shown in Figure 7.5(f). The same in-pixel ToA pattern is observed as in a pixel located in the middle of the pixel matrix.

An asymmetry is still visible in Figure 7.5(d), where the top-right region of the pixel shows a slower charge collection compared to the top-left. The extension of a small part of the n-wells

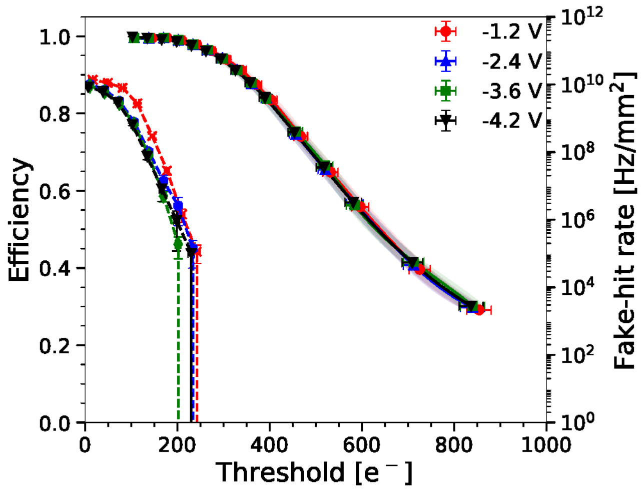

Figure 7.6: Efficiency (left axis) in solid lines and fake-hit rate (right axis) in dashed lines as a function of the threshold for three different sensor bias voltages in triggered mode, and using the *low ikrum* setting. The uncertainty is dominated by the threshold calibration factor, which is represented by a band.

into the top area is supposed to be still sufficient to impact the electric field in the corner of the pixel, creating a similar effect.

These results demonstrate the strong impact of the n-well layout and motivate alternative layouts in which the n-wells are placed in areas with a larger electric field. Those mitigation studies have been performed through simulations in [103], and are briefly summarised in Section 8.5.

7.2 Efficiency and Fake-Hit Rate

One of the main performance parameters of a silicon pixel detector is its MIP detection efficiency. It depends on several operational parameters. Following the in-pixel efficiency maps presented in Section 7.1, this section examines the global chip efficiency for different chip configurations and acquisition modes.

7.2.1 Threshold and Sensor Bias Dependence

Figure 7.6 shows the efficiency and fake hit rate as a function of the threshold for various sensor bias voltages obtained in triggered mode. By raising the threshold, the probability of detecting a hit (from either a particle or noise) decreases. At low bias voltages (<1.2 V), the increased sensor capacitance leads to higher noise and, consequently, a higher fake-hit rate. This is consistent with the noise measurements performed in the lab (see Figure 5.5(b)). In contrast, the efficiency does not show a significant dependence on the sensor bias voltage, as expected from simulations presented in Section 4.2.2. Although these trends are similar to those reported for other chips manufactured in the same 65 nm ISC process, such as APTS [149], H2M shows lower efficiency above 200 electrons. The cause of this loss of efficiency at higher thresholds is attributed to the ballistic deficit, as explained in Section 7.1.

Table 7.1: Highest threshold at which an efficiency above 99% and 99.5% is maintained for different sensor bias voltages in triggered mode.

	−1.2 V	−2.4 V	−3.6 V	−4.2 V
99%	$(205 \pm 6)\,e^-$	$(208 \pm 6)\,e^-$	$(208 \pm 6)\,e^-$	$(208 \pm 6)\,e^-$
99.5%	$(179 \pm 6)\,e^-$	$(178 \pm 6)\,e^-$	$(182 \pm 6)\,e^-$	$(183 \pm 6)\,e^-$

An efficiency of 99.6% is achieved at a threshold of 144 electrons when the sensor is biased at −3.6 V. The fake-hit rate at this threshold is around 1.5×10^7 Hz/mm^2 (i.e., 18.4 kHz per pixel), corresponding to a matrix occupancy of approximately nine pixels (<1% of the active pixels) per 500 ns frame. The uncertainty is dominated by the threshold calibration factor, which is represented by a band in Figure 7.6.

Table 7.1 lists the highest threshold at which efficiencies above 99% and 99.5% are measured for different sensor bias voltages. Efficiencies above 99.5% are reached at a threshold of approximately 180 electrons, where the fake-hit rate is around 1×10^6 Hz/mm^2 (i.e., an occupancy lower than one pixel per frame).

The APTS paper [149] reports similar studies for different test structures with pixel pitches from 10 µm up to 25 µm. The results in the paper show that structures employing the n-gap layout with larger pixel pitches have reduced charge sharing, allowing efficiencies above 99% to be maintained at higher thresholds. In particular, the n-gap APTS with a 25 µm pitch and a sensor bias of −1.2 V maintains an efficiency above 99% up to a threshold of 211 electrons. For H2M, the highest threshold at which 99% efficiency is achieved is (205 ± 6) electrons. Therefore, a slightly higher threshold was expected to still yield efficiencies above 99%, as extrapolated from the APTS results. The observed non-uniform in-pixel response may explain why this efficiency is not preserved at larger thresholds. Further discussion is given in Section 8.1, where the results are compared with the Monte Carlo simulations.

The single-pixel noise reported for the n-gap APTS with a 25 µm pitch and a sensor bias of −1.2 V is 28 e^-_{RMS}, which is lower the 40 e^-_{RMS} measured for H2M in Section 5.3. This higher single-pixel noise, together with the threshold dispersion between pixels, results in a higher fake-hit rate in the H2M chip. Noise differences between the two chips can be attributed to the different front-end architecture.

7.2.2 Feedback Current Dependence

Figure 7.7(a) shows the measured efficiency as a function of the feedback current. Although the threshold has not been independently calibrated for each *ikrum* setting, it is approximately (300 ± 30) electrons for all the settings. At such a high threshold, the fake-hit rate is negligible and therefore not shown in the figure. According to Figure 7.6, efficiency variations between 270 and 330 electrons are below 10%, thus the threshold variations cannot account for the large differences observed in Figure 7.7(a). Consistent with the lab measurements (see Section 5.7), the efficiency peaks at an *ikrum* setting of 10 DAC. For higher *ikrum* values, the gain decreases with increasing feedback current, leading to a reduction in signal amplitude and, consequently, in efficiency.

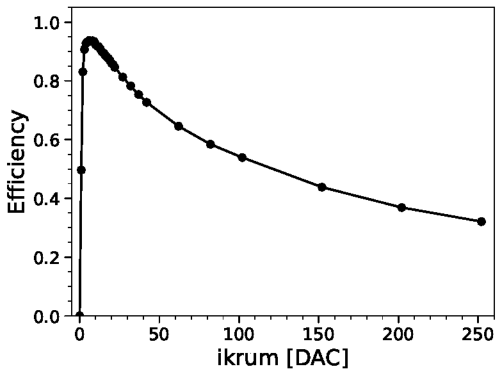

(a)

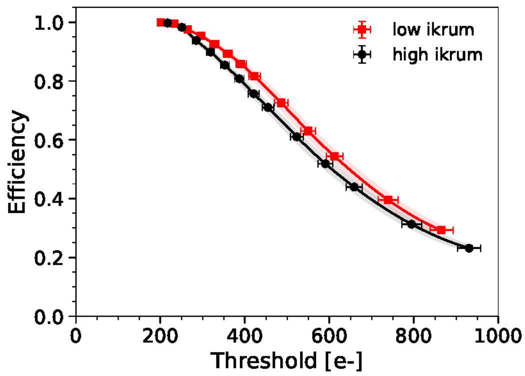

(b)

Figure 7.7: Efficiency as a function of the feedback current for a threshold of approximately 300 electrons (a), and as a function of the threshold for two different *ikrum* settings (b). The sensor is biased at −1.2 V, and the data is acquired in ToA mode. The uncertainty is dominated by the threshold calibration factor, which is represented by a band.

Figure 7.7(b) shows the efficiency as a function of the calibrated threshold for the *low ikrum* and the *high ikrum* settings to prove that this holds after calibration. Even though they have different threshold calibration factors (see Section 5.5.2), the *low ikrum* setting consistently yields higher efficiency. This improvement is attributed to the mitigation of signal amplitude losses caused by ballistic deficit in the slow region of the pixel, as explained in Section 7.1.

7.2.3 Comparison Between Acquisition Modes and Lowest Achievable Threshold

The primary difference in efficiency and fake-hit rate between the triggered, ToT, and ToA acquisition modes arises from differences in the used shutter duration. In ToT and ToA modes, the shutter is opened after the previous readout is finished and closed by the incoming trigger signal (typically remaining open for a few microseconds), thus depending on the beam rate. In contrast, the shutter duration in triggered mode is fixed at 500 ns, corresponding to the strobe duration. This makes a difference of more than three orders of magnitude.

Figure 7.8 shows the efficiency as a function of the threshold in ToT, ToA, and triggered mode. The shorter shutter duration in triggered mode reduces the probability of a noise pixel firing, allowing the chip to operate at a lower threshold. However, the shorter shutter duration also reduces the likelihood of detecting a particle at a given threshold, particularly in cases of slow charge collection where the delayed carry signal may fall outside the coincidence window. This effect results in a lower efficiency compared to ToT and ToA.

These results are summarised in table 7.2, where the minimal achievable threshold is defined as the value at which the fake hit occupancy is below 1%. In triggered mode, this corresponds to 144 electrons, whereas in ToT and ToA modes, it is approximately 224 electrons, which limits the highest achievable efficiency to (98.9 ± 0.1)%.

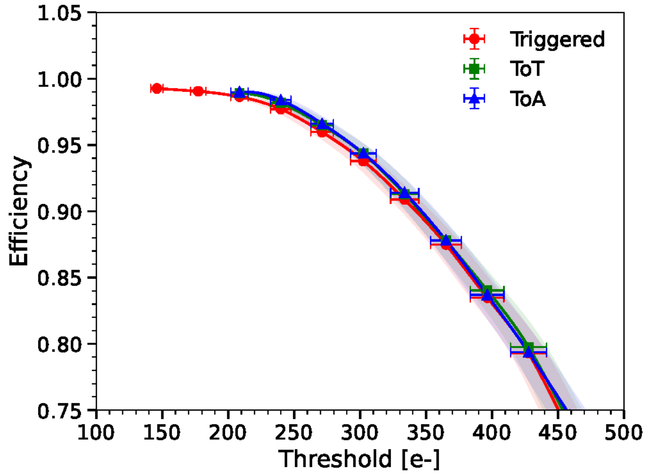

Figure 7.8: Efficiency as a function of the threshold in triggered, ToT and ToA mode. The sensor is biased at -1.2 V. The uncertainty is dominated by the threshold calibration factor, which is represented by a band.

In triggered mode, the shutter duration is constrained by the need to accommodate the H2M time walk (and non-uniform in-pixel response), and cannot be further shortened without degrading the efficiency (see Section 6.5.5). In the case of ToT and ToA, the shutter length could be reduced by using an external trigger synchronous to the accelerator clock to open and close the shutter after a fixed interval (on the order of the H2M time walk).

Table 7.2: Efficiency and lowest achieved threshold comparison between acquisition modes. The measured efficiency at the lowest achieved threshold in ToA and ToT acquisition modes is included. The sensor is biased at -1.2 V.

	ToA	ToT	Triggered
Lowest achieved threshold	(224 ± 8) e^-	(224 ± 8) e^-	(144 ± 6) e^-
Efficiency at the lowest threshold	(98.9 ± 0.1)%	(98.9 ± 0.1)%	(99.5 ± 0.1)%
Efficiency at 224 electrons	(98.9 ± 0.1)%	(98.9 ± 0.1)%	(97.8 ± 0.1)%

7.2.4 Impact of the Test Pulse Capacitor

All the measurements presented so far have been performed with the parameter `tp_enable` introduced in Section 3.2 enabled, which allows for test pulse injection at the CSA input. In this way, the ToT calibration for the chip in this configuration is obtained (see Section 5.5.4). However, enabling it connects an additional parallel capacitance to the CSA input, which increases the noise levels, as shown in Figure 7.9(a) for different sensor bias voltages, as well as the gain, as measured with radioactive sources to determine the calibration factor. To evaluate how this affects the performance of the chip under particle detection, dedicated test beam measurements have been conducted.

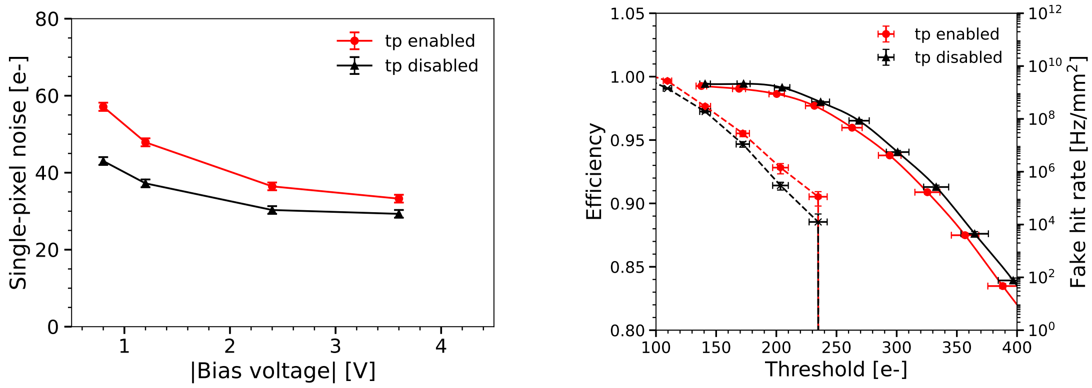

(a) (b)

Figure 7.9: (a) Single-pixel noise as a function of the sensor bias voltage with enabled/disabled `tp_pulse`. (b) Efficiency measured in triggered mode as a function of the threshold with enabled/disabled `tp_pulse`. The sensor is biased at −1.2 V and the *low ikrum* setting is used.

Figure 7.9(b) shows the efficiency and fake hit rate as a function of the threshold for the two settings, individually calibrated. As expected, when `tp_enable` is disabled, the capacitance and noise are reduced and thereby the fake-hit rate. This reduction in the input capacitance also increases the gain, leading to a higher efficiency. Therefore, the chip achieves its best performance in terms of efficiency and fake-hit-rate with `tp_enable` disabled.

However, since ToT calibration has proven to be essential for fine reconstruction of the hit position (see Section 7.5), no further measurements have been performed with this setting.

7.2.5 Limitations on the Efficiency, Fake-Hit Rate and Lowest Achievable Threshold

The lowest achievable threshold is limited by single-pixel noise and threshold dispersion, measured to be of the order of 40 and 25 electrons, respectively, and depends on the bias voltage (see Section 5.3). Towards smaller bias voltages, the sensor capacitance increases, and thus the single-pixel noise, which dominates the fake-hit rate. This high single-pixel noise leads to a fake-hit rate higher than that of other prototypes produced in the same technology.

The highest threshold that achieves an efficiency above 99% is approximately 205 electrons at −1.2 V. A slightly higher threshold was expected from the APTS studies by extrapolating the results of the largest pitches. The reason for that is the non-uniform charge collection of H2M, which causes the efficiency to start dropping earlier.

7.3 Cluster size

Charge carriers generated in a pixel can diffuse into neighboring pixels, increasing the measured cluster size. In particular, charge carriers generated near the edges between two pixels may lead

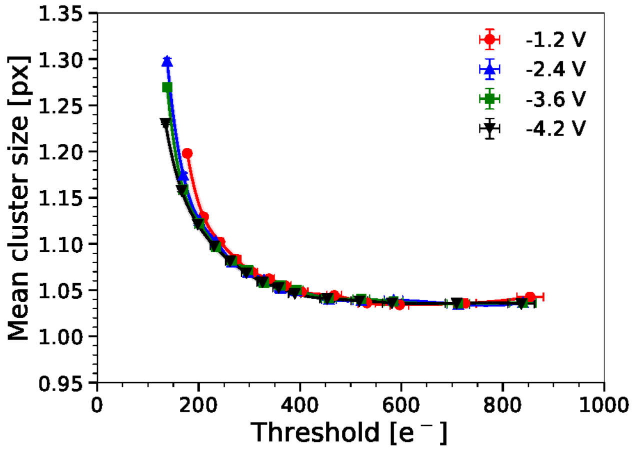

Figure 7.10: Cluster size as a function of the threshold for different sensor bias voltages in triggered mode. The sensor is biased at -1.2 V and the *low ikrum* setting is used. The uncertainty is dominated by the threshold calibration factor, which is represented by a band.

to clusters of size two, while charge deposited at the corner of a pixel can produce clusters of size up to four. When a particle crosses a thin sensor perpendicularly and deposits charge close to the collection electrode, the majority of events will be single-pixel clusters. Delta-rays, however, can traverse large distances in silicon and thereby increase the cluster size.

The way the charge diffuses depends on the electric field configuration within the pixel and has a direct impact on the spatial resolution of the sensor. This section presents and discusses the cluster size distributions measured on H2M and analyzes their dependence on the threshold, sensor bias voltage, feedback current setting, and acquisition mode. In-pixel maps at different thresholds have been shown in Figure 7.1(d) and 7.4(d).

In the following, all clusters presented are associated clusters (i.e., a track has been associated with the H2M cluster, as explained in Section 6.4.4).

7.3.1 Threshold and Sensor Bias Dependence

The large pixel pitch of 35 µm makes it less likely that the charge deposited in a pixel reaches its neighbor via diffusion (see Equation 2.13), leading to a mean cluster size close to unity. Additionally, the thin epitaxial layer of ~10 µm limits the lateral diffusion of the electrons and holes before they are collected. Both geometrical factors lead to a majority of single-pixel clusters in H2M. Additionally, the *n-gap* sensor layout further suppresses charge sharing between pixels due to the strong lateral component of the electric field, which pushes charges toward the nearby collection electrode.

Figure 7.10 shows the mean cluster size as a function of the threshold for different sensor bias voltages. For the same deposited charge, a lower threshold increases the probability to collect charge in neighboring pixels, and the mean cluster size increases. As the sensor bias voltage increases, the electric field becomes stronger, speeding up the charge collection and limiting the

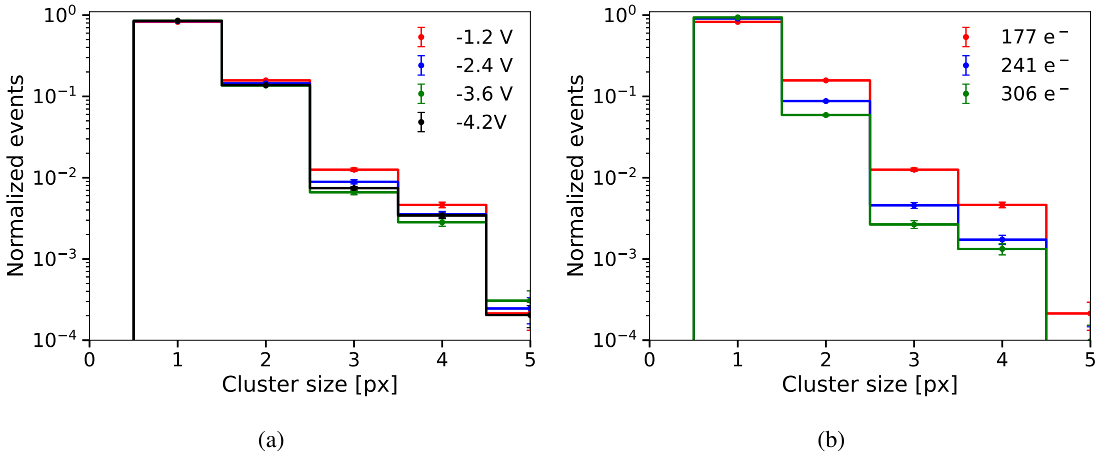

Figure 7.11: Cluster size distributions at different sensor bias voltages at a threshold of approximately 177 electrons (a) and for different thresholds at a sensor bias voltage of −1.2 V (b).

lateral diffusion of charge carriers away from the closest collection electrode. As a result, the largest cluster sizes are observed at the lowest achievable thresholds, and when the sensor is biased with a low voltage.

Figure 7.11(a) shows the cluster size distribution for different sensor bias voltages at a fixed threshold of 177 electrons, while Figure 7.11(b) displays the distributions for three different thresholds with the sensor biased at −1.2 V, respectively. In all cases, two-pixel clusters are the most common multi-pixel clusters. For a threshold of 177 electrons at −1.2 V, the mean cluster size is (1.19 ± 0.01). Single-pixel clusters occur in 82% of the events, 16% correspond to two-pixel clusters, and the remaining 2% have a cluster size greater than two.

7.3.2 Feedback Current Dependence

Figure 7.12(a) shows the mean cluster size as a function of the threshold for two different feedback current settings. For the *low ikrum* setting, the efficiency improves in the low-field regions. These events, which are not detected with the *high ikrum* setting, produce larger clusters due to their location at the pixel edge, and lead to a slight increase in the mean cluster size. Therefore, the lowest *ikrum* setting not only improves the efficiency, but also increases the cluster size, which is beneficial for the spatial resolution.

7.3.3 Comparison Between Acquisition Modes

Figure 7.12(b) compares the mean cluster size for the ToT, ToA, and triggered modes. For smaller thresholds (below 300 electrons), the mean cluster size differs due to the different noise sensitivities of the acquisition modes (see Section 7.2.3). At larger thresholds, where the noise impact is suppressed, no significant difference between the acquisition modes is observed.

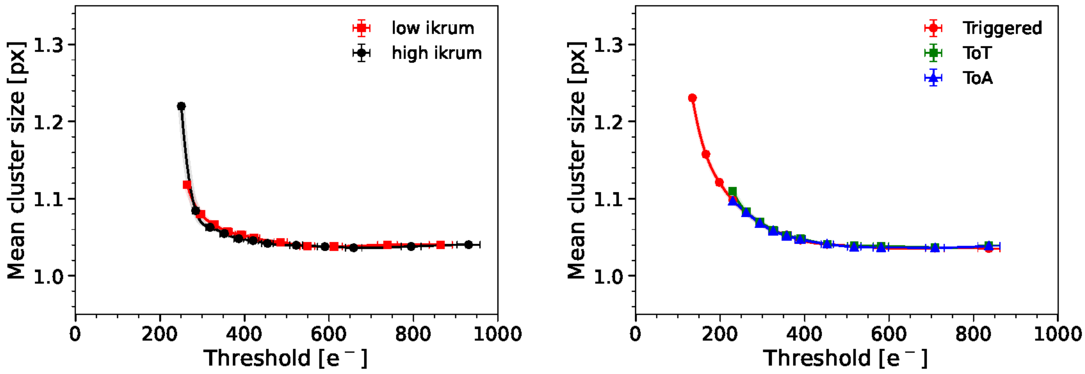

Figure 7.12: (a) Cluster size as a function of the threshold for different feedback currents in ToA mode. Note that the two feedback currents have different calibration factors (i.e., the data points are not aligned along the x-axis). (b) Cluster size as a function of the threshold for different acquisition modes. In both figures, the sensor is biased at −4.2 V. The uncertainty is dominated by the threshold calibration factor, which is represented by a band.

7.4 Signal Distribution

The charge collected from an incident MIP is measured in ToT mode, where the pulse duration above a fixed threshold is proportional to the collected charge. Unlike the triggered mode, which provides only hit/no-hit information, the 8-bit ToT counter of H2M allows for a high-resolution charge measurement that can be used to refine the spatial reconstruction of the hit (see Section 4.1.3). Therefore, the charge collection signal is a key parameter for studying the performance of the sensor in tracking applications. The following section presents the H2M charge measurements for different chip operating settings.

7.4.1 Seed Pixel ToT and Cluster ToT

For each cluster, the seed pixel is defined as the one with the highest signal, i.e., the longest ToT. The cluster charge is given by the sum of the ToT values of all pixels in a cluster.

Figure 7.13(a) shows the seed pixel ToT distributions measured in the test beam. The threshold is approximately 300 electrons, and different feedback currents and sensor bias voltages are used. The same trends are observed as in the ^{55}Fe measurements presented in Section 5.4. At lower *ikrum* settings, the measured ToT values are longer and the ToT distribution becomes broader. This is due to the slower signal falling edge of the signal and the increased impact of pixel-to-pixel variations, respectively.

Since the majority of clusters have a size of one, the seed pixel and cluster charge distributions look similar, as shown in Figure 7.13(b). Noisy pixels saturate the in-pixel 8-bit counter at 256 clock cycles. As the cluster ToT is the sum of the charges of all pixels in the cluster, its distribution does not saturate at 256 and therefore deviates from the seed pixel distribution at larger ToT values.

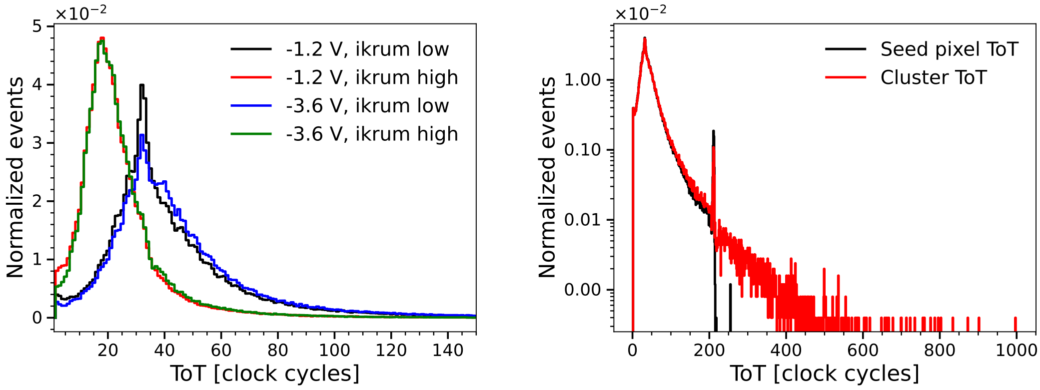

(a) (b)

Figure 7.13: (a) Seed pixel ToT distribution for two different feedback currents and sensor bias voltages. The threshold is approximately 300 electrons. (b) Seed pixel and cluster ToT distributions for the *low ikrum* setting and sensor bias voltage of -1.2 V.

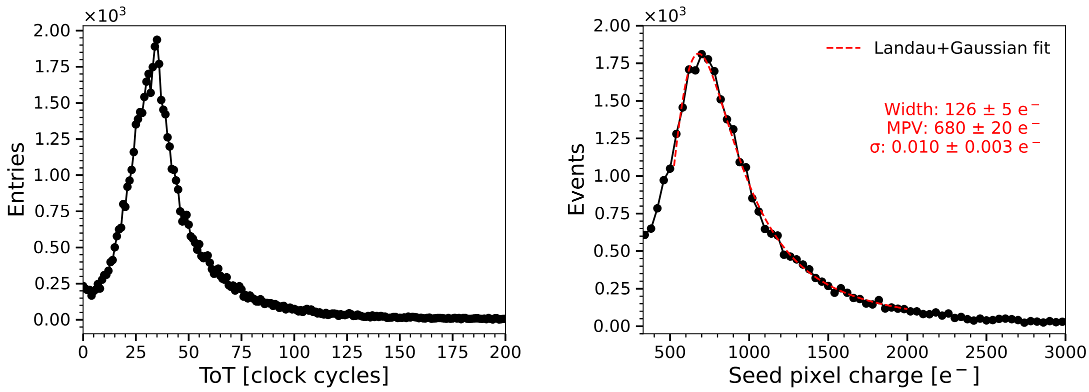

(a) Uncalibrated (b) Calibrated

Figure 7.14: Seed-pixel charge distribution before (a) and after (b) calibration. The sensor is biased at -1.2 V, the threshold is approximately 300 electrons, and the *low ikrum* setting is used. For the calibrated distribution, a Landau-Gaussian convolution is used for fitting. The fit parameters of the *width* and *MPV* of the Landau distribution, and the standard deviation of the Gaussian component σ, are displayed.

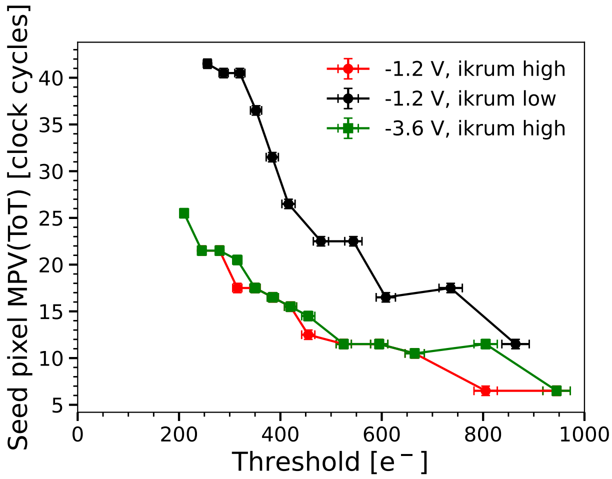

Figure 7.15: MPV of the seed pixel ToT as a function of the threshold, shown for different feedback currents and sensor bias voltages.

A second peak appears at around 210 clock cycles in Figure 7.13(b). This originates from the fixed delay between receiving the trigger signal and closing the shutter. For signals with large ToT values, the shutter closing can occur before the pulse returns to baseline, resulting in a truncation of the ToT measurement to ~ 210 clock cycles. Therefore, this effect is an artifact of the readout scheme, and since it is far from the MPV of a MIP, it can be ignored.

The ToT distributions can be converted to electrons by applying the ToT calibration (see Section 5.5.4). As an example, Figure 7.14(a) and Figure 7.14(b) show the uncalibrated and calibrated ToT distributions, respectively. The threshold is approximately 300 electrons, with the *low ikrum* setting, and a sensor bias of -1.2 V. For the calibrated distribution, a convolution of a Landau and a Gaussian function is used to fit the data. The extracted MPV value of (680 ± 20) electrons, which is slightly higher than the expected value from other chips from the same submission [149]. A possible explanation is the recording of higher ToT values across the large right part of the pixel cell (see Figure 7.4(c)), which is caused by the slower charge collection, and for which the calibration process does not account. Further discussion can be found in Chapter 8, where the results are compared with simulations.

7.4.2 Threshold and Sensor Bias Dependence

Figure 7.15 shows the MPV of the seed pixel ToT distribution as a function of the threshold for different feedback currents and sensor bias voltages. Larger thresholds and higher *ikrum* settings result in lower MPV values. The difference between sensor bias voltages is insignificant. Since the data are not ToT-calibrated, the points do not follow a smooth trend. Nevertheless, the results demonstrate the functionality of the front-end, following the expected trends observed in the laboratory measurements and discussed in Section 5.4.

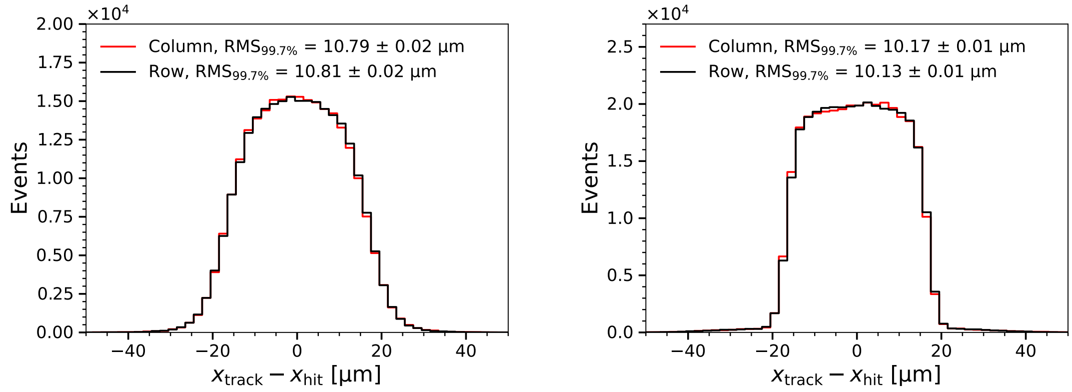

(a) ADENIUM beam telescope at DESY II

(b) CLICdp Timepix3 beam telescope at SPS

Figure 7.16: Spatial residuals in column (X) and row (Y) direction recorded in ToT mode. The sensor is biased at −3.6 V and the threshold is 224 electrons. The data is recorded using the ADENIUM beam telescope at DESY II (a), and the CLICdp Timepix3 beam telescope at SPS (b).

7.5 Spatial Resolution

Primary and secondary vertices reconstruction is the primary task of a vertex detector in a particle collider. Similarly, tracker detectors determine the momentum of the particles through the reconstruction of their trajectories. Achieving these goals requires an accurate determination of the particle impact position in the sensor (see Chapter 1). Spatial resolution studies of the sensor are thus essential to quantify the precision of this reconstruction.

This section presents the spatial resolution measurements of H2M and its dependence on the threshold and sensor bias voltage. The impact of the acquisition mode, whether charge information is used or not, is also examined.

7.5.1 Spatial Residuals and Contributions from Different Cluster Sizes

Figure 7.16(a) shows the spatial residuals along the column and row direction for a threshold of 224 electrons. The width of the residuals ($RMS_{97.7\%}$) is calculated as the truncated RMS of the central 97.7% of the entries in the distribution.

For the same chip settings, Figure 7.16(b) presents the spatial residuals measured at SPS [147] using the CLICdp beam telescope [12], which provides a track resolution of about 1.5 µm. The narrow box-like residual distribution is consistent with the dominance of single-pixel clusters. In contrast, the edge smearing for the DESY II data is explained by the worse track resolution of the ADENIUM telescope, as discussed in Section 6.5.4.

The residual distributions for different projected cluster sizes and acquisition modes are compared in Figure 7.17. In triggered mode, the charge information is binary (hit or no hit). In ToT mode, however, charge information is stored, and the hit position is reconstructed using a ToT-weighted average method (see Section 4.1.3). This *uncorrected hit position* is further refined by applying the ToT calibration and the η-correction, which together determine the *corrected hit position*.

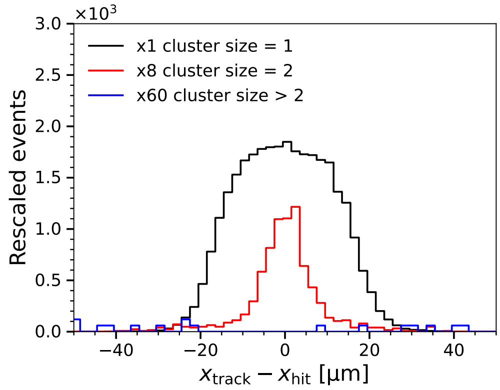

(a) Triggered, X direction

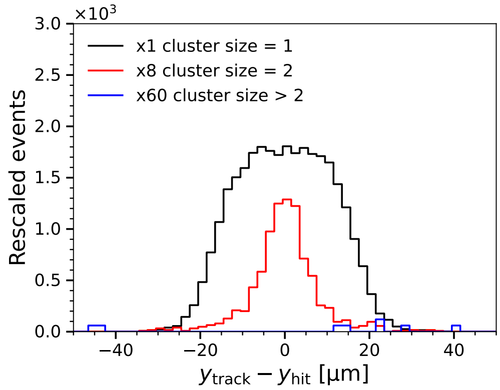

(b) Triggered, Y direction

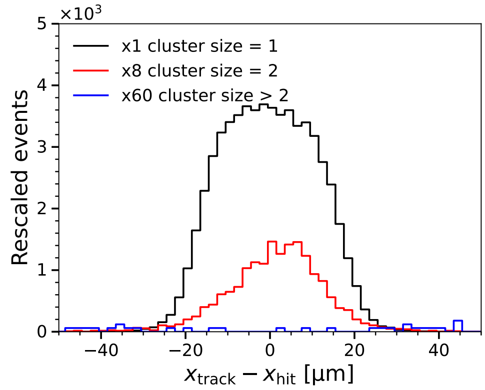

(c) *Uncorrected ToT*, X direction

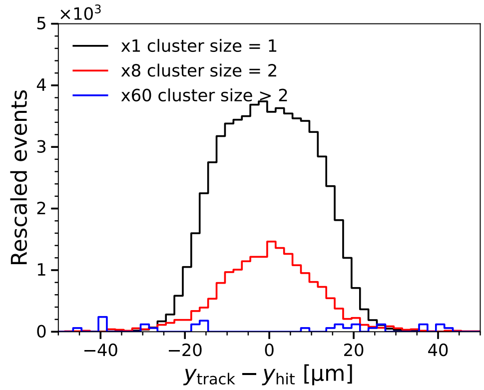

(d) *Uncorrected ToT*, Y direction

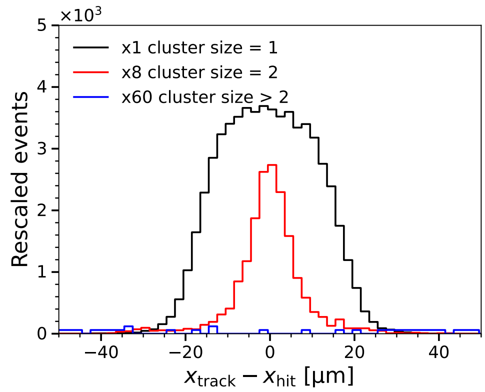

(e) *Corrected ToT*, X direction

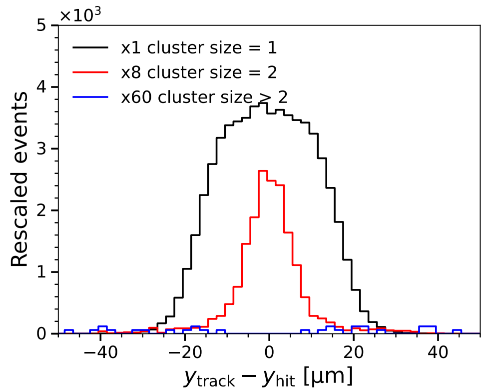

(f) *Corrected ToT*, Y direction

Figure 7.17: Spatial residuals in X and Y directions obtained in triggered and ToT acquisition modes. The result labeled *corrected ToT* is obtained by applying the ToT calibration and η-correction, while the *uncorrected* ToT lacks these corrections. The cluster sizes in the legend refer to the projected cluster size in the X (a,c,e) and Y (b,d,f) directions. The sensor is biased at −1.2 V and the threshold is approximately 300 electrons.

In all cases, single-pixel clusters result in a box-like distribution that dominates the residual distributions shown in Figure 7.16(a), with no difference observed between X and Y directions. For two-pixel projected clusters, the width of the residuals is observed to be smaller due to the improved position reconstruction provided by charge sharing.

In ToT mode, in the X direction, the uncorrected residuals for two-pixel clusters are biased to the right and broader than those in triggered mode. The displacement in the right direction is caused by the non-uniform charge collection, which leads to larger ToT values on the right part of the pixel (see Figure 7.1(c) and 7.4(c)). After applying the η-correction algorithm introduced in Section 6.5.3, the residuals become centered and more narrow. In the Y direction, the residuals are already centered even without corrections, as they are not significantly influenced by the non-uniform charge collection. The broadening of the residuals (reconstructed in ToT mode compared to triggered mode) has four main causes: ToT pixel-to-pixel variations measured for the same input signal, non-linear ToT gain in the charge sharing region, non-linear charge sharing in the sensor, and non-uniform collection. The calibration procedure compensates for the first two effects, while the η-correction addresses the latter two. After applying these corrections, the residuals are more narrow and comparable to those of the other acquisition modes.

The residuals shown in Figure 7.17 are obtained with a threshold of about 300 electrons. At higher thresholds (>400 electrons), the loss of efficiency in the right part of the pixel cell leads to asymmetric spatial residuals.

7.5.2 Threshold, Sensor Bias and Acquisition Mode Dependence

The spatial resolution is calculated by subtracting the pointing resolution of the beam telescope from the $\mathrm{RMS}_{97.7\%}$ of the residuals (see Equation 6.1). Figure 7.18 shows the spatial resolution in X and Y of H2M as a function of the threshold for four different sensor bias voltages obtained in triggered mode. At a threshold of 300 electrons, the *corrected ToT* data is also included. As discussed in Figure 7.17, the reconstructed position of events with a cluster size of two is refined with the ToT calibration and η-correction, and similar resolutions are obtained as in the binary readout because of the small fraction of cluster size two events. At a threshold of 224 electrons, the ToT data with the applied $\eta-$correction is also shown, and the spatial resolution is improved by 0.1 µm. For the reasons discussed in Section 5.5.5, the ToT calibration cannot be applied at this low threshold.

No significant differences are observed between sensor bias voltages. The increase in charge sharing below 240 electrons leads to an improvement of the spatial resolution. Between approximately 240 and 400 electrons, the spatial resolution changes hardly, it is about 9.7 µm, and is dominated by single-cluster events. Above 400 electrons, the asymmetric residuals in the X direction (due to the non-uniform efficiency) lead to a reduction of the $\mathrm{RMS}_{97.7\%}$, and of the spatial resolution in the X direction. A spatial resolution of (9.3 ± 0.1) µm is measured at a threshold of (178 ± 5) electrons. This value is slightly better than the one expected from a binary readout and a cluster size of one, pitch/$\sqrt{12}$ ≈10.1 µm.

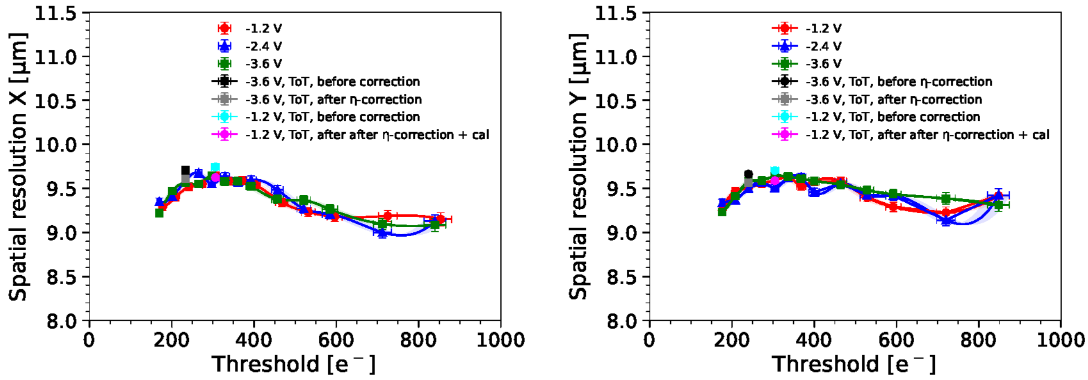

(a) (b)

Figure 7.18: Spatial resolution in X (a) and Y (b) as a function of the threshold for different sensor bias voltages in triggered (if not labeled explicitly) and ToT modes. The uncertainty is dominated by the threshold calibration factor, which is represented by a band.

7.5.3 Limitations on the Spatial Resolution

For data recorded in ToT mode, where charge information is stored, the ToT-weighted average method can ideally reconstruct the hit position with high resolution. However, the non-linearity of the ToT gain for charges below the MPV, the pixel-to-pixel variations, the non-linear field within the sensor, and the non-uniform charge collection lead to a deteriorated spatial resolution. After accounting for these effects (by applying the ToT calibration and η-correction), the achieved spatial resolution is slightly improved, but it remains close to that obtained with a binary readout. Since charge sharing only occurs in a small region across pixel boundaries, the arithmetic mean used in triggered mode with binary charge information is sufficient and yields a spatial resolution similar to that in ToT mode. The main limitation on the spatial resolution is the predominance of single-pixel clusters, arising from the large pitch, thin epitaxial layer, and n-gap sensor layout, which needs to be employed to reach sufficiently high efficiency.

The long shutter windows in ToT mode prevent the chip from being operated at low thresholds (below 200 electrons), so data in this region is only recorded in triggered mode, and the ToT-weighted average method is not used. Additionally, for thresholds below 300 electrons, the ToT calibration is not applied because of noise, which limits the spatial resolution improvements from charge sharing.

7.6 Temporal Resolution

In the case of lepton colliders, hit time tagging with a precision of a few nanoseconds is required to suppress the beam-induced background (see Chapter 1). The temporal resolution of a detector is therefore a crucial parameter to study for the mentioned application.

This section discusses the time resolution of H2M and its dependence on the threshold, sensor bias, feedback current, cluster size, and the deposition of charge in the pixel.

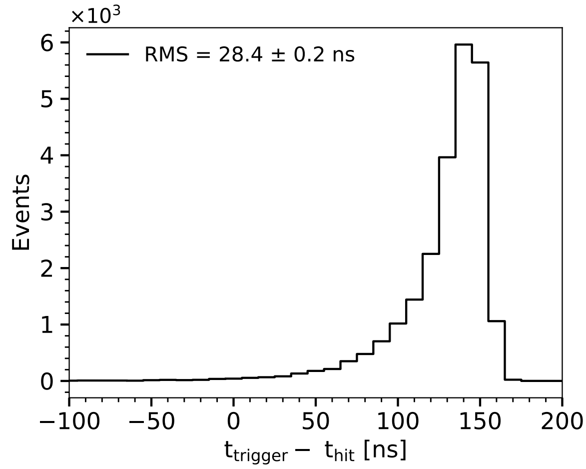

Figure 7.19: Time residual distribution. The sensor is biased at −3.6 V, the threshold is 224 electrons, and a low *ikrum* setting is used.

7.6.1 Time Residuals Distributions

The time walk, together with a non-uniform charge collection time visible in Figure 7.4(a), leads to non-Gaussian time residuals, characterized by a long tail to the left. Figure 7.19 shows an example of a time residual distribution for a threshold of 224 electrons and a sensor bias of −3.6 V. Since the time resolution of the trigger plane is negligible (better than 4 ns), the RMS of the distribution in the given range is taken as an estimate of the time resolution. For these settings, a time resolution of (28.4 ± 0.2) ns is achieved.

Furthermore, as the chip does not provide a simultaneous ToT and ToA measurement, time walk corrections cannot be applied. In order to quantify the contributions from sensor time walk and non-uniform charge collection, the in-pixel time resolution is studied in the following.

7.6.2 In-pixel Time Resolution

The RMS of the time residuals, $\sigma_{t_{\text{trigger}}-t_{\text{hit}}}$, is shown in Figure 7.20 as a function of the pixel position. The slower and non-uniform charge collection in the right part of the pixel cell leads to a larger spread of the residual values (i.e., a worse time resolution). At the location of the n-well opening of the analog front-end (see Figure 7.2), the time resolution is better compared to the top-right corner. As in the case of the time residuals, the pattern remains visible at the lowest achievable thresholds and at high sensor bias voltages.

In Appendix C.3, the in-pixel efficiency maps, ToA, and time resolution are compared for different chip settings at a sensor bias of −4.2 V. Even at this large bias voltage and the lowest measured thresholds, where the chip is operated in the noise regime, the ToA and time resolution patterns remain visible.

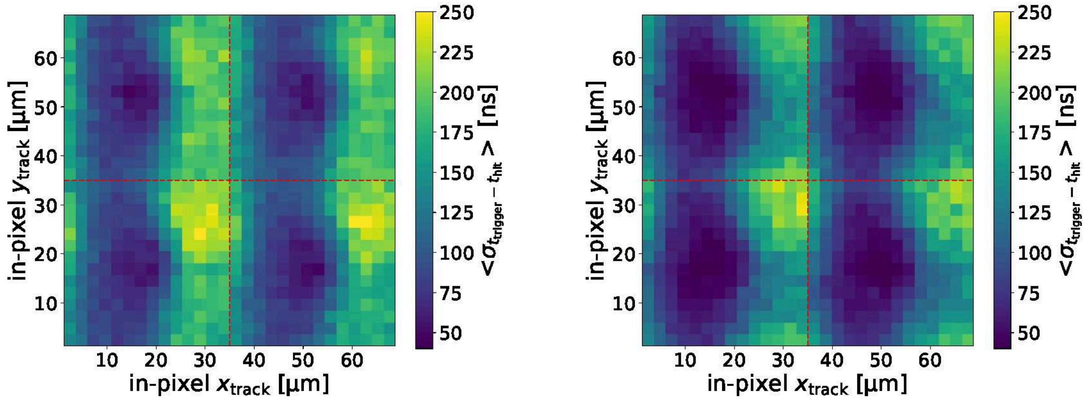

(a) *High ikrum*, −1.2 V, 330 e-

(b) *Low ikrum*, −3.6 V, 224 e-.

Figure 7.20: Time resolution maps projected onto four pixels for different feedback currents, sensor bias voltages, and thresholds. The pixel cell boundary is marked with a dashed red line.

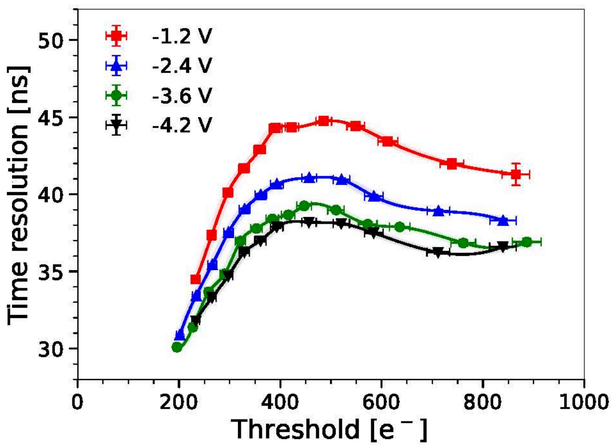

Figure 7.21: Time resolution as a function of the threshold for different sensor bias voltages. A low *ikrum* is used. The uncertainty is dominated by the threshold calibration factor, which is represented by a band.

7.6.3 Threshold and Sensor Bias Dependence

Figure 7.21 shows the time resolution of H2M as a function of the threshold for different sensor bias voltages. For higher sensor bias voltages, the electric field becomes stronger, which speeds up charge collection, mitigating the time walk effect. A stronger lateral electric field also helps overcome the local potential wells created by the n-well of the analog front-end, improving the time resolution significantly.

At lower thresholds, the time resolution also improves because the signal requires less time to cross the threshold, reducing the charge collection time. An additional contribution comes from

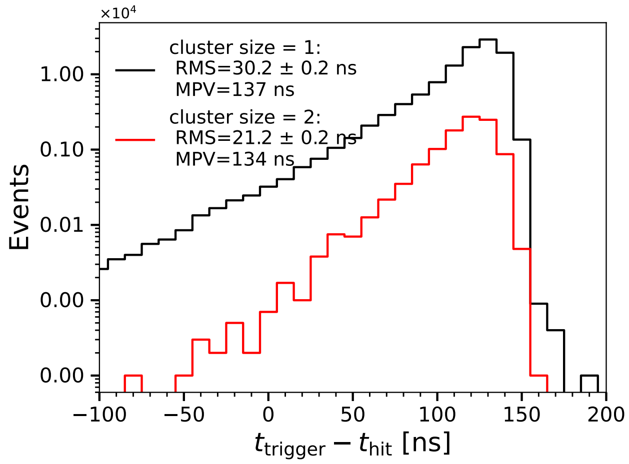

Figure 7.22: Cluster size of one and two contributions to the time residuals. The sensor is biased at −3.6 V and the threshold is approximately 224 electrons.

the higher probability of forming multi-pixel clusters at low thresholds, which will be discussed in Section 7.6.4, resulting in a better timing performance.

For thresholds above 400 electrons, the main loss of efficiency occurs for signals generated at the pixel edges, corners, or in regions where charge collection is slower and non-uniform. Since these events typically have poorer time resolution, excluding them leads to an overall improvement of the time resolution. This effect is more pronounced at lower sensor bias voltages, where the efficiency drops more quickly, and more of those events are excluded.

7.6.4 Contributions from Different Cluster Sizes

Figure 7.22 shows the time residuals distributions for cluster sizes of one and two. For two-pixel clusters where charge sharing happens far from the collection electrode, the slow induced signal is small and affected by time walk. Therefore, two-pixel clusters would be expected to exhibit a worse time resolution compared to single-pixel clusters. However, the data show that two-pixel clusters have a better time resolution than single-pixel clusters. The reason lies in the definition of t_{hit} as the timestamp of the earliest pixel in a cluster. For charges generated in the non-uniform charge collection region, single-pixel clusters induce a slow signal at the closest collection electrode. This slow signal contributes to the long tail in the time residuals. In two-pixel clusters, part of the charge may also be collected by the right neighbor, without crossing the local potential wells under the n-well of the analog front-end. Consequently, the t_{hit} is determined by this neighbor pixel, reducing the left tail of the time residuals observed for two-pixel clusters.

Since single-pixel clusters are typically created close to the collection electrode, they are, on average, faster (higher $t_{trigger}$ - t_{hit}) than two-pixel clusters. The latter are likely generated at the edges or corners of the pixels and need to travel larger distances through low-field regions. As a result, the MPV of the distribution of single-pixel clusters is shifted to the right with respect to that of two-pixel clusters.

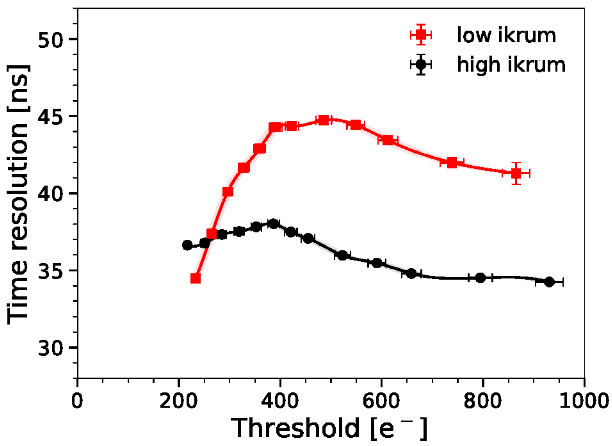

Figure 7.23: Time resolution for different feedback currents. The sensor is biased at −1.2 V.

7.6.5 Feedback Current Dependence

Smaller feedback currents allow the slow collection of charge carriers generated in the non-uniform charge collection region, which helps efficiency but degrades the timing performance. This is shown in Figure 7.23, where the time resolution is compared for the *low ikrum* and the *high ikrum* settings. Overall, the time resolution is better for the *high ikrum* setting. This effect is intensified at higher thresholds, where the slower signals require more time to cross the threshold, thereby increasing the time walk effect.

7.6.6 Limitations on the Time Resolution

The main limitation of the H2M chip in terms of time resolution is the non-uniform charge collection, which results in a long tail in the non-Gaussian time residuals. By suppressing the majority of these events (through studying two-pixel clusters and defining the H2M timestamp as the earliest pixel in the cluster), the time resolution improves. Time corrections similar to the one applied in [104] could be used; however, the expected improvement is minimal, as differences in the MPV between single-pixel clusters and two-pixel clusters in 3 ns for the best settings (Figure 7.22).

7.7 Impact of Chip Backside Thinning

Reducing the material budget improves tracking, since thicker material increases multiple Coulomb scattering and deteriorates track reconstruction, as introduced in Section 2.2.1. Therefore, thin sensors that can maintain a good tracking performance are preferred.

H2M samples have been thinned at the single-die level by backside grinding (i.e., reducing the substrate thickness) to study the limitations on the sensor thickness. This section investigates the impact of backside thinning on MIP detection performance in samples as thin as 21 µm.

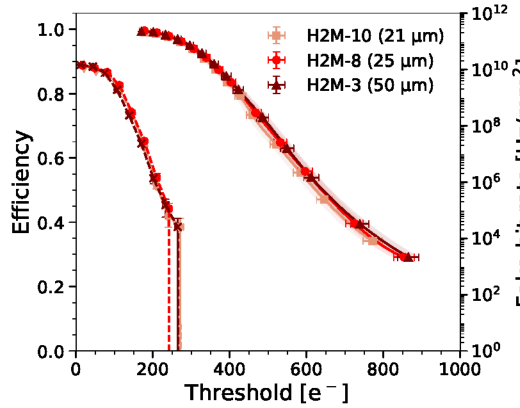

(a) Efficiency

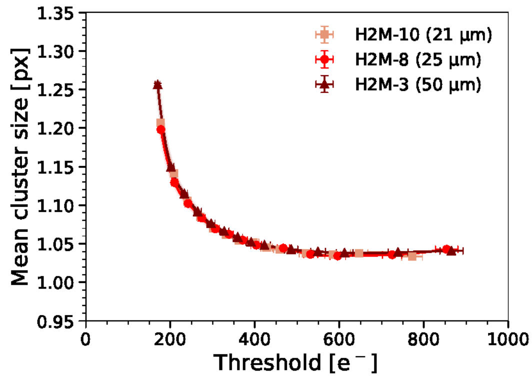

(b) Cluster size

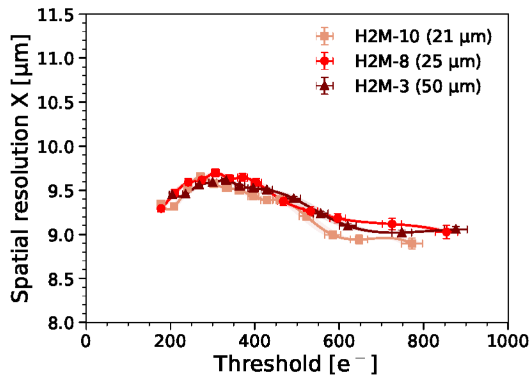

(c) Spatial resolution

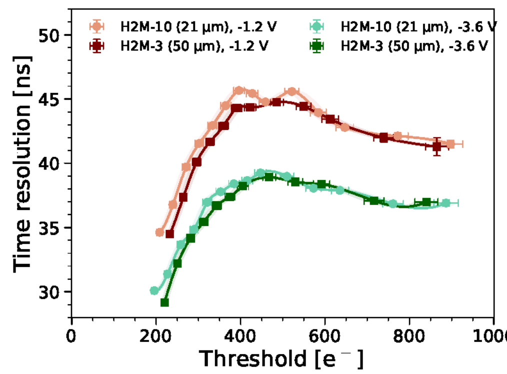

(d) Time resolution

Figure 7.24: Efficiency and fake-hit rate (a), cluster size (b), spatial (c) and time (d) resolution as a function of the threshold for samples with different total chip thicknesses. In (a), (b), and (c), the data is recorded in triggered mode and the sensor is biased at −1.2 V. In (d), the data is measured in triggered mode. The *low ikrum* setting is used for all plots. The uncertainty is dominated by the threshold calibration factor, which is represented by a band.

The quoted 21 μm include about 5 μm metal interconnection layers, the epitaxial layer and a few micrometers of low resistivity substrate for bias voltage distribution acrros the pixel matrix. Laboratory measurement results obtained with these samples have been presented in Chapter 5.

7.7.1 Efficiency, Cluster Size, Spatial and Time Resolution

Figure 7.24(a) shows the efficiency as a function of the thresholds for three chips thinned to different total thicknesses. No deterioration in efficiency or fake hit rate is observed between samples for thresholds below 450 electrons. In particular, all samples achieve an efficiency above 99% at a threshold of approximately 200 electrons. At this point, the measured fake-hit rate is around 4×10^5 Hz/mm^2, corresponding to a matrix occupancy of fewer than one pixel

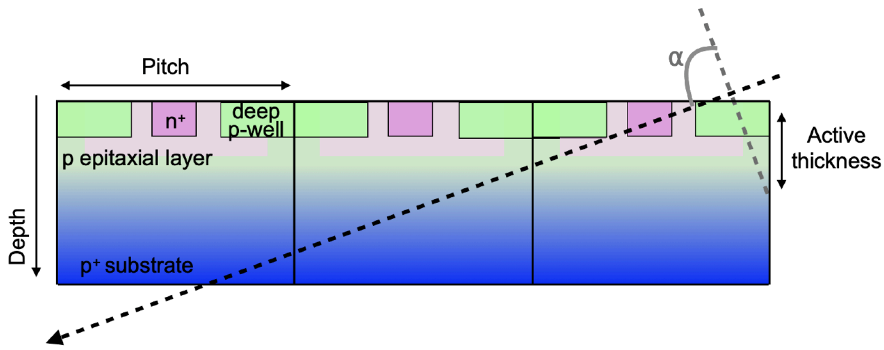

Figure 7.25: Illustration of the measurement principle used to determine the active thickness of the sensor. An ionising particle traverses three pixels at an incident angle α.

hit per 500 ns frame. These noise results are consistent with those observed in the laboratory measurements presented in Figure 5.5, where the same noise levels have been measured and reported to be similar for all samples.

Figure 7.24(b) shows the mean cluster size as a function of the threshold. No significant differences are observed between samples, indicating that although the substrate has been thinned, the charge collection from this highly doped region was minimal and did no increase the mean cluster size.

The spatial resolution in X as a function of the threshold is displayed in Figure 7.24(c). As expected from the cluster size, the measured spatial resolution is similar for all the samples. Slight differences could be attributed to setup variations during the different test beam campaigns, which lead to different track resolution (see Section 6.5.4).

Figure 7.24(d) shows the time resolution as a function of the threshold for the nominal and the thinnest tested samples, measured at two different sensor bias voltages. Similar time resolutions are observed between samples.

7.7.2 Active Thickness Studies

The active thickness of the H2M sensor is approximately 10 µm [13]. However, its exact value is not known, as it strongly depends on the substrate resistivity used by the foundry (see Equation 2.5) and the dopant diffusion during the epitaxial growth. Determining this value is of interest to optimise the front-end design, make the generic simulations presented in Chapter 4 more realistic, and define a lower limit on the substrate thickness in order to reduce the material budget while maintaining a high MIP detection performance.

One way to determine the active thickness in the test beam is to rotate the sensor so that the impinging particle traverses several pixel cells, as illustrated in Figure 7.25. In this way, charge carriers generated at different depths contribute differently to the signal, and the following geometrical relation applies:

$$\text{Projected cluster size (tilt direction)} = \frac{d \cdot \tan(\alpha)}{\text{Pitch}} + c_{\text{ort}} \qquad (7.1)$$

where the projected cluster size along the tilt direction is related to the active thickness (d), the pixel pitch, the incident angle (α), and the projected cluster size at perpendicular incidence (c_{ort}). While this approach has been proven to work on sensors manufactured by the same foundry with an active thickness of about 30 µm [85, 150, 151], it is not suitable for thinner active thicknesses for the reasons discussed below.

Due to the small active thickness and the large pixel pitch of H2M, achieving a cluster size larger than three requires rotating the sensor to incident angles (α) above 80° [152]. At such grazing angles, the projected pointing resolution of the beam telescope at the H2M plane makes it impossible to use the reconstructed tracks reliably. In addition, small displacements of the DUT caused by temperature variations in the area (see Appendix C.2) would require constant alignment of the DUT, which becomes challenging as the impinging particle is scattered along the column direction within about 2 mm silicon. Moreover, at larger incident angles, the cluster size increases drastically due to the tangent dependence in Equation 7.1, causing systematic uncertainties to dominate the extracted active thickness. Therefore, a method relying only on the charge collection profile of H2M has been developed in the master's thesis [152], supervised in this work, and is based on [73]. The approach and main results are summarised below.

With the sensor oriented at approximately 89°, data are recorded in ToT mode and calibrated. Such large incident angles are achievable thanks to the placement of H2M at the edge of the chipboard. The events are classified according to their projected cluster size. For example, for a fixed projected cluster size of 28 pixels, 28 signal distributions are built, each containing the measured ToT value of the n-th pixel. A Gaussian-Landau function is fitted to each distribution, and the MPV is extracted. Next, the MPV value is plotted as a function of the pixel position, which is converted into depth by using the trigonometric relation

$$\text{depth}[\mu\text{m}] = \cot(\alpha) \cdot \text{Position [pixel number]} \cdot \text{Pitch } [\mu\text{m}]. \tag{7.2}$$

Due to the Gaussian spread of the beam and the fact that the beam telescope is not used for track reconstruction, the rotation angle varies for each event and needs to be inferred from charge collection properties. For that, the following equation is used

$$\cos(\alpha) = \frac{Q_{ort}}{Q_{total}} \tag{7.3}$$

with Q_{total} denoting the total charge collected (sum of the in-pixel ToT values in a cluster), and Q_{ort} corresponding to the total charge collected at perpendicular incidence ($\alpha = 0^{\circ}$). The latter has been measured in Section 7.4.

Following this approach, Figure 7.26 shows the collected charge as a function of the depth, where a depth equal to 0 µm corresponds to the sensor surface. Three regions can be identified. The first region extends up to a depth of approximately 1.3 µm, where charge collection is incomplete due to the presence of the deep p-wells that host the in-pixel electronics. The second region exhibits a plateau in the collected charge, corresponding to the depleted epitaxial layer. Finally, in the third region, the charge collection becomes incomplete again, corresponding to the transition region between the fully depleted epitaxial layer and the highly doped substrate. This transition region is created by diffusion of the doping during the epitaxial layer grown on the

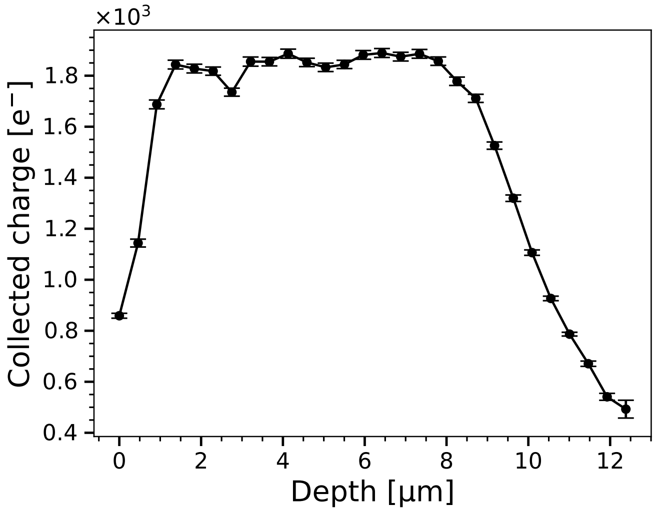

Figure 7.26: Collected charge as a function of the depth. Data obtained with H2M-8 (25 µm), at a sensor bias of −1.2 V, a threshold of 300 electrons, and with the *low ikrum* setting. The sensor is rotated by 89° and the projected cluster size is 28 pixels. Adapted from [152].

high-resistivity substrate. Beyond 12.5 µm, no charge is collected. Here, all generated charge carriers are quickly recombined before contributing to the signal. Therefore, the active region extends for about 12.5 µm, of which approximately 5.8 µm are fully depleted.

More details about the method, such as the classification of particles crossing the sensor from frontside to backside and vice versa, rejection of events with charge collected by the outer columns, and the rejection of delta rays, are described in [152].

Figure 7.26 is obtained from measurements with the H2M-8 sample, at a sensor bias voltage of −1.2 V, and taking into account a projected cluster size of 28 pixels. The plot also shows that the larger the projected cluster size (i.e., the number of entries in the figure), the better the sampling of the depth. Systematic studies have been carried out for different sensor bias voltages (from −0.8 V to −3.6 V), projected cluster sizes (28 to 30 pixels), thresholds, rotational angles (89° to 91°), and samples (H2M-10 and H2M-8) in [152]. Consistent active thicknesses and fully depleted depths have been obtained across all settings.

Additionally, via an exponential fit in the transition region between the epitaxial layer and the highly-doped substrate, the diffusion length and carrier lifetime (see Chapter 2) can be determined. Those values have been obtained in [152], and correspond to approximately 3 µm and 2.5 ns, respectively.

7.7.3 Limitations of Backside Thinning

The laboratory measurements presented in Chapter 5, together with the above-described test beam measurements, have shown no performance losses of the samples down to a total chip thickness of 21 µm. Grazing angle measurements indicate an active thickness of about 12.5 µm, suggesting that further thinning of the substrate may be possible without degrading the performance of the sensor. However, since a finite substrate thickness is needed to establish a low-resistivity sheet to homogeneously bias the sensor, reducing the substrate thickness could result in non-uniform biasing across the pixel matrix. This, together with the challenges of the thinning process, is currently under investigation.

CHAPTER 8

Comparison between Data and Simulations

This chapter presents a comparison between the Monte Carlo simulations introduced in Chapter 4 and the test beam results presented in Chapter 7.

8.1 Efficiency

Figure 8.1 compares the efficiency obtained from test beam measurements and simulations as a function of the threshold. Since no significant dependence on the sensor bias is observed in simulations and data, only the -1.2 V case is shown. Below a threshold of 200 electrons, both simulations and data yield efficiencies above 99%. However, beyond approximately 200 electrons, the measured efficiency begins to decrease, while the simulations continue to predict efficiencies above 99% up to a threshold of 250 electrons. At this threshold of 250 electrons, the measured efficiency is $(97.5 \pm 0.3)\%$, resulting in a relative discrepancy of about 1.5% with respect to the simulations. These results are summarised in Table 8.1.

The slower decrease in efficiency observed in simulations, but not in the data, follows the trend observed in the APTS measurements for larger pixel sizes [149]. The earlier drop in efficiency in data is caused by the distortions in the electric field caused by the n-well of the analog front-end, as explained in Section 7.1. This can be seen in Figure 8.2, where the data in-pixel efficiency maps are subtracted from the simulation in-pixel efficiency maps, at a threshold of 224 and 300 electrons. In the simulations, the loss of efficiency is confined to the pixel edges and corners, whereas in the measurements, it is extended further into the region of the wide n-well of the analog front-end.

Table 8.1: Comparison of efficiency between data and simulations. The sensor is biased at -1.2 V. The first row indicates the highest threshold at which the efficiency remains above 99% ($T_{99\%}$). The second and third rows list the efficiencies obtained at thresholds of 205 electrons and 250 electrons, respectively.

	Simulations	Data
$T_{99\%}$	250 e^-	(205 ± 6) e^-
ϵ_{205e^-}	$(99.64 \pm 0.01)\%$	$(99.0 \pm 0.2)\%$
ϵ_{250e^-}	$(99.00 \pm 0.02)\%$	$(97.5 \pm 0.3)\%$

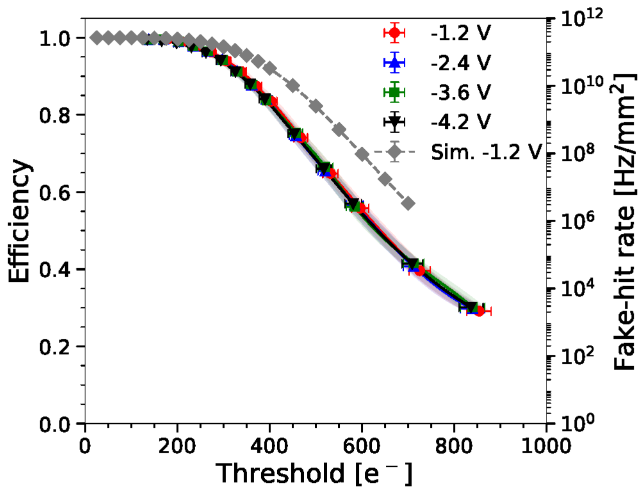

Figure 8.1: Comparison of efficiency between data and simulations as a function of the threshold. The measurement curves are presented in Figure 7.6, and the simulation curve in Figure 4.4.

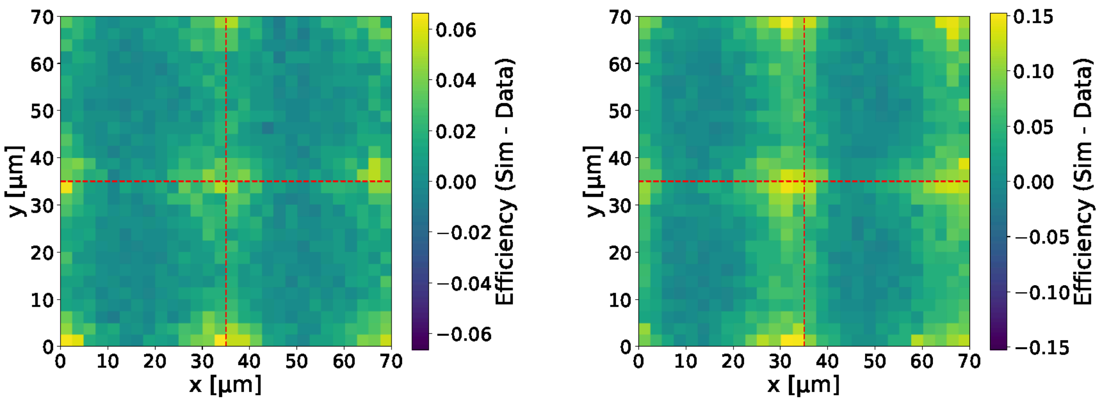

(a) 224 electrons

(b) 300 electrons

Figure 8.2: In-pixel efficiency difference maps between simulation and data. A threshold of 224 electrons (a) and 300 electrons (b) is compared. The pixel cell boundary is marked with a dashed red line. The sensor is biased at -1.2 V.

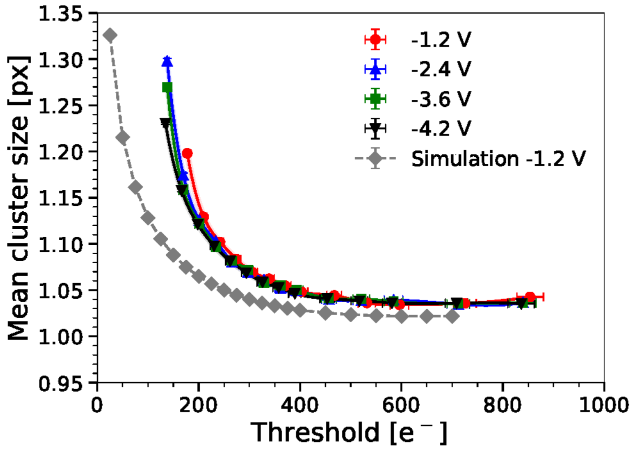

Figure 8.3: Comparison of cluster size between data and simulations. The data are recorded in triggered mode. The measurement curves are presented in Figure 7.10, and the simulation curve in Figure 4.6(a).

8.2 Cluster Size

Figure 8.3 shows the mean cluster size as a function of the threshold for data and simulations, with the measured mean cluster size being larger than predicted by the simulations. In adition, Figure 8.4 shows the cluster size distributions for data and simulations for two different thresholds. At a threshold of 224 electrons, the mean cluster size in simulation is (1.056 ± 0.003), whereas in data is (1.11 ± 0.01). At this threshold, a fraction of $(16.5 \pm 0.1)\%$ of two-cluster events is measured, while simulations predict only $(2.85 \pm 0.02)\%$. Differences are also observed at a cluster size of three, where the $(3.30 \pm 0.02)\%$ of the events are found in the data, compared to nearly zero in the simulations. At a threshold of 300 electrons the situation is similar: simulations still underestimate the observed cluster size in data, but the effect of the higher threshold is more pronounced, reducing charge sharing and bringing data and simulations closer together.

The underestimation of the mean cluster size has been attributed to a simplified model of the deep n-type implant in the TCAD simulations. In the performed simulations, no lateral doping diffusion is included between the deep n-type implant and the gap region. This results in a smaller diffusion region for charge carriers, leading to smaller cluster sizes. Later simulations carried out within the project include this lateral diffusion.

8.3 Spatial Resolution

As a consequence of a smaller cluster size, the spatial resolution, shown in Figure 8.5, is worse in simulations and approaches the binary resolution. Although simulations use a charge-weighted center-of-gravity method to reconstruct the hit position (compared to the arithmetic mean used in the binary readout for data in triggered mode), the single-pixel cluster events dominate, and the reconstructed positions in simulations are still mainly located at the pixel centers.

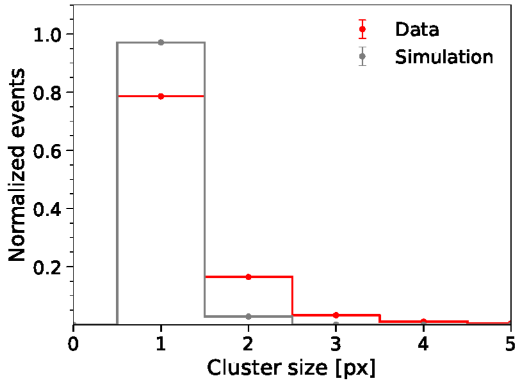

(a) 224 e$^-$

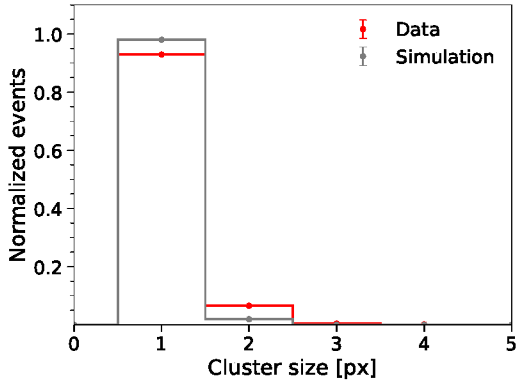

(b) 300 e$^-$

Figure 8.4: Comparison of cluster size distributions between data and simulations for a threshold of 224 electrons (a) and 300 electrons (b). The sensor is biased at −1.2 V.

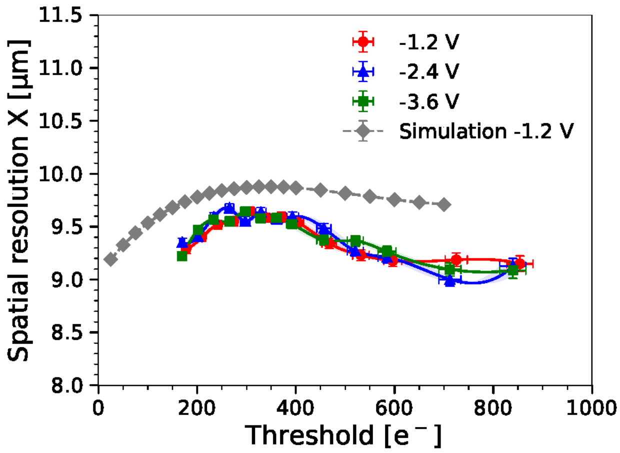

Figure 8.5: Comparison of spatial resolution between data and simulations. The data are recorded in triggered mode. The measurement curves are presented in Figure 7.18(a), and the simulation curve in Figure 4.6(b).

Additionally, because the drop in efficiency at high thresholds is less pronounced and the simulated residuals do not become asymmetric due to the non-uniform in-pixel efficiency, an artificially larger improvement in spatial resolution is observed in the data compared to simulations.

8.4 Signal Distribution

Figure 8.6 shows the single-pixel charge distributions for data and simulations. Both distributions follow a Landau-Gaussian shape, and their respective MPVs are indicated. These MPVs differ by

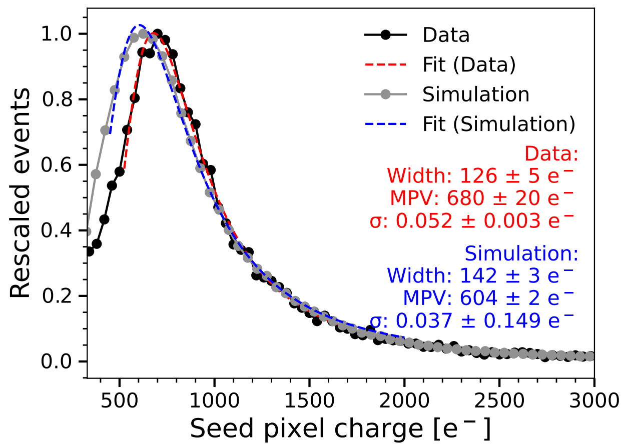

Figure 8.6: Comparison of seed-pixel charge distributions between data and simulations. The threshold is 300 electrons, and the sensor bias −1.2 V. A low *ikrum* is used in measurements. The measurement distribution is presented in Figure 7.14(b), and the simulation distribution in Figure 4.8.

about 12%, with the measured MPV being higher than the simulated one.

The discrepancy could be explained by the ToT calibration procedure, in which test pulses are injected and their ToT values measured. This procedure assumes a homogeneous in-pixel response, mapping each ToT value in clock cycles to a corresponding value in electrons. However, the non-uniform in-pixel response of the sensor leads to a large fraction of the pixel cell recording higher ToT values (see Figure 7.4(c)), and as a result, the MPV value of the seed-pixel charge distribution in measurements is shifted towards higher values. In addition, this effect is more pronounced here due to the use of a low *ikrum* setting during data recording.

8.5 A More Realistic Simulation

Due to the limitations mentioned in Section 4.1.4, the simulation method employed here is not sufficient to reproduce and fully explain the measurement results. Proprietary information is required to include the n-well of the analog front-end within the deep p-well in the simulations, as the magnitude of the effect is very sensitive to the actual doping concentrations. In addition, the response of the CSA needs to be modeled in order to describe the ballistic deficit effects.

Such an approach has been performed by a colleague, and it is presented in [103, 126]. The sensor is first simulated in TCAD using the actual doping profiles. The resulting electric fields and weighting potentials are then imported into the Allpix^2 framework with a configuration based on the parameters given in Section 4.1.2. After charge collection from the implant defined in Allpix^2, the electronic response is simulated using the electronic circuit simulator Spectre [153].

Figure 8.7 shows the simulated in-pixel efficiency map projected onto one pixel and its average projected on the X and Y axes. An agreement within approximately 3% is obtained with the test beam result presented in Figure 7.1(b). The non-uniform charge collection is also well predicted

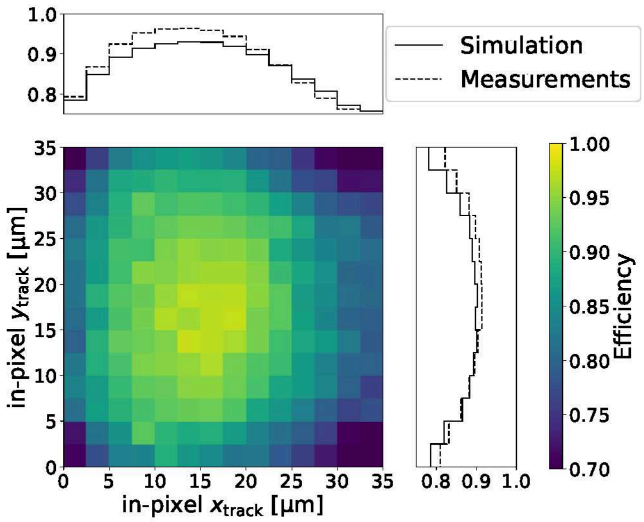

Figure 8.7: Simulated in-pixel efficiency map of the H2M for one pixel and its average projected on each axis. The sensor is biased at -1.2 V, and the *high ikrum* setting is used. The threshold is approximately 330 electrons. The projected average is compared to measured data from Figure 7.1(b). Taken from [103].

by the simulation. Therefore, this complex approach not only provides a clear understanding of the non-uniform in-pixel charge collection, but also achieves good agreement with test beam results.

Additionally, this simulation method can be used to explore mitigation strategies for future chip submissions with similar features to those of H2M (i.e., a large pixel pitch and a fast front-end response) manufactured using the same process. An example is presented in [103] and it is briefly explained below.

Keeping the same area of the n-wells, the large n-well of the analog front-end is re-positioned closer to the n-well collection electrode, in a region with a higher electric field. With this proposed configuration sketched in Figure 8.8, the simulated efficiency increases from 86% to 95% and the maximum rise time is reduced by a factor of three.

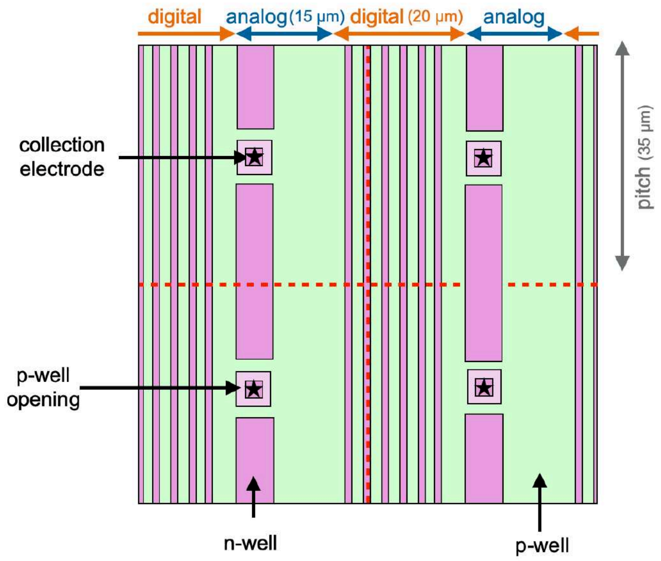

Figure 8.8: Simplified proposed layout of the n-well and p-well positions within the deep p-well in four pixels. The position of the collection electrode, analog front-end, and digital logic is also indicated. The pixel boundary is marked with a red dashed line. Modified from [103].

Conclusion and Outlook

The H2M test chip has been simulated and characterised through laboratory and test beam measurements after optimisation of its front-end parameters. The chip has been proven to be fully functional, with both the analog and digital circuitry working as foreseen. These results demonstrate successful porting of readout concepts from a hybrid readout ASIC and usage of the digital-on-top workflow in a 65 nm CMOS imaging technology.

IV measurements of the sensor have shown that it can be reverse biased up to 4.2 V by applying the same potential to the p-well and the p-substrate. After threshold equalisation, a threshold dispersion of the order of 40 electrons has been measured. The single-pixel noise has found to be approximately 25 electrons. Both the threshold dispersion and single-pixel noise are observed to strongly depend on the sensor bias voltage, and limit the minimum achievable operation threshold.

Threshold calibration has been performed using radioactive sources, and the obtained gain is consistent with the expectations from analog front-end simulations. The combination of test pulse and source measurements enabled a per-pixel ToT calibration. This calibration has been applied to the ToT spectrum recorded under exposure to an ^{55}Fe source, and its characteristic peak was measured with a 5% accuracy.

Test beam measurements revealed a MIP detection efficiency above 99% reached at thresholds below 205 electrons. The relatively large pitch of 35 µm, the largest used in this process so far, shows that the n-gap sensor modification achieves high detection efficiency even for large pixel pitches. These results support the use of this technology in tracking detectors where large areas need to be covered.

However, one consequence of the large pixel pitch is the reduction of the electric field between the collection electrode and the pixel edge. In this region, local potential wells caused by the H2M layout of n-wells within the deep p-well slow down the charge collection, leading to an asymmetric temporal in-pixel response. Furthermore, the fast response of the CSA reduces the pulse amplitude, resulting in a non-uniform in-pixel efficiency due to ballistic deficit. As a consequence, the efficiency drops abruptly as a function of the threshold. Operational parameters of the chip have been tuned in order to mitigate this effect. The results have been reproduced and fully understood with the help of simulations.

The spatial resolution and cluster size at a threshold of 178 electrons are (9.3 ± 0.1) µm and (1.19 ± 0.01), respectively, constrained by the large pitch and sensor n-gap layout, which reduces the charge sharing and prevents full exploitation of the 8-bit ToT resolution. The measured time resolution is (28.4 ± 0.2) ns at a threshold of 224 electrons, limited by the non-uniform in-pixel response. Currently, samples are being irradiated at different TIDs and fluences in order to study how the key performance parameters evolve after irradiation.

Single-die chips have been thinned by backside grinding down to a total chip thickness of 21 µm without affecting their performance. These represent the thinnest samples tested in this process and demonstrate the capabilities of the sensor in low material budget applications. Grazing angle measurements indicate that the active thickness of the sensor is approximately 12.5 µm, of which about 5.8 µm are fully depleted. Further backside thinning is currently being investigated to explore the ultimate limits of chip thickness while maintaining their performance.

Finally, all the results presented in this work, as well as the techniques developed, directly contribute to projects such as Octopus, which aims to develop the technology required for a vertex detector at a lepton collider.

Part II

Contributions to the End-of-Substructure Project

CHAPTER 9

The ATLAS Inner Tracker Detector

The High-Luminosity Large Hadron Collider (HL-LHC) [5] is an upgrade of the LHC [4] that aims to increase the integrated luminosity by a factor of ten with respect to the design value. This increase in luminosity will enhance the precision of already existing SM measurements, and potentially make low-probability phenomena accessible that address some of the SM shortcomings presented in Section 1.2.

The HL-LHC is expected to collide protons at a center-of-mass energy of 14 TeV, and reach a peak instantaneous luminosity of $7.5 \times 10^{34}\,\mathrm{cm}^{-2}\,\mathrm{s}^{-1}$ [5]. This luminosity value corresponds to approximately 200 simultaneous collisions per bunch crossing, which results in more than three times the present pile-up levels.

To maintain the vertexing and tracking performance under the HL-LHC conditions, the tracking systems of all four LHC experiments will be replaced. In the case of the ATLAS detector, the current Inner Detector (ID) [154] will be replaced by an all-silicon tracking detector, known as the Inner Tracker (ITk). Compared with the ID, the ITk detector will offer higher radiation tolerance, increased granularity with smaller pixel sizes, faster response, novel power distribution architectures, a reduced material budget, higher trigger rate, and larger sensitive surface with extended coverage in η. Table 9.1 quantifies some of these improvements.

Table 9.1: Comparison between the ATLAS ID and ATLAS ITk detectors. Data from [15, 56, 154].

	Inner Detector (ID)	Inner Tracker (ITk)
Technology	Gas + silicon	All-silicon
Peak integrated luminosity	$1 \times 10^{34}\,\mathrm{cm}^{-2}\,\mathrm{s}^{-1}$	$7.5 \times 10^{34}\,\mathrm{cm}^{-2}\,\mathrm{s}^{-1}$
η range covered	2.5	4
Average number of pileup collisions	57	200
Trigger rate	100 kHz	1 MHz
Sensitive surface	$63\,\mathrm{m}^2$	$178\,\mathrm{m}^2$
Number of modules	4 000	28 000
Number of channels	100×10^6	$5\,000 \times 10^6$

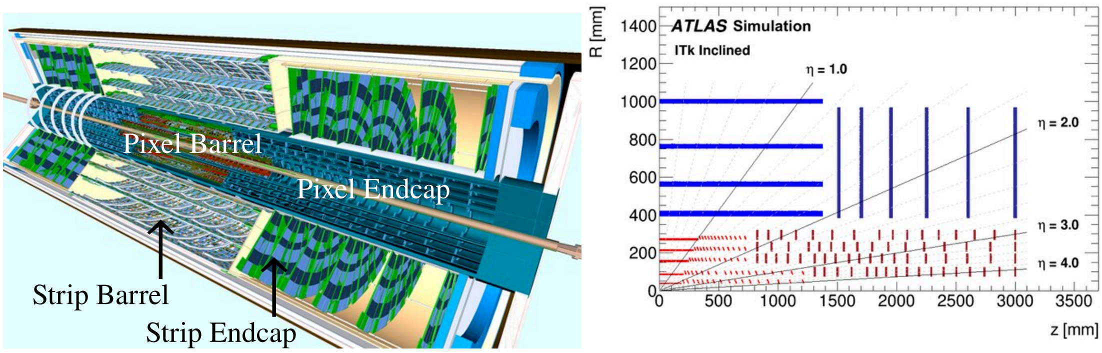

(a) (b)

Figure 9.1: (a) 3D view of the ATLAS ITk detector. Taken from [15]. (b) Schematic layout of one quadrant of the ATLAS ITk detector in the r-z plane. The pixel layers are shown in red, and the strip layers in blue. Adapted from [15].

The ITk detector layout is shown in Figure 9.1. It consists of a pixel detector [56] close to the interaction point, surrounded by a strip detector [15]. The pixel detector enables the reconstruction of primary and secondary vertices, while the strip detector provides tracking and momentum measurements for charged particles.

With the ITk detector currently under construction, part of this thesis has focused on the testing of the End-of-Substructure cards, which serve as the interface between the on- and off-detector systems. Because the pixel and strip detectors use different readout architectures, these cards are only required in the strip detector. Thus, the next section introduces the strip system, while a detailed description of the pixel detector can be found elsewhere [56]. At the end of the chapter, the End-of-Substructure cards are presented, focusing on their specifications, in order to provide the context of the measurements and results presented in Chapter 10.

9.1 ATLAS Inner Tracker Strip Detector

The ATLAS ITk strip detector [15] consists of a central barrel and two endcaps (see Figure 9.1), covering a range up to $|\eta| < 2.7$ and with a total silicon area of $165\,\mathrm{m}^2$. The silicon sensors are designed as n-in-p devices with a physical thickness of approximately $\sim 320\,\mu\mathrm{m}$ [155].

The barrel region comprises of 392 rectangular *staves* arranged in four concentric layers, while the two endcaps consist of 384 trapezoidal *petals* distributed over twelve disks (six per forward region). There is one unique petal design (flavor) for the entire tracker, with each endcap disk being populated with 32 petals. In contrast, there are four different stave flavors, and the number of staves per barrel layer increases with the distance from the beam pipe (58 and 80 staves in the two inner barrel layers, and 112 and 140 in the two outer layers).

Staves and petals are collectively referred to as *substructures*. In total, the ITk comprises 776 substructures. Each substructure is made of a lightweight carbon fiber support structure to which the modules (silicon strip sensors, readout boards, and power boards) are glued on each side. At the end of each substructure, a pair of *End-of-Substructure (EoS)* cards are placed. An

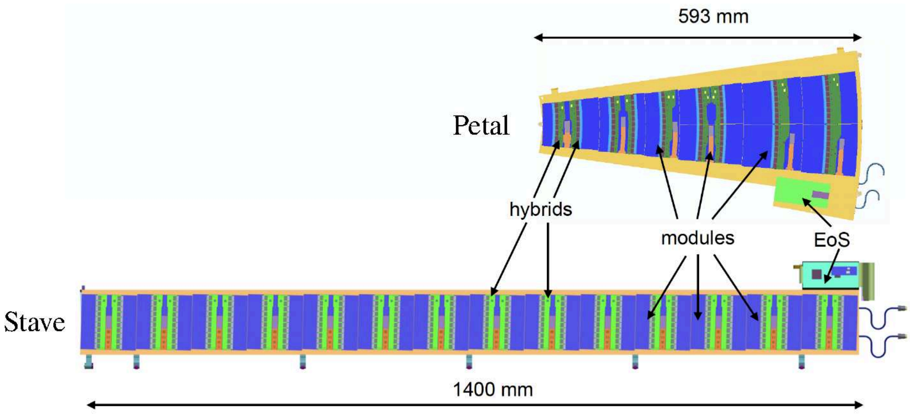

Figure 9.2: Illustration of the EoS cards located at the end of the carbon-fiber structure in a petal (top) and stave (bottom). Taken from [15].

illustration of the staves and petals, including their EoS cards, is shown in Figure 9.2. Overall, the ITk contains 1 552 EoS cards, which are described in Section 9.2.

The two inner barrel layers contain short-strip sensors, and the two outer barrel layers have long-strip sensors. The strip pitch is 75.5 µm in all cases, while the strip length is 23.9 mm for the short-strip and 47.75 mm for the long-strip sensors [155]. This design results in twice as many readout channels per stave in the inner barrel compared to the outer barrel. Six different sensor shapes are available to cover a whole petal, with strip lengths ranging from 15.1 mm to 60.2 mm.

The readout and power electronics are glued and wire-bonded to each readout channel on top of the silicon sensors. The readout electronics are hosted in the so-called *hybrid* PCBs. The signal created in the silicon sensor is sent to the ATLAS Binary Chip (ABC) [156]. Each ABC has 256 channels, and converts the analog signal into a binary readout through amplification, shaping, and discrimination. This binary information is then sent to the Hybrid Controller Chip (HCC) [157], which builds the data packets and transmits them to the EoS card at a data rate of 640 Mb/s. In the barrel region, long-strip sensors are connected to one hybrid, while short-strip sensors are connected to two hybrids, as they have twice the number of channels. In the endcap region, each sensor is connected to one hybrid. Power boards handle low-voltage power distribution for the front-end electronics, high-voltage sensor biasing, and monitoring and control functionalities. Receiving 11 V from the off-detector power system via the EoS cards, they output 1.5 V via a DC-DC converter. Monitoring (e.g., temperature or voltage) and control (e.g., interrupts) functionalities are performed by the Autonomous Monitor And Control (AMAC) chip [158]. Each module contains one power board.

Thus, a module in the inner barrel consists of a short-strip sensor, two hybrids and a power board. A long-strip sensor, a hybrid, and a power board constitute a module in the outer barrel region. In the endcaps, a module consists of one or two silicon sensors, each with a hybrid, and a single power board. The number of sensors per module depends on the radial position, as visible in Figure 9.2. The modules are connected to the EoS via a kapton-copper *bus tape*, which is a stack-up circuit routed along the surface of the carbon fiber core, carrying all electrical signals.

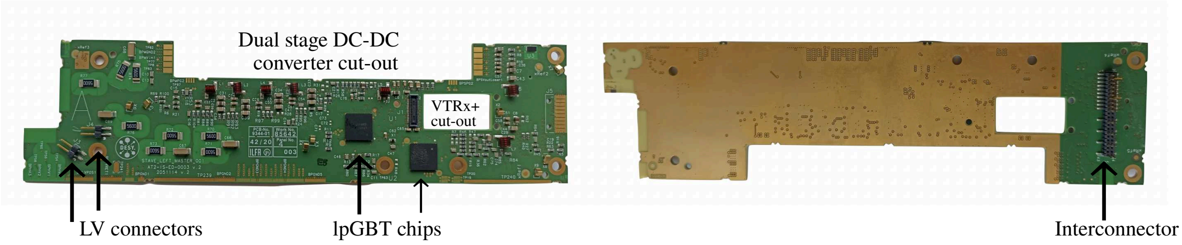

Figure 9.3: Photo of the frontside (left) and backside (right) of an EoS card. It is an inner barrel EoS main card prototype with two lpGBT chips and a cut-out for the Dual-Stage DC-DC converter and VTRx+. The interconnector to the secondary card is visible on the backside of the EoS photo.

9.2 The End-of-Substructure Cards

The EoS cards are PCBs that are placed on the "ears" of the staves and petals. Each substructure has a pair of EoS cards, one on each side. The card on the front of the substructure is referred to as the *main EoS card*, and the one on the back is the *secondary EoS card*. The cards are electrically interconnected by dedicated connectors that mate the main and secondary cards outside the carbon structure. A photo of a main inner barrel EoS card is shown in Figure 9.3. The backside of the EoS card, with the interconnector, is also depicted in the picture.

The EoS cards act as the interface between the on-detector and off-detector systems. They enable the transmission of data, low-voltage (LV) and high-voltage (HV) power, and trigger control signals between the modules and the off-detector systems.

Figure 9.4 illustrates the block diagram of the EoS card. The EoS card receives the data from the strip modules via up to 28 differential lines: 14 in the outer barrel and endcaps, and 28 in the inner barrel. Each 640 Mb/s data line is connected to one (in the outer barrel and endcaps) or two (in the inner barrel) low-power Gigabit Transceiver (lpGBT) [159] hosted on the boards. Each lpGBT multiplexes the 640 Mb/s signals into a single 10 Gb/s signal, which is sent to the Versatile Link Transceiver (VTRx+) [160]. The VTRx+ converts the 10 Gb/s electrical signals from the lpGBTs into optical signals (TX) and transmits them via one (in the outer barrel and endcaps) or two (in the inner barrel) optical fibers out of the detector. Conversely, the VTRx+ module also converts the input of the receiver fiber signal (RX) at 2.5 Gb/s into electrical signals. In this way, for example, the first lpGBT recovers the LHC-clock signal and generates clock and control signals. These 160 Mb/s signals are sent to the modules via the four Clock, Control, Reject (CCR) buses. Slow control signals for configuration and monitoring are exchanged with the AMAC chip in the power boards.

The modules operate at 11 V, whereas the VTRx+ and lpGBT require 2.5 V and 1.26 V, respectively. To generate the 2.5 V and 1.26 V, a dual-stage DC-DC converter is bonded to the EoS card, and the resulting supply voltage is distributed to the VTRx+ and lpGBT ASICs. Each DC-DC converter is equipped with a bPOL2.5 [161] and a bPOL12 [162] which convert the 11 V supply to 2.5 V, and the 2.5 V to 1.26 V, respectively. The bPOL chips are radiation hard and magnetic field tolerant. To minimise the overall height, the main EoS cards have a cut-out for the DC-DC converters (see Figure 9.3). One dual-stage DC-DC converter supplies the main card,

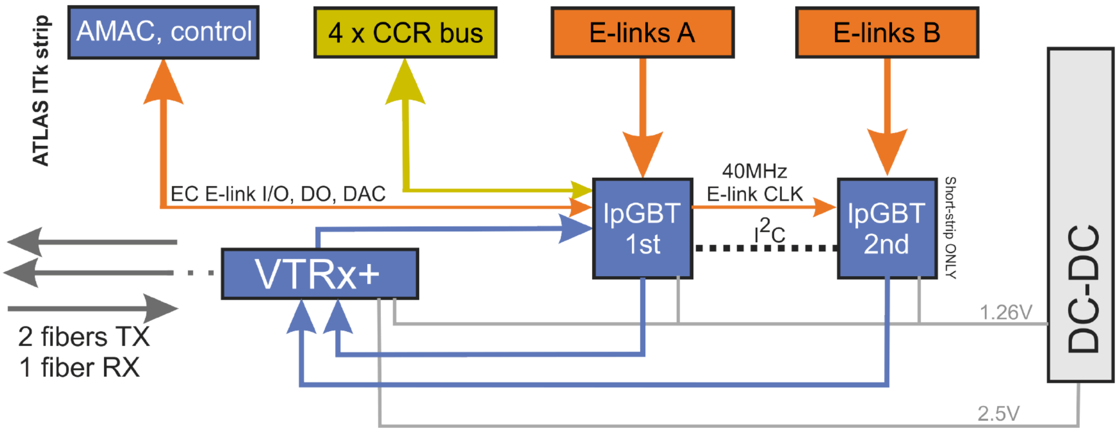

Figure 9.4: Block diagram of an EoS card. The second lpGBT is only present in the cards placed in the inner barrel staves (short strips). Taken from [166].

and the second one supplies the secondary card via the interconnection layer.

In each pair of EoS cards, one card is extended with a flex lead to accommodate a Glenair connector and two MPOs (Multi-fiber Push On) connectors, in a region of the support structure where there is more space available. The custom Glenair connector provides the HV, LV and monitoring lines for voltage and temperature. The MPOs connect the optical fibers from the VTRx+ chips on the main and secondary cards to the off-detector systems, thus enabling signal transmission.

The EoS card has a physical thickness less than 1.8 mm (bare PCB). It consists of 14 layers, two of which are dedicated to impedance-controlled signals. The PCB is designed using a hierarchical approach with configurable and modular blocks. This allows for the faster design of all EoS flavors. In total, 14 EoS card flavors exist to meet the different physical layouts of staves and petals, various flex lead geometries, and card variants with one or two lpGBT chips. Table 9.2 summarises the different EoS card flavors. All the mentioned constraints, including radiation hardness, physical dimensions, and the 0.5 mm fine pitch of the lpGBT, have resulted in a vendor-specific design.

Further details about the EoS design can be found in [17], while the latest project developments are described in [163–165].

Table 9.2: The fourteen EoS card flavors.

Location and features					Name
Stave	A-side	Main	Short-strip		Stave A-side Main Short-Strip
			Long-strip		Stave A-side Main Long-Strip
		Secondary	Short-strip	Flex-lead	Stave A-side Secondary Short-Strip
			Long-strip	Long-flex	Stave A-side Secondary Long-Strip Long-Flex
				Short-flex	Stave A-side Secondary Long-Strip Short-Flex
				Special-flex	Stave A-side Secondary Long-Strip Special-Flex
	C-side	Main	Short-strip		Stave C-side Main Short-Strip
			Long-strip		Stave C-side Main Long-Strip
		Secondary	Short-strip	Flex-lead	Stave C-side Secondary Short-Strip
			Long-strip	Long-flex	Stave C-side Secondary Long-Strip Long-Flex
				Short-flex	Stave C-side Secondary Long-Strip Short-Flex
				Special-flex	Stave C-side Secondary Long-Strip Special-Flex
Petal	Main			Flex-lead	Petal Main
	Secondary				Petal Secondary

CHAPTER 10

Quality Control and Quality Assurance of EoS Cards

The HL-LHC program is expected to start around 2030; therefore, production of all the ITk components described in Chapter 9 has already begun. In the case of the EoS cards, the PCBs are being produced and populated with all the electrical components. Once they are produced, the cards undergo extensive testing before being packaged and sent to the loading sites for their final installation on the substructures.

As a failure of an EoS card could result in the malfunction of an entire side of an stave or petal (e.g., inability to power the modules or to send data out of the detector), the individual card evaluation is crucial. This examination is known as *Quality Assurance* (QA) and *Quality Control* (QC), and has been developed over the past few years during the pre-production stage. These tests ensure not only that the EoS cards are functioning properly, but also their durability in the detector after installation and throughout the entire HL-LHC program.

QA measurements are (possibly destructive) tests performed on early production during the development phase, to exclude possible failures in the design and production procedures. In contrast, QC tests are non-destructive tests that are performed for each single card prior to distributing it. In this chapter, Section 10.1 presents the QA and QC tests performed in the context of this thesis, while Section 10.2 focuses on the development of one of the setups, the so-called *flatness setup with capacitive sensors*.

10.1 Quality Assurance and Quality Control

The bare EoS cards are manufactured externally in industry and received in panels. Each panel includes a set of unpopulated EoS cards and a Customer Test Coupon (CTC). As the CTCs are produced alongside the EoS cards, their dimensions and electrical properties are similar to those of the cards in the same panel. Therefore, initial electrical, bonding, soldering and bond-pull tests can be performed on the CTC PCBs, and the results can be extrapolated to the EoS cards. The test coupons include various test structures, such as long traces with well-defined impedances and long traces with measurable resistivity. These test structures probe the PCB quality within a layer. In addition, there are test structures with many vias (layer interconnections) in series

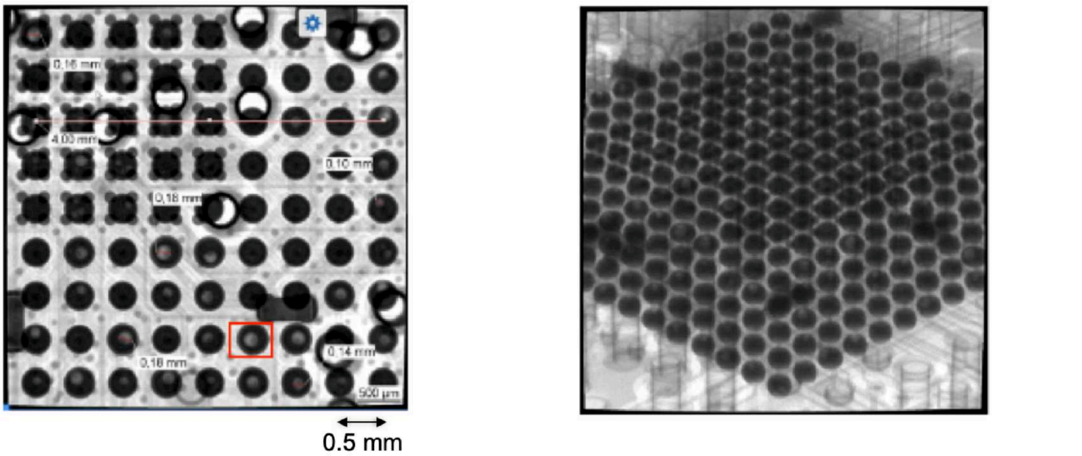

(a) Top view

(b) Side view

Figure 10.1: 3D X-ray image of the solder joints of the lpGBT BGA from the top view (a) and from a different angle (b). A solder joint with a large identified air bubble is highlighted in red. Taken from [163].

and a dedicated ball grid area (BGA) test structure. Bonding quality, as well as resistivities and impedances of the test structures, are measured and compared with predefined tolerance values. If this QC test is passed, the corresponding EoS cards in the panel are populated with the electrical components.

With the lpGBT ASICs bonded to the EoS cards, an external company uses X-ray imaging to investigate the solder joints of the ball grid array (BGA). This study detects potential connection defects between the lpGBT gates and EoS bonding pads to ensure long-term operation. Figure 10.1(a) highlights an example of a solder joint, where the gray bubbles within the solder joints correspond to a reduced amount of solder metal, presumably due to gas bubbles. The image shows a 3D X-ray image of the solder joints arranged in the 0.5 mm grid. Repeating the measurement from a different angle of incidence of the X-ray source allows the 70 µm trace structures of the top two layers of the board to be observed, as shown in Figure 10.1(b).

The following QC tests are performed in the Detector Assembly Facility (DAF) at DESY. These tests are carried out on four *test benches*, which are briefly described below.

After identification of the EoS card by its imprint numbers on the PCB and Radio Frequency Identification (RFID) chip in the first test bench, high-resolution optical images are taken and flatness measurements are performed. Initial electrical and communication tests are also carried out at room temperature. The optical images are recorded of the front and back sides of the EoS card. Next, the physical dimensions of the card are measured, including the length of the solder LV cables and the flatness of the back of the card (see Section 10.2), to ensure a smooth mechanical integration of the EoS card into the substructures at a later stage. The EoS cards are switched on and the power consumption is measured, while infrared images are taken to detect major electrical failures. Basic functional tests of the VTRx+ and lpGBT are performed, such as configuration tests. The lpGBT identifier and ADC values are read and cross-checked with those provided by the chip designer. A Cyclic Redundancy Check (CRC) test is used to verify the

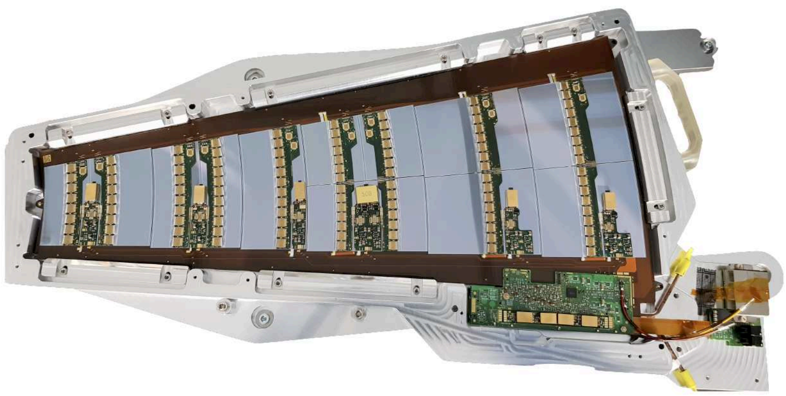

Figure 10.2: Photo of a fully loaded pre-production petal with the EoS card mounted. Taken from [163].

response of the lpGBT drivers to the 10 Gb/s signal.

As part of the operational cycle, the ATLAS ITk detector is expected to be cooled and warmed a number of times from approximately −35 °C to room temperature [167]. Thus, all the detector components undergo thermal stress testing. In the case of the EoS cards, the second test bench involves placing the EoS card inside a temperature chamber with dry air. The cards are cycling ten times from −35 °C to 25 °C. At −35 °C and 25 °C, turned on, and electrical and functional tests similar to those in the first test bench are performed at these extreme temperatures. Up to 24 boards fit inside the temperature chamber. While the cards can all be turned on simultaneously, only one board can be connected via optical fiber to the FPGA at a time. Consequently, this test takes the longest.

The strip sensors are planned to operate at a sensor bias voltage of 500 V [155]. The HV from the off-detector system is first received by one of the EoS cards via the flex lead and filtered using T-type RCR filters before being transferred to the modules. Therefore, the HV lines of the boards need to be tested, and this is done in the third test bench. The setup consists of a box with an interlock system, into which up to two cards can be inserted and biased. Either one board with a flex lead (with eight HV channels) or two boards without a flex lead (with four HV channels, that get the HV via the EoS interconnection from its partner board) can be measured simultaneously. Each HV line is ramped up to 1.1 kV (more than twice the nominal operating voltage) while the others are kept at ground level. The leakage current, which must not exceed 5 nA, is monitored every two seconds for one minute.

The fourth test bench consists of a needle prober setup for performing the complete electrical test and Bit Error Rate Test (BERT) of all 640 Mb/s signals. For that, the EoS card is contacted through test points located on the back side, close to the bonding pads which connect the EoS card to the bus tape. The test points are arranged on a 0.7 mm grid. The BERT runs for about 8 minutes and the error rate must be lower than 10^{-12}. Data is sent and received by an FPGA, and eye diagrams of the outgoing 10 Gb/s and incoming 2.5 Gb/s signals to the EoS cards are recorded. The FPGA counts the frame errors in the outgoing signals via a CRC test, while the lpGBT ASIC uses a counter for Forward Error Corrections (FEC) to compensate for bit flips in the data stream from the off-detector on the incoming signal.

Once the EoS card has passed all the tests and the results have been uploaded to the *ITk*

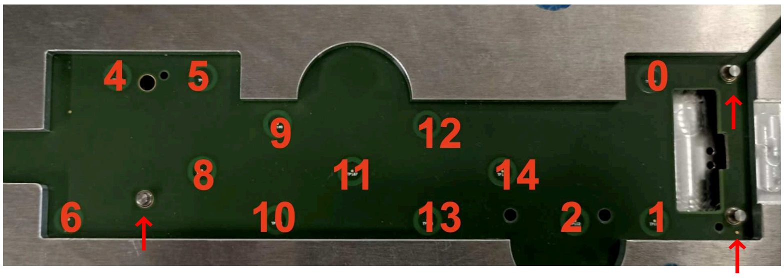

Figure 10.3: Photo of the flatness setup. The position and number of the capacitive sensors are indicated. *Sensor3* and *Sensor7* are not visible. Three red arrows mark where the EoS card is held in the setup, which is the same location where the washers are placed to increase the distance between the card and the sensors.

Production Database (IPD), it is packed in a specially designed, sealed, ESD-proof bag in a dry nitrogen atmosphere. A label with a QR code is then printed and attached to the bag for identification purposes and to indicate the final QA and QC status of the board. The card is then shipped to the loading sites, where it will be mounted on the substructures. Final tests of the entire petal or stave with the EoS card will be performed there. Figure 10.2 shows a fully loaded pre-production petal with the EoS card mounted.

10.2 Development of the Flatness Measurement Setup

The flatness of the backside of the EoS card is a critical specification. A tolerance of 300 µm has been set to ensure proper gluing to the carbon-fiber core and effective heat dissipation. While a smartscope can be used to measure the flatness of an EoS card, this process is very slow and offers a higher level of resolution than is required. Furthermore, it blocks the smartscope from being used for other tasks that require higher precision, such as measuring the flatness of an entire petal. Thus, it is not practical to use a smartscope to measure the flatness of each EoS card during the production QC stage.

As an alternative, a setup based on capacitive sensors has been developed and integrated into the first test bench. This setup allows for fast flatness measurements to be performed alongside the initial electrical and communication tests. This section describes the development of the flatness measurement setup, including sensor calibration, comparison of results with smartscope measurements, as well as providing statistics on the boards measured during production.

10.2.1 Description of the Flatness Setup

The flatness setup consists of fifteen capacitive sensors [168] distributed across a metal box into which the EoS card is inserted. Thirteen of these sensors are located on the base, as shown in Figure 10.3. Two sensors (*Sensor3* and *Sensor7*) are on the cover of the box, and only make contact with the front of the EoS card when the cover is closed.

Each sensor measures the capacitance between the sensor area and the ground (GND) structure of the EoS card. Since the bottom side of the EoS card is mostly a continuous GND plane (see Figure 10.5 left), the measured capacitance depends strongly on the distance between the sensor

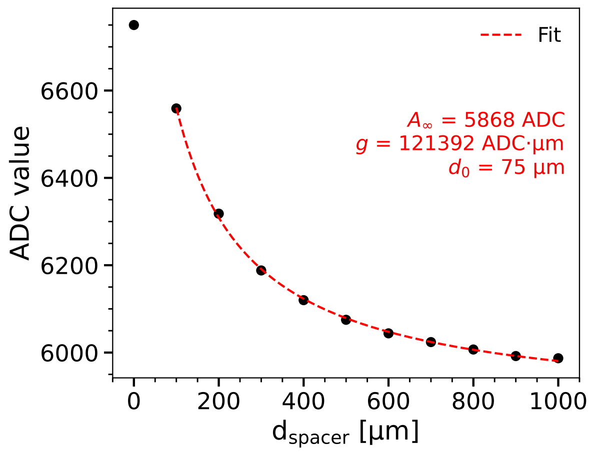

Figure 10.4: Signal from a single capacitive sensor as a function of the spacer distance. The calibration parameters are obtained from the fit of Equation 10.1. Data are recorded with *Sensor1* and the box cover is open.

and the bottom side of the card. Therefore, each sensor, ideally, records raw data (ADC value) that is inversely proportional to the distance to the board. These raw ADC readings can be obtained by reading out the chip in *debug* mode [168]. The setup is connected to an FPGA, and the LabVIEW framework [169] is used for sensor readout.

Each EoS card flavor uses a different metal-box setup due to its geometry, with sensors arranged differently. Nevertheless, the procedure used to determine the flatness is the same for all flavors and is explained below.

10.2.2 Sensor Calibration

The sensor signals in ADC units are recorded as a function of the distance between the sensor and the EoS card to demonstrate the capacitive behavior of the sensors and perform their calibration. To do so, an EoS card previously measured with the smartscope and confirmed to be flat is used. To vary the spacer distance (d_{spacer}) between the EoS card and the sensors, 100 µm-thick washers are placed under the three contact points between the card and the box base (see Figure 10.3).

Figure 10.4 shows the recorded ADC value as a function of d_{spacer} for *Sensor1*. The gain (g), distance offset (d_0), and asymptotic ADC offset at large distances (A_∞) are extracted from this measurement for each sensor using the following fit equation:

$$\text{ADC value} = A_\infty + \frac{g}{d_0 + d_{spacer}}. \tag{10.1}$$

This measurement is repeated for all the sensors with the cover both open and closed. Comparing the two configurations (open/closed) allows identification of any effects from the cover, such as physical interactions between the cover and the electric components on the frontside of the EoS card. These interactions modify the sensor readings, as presented in Appendix C.5. The three

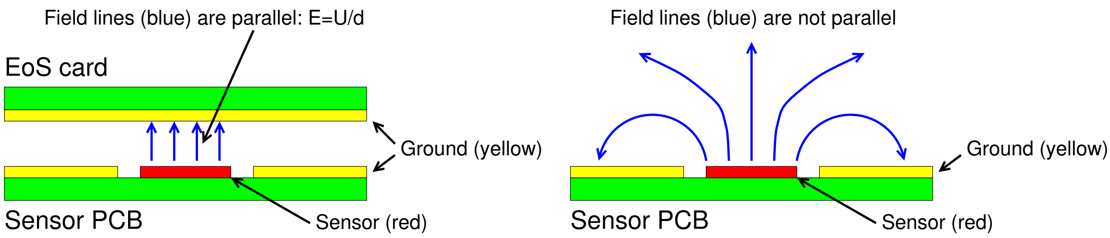

Figure 10.5: Sketch of the electric field lines of a capacitive sensor setup. On the left, an EoS card is placed at a small distance. The electric field lines are straight and parallel in the region between the sensor and the EoS card, and the measured capacitance is inversely proportional to the distance between them. On the right, no board is present, resulting in an open electric field configuration and a smaller effective capacitance. In both cases, the electric field lines enter the surfaces perpendicularly. Taken from [170].

calibration parameters (A_∞, g, d_0) are extracted for each sensor from these curves. The point at d_{spacer} equal zero is excluded from the fit because the EoS card may be touching the sensors, and therefore, d_{spacer} does not correspond to the proper distance between sensor and EoS card.

10.2.3 Flatness Measurememnt

Now that all the sensors in the setup have been calibrated and their capacitive behavior verified, they can be used to predict the flatness of the EoS boards. This is performed in two steps: first, the distance from each sensor to the board is obtained, and then the flatness value is calculated.

To determine the distance from a sensor to the EoS card (d_{EOS}), the following relation is used:

$$\mathrm{ADC}_{\mathrm{EoS}} - \mathrm{ADC}_{\mathrm{empty}} = A_\infty + \frac{g}{d_{\mathrm{spacer}} + d_0 + d_{\mathrm{EoS}}}. \tag{10.2}$$

Here, A_∞, g, and d_0 are obtained from the sensor calibration (see Section 10.2.2), d_{spacer} is set by the chosen spacer thickness, and $\mathrm{ADC}_{\mathrm{EOS}}$ and $\mathrm{ADC}_{\mathrm{empty}}$ are the raw sensor readings with and without the EoS card, respectively. Compared to Equation 10.1, the asymptotic behaviour A_∞ is corrected using the $\mathrm{ADC}_{\mathrm{empty}}$ measurement, both performed in the calibration run, in order to perform baseline suppression and to account for the field distortion around the sensor when there is no board. This effect is sketched in Figure 10.5. Solving Equation 10.2 for d_{EoS}, the distance between each sensor and the board is determined.

Next, a reference plane is fitted to the calculated d_{EoS} values by minimizing the sum of squared perpendicular distances using the least-squares method. The plane determination excludes *Sensor3* and *Sensor7* located in the box cover. For each sensor, d_z is defined as the perpendicular distance from the fitted plane to the measured d_{EoS} at that sensor position.

Finally, the flatness of the EoS card is calculated as the difference between the maximum and minimum $|d_z|$ values, representing the maximum deviation of the board backside surface from a reference plane.

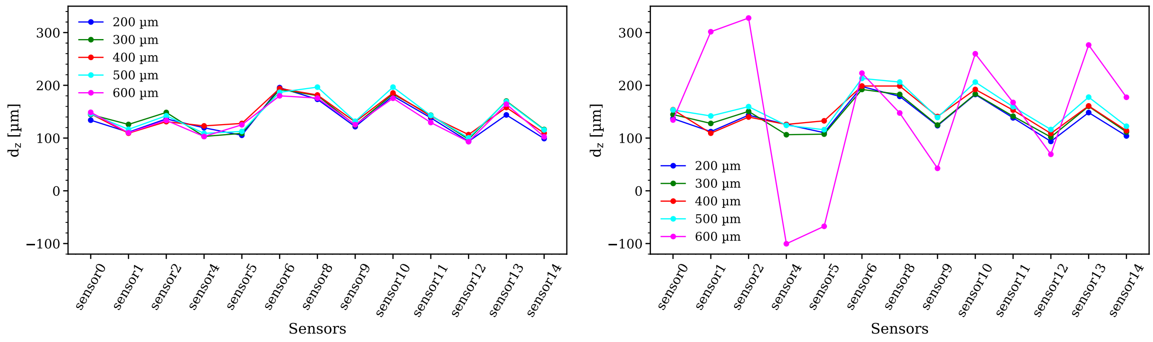

(a) Cover open

(b) Cover closed

Figure 10.6: d_z as a function of the sensor with the cover (a) open and (b) closed for different d_{spacer}. Data obtained with a main stave long-strip short-flex pre-production EoS card.

10.2.4 Performance on Pre-production Boards

Figure 10.6 shows the obtained d_z values for each sensor with the cover open and closed for different d_{spacer}. As expected, there are no significant variations in the measured distances when the cover is open. However, for the largest spacer distance (d_{spacer} = 600 µm), some of the components on the front side of the EoS card come into contact with the cover when the box is closed, pushing down the card and affecting the sensor readings. Having verified that the measurements remain consistent for spacer distances below 600 µm, a value of d_{spacer} = 200 µm is used for all the following measurements.

Furthermore, Figure 10.7 shows the obtained d_z values for each sensor with the cover open and closed for seven similar pre-production EoS boards. The figure legend includes the computed flatness value for each board. All the boards exhibit similar shape trends, and no significant differences are observed between the open- and closed-cover configurations — that is, none of the cards bend excessively to touch the cover with their electrical components. *Sensor4* and *Sensor6* overestimate the distance to the EoS board due to the absence of a metal layer on the back of the EoS card in that region (see Figure 9.3 right). Similarly, *Sensor0* is located near the boundary between the metal layer and the green protective layer, resulting in slightly less precise measurements.

The flatness values for these seven boards, in Figure 10.7, are close to the tolerance limit. At the time of this study, only a limited number of boards of the same type were available, and they came from a different vendor than the one producing the final EoS cards. Smartscope measurements (see Section 10.2.5) confirm the reported values. This observed bending is likely due to the repeated handling of these boards during testing, which can degrade their flatness. Such repeated handling is not expected for individuals board during production. In contrast, the data in Figure 10.6 correspond to a board produced by the vendor responsible for producing the final EoS cards, and the tolerance flatness limit is satisfied.

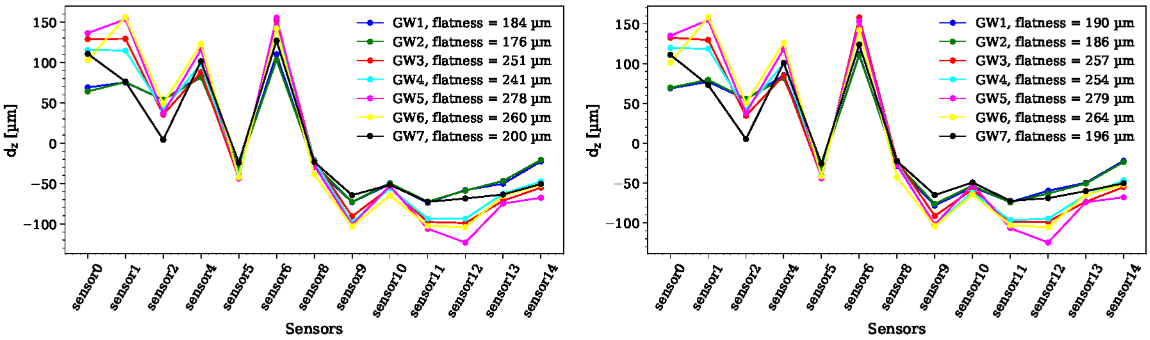

(a) Cover open (b) Cover closed

Figure 10.7: d_z as a function of the sensor with the cover (a) open and (b) closed for different main stave long-strip short-flex pre-production EoS cards. A spacer distance of d_{spacer} = 200 µm is used in the flatness setup. The obtained flatness value is indicated in the legend.

10.2.5 Comparison with the Smartscope Measurements

Smartscope measurements are performed to determine the actual flatness of an EoS card and to validate the method described above using the capacitative sensors. Using Computer Aided Design (CAD), a pattern is defined to scan the entire back surface of the EoS board, as illustrated in Figure 10.8(a). At each scanned position (x,y), the distance z from the lens to the backside of the EoS card is measured via optical focusing.

To enable comparison with the results obtained in the previous section, the same method is applied. First, a reference plane is fitted using only the thirteen points closest to the sensor positions of the setup, as explained above. Next, d_z is calculated as the distance from each point's z-coordinate to the fitted plane. The flatness is then defined as the difference between the maximum and minimum $|d_z|$ values.

Figure 10.8(b) shows the measured points in x,y, and z coordinate points obtained with the smartcope. The fitted plane determined using the least-squares method is depicted in gray. The color scale represents the d_z values from each point to the reference plane. Using the same thirteen points as in the other setup, a flatness value of 144 µm is determined.

Figure 10.9 shows the d_z values obtained at all the sensor positions for both the smatscope and the flatness setups. Trends are consistent across all points, indicating that the flatness setup can predict the bending of the EoS cards. Additionally, the flatness setup slightly predicts higher bending of the card than the smartscope, especially at *Sensor6*. This is due to its position near the board edge and the absence of a metal layer on the outer surface of the EoS card (visible on the right in Figure 9.3 as light yellow rings of PCB-base material in the left part). Thus, corrections derived from the smartscope measurements could be applied to refine the results. However, since such high precision is not required, this has not been done.

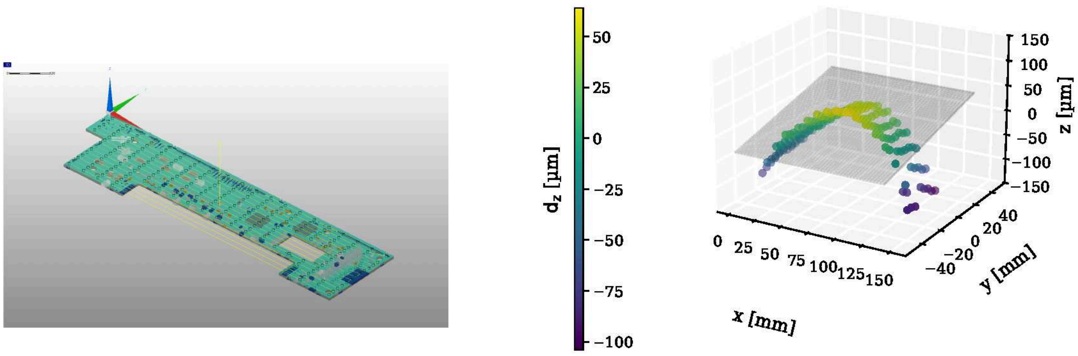

(a) (b)

Figure 10.8: (a) CAD scheme of the front side of the EoS card showing the pattern and the positions of the points measured with the smartscope in x and y. (b) 3D reconstruction of the measured points with the smartscope. The fitted plane is shown in gray, and the distances (d_z) from all measured points to the plane are indicated by the color scale.

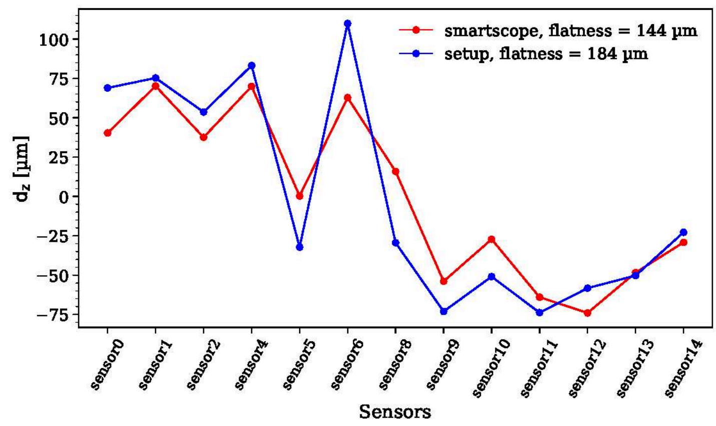

Figure 10.9: d_z as a function of the sensor obtained with the smartscope and the flatness setup. A spacer distance of d_{spacer} = 200 µm is used in the flatness setup. The obtained flatness value is indicated in the legend. The data have been obtained with the board GW1 measured in Figure 10.7.

10.2.6 Optimisation, Current Status and Performance on Production Boards

Having proven that the developed setup is capable of providing accurate flatness values, further optimisations have been implemented to speed up the measurement. In particular, varying the spacer distances is not feasible because manually positioning and removing the washers from the holders at each height is time-consuming. Therefore, the method has been modified such that only two measurements are required with the EoS card after calibration at $d_{spacer} = 200\,\mu m$: one with the cover open and one with the cover closed.

First, raw data from the fifteen sensors is recorded (x_i, y_i, z_i), and a triangular mesh is built from a geometry file. The height z_j of the board is reconstructed at every mesh node (x_j, y_j, z_j): each measurement point is assigned to the triangle in which it lies, its barycentric weights are computed, and these weights create one linear equation — relating the measured height and the height of the three mesh nodes of the triangle.

A system of equations is generated, with one equation per triangle in the mesh, and the system is solved using the least-squares method. In this way, a smooth surface can be used instead of a limited number of measurements.

Once the entire mesh is reconstructed, a reference plane of the form $z = ax + by + c$ is fitted to the mesh nodes using the least-squares method:

$$\min_{a,b,c} \sum_j (z_j - (ax_j + by_j + c))^2. \tag{10.3}$$

The perpendicular distance between each mesh node and the fitted plane is computed as:

$$d_j = z_j - (ax_j + by_j + c), \tag{10.4}$$

and the flatness is defined as the difference between the maximum and minimum deviations:

$$\text{flatness} = |\max(d_j)| - |\min(d_j)|. \tag{10.5}$$

This procedure is repeated twice: once with the cover open and once with the cover closed. In both cases, the requirement is that the flatness value must be below 300 µm. After the measurement with the cover closed, the distances of all sensors d_j are compared to those from the cover-open measurement as:

$$\Delta d_j = d_j(\text{open}) - d_j(\text{closed}) \tag{10.6}$$

A deformation Δd_j greater than 50 µm is considered to be caused by the contact of some components on the frontside of the card with the cover. Therefore, the deformation value must not exceed 50 µm.

With the described methodology and the constraints on flatness and deformation, production boards that will go under the ATLAS ITk detector are currently being measured during QC, and statistics for this test are being collected. Figure 10.10 shows a boxplot of the flatness values for different EoS flavors that have undergone the QC test so far. Board flavors not included have not been produced/tested during the production stage yet. In all cases, the median value, marked in red, is below the 300 µm requirement. Some distributions, such as *Stave A-side Secondary Special-Flex* and *Stave C-side Secondary Special-Flex*, show a slightly higher spread, which is

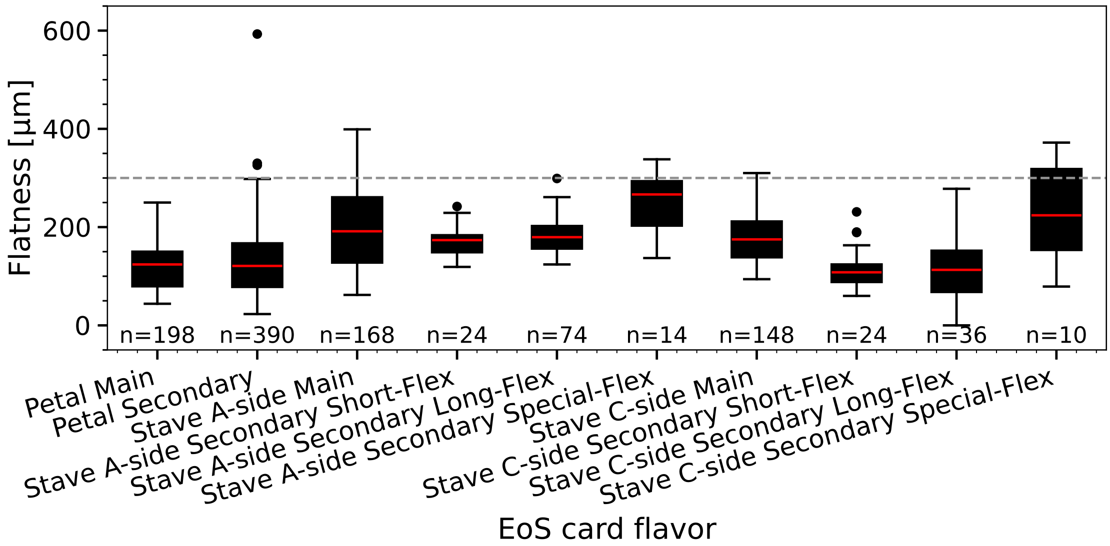

Figure 10.10: Flatness statistics for each flavor of production board tested by 8th December 2025. Each box shows the interquartile range (IQR), from the 25th to the 75th percentile. Whiskers extend to the minimum and maximum values within 1.5×IQR. Data points outside the whiskers are considered outliers and are indicated as black dots. The red line marks the median (50th percentile) flatness value. The discontinuous critical value of 300 µm is indicated with a dashed gray line. The total number of boards of each type n is also included below each box.

dominated by low statistics and with most of the boards under the flatness specification.

Out of the 1 086 tested boards, 1 068 fulfill the requirements, while 18 do not pass this QC test. This corresponds to a success rate above 98%, with around two thirds of the EoS cards produced so far already produced and tested.

Conclusion and Outlook

The HL-LHC upgrade of the LHC will increase the number of collisions and expand the dataset collected by the experiments. This will enable more precise tests of the SM and increase the potential for new physics discoveries. To maintain the performance of the detectors in this new scenario, significant upgrades will be carried out. In particular, the current ATLAS ID will be replaced by the ATLAS ITk, an all-silicon tracker consisting of a pixel detector and a strip detector. The new strip detector will be composed of substrates (staves and petals). To facilitate its communication with the off-detector systems, a pair of EoS cards will be placed at the end of each substructure.

With the EoS cards being the only point of communication between the substructures and the off-detector system and being responsible for crucial tasks related to module operation and data transmission, strict QA and QC procedures have been developed and performed as part of this work. These tests cover the entire process, from reception of the EoS cards to their packaging for shipment to the assembly sites, where they will be installed on the detector.

A setup based on capacitive sensors has been developed to quickly and accurately measure the flatness of the backside of the EoS cards, ensuring proper gluing to substructures and efficient heat dissipation. The easy-to-operate setup is equipped with a LabVIEW interface that automatically updates the relevant test results to the ITk Production Database. After calibrating the sensors, systematic flatness measurements consistent with smartscope results have been obtained for different EoS flavors during both the pre-production and production stages. In parallel, routines for smartsope operation have also been developed to measure the flatness of the EoS cards. These include generating CAD files with defined scanning patterns, lens-focusing and illumination routines, as well as an analysis workflow similar to that used for the capacitive sensor setup.

Now that the EoS project is in the second third of the production stage, statistics and operational experience from the QA and QC tests are being accumulated. The manufacturing and testing of the remaining boards will continue over the next few months.

APPENDIX A

Allpix^2 Configuration Files

The configuration files used for the Monte Carlo simulations with the Allpix^2 framework (version 3.2.0.) are provided below.

```
[Allpix]
detectors_file = /path/to/geometry_configuration_file
multithreading = true
root_file = "output.root"
number_of_events = 500000
random_seed = 1

[GeometryBuilderGeant4]

[DepositionGeant4]
physics_list = QGSP_BERT_EMZ
enable_pai = 1
number_of_particles = 1
particle_type = "e-"
source_energy = 5GeV
source_type = "beam"
source_position = 0 0 -10mm
beam_size = 100um
beam_divergence = 0mrad 0mrad
beam_direction = 0 0 1
max_step_length = 0.5um

[ElectricFieldReader]
model = "mesh"
file_name = /path/to/tcad_electric_field
```

```
field_mapping = PIXEL_FULL_INVERSE
field_depth = 10um

[DopingProfileReader]
model = "mesh"
file_name = /path/to/tcad_doping_profile
field_mapping = PIXEL_FULL_INVERSE
doping_depth = 10um

[GenericPropagation]
temperature = 293K
mobility_model = "masetti_canali"
recombination_model = "srh_auger"
charge_per_step = 5
timestep_min = 0.5ps
timestep_max = 0.05ns
integration_time = 25ns
propagate_electrons = true

[PulseTransfer]
collect_from_implant = true

[DefaultDigitizer]
electronics_noise = 40e
threshold = 224e
threshold_smearing = 17e
output_plots = true

[DetectorHistogrammer]
matching_cut = 200um 200um
track_resolution = 3.7um 3.7um

[ROOTObjectWriter]
file_name = "objectwriter_output.root"
```

Listing 1: Configuration file for the Allpix^2 framework.

```
type = "monolithic"
geometry = pixel
number_of_pixels = 20 20
pixel_size = 35um 35um
sensor_thickness = 50um
sensor_excess_top = 200um
sensor_excess_bottom = 200um
sensor_excess_left = 200um
sensor_excess_right = 200um

[implant]
type = frontside
shape = rectangle
size = 2.2um 2.2um 1.3um
```

Listing 2: Detector model configuration.

```
[dut]
type = path/to/detector_model_configuration
position = 0 0 0
orientation = 0 0 0
```

Listing 3: Geometry configuration.

APPENDIX B

Corryvreckan Configuration Files

The configuration and geometry files for the Corryvreckan are provided in Listing 4 and Listing 5, respectively. In the configuration file, an example is provided for reconstructing data acquired in ToT mode, where the calibration file is loaded and the ToT-weighted method is utilized for hit position reconstruction. An example of parameters for the η-correction is provided.

```
[Corryvreckan]
detectors_file = /path/to/detector_file
detectors_file_updated = /path/to/detector_file_updated
histogram_file = output.root

[EventLoaderEUDAQ2]
type = "h2m"
file_name = /path/to/H2M/data
acq_mode = 1
delay_to_frame_end = 400000
incluse = true
calibration_path_tot = /path/to/calibration_tot_file

[EventLoaderEUDAQ2]
type = "tlu"
file_name= /path/to/TLU/data
get_time_residuals = true

[EventLoaderEUDAQ2]
type = "AdeniumRawDataEvent"
file_name = /path/to/ADENIUM/data
get_time_residuals = true
```

```
[Clustering4D]
time_cut_abs = 500us
charge_weighting = true

[Tracking4D]
track_model = "gbl"
momentum = 4.6GeV
spatial_cut_abs=200um,200um
min_hits_on_track = 6

[EtaCorrection]
eta_formula_x = "[0] + [1]*x + [2]*x^2 + [3]*x^3 + [4]*x^4 + [5]*x^5"
eta_constants_x =  0.000642 0.0900233 0.0740727 -372.394 -9985.84 4.14957e+06
eta_formula_y = "[0] + [1]*x + [2]*x^2 + [3]*x^3 + [4]*x^4 + [5]*x^5"
eta_constants_y =  -0.0001654 0.071563 3.21918 -544.435 -14920.6 5.34185e+06

[DUTAssociation]
time_cut_abs = 500us
spatial_cut_abs = 52.5um, 52.5um

[AnalysisDUT]
chi2ndof_cut = 5

[AnalysisEfficiency]
chi2ndof_cut = 5
```

Listing 4: Configuration file for the Corryvreckan framework.

```
[adenium_0]
coordinates = "cartesian"
material_budget = 0.00075
number_of_pixels = 1024, 512
orientation = -0.740147deg,180.714deg,-0.426968deg
orientation_mode = "xyz"
pixel_pitch = 29.24um,26.88um
position = -1.67418mm,185.443um,8mm
roi = [[525,200],[525,330],[580,330],[580,200]]
spatial_resolution = 5um,5um
time_resolution = 10us
type = "adeniumrawdataevent"
```

```
[TLU_0]
coordinates = "cartesian"
orientation = 0deg,0deg,0deg
orientation_mode = "xyz"
position = 0um,0um,16.2mm
role = "auxiliary"
time_resolution = 1ns
type = "tlu"

[adenium_1]
coordinates = "cartesian"
material_budget = 0.00075
number_of_pixels = 1024, 512
orientation = 0.0949964deg,179.381deg,0.187414deg
orientation_mode = "xyz"
pixel_pitch = 29.24um,26.88um
position = -645.984um,516.127um,36mm
roi = [[565,190],[565,320],[620,320],[620,190]]
spatial_resolution = 5um,5um
time_resolution = 10us
type = "adeniumrawdataevent"

[adenium_2]
coordinates = "cartesian"
material_budget = 0.00075
number_of_pixels = 1024, 512
orientation = -1.91425deg,179.92deg,0.0213713deg
orientation_mode = "xyz"
pixel_pitch = 29.24um,26.88um
position = -791.684um,234.462um,64mm
roi = [[560,210],[560,330],[610,330],[610,210]]
spatial_resolution = 5um,5um
time_resolution = 10us
type = "adeniumrawdataevent"

[H2M_0]
coordinates = "cartesian"
mask_file = /path/to/H2M/mask_file
material_budget = 0.00075
```

```
number_of_pixels = 64, 16
orientation = 184.058deg,1.0221deg,90.218deg
orientation_mode = "xyz"
pixel_pitch = 35um,35um
position = -2.9815mm,550.954um,95mm
role = "dut"
spatial_resolution = 10um,10um
time_resolution = 10us
type = "h2m"

[adenium_3]
coordinates = "cartesian"
material_budget = 0.00075
number_of_pixels = 1024, 512
orientation = 0deg,180deg,0deg
orientation_mode = "xyz"
pixel_pitch = 29.24um,26.88um
position = 0um,0um,123mm
roi = [[585,210],[585,340],[640,340],[640,210]]
role = "reference"
spatial_resolution = 5um,5um
time_resolution = 10us
type = "adeniumrawdataevent"

[adenium_4]
coordinates = "cartesian"
material_budget = 0.00075
number_of_pixels = 1024, 512
orientation = 0.447996deg,179.065deg,0.0153553deg
orientation_mode = "xyz"
pixel_pitch = 29.24um,26.88um
position = 178.442um,237.204um,148mm
roi = [[595,210],[595,330],[650,330],[650,210]]
spatial_resolution = 5um,5um
time_resolution = 10us
type = "adeniumrawdataevent"

[adenium_5]
coordinates = "cartesian"
material_budget = 0.00075
```

```
number_of_pixels = 1024, 512
orientation = -0.189248deg,181.941deg,0.103648deg
orientation_mode = "xyz"
pixel_pitch = 29.24um,26.88um
position = 100.251um,84.155um,176mm
roi = [[595,210],[595,340],[640,340],[640,210]]
spatial_resolution = 5um,5um
time_resolution = 10us
type = "adeniumrawdataevent"
```

Listing 5: Configuration geometry file for the Corryvreckan framework.

APPENDIX C

Additional Figures

C.1 Triggering on Telepix2

Figure C.1 shows the spatial correlations in the x-direction between H2M and the reference plane, comparing the case where the full Telepix2 chip is used to that where only the ROI matching the H2M area is considered as a trigger. A reduction in the background is observed in the last case, increasing the on-DUT tracking efficiency.

The background reduction speeds up both the alignment convergence and the data processing, where fewer events are taken into account.

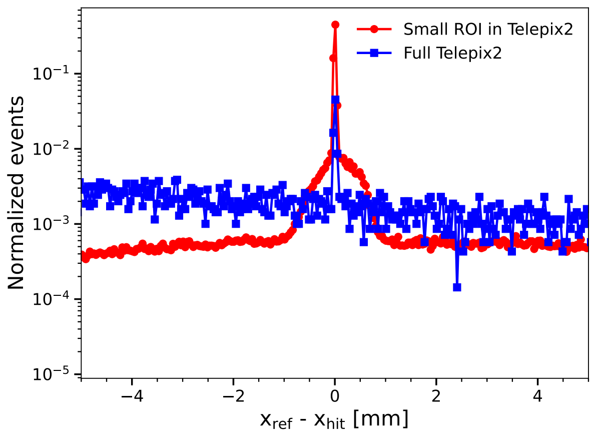

Figure C.1: Spatial correlations of H2M with (red) and without (blue) TelePix2 ROI trigger along the x-direction.

C.2 DUT alignment

Figure C.2 shows the DUT position after alignment in the X and Y directions during five consecutive days of data taking. For each data point, corresponding to a different setting of H2M, an independent alignment is performed. The DUT displacement correlates with the temperature in the test beam area, indicating that the shifts are mainly caused by thermal expansion of the positioning stage and the plastic support plate on which the DUT is mounted. In particular, a maximum displacement of about 70 µm (equivalent to two pixel pitches) is observed along the y-axis, highlighting the necessity of aligning the DUT for all the runs. Each run has a maximum duration of about 40 minutes.

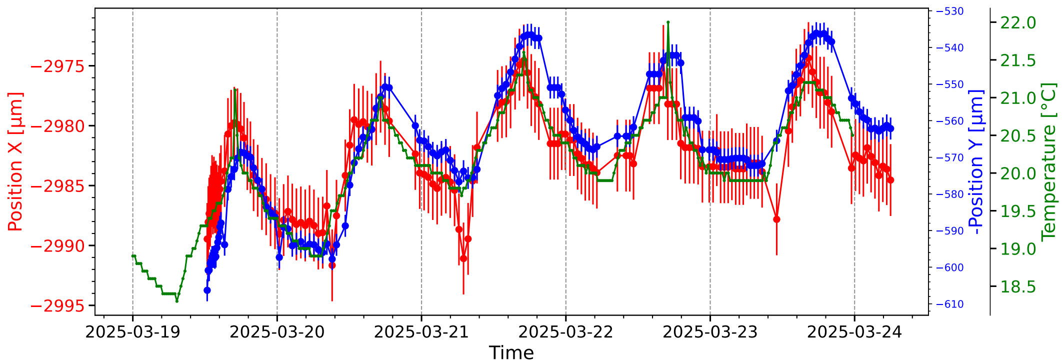

Figure C.2: Correlation between temperature in the test beam area and DUT position (in x and y) during five consecutive days of data taking. The position is given relative to the stage on which the H2M chip is mounted. Each data point corresponds to a different run, and they are aligned independently. Outliers correspond to runs with extreme chip settings (e.g., low threshold).

C.3 In-Pixel Response at −4.2 V

Figure C.3 shows in-pixel maps of the efficiency, ToA, and time resolution projected onto four pixels for different threshold values. The data is recorded in ToA mode with the *low ikrum* setting. For thresholds below 201 electrons, the fake-hit rate exceeds 12 pixels per event, i.e., the noise contribution is comparably high.

The in-pixel efficiency maps are symmetric and only statistical fluctuations are visible. In contrast, the ToA and time resolution maps exhibit the same pattern discussed in Section 7.1, even at a threshold as low as 138 electrons. As the threshold increases, the deterioration of all observables is visible, particularly in the region below the n-wells of the analog front-end.

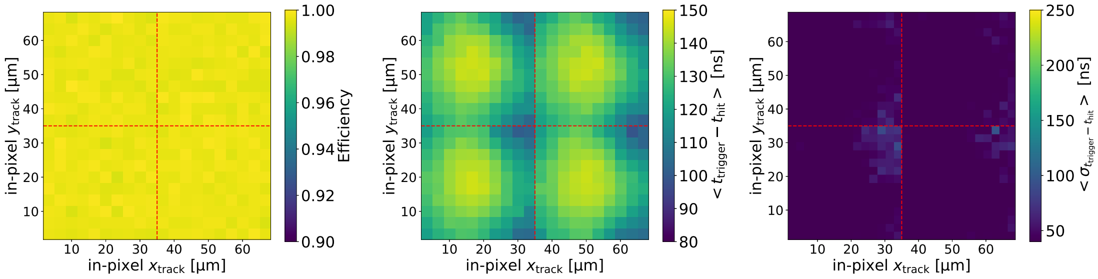

(a) Efficiency, 138 e⁻ (b) ToA, 138 e⁻ (c) Time resolution, 138 e⁻

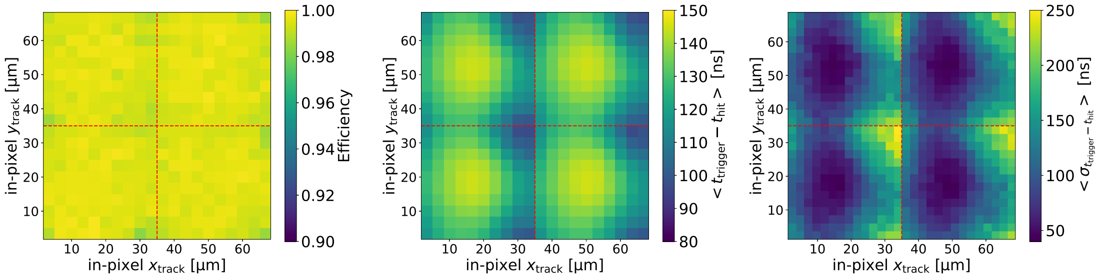

(d) Efficiency, 169 e⁻ (e) ToA, 169 e⁻ (f) Time resolution, 169 e⁻

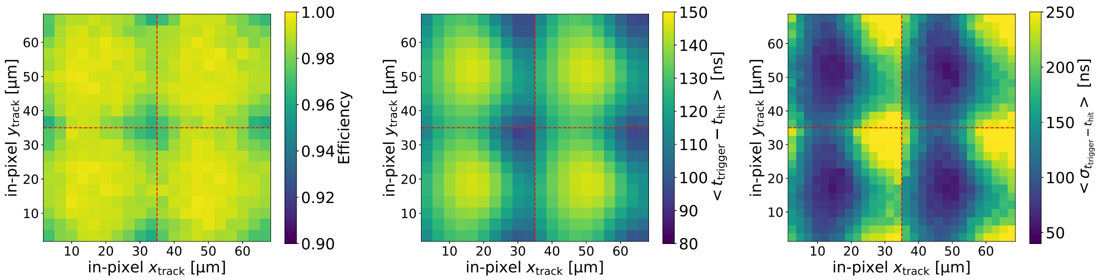

(g) Efficiency, 201 e⁻ (h) ToA, 201 e⁻ (i) Time resolution, 201 e⁻

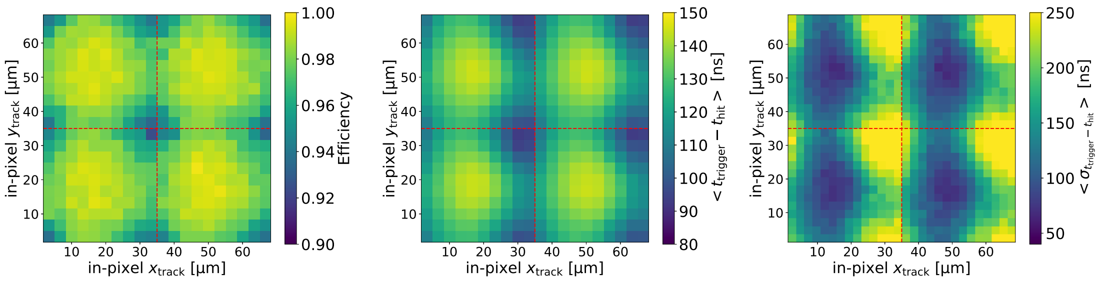

(j) Efficiency, 233 e⁻ (k) ToA, 233 e⁻ (l) Time resolution, 233 e⁻

Figure C.3: In-pixel maps projected onto four pixels. From top to bottom, the threshold increases. The left column shows the efficiency maps, the middle column the ToA maps, and the right column the time residuals. Data is obtained in ToA mode with the *low ikrum* setting and with the sensor biased at −4.2 V.

C.4 Track Resolution Simulation

The use of Equation 6.2 relies on the assumption that spatial residuals from single-pixel cluster events follow a box-like function. Figure 7.16(a) and 7.16(b) show the measuasured spatial residuals with two different beam telescope setups for the same sample operated under identical settings. The smearing of the edges of the box-like function is assumed to originate from the track resolution.

To verify this effect, Monte Carlo simulations have been performed using the setup described in Chapter 4. Figure C.4(a) presents the spatial residuals in Y for different values of the `track_resolution` parameter. The Monte Carlo true position is smeared with a Gaussian lateral spread of 0 and 3.7 µm.

Figure C.4(b) shows the spatial residual in Y for single-pixel clusters with a track resolution of 3.7 µm. Equation 6.2 is fitted to quantify the edge smearing, obtaining a value for σ of (3.95 ± 0.01) µm. The recovered track resolution is 6 % higher than the expected value. However, given the large $\mathrm{RMS}_{99.7\%}$ of H2M spatial residuals, this difference is negligible after quadratic subtraction to determine the H2M spatial resolution (see Equation 6.1).

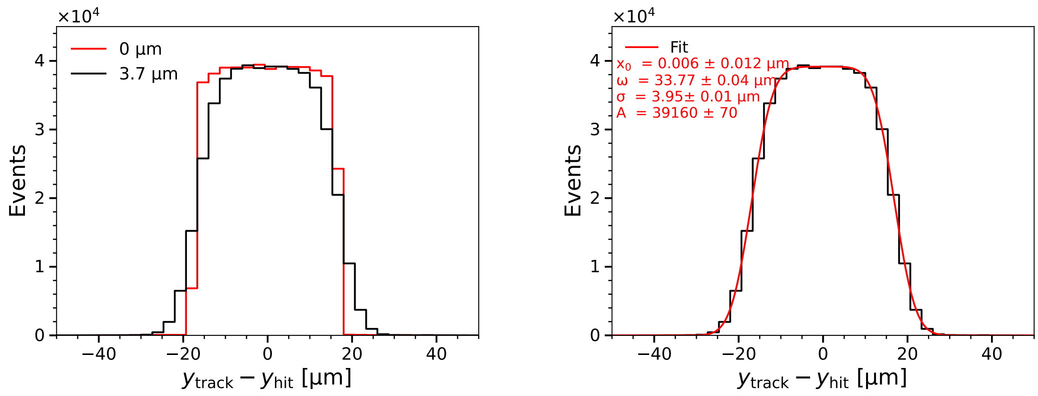

(a) (b)

Figure C.4: (a) Simulated spatial residuals in the Y direction for track resolutions of 0 and 3.7 µm. (b) Simulated spatial residual in Y for a track resolution of 3.7 µm fitted with Equation 6.2 for single-pixel clusters. The sensor is biased at −1.2 V, and the threshold is 224 electrons.

C.5 Capacitive Sensor Calibration of the Flatness Setup

Figure C.5 shows the calibration curves for all the capacitive sensors in the flatness setup with the cover open. The measured ADC value is recorded as a function of the sensor-EoS card distance (d_{sensor}). All the sensors located in the base of the box exhibit the expected behavior ($\propto 1/d$). *Sensor3* and *Sensor7* are located in the cover, and *Sensor15* is far away; therefore, no distance spacer is placed on them, and they never come into contact with the EoS card. As a result, their signals remain constant.

Similarly, Figure C.6 shows the calibration curves for all the capacitive sensors in the flatness setup with the cover closed. Compared with the results obtained with the cover open (Figure C.5), only slight differences are observed for sensors located near the PCB edges (see Figure 10.3), such as *Sensor4*. At larger d_{sensor} values (above 600 µm), the cover appears to come into contact with some components on the frontside of the PCB, altering the measurement. A similar behavior is observed in Figure 10.6(b).

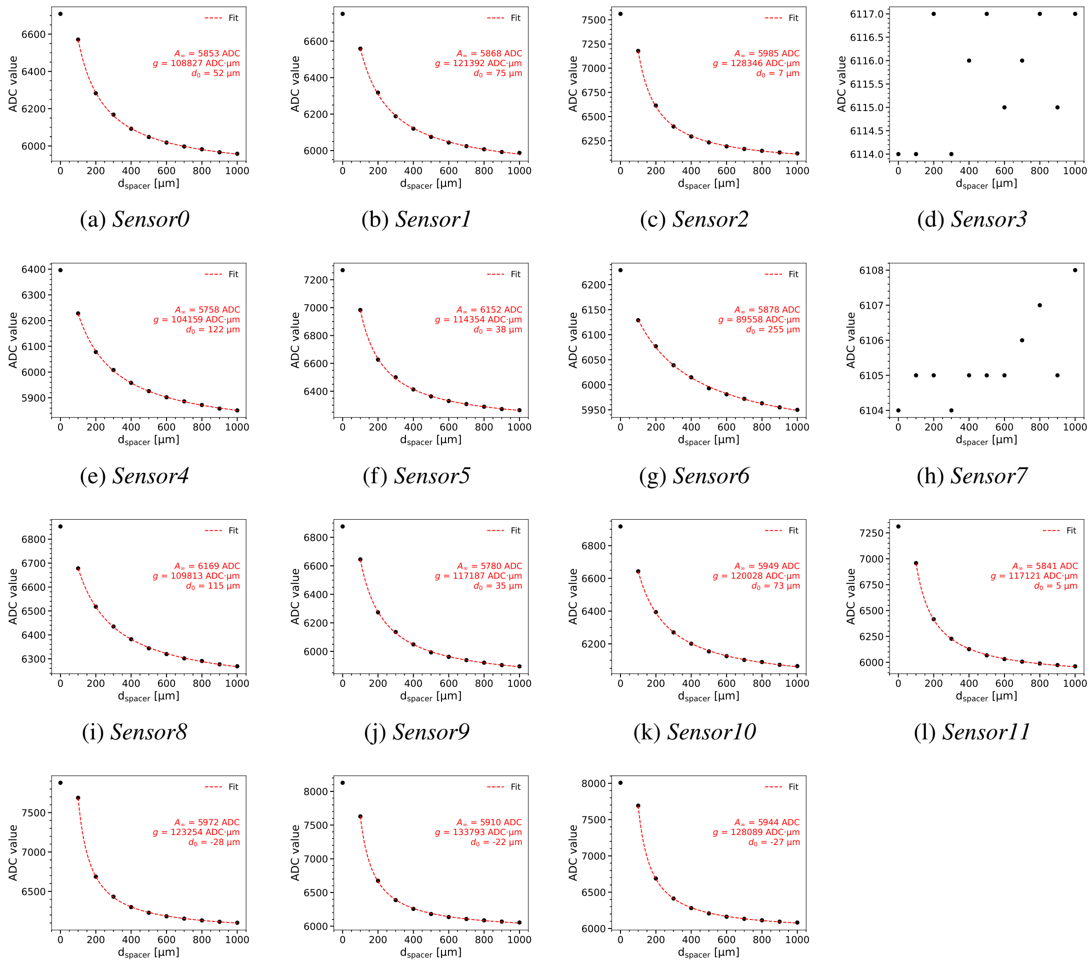

(a) *Sensor0* (b) *Sensor1* (c) *Sensor2* (d) *Sensor3*

(e) *Sensor4* (f) *Sensor5* (g) *Sensor6* (h) *Sensor7*

(i) *Sensor8* (j) *Sensor9* (k) *Sensor10* (l) *Sensor11*

(m) *Sensor12* (n) *Sensor13* (o) *Sensor14*

Figure C.5: Signal from all capacitive sensors as a function of the spacer distance. Data are recorded with the box cover open.

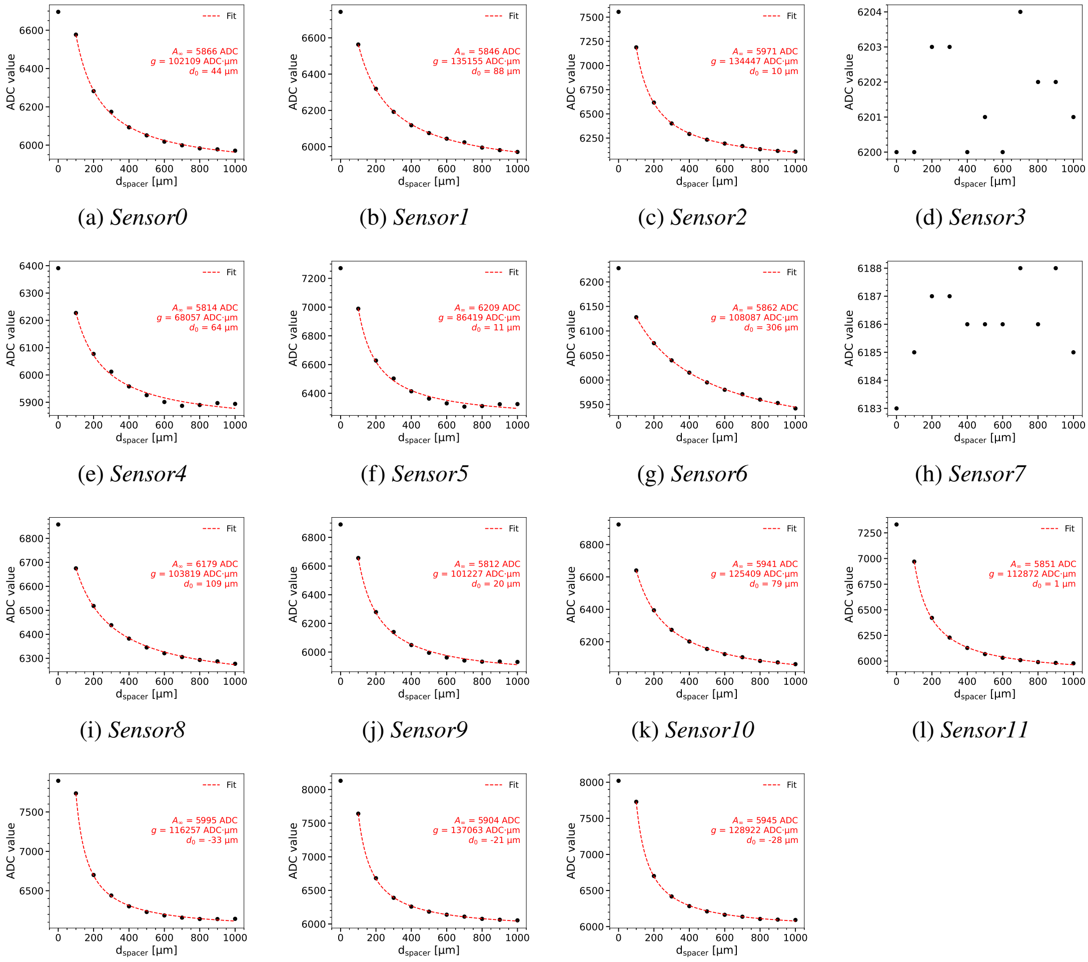

(a) *Sensor0* (b) *Sensor1* (c) *Sensor2* (d) *Sensor3*

(e) *Sensor4* (f) *Sensor5* (g) *Sensor6* (h) *Sensor7*

(i) *Sensor8* (j) *Sensor9* (k) *Sensor10* (l) *Sensor11*

(m) *Sensor12* (n) *Sensor13* (o) *Sensor14*

Figure C.6: Signal from all capacitive sensors as a function of the spacer distance. Data are recorded with the box cover closed.

Bibliography

[1] M. K. Gaillard, P. D. Grannis and F. J. Sciulli, *The standard model of particle physics*, Rev. Mod. Phys. **71** (2 1999) S96, URL: https://link.aps.org/doi/10.1103/RevModPhys.71.S96 (cit. on pp. 1, 3).

[2] M. Thomson, *Modern Particle Physics*, Cambridge University Press, 2013 (cit. on pp. 1, 3, 5).

[3] G. Bertone, D. Hooper and J. Silk, *Particle dark matter: evidence, candidates and constraints*, Physics Reports **405** (2005) 279, ISSN: 0370-1573, URL: https://www.sciencedirect.com/science/article/pii/S0370157304003515 (cit. on pp. 1, 5).

[4] O. S. Brüning et al., eds., *LHC Design Report. 1. The LHC Main Ring*, CERN-2004-003-V-1, CERN-2004-003, Geneva, 2004, URL: https://cdsweb.cern.ch/record/782076 (cit. on pp. 1, 3, 133).

[5] O. Aberle et al., *High-Luminosity Large Hadron Collider (HL-LHC): Technical design report*, CERN Yellow Reports: Monographs, Geneva: CERN, 2020, URL: https://cds.cern.ch/record/2749422 (cit. on pp. 1, 6, 133).

[6] *Highlights of the HL-LHC physics projections by ATLAS and CMS*, tech. rep., CERN, 2025, URL: https://cds.cern.ch/record/2928907 (cit. on pp. 1, 6).

[7] T. E. S. Group, *Deliberation document on the 2020 Update of the European Strategy for Particle Physics*, tech. rep., 2020, URL: https://cds.cern.ch/record/2720131 (cit. on pp. 1, 8).

[8] H. Kolanoski and N. Wermes, *Particle Detectors*, Oxford University Press, 2020, ISBN: 978-0-19-885836-2 (cit. on pp. 1, 13–18, 21–24, 26, 52).

[9] F. Hartmann, *Silicon-based detectors at the HL-LHC*, Nuclear Instruments and Methods in Physics Research Section A: Accelerators, Spectrometers, Detectors and Associated Equipment **924** (2019) 250, 11th International Hiroshima Symposium on Development and Application of Semiconductor Tracking Detectors, ISSN: 0168-9002, URL: https://www.sciencedirect.com/science/article/pii/S0168900218310593 (cit. on p. 1).

[10] E. Berger et al., *CLIC CDR - physics and detectors: CLIC conceptual design report*, (2012) (cit. on pp. 1, 8, 10, 31).

[11] A. Abada et al., *FCC-ee: The Lepton Collider*, Eur. Phys. J. Spec. Top. **228** (2019) 261 (cit. on pp. 1, 8, 13, 31).

[12] D. Dannheim, K. Krüger, A. Levy, A. Nürnberg and E. Sicking, eds., *Detector Technologies for CLIC*, vol. 1, CERN Yellow Reports: Monographs, Geneva: CERN, 2019 (cit. on pp. 1, 11, 13, 88, 108).

[13] G. A. Rinella et al., *Optimization of a 65 nm CMOS imaging process for monolithic CMOS sensors for high energy physics*, PoS **Pixel2022** (2023) 083 (cit. on pp. 1, 28, 32, 40, 117).

[14] H. Wennlöf et al., *Simulating monolithic active pixel sensors: A technology-independent approach using generic doping profiles*, Nuclear Instruments and Methods in Physics Research Section A: Accelerators, Spectrometers, Detectors and Associated Equipment **1073** (2025) 170227, ISSN: 0168-9002, URL: `https://www.sciencedirect.com/science/article/pii/S0168900225000282` (cit. on pp. 1, 43, 44, 46).

[15] *Technical Design Report for the ATLAS Inner Tracker Strip Detector*, tech. rep., CERN, 2017, URL: `https://cds.cern.ch/record/2257755` (cit. on pp. 2, 11, 13, 133–135).

[16] The ATLAS Collaboration, *The ATLAS experiment at the CERN LHC*, Journal of Instrumentation **3** (2008) S08003, URL: `https://doi.org/10.1088/1748-0221/3/08/S08003` (cit. on pp. 2, 6, 13).

[17] A. Boebel et al., *Current status of the end-of-substructure (EoS) card project for the ATLAS strip tracker upgrade using final ASICs*, Journal of Instrumentation **18** (2023) C03016, URL: `https://doi.org/10.1088/1748-0221/18/03/C03016` (cit. on pp. 2, 137).

[18] C. Burgard and D. Galbraith, *Standard Model of Physics*, CERN Webfest, `http://davidgalbraith.org/portfolio/ux-standard-model-of-the-standard-model/`, 2012 (cit. on p. 4).

[19] F. Halzen and A. D. Martin, *QUARKS AND LEPTONS: An Introductory Course in Modern Particle Physics*, 1984, ISBN: 978-0-471-88741-6 (cit. on p. 3).

[20] R. L. Workman et al., *Review of Particle Physics*, PTEP **2022** (2022) 083C01 (cit. on pp. 3, 19, 20, 22).

[21] T. K. Kuo and J. Pantaleone, *Neutrino oscillations in matter*, Rev. Mod. Phys. **61** (4 1989) 937, URL: `https://link.aps.org/doi/10.1103/RevModPhys.61.937` (cit. on p. 4).

[22] S.-K. Choi et al.,
Observation of a Narrow Charmoniumlike State in Exclusive $B^{\pm} \to K^{\pm}\pi^{+}\pi^{-}J/\psi$ Decays,
Phys. Rev. Lett. **91** (26 2003) 262001,
URL: `https://link.aps.org/doi/10.1103/PhysRevLett.91.262001`
(cit. on p. 4).

[23] R. Aaij et al., *Observation of $J/\psi p$ Resonances Consistent with Pentaquark States in $\Lambda_b^0 \to J/\psi K^{-} p$ Decays*, Phys. Rev. Lett. **115** (7 2015) 072001,
URL: `https://link.aps.org/doi/10.1103/PhysRevLett.115.072001`
(cit. on p. 4).

[24] L. Di Ciaccio, *Measurement of lifetimes and masses of B hadrons at LEP*, (1995),
URL: `https://cds.cern.ch/record/295512` (cit. on p. 4).

[25] A. Malara, *Exploring jets: substructure and flavour tagging in CMS and ATLAS*,
PoS **LHCP2024** (2025) 150, arXiv: `2410.14330 [hep-ex]` (cit. on p. 4).

[26] I. I. Bigi, Y. L. Dokshitzer, V. Khoze, J. Kühn and P. M. Zerwas,
Production and decay properties of ultra-heavy quarks, Phys. Lett. B **181** (1986) 157,
URL: `https://cds.cern.ch/record/171099` (cit. on p. 4).

[27] P. W. Higgs, *Broken Symmetries and the Masses of Gauge Bosons*,
Phys. Rev. Lett. **13** (16 1964) 508,
URL: `https://link.aps.org/doi/10.1103/PhysRevLett.13.508`
(cit. on pp. 4, 5).

[28] F. Englert and R. Brout, *Broken Symmetry and the Mass of Gauge Vector Mesons*,
Phys. Rev. Lett. **13** (9 1964) 321,
URL: `https://link.aps.org/doi/10.1103/PhysRevLett.13.321`
(cit. on pp. 4, 5).

[29] G. Degrassi et al., *Higgs mass and vacuum stability in the Standard Model at NNLO*,
Journal of High Energy Physics **2012** (2012) 98 (cit. on p. 4).

[30] The CMS Collaboration,
Observation of a new boson at a mass of 125 GeV with the CMS experiment at the LHC,
Physics Letters B **716** (2012) 30, ISSN: 0370-2693, URL: `https://www.sciencedirect.com/science/article/pii/S0370269312008581`
(cit. on p. 5).

[31] The ATLAS Collaboration, *Observation of a new particle in the search for the Standard Model Higgs boson with the ATLAS detector at the LHC*, Physics Letters B **716** (2012) 1,
ISSN: 0370-2693, URL: `https://www.sciencedirect.com/science/article/pii/S037026931200857X`
(cit. on p. 5).

[32] M. Blagojević and F. W. Hehl, *Gauge Theories of Gravitation*, 2022,
arXiv: `1210.3775 [gr-qc]`, URL: `https://arxiv.org/abs/1210.3775`
(cit. on p. 5).

[33] N. Arkani–Hamed, S. Dimopoulos and G. Dvali, *The hierarchy problem and new dimensions at a millimeter*, Physics Letters B **429** (1998) 263, ISSN: 0370-2693, URL: https://www.sciencedirect.com/science/article/pii/S0370269398004663 (cit. on p. 5).

[34] E. J. Copeland, M. Sami and S. Tsujikawa, *Dynamics of dark energy*, International Journal of Modern Physics D **15** (2006) 1753, ISSN: 0218-2718 (cit. on p. 5).

[35] M. Dine and A. Kusenko, *Origin of the matter-antimatter asymmetry*, Rev. Mod. Phys. **76** (1 2003) 1, URL: https://link.aps.org/doi/10.1103/RevModPhys.76.1 (cit. on p. 5).

[36] C. Englert and M. Russell, *Top quark electroweak couplings at future lepton colliders*, The European Physical Journal C **77** (2017) 535 (cit. on pp. 5, 7).

[37] A. Dainese et al., *Report on the Physics at the HL-LHC, and Perspectives for the HE-LHC*, tech. rep., 2019, URL: https://cds.cern.ch/record/2703572 (cit. on p. 6).

[38] *Snowmass White Paper Contribution: Physics with the Phase-2 ATLAS and CMS Detectors*, tech. rep., All figures including auxiliary figures are available at https://atlas.web.cern.ch/Atlas/GROUPS/PHYSICS/PUBNOTES/ATL-PHYS-PUB-2022-018: CERN, 2022, URL: https://cds.cern.ch/record/2805993 (cit. on p. 6).

[39] *Projections of sensitivities for tttt production at HL-LHC and HE-LHC*, tech. rep., CERN, 1900, URL: https://cds.cern.ch/record/2650211 (cit. on p. 6).

[40] R. A. Khalek, S. Bailey, J. Gao et al., *Towards ultimate parton distributions at the high-luminosity LHC*, European Physical Journal C **78** (2018) 962 (cit. on p. 6).

[41] J. Nielsen and on behalf of the ATLAS Collaboration, *Physics prospects for ATLAS at the HL-LHC*, Journal of Physics: Conference Series **1690** (2020) 012156, URL: https://doi.org/10.1088/1742-6596/1690/1/012156 (cit. on p. 6).

[42] A. Dainese et al., *The physics potential of HL-LHC*, 20218, URL: https://indico.cern.ch/event/765096/contributions/3295995/ (cit. on p. 6).

[43] *Expected Performance of the ATLAS Inner Tracker at the High-Luminosity LHC*, (2016) (cit. on p. 6).

[44] P. Lebrun et al., *Updated Baseline for a Staged Compact Linear Collider*, 2016 (cit. on pp. 7, 9).

[45] The CEPC Study Group, *CEPC Technical Design Report – Reference Detector*, 2025, arXiv: 2510.05260 [hep-ex], URL: https://arxiv.org/abs/2510.05260 (cit. on p. 8).

[46] T. Behnke et al.,
The International Linear Collider Technical Design Report - Volume 4: Detectors, 2013,
arXiv: 1306.6329 [physics.ins-det],
URL: https://arxiv.org/abs/1306.6329 (cit. on p. 8).

[47] R. K. Ellis et al., *Physics Briefing Book*, tech. rep., 254 p, 2019, arXiv: 1910.11775,
URL: https://cds.cern.ch/record/2691414 (cit. on p. 8).

[48] P. Roloff, *Detectors at CLIC*, Seminar presented at the KEK Physics Seminar, 2012, URL:
https://www2.kek.jp/physics-seminar/files2012/20120608_roloff.pdf
(cit. on p. 8).

[49] *The CLICdp webpage.* Accessed: 12-11-2025, URL: https://clicdp.web.cern.ch
(cit. on p. 9).

[50] D. Dannheim, *Requirements for Future Vertex Detectors*,
Presentation at the OCTOPUS Meeting, 2025,
URL: https://indico.cern.ch/event/1541679/contributions/6624989/
(cit. on pp. 10–12).

[51] G. Wilkinson, *Particle identification at FCC-ee*, Eur. Phys. J. Plus **136** (2021) 835,
URL: https://doi.org/10.1140/epjp/s13360-021-01810-4 (cit. on p. 10).

[52] E. Perez Codina, *Timepix3 performance in power pulsing operation*,
PoS **VERTEX2018** (2019) 059, URL: https://cds.cern.ch/record/2665318
(cit. on p. 10).

[53] S. Ruiz Daza, *Power pulsing with CLICpix2*, 2029,
URL: https://cds.cern.ch/record/2690112 (cit. on p. 10).

[54] D. Schulte, "Beam–beam Effects in Linear Colliders",
CERN Yellow Reports: School Proceedings, ed. by W. Herr, vol. 3, 2017 431
(cit. on p. 10).

[55] D. Dannheim, L. Linssen and A. Sailer,
Progress on Detector Ramp;D for CLIC 2019–2025, (2025),
URL: https://cds.cern.ch/record/2927639 (cit. on p. 10).

[56] *Technical Design Report for the ATLAS Inner Tracker Pixel Detector*, tech. rep.,
CERN, 2017, URL: https://cds.cern.ch/record/2285585
(cit. on pp. 11, 13, 133, 134).

[57] A. M. Nurnberg and D. Dannheim, *Requirements for the CLIC tracker readout*, (2017),
URL: https://cds.cern.ch/record/2261066 (cit. on p. 11).

[58] S. Spannagel, *Silicon Vertex & Tracking Detectors for the Compact Linear Collider*,
VERTEX2018 (2019), arXiv: 2002.10169,
URL: https://cds.cern.ch/record/2703588 (cit. on p. 11).

[59] H. Wennlöf et al.,
The Tangerine project: Development of high-resolution 65 nm silicon MAPS,
Nuclear Instruments and Methods in Physics Research Section A: Accelerators, Spectrometers, Detectors and Associated Equipment **1039** (2022) 167025,
ISSN: 0168-9002, URL: https://www.sciencedirect.com/science/article/pii/S0168900222004508
(cit. on pp. 12, 43).

[60] A. Chauhan et al., *Towards a new generation of Monolithic Active Pixel Sensors*,
Nuclear Instruments and Methods in Physics Research Section A: Accelerators, Spectrometers, Detectors and Associated Equipment **1047** (2023) 167821,
ISSN: 0168-9002, URL: https://www.sciencedirect.com/science/article/pii/S0168900222011135
(cit. on pp. 12, 43).

[61] *The OCTOPUS webpage.* Accessed: 16-11-2025,
URL: https://octopus.web.cern.ch/ (cit. on p. 12).

[62] The CMS Collaboration, *The CMS experiment at the CERN LHC*,
Journal of Instrumentation **3** (2008) S08004,
URL: https://doi.org/10.1088/1748-0221/3/08/S08004 (cit. on p. 13).

[63] The LHCb Collaboration, *The LHCb Detector at the LHC*,
Journal of Instrumentation **3** (2008) S08005,
URL: https://doi.org/10.1088/1748-0221/3/08/S08005 (cit. on p. 13).

[64] The ALICE Collaboration, *The ALICE experiment at the CERN LHC*,
Journal of Instrumentation **3** (2008) S08002,
URL: https://doi.org/10.1088/1748-0221/3/08/S08002 (cit. on p. 13).

[65] *Technical design of the phase I Mu3e experiment*,
Nuclear Instruments and Methods in Physics Research Section A: Accelerators, Spectrometers, Detectors and Associated Equipment **1014** (2021) 165679,
ISSN: 0168-9002 (cit. on p. 13).

[66] Y. Liu et al.,
ADENIUM — A demonstrator for a next-generation beam telescope at DESY,
Journal of Instrumentation **18** (2023) P06025, ISSN: 1748-0221,
URL: http://doi.org/10.1088/1748-0221/18/06/P06025 (cit. on pp. 13, 80).

[67] L. Rossi, P. Fischer, T. Rohe and N. Wermes,
Particle Detectors — From Fundamentals to Applications,
Springer Berlin, Heidelberg, 2006 (cit. on pp. 13, 14, 16, 18, 22, 34, 56).

[68] H. Spieler, *Semiconductor detector systems*,
Series on semiconductor science and technology, Oxford: Oxford Univ. Press, 2005,
URL: https://cds.cern.ch/record/1010490 (cit. on pp. 13, 17).

[69] C. Kittel, *Introduction to Solid State Physics*, 8th ed., Wiley, 2005 (cit. on pp. 13, 14).

[70] H. A. Bethe and J. Ashkin, *Passage of Radiation Through Matter*, ed. by E. Segre, New York: Wiley, 1953 (cit. on p. 19).

[71] L. D. Landau, *On the energy loss of fast particles by ionization*, Journal of Physics **8** (1944) 201, URL: https://cds.cern.ch/record/216256 (cit. on p. 19).

[72] P. V. Vavilov, *Ionization losses of high-energy heavy particles*, Journal of Experimental and Theoretical Physics **5** (1957) 749 (cit. on p. 19).

[73] S. Meroli, D. Passeri and L. Servoli, *Measurement of charge collection efficiency profiles of CMOS active pixel sensors*, Journal of Instrumentation **7** (2012) P09011, URL: https://doi.org/10.1088/1748-0221/7/09/P09011 (cit. on pp. 19, 118).

[74] H. Bichsel, *Straggling in thin silicon detectors*, Rev. Mod. Phys. **60** (3 1988) 663, URL: https://link.aps.org/doi/10.1103/RevModPhys.60.663 (cit. on p. 20).

[75] J. Apostolakis et al., *An implementation of ionisation energy loss in very thin absorbers for the GEANT4 simulation package*, Nuclear Instruments and Methods in Physics Research Section A: Accelerators, Spectrometers, Detectors and Associated Equipment **453** (2000) 597, ISSN: 0168-9002, URL: https://www.sciencedirect.com/science/article/pii/S0168900200004575 (cit. on pp. 20, 46).

[76] G. R. Lynch and O. I. Dahl, *Approximations to multiple Coulomb scattering*, Nuclear Instruments and Methods in Physics Research Section B: Beam Interactions with Materials and Atoms **58** (1991) 6 (cit. on p. 20).

[77] V. L. Highland, *Some Practical Remarks on Multiple Scattering*, Nuclear Instruments and Methods **129** (1975) 497 (cit. on p. 20).

[78] D. F. Swinehart, *The Beer-Lambert Law*, Journal of Chemical Education **39** (1962) 333, eprint: https://doi.org/10.1021/ed039p333, URL: https://doi.org/10.1021/ed039p333 (cit. on p. 21).

[79] A. H. Compton, *A Quantum Theory of the Scattering of X-rays by Light Elements*, Phys. Rev. **21** (5 1923) 483, URL: https://link.aps.org/doi/10.1103/PhysRev.21.483 (cit. on p. 21).

[80] M.-M. Bé et al., *Table of radionuclides (Vol. 3 - $A = 3$ to 244)*, ed. by B. I. des Poids et Mesures, vol. 3, 2006, URL: https://cea.hal.science/cea-02476243 (cit. on p. 22).

[81] *ATLAS User's Manual*, tech. rep., Silvaco International, 2011, URL: https://www.eng.buffalo.edu/~wie/silvaco/atlas_user_manual.pdf (cit. on pp. 23, 24).

[82] K. Wolters, S. Spannagel and D. Hynds, *User Manual for the Allpix^2 Simulation Framework*, Accessed: 15-10-2025, URL: https://cern.ch/allpix-squared/usermanual/allpix-manual.pdf (cit. on pp. 23, 25).

[83] C. Jacoboni, C. Canali, G. Ottaviani and A. Alberigi Quaranta, *A review of some charge transport properties of silicon*, Solid-State Electronics **20** (1977) 77, ISSN: 0038-1101, URL: https://www.sciencedirect.com/science/article/pii/0038110177900545 (cit. on pp. 23, 47).

[84] G. Masetti, M. Severi and S. Solmi, *Modeling of carrier mobility against carrier concentration in arsenic-, phosphorus-, and boron-doped silicon*, IEEE Transactions on Electron Devices **30** (1983) 764 (cit. on p. 23).

[85] K. Dort, *Simulation Studies and Characterisation of Monolithic Silicon Pixel-Detector Prototypes for Future Collider Detectors & Unsupervised Anomaly Detection in Belle II Pixel-Detector Data*, Dissertation: University of Giessen, 2022, URL: http://doi.org/10.22029/jlupub-1097 (cit. on pp. 23, 118).

[86] M. A. Del Rio Viera, *Charge collection studies of MAPS in a 65 nm CMOS imaging process*, Dissertation: Rheinische Friedrich-Wilhelms-Universität Bonn, 2025, URL: https://hdl.handle.net/20.500.11811/13752 (cit. on pp. 23, 25, 44, 46).

[87] C. Canali and G. Ottaviani, *Saturation values of the electron drift velocity in silicon between 300°K and 4.2°K*, Physics Letters A **32** (1970) 147, ISSN: 0375-9601, URL: https://www.sciencedirect.com/science/article/pii/0375960170902446 (cit. on p. 23).

[88] W. Shockley and W. T. Read, *Statistics of the Recombinations of Holes and Electrons*, Physical Review **87** (1952) 835 (cit. on pp. 24, 47).

[89] J. Fossum and D. Lee, *A physical model for the dependence of carrier lifetime on doping density in nondegenerate silicon*, Solid-State Electronics **25** (1982) 741, ISSN: 0038-1101, URL: https://www.sciencedirect.com/science/article/pii/0038110182902039 (cit. on p. 24).

[90] W. Shockley, *Currents to Conductors Induced by a Moving Point Charge*, Journal of Applied Physics **9** (1938) 635, ISSN: 0021-8979, eprint: https://pubs.aip.org/aip/jap/article-pdf/9/10/635/18304047/635_1_online.pdf, URL: https://doi.org/10.1063/1.1710367 (cit. on p. 25).

[91] S. Ramo, *Currents induced by electron motion*, Proc. Ire. **27** (1939) 584 (cit. on p. 25).

[92] J. Kröger, S. Spannagel and M. Williams, *Corryvreckan User Manual*, Accessed: 20-10-2025, URL: http://cern.ch/go/db9Z. (cit. on p. 25).

[93] J. Albrecht et al., *Summary of the trigger systems of the Large Hadron Collider experiments ALICE, ATLAS, CMS and LHCb*, Journal of Physics G: Nuclear and Particle Physics **52** (2025) 030501, URL: https://doi.org/10.1088/1361-6471/adaadc (cit. on p. 26).

[94] R. Marco-Hernández, *Overview of CMOS Sensors for Future Tracking Detectors*, Instruments **4** (2020), ISSN: 2410-390X, URL: https://www.mdpi.com/2410-390X/4/4/36 (cit. on p. 27).

[95] I. Peric, *A novel monolithic pixelated particle detector implemented in high-voltage CMOS technology*, Nucl. Instrum. Meth. A **582** (2007) 876, ed. by G. Ambrosi et al. (cit. on p. 27).

[96] W. Snoeys, *Monolithic pixel detectors for high energy physics*, Nuclear Instruments and Methods in Physics Research Section A: Accelerators, Spectrometers, Detectors and Associated Equipment **731** (2013) 125, PIXEL 2012, ISSN: 0168-9002, URL: https://www.sciencedirect.com/science/article/pii/S0168900213006840 (cit. on pp. 27, 28).

[97] T. T. Rudzki et al., *An ultra-light helium cooled pixel detector for the Mu3e experiment*, Journal of Instrumentation **18** (2023) C10022, URL: https://doi.org/10.1088/1748-0221/18/10/C10022 (cit. on p. 27).

[98] M. Šuljić, *ALPIDE: the Monolithic Active Pixel Sensor for the ALICE ITS upgrade*, Journal of Instrumentation **11** (2016) C11025, URL: https://doi.org/10.1088/1748-0221/11/11/C11025 (cit. on p. 28).

[99] The ALICE Collaboration, *Technical Design report for the ALICE Inner Tracking System 3 - ITS3 ; A bent wafer-scale monolithic pixel detector*, tech. rep., CERN, 2024, URL: https://cds.cern.ch/record/2890181 (cit. on p. 28).

[100] R. Vértesi, *The ALICE 3 detector concept for LHC Runs 5 and 6 and its physics performance*, European Physical Journal Special Topics **234** (2025) 2949 (cit. on p. 28).

[101] V. Sriskaran et al., *High-rate, high-resolution single photon X-ray imaging: Medipix4, a large 4-side buttable pixel readout chip with high granularity and spectroscopic capabilities*, 2023, arXiv: 2310.10188 [physics.ins-det], URL: https://arxiv.org/abs/2310.10188 (cit. on pp. 31, 38).

[102] X. Llopart et al., *Timepix4, a large area pixel detector readout chip which can be tiled on 4 sides providing sub-200 ps timestamp binning*, Journal of Instrumentation **17** (2022) C01044, URL: https://doi.org/10.1088/1748-0221/17/01/C01044 (cit. on pp. 31, 38).

[103] R. Ballabriga et al., *Characterization of the H2M monolithic CMOS sensor*, Nuclear Instruments and Methods in Physics Research Section A: Accelerators, Spectrometers, Detectors and Associated Equipment (2026) 171353, ISSN: 0168-9002, URL: https://www.sciencedirect.com/science/article/pii/S0168900226000793 (cit. on pp. 32, 48, 58, 61, 65, 68, 73, 74, 93, 98, 125–127).

[104] G. A. Rinella et al., *Time performance of Analog Pixel Test Structures with in-chip operational amplifier implemented in 65 nm CMOS imaging process*, Nuclear Instruments and Methods in Physics Research Section A: Accelerators, Spectrometers, Detectors and Associated Equipment **1070** (2025) 170034, ISSN: 0168-9002, URL: https://www.sciencedirect.com/science/article/pii/S0168900224009604 (cit. on pp. 32, 115).

[105] J. A. Ballin et al., *Monolithic Active Pixel Sensors (MAPS) in a quadruple well technology for nearly 100% fill factor and full CMOS pixels*, 2008 (cit. on p. 32).

[106] F. Krummenacher, *Pixel detectors with local intelligence: an IC designer point of view*, Nuclear Instruments and Methods in Physics Research Section A: Accelerators, Spectrometers, Detectors and Associated Equipment **305** (1991) 527 (cit. on p. 34).

[107] C. Reckleben, Private communication, 2025 (cit. on pp. 34, 62, 68, 72).

[108] T. Vanat, *Caribou — A versatile data acquisition system*, PoS **TWEPP2019** (2020) 100, URL: https://cds.cern.ch/record/2703500 (cit. on p. 38).

[109] Y. Otarid et al., *Caribou — A versatile data acquisition system for silicon pixel detector prototyping*, Journal of Instrumentation **20** (2025) C07043, URL: https://doi.org/10.1088/1748-0221/20/07/C07043 (cit. on p. 38).

[110] *ZC706 Evaluation Board for the Zynq-7000 XC7Z045 SoC*, Accessed: 8-10-2025, URL: https://www.xilinx.com/support/documentation/boards_and_kits/zc706/%20ug954-zc706-eval-board-xc7z045-ap-soc.pdf (cit. on p. 38).

[111] T. Ylönen and C. Lonvick, *The Secure Shell (SSH) Protocol Architecture*, RFC 4251, https://www.rfc-editor.org/info/rfc4251, 2006, URL: https://www.rfc-editor.org/info/rfc4251 (cit. on p. 38).

[112] *OPTIM Wafer Processing Services*, Accessed: 31-07-2025, URL: https://www.optimwaferservices.com (cit. on p. 40).

[113] A. Simancas et al., *Developing a Monolithic Silicon Sensor in a 65nm CMOS Imaging Technology for Future Lepton Collider Vertex Detectors*, IEEE Nuclear Science Symposium and Medical Imaging Conference (2022) 1 (cit. on p. 43).

[114] M. Aleksa et al., *Strategic R&D Programme on Technologies for Future Experiments*, tech. rep., CERN, 2018, URL: https://cds.cern.ch/record/2649646 (cit. on p. 43).

[115] *Technology Computer Aided Design (TCAD) - Synopsys*, Accessed: 19-09-2025, URL: https://www.synopsys.com/silicon/tcad.html (cit. on pp. 43, 44).

[116] S. Spannagel et al., *Allpix^2: A modular simulation framework for silicon detectors*, Nuclear Instruments and Methods in Physics Research Section A: Accelerators, Spectrometers, Detectors and Associated Equipment **901** (2018) 164, URL: https://doi.org/10.1016%2Fj.nima.2018.06.020 (cit. on pp. 43, 46, 47).

[117] A. Simancas, *TCAD Simulations and Test Beam Characterization of MAPS for Future Lepton Colliders*, Dissertation: Rheinische Friedrich-Wilhelms-Universität Bonn, 2025, URL: https://nbn-resolving.org/urn:nbn:de:hbz:5-80379 (cit. on p. 44).

[118] A. Simancas et al., *Simulations and performance studies of a MAPS in 65 nm CMOS imaging technology*, Nuclear Instruments and Methods in Physics Research Section A: Accelerators, Spectrometers, Detectors and Associated Equipment **1064** (2024) 169414, ISSN: 0168-9002, URL: https://www.sciencedirect.com/science/article/pii/S0168900224003401 (cit. on p. 44).

[119] A. Simancas and A. Velyka, Private communication, 2025 (cit. on pp. 45, 46).

[120] S. Ruiz Daza, *Monte Carlo Simulations of Detector Prototypes Designed in a 65 nm CMOS Imaging Process*, Masterarbeit: Rheinischen Friedrich-Wilhelms-Universität, 2022, URL: https://bib-pubdb1.desy.de/record/491590 (cit. on pp. 46, 47).

[121] S. Agostinelli et al., *Geant4—a simulation toolkit*, Nuclear Instruments and Methods in Physics Research Section A: Accelerators, Spectrometers, Detectors and Associated Equipment **506** (2003) 250, ISSN: 0168-9002, URL: https://www.sciencedirect.com/science/article/pii/S0168900203013688 (cit. on p. 46).

[122] R. C. Alig, S. Bloom and C. W. Struck, *Scattering by ionization and phonon emission in semiconductors*, Phys. Rev. B **22** (12 1980) 5565, URL: https://link.aps.org/doi/10.1103/PhysRevB.22.5565 (cit. on p. 46).

[123] E. Fehlberg, *Low-order classical Runge-Kutta formulas with stepsize control and their application to some heat transfer problems*, (1969), URL: http://hdl.handle.net/2060/19690021375 (cit. on p. 47).

[124] R. Turchetta, *Spatial resolution of silicon microstrip detectors*, Nuclear Instruments and Methods in Physics Research Section A: Accelerators, Spectrometers, Detectors and Associated Equipment **335** (1993) 44, ISSN: 0168-9002, URL: https://www.sciencedirect.com/science/article/pii/016890029390255G (cit. on pp. 48, 82).

[125] D. Dannheim et al., *Corryvreckan: a modular 4D track reconstruction and analysis software for test beam data*, Journal of Instrumentation **16** (2021) P03008, URL: https://doi.org/10.1088%2F1748-0221%2F16%2F03%2Fp03008 (cit. on pp. 48, 81).

[126] C. Lemoine, R. Ballabriga, E. Buschmann, M. Campbell, R. Casanova Mohr et al., *Impact of the circuit layout on the charge collection in a monolithic pixel sensor*, Journal of Instrumentation **20** (2025) C06052, URL: https://doi.org/10.1088/1748-0221/20/06/C06052 (cit. on pp. 48, 93, 125).

[127] T. Heim and M. Garcia-Sciveres, *Self-adjusting threshold mechanism for pixel detectors*, Nucl. Instrum. Methods Phys. Res. A **867** (2017) 209 (cit. on p. 56).

[128] I. Kremastiotis, R. Ballabriga, K. Dort, N. Egidos and M. Munker, *CLICTD: A monolithic HR-CMOS sensor chip for the CLIC silicon tracker*, PoS **TWEPP2019** (2020) 039 (cit. on p. 56).

[129] J. Schlaadt, *Laboratory Characterisation of the Hybrid-to-Monolithic Pixel Sensor Prototype*, Unpublished Masterarbeit, MA thesis: Johannes Gutenberg University, Mainz, 2024 (cit. on p. 57).

[130] F. M. Puglisi, A. Padovani, L. Larcher and P. Pavan, *Random telegraph noise: Measurement, data analysis, and interpretation*, IEEE 24th International Symposium on the Physical and Failure Analysis of Integrated Circuits (IPFA) **PP** (2017) 1 (cit. on p. 58).

[131] R. D. Deslattes et al., *X-ray Transition Energies (version 1.2)*, Accessed: 13-05-2025, 2005, URL: http://physics.nist.gov/XrayTrans (cit. on pp. 62, 64).

[132] Y. He et al., *Timing performance of the DESY ER1 chip in a 65 nm CMOS imaging technology*, Nuclear Instruments and Methods in Physics Research Section A: Accelerators, Spectrometers, Detectors and Associated Equipment **1080** (2025) 170762, ISSN: 0168-9002, URL: https://www.sciencedirect.com/science/article/pii/S0168900225005637 (cit. on p. 65).

[133] J. Dilg, *Timing Performance of the DESY Chip V2 in a 65 nm CIS Technology*, Masterarbeit: Rheinische Friedrich-Wilhelms-Universität Bonn, 2025, URL: https://bib-pubdb1.desy.de/record/637539 (cit. on p. 65).

[134] J. Jakubek, *Precise energy calibration of pixel detector working in time-over-threshold mode*, Nuclear Instruments and Methods in Physics Research Section A: Accelerators, Spectrometers, Detectors and Associated Equipment **633** (2011) S262, 11th International Workshop on Radiation Imaging Detectors (IWORID), ISSN: 0168-9002 (cit. on p. 68).

[135] G. Aglieri Rinella et al., *Further characterisation of Digital Pixel Test Structures implemented in a 65 nm CMOS process*, Nuclear Instruments and Methods in Physics Research Section A: Accelerators, Spectrometers, Detectors and Associated Equipment **1083** (2026) 171082, ISSN: 0168-9002, URL: https://www.sciencedirect.com/science/article/pii/S0168900225008848 (cit. on p. 74).

[136] D. Rastorguev, *Ensuring superior performance: Characterizations of novel silicon detectors for High-Luminosity LHC and beyond*, Dissertation: Bergische Universität Wuppertal, 2025, URL: https://bib-pubdb1.desy.de/record/642214 (cit. on p. 75).

[137] R. Diener et al., *The DESY II test beam facility*, Nuclear Instruments and Methods in Physics Research Section A: Accelerators, Spectrometers, Detectors and Associated Equipment **922** (2019) 265, ISSN: 0168-9002, URL: http://doi.org/10.1016/j.nima.2018.11.133 (cit. on pp. 79, 80).

[138] M. Mager, *ALPIDE, the Monolithic Active Pixel Sensor for the ALICE ITS upgrade*, Nuclear Instruments and Methods in Physics Research Section A: Accelerators, Spectrometers, Detectors and Associated Equipment **824** (2016) 434, Frontier Detectors for Frontier Physics: Proceedings of the 13th Pisa Meeting on Advanced Detectors, ISSN: 0168-9002, URL: https://www.sciencedirect.com/science/article/pii/S0168900215011122 (cit. on p. 80).

[139] L. Huth et al., *TelePix2: Full scale fast region of interest trigger and timing for the EUDET-style telescopes at the DESY II test beam facility*, Nuclear Instruments and Methods in Physics Research Section A: Accelerators, Spectrometers, Detectors and Associated Equipment **1080** (2025) 170720, ISSN: 0168-9002, URL: https://www.sciencedirect.com/science/article/pii/S0168900225005212 (cit. on p. 80).

[140] P. Baesso, D. Cussans and J. Goldstein, *The AIDA-2020 TLU: a flexible trigger logic unit for test beam facilities*, Journal of Instrumentation **14** (2019) P09019, ISSN: 1748-0221, URL: http://doi.org/10.1088/1748-0221/14/09/P09019 (cit. on p. 80).

[141] Y. Liu et al., *EUDAQ2—A flexible data acquisition software framework for common test beams*, Journal of Instrumentation **14** (2019) P10033, ISSN: 1748-0221, URL: http://doi.org/10.1088/1748-0221/14/10/P10033 (cit. on p. 80).

[142] S. Spannagel et al., *Constellation: The autonomous control and data acquisition system for dynamic experimental setups*, Nuclear Instruments and Methods in Physics Research Section A: Accelerators, Spectrometers, Detectors and Associated Equipment (2026) 171279, ISSN: 0168-9002,

URL: https://www.sciencedirect.com/science/article/pii/S0168900226000057 (cit. on p. 81).

[143] C. Kleinwort, *General broken lines as advanced track fitting method*, Nuclear Instruments and Methods in Physics Research Section A: Accelerators, Spectrometers, Detectors and Associated Equipment **673** (2012) 107, URL: https://doi.org/10.1016%2Fj.nima.2012.01.024 (cit. on p. 82).

[144] R. Turchetta, *Spatial resolution of silicon microstrip detectors*, Nuclear Instruments and Methods in Physics Research Section A: Accelerators, Spectrometers, Detectors and Associated Equipment **335** (1993) 44, ISSN: 0168-9002, URL: https://www.sciencedirect.com/science/article/pii/016890029390255G (cit. on p. 86).

[145] S. Spannagel and H. Jansen, *GBL Track Resolution Calculator v2.0*, 2016, URL: https://zenodo.org/records/48795 (cit. on p. 87).

[146] M. Antonello et al., *Precision determination of the track-position resolution of beam telescopes*, Nuclear Instruments and Methods in Physics Research Section A: Accelerators, Spectrometers, Detectors and Associated Equipment **1072** (2025) 170185, ISSN: 0168-9002, URL: https://www.sciencedirect.com/science/article/pii/S0168900224011112 (cit. on p. 87).

[147] CERN, *Secondary Beam Areas of the PS, SPS machines*, Accessed: 16-09-2025, 2019, URL: http://sba.web.cern.ch/sba/ (cit. on pp. 88, 108).

[148] S. Ruiz Daza et al., *The H2M Monolithic Active Pixel Sensor — characterizing non-uniform in-pixel response in a 65 nm CMOS imaging technology*, Journal of Instrumentation **20** (2025) C06037, URL: https://doi.org/10.1088/1748-0221/20/06/C06037 (cit. on pp. 93, 95).

[149] G. Aglieri Rinella, G. Alocco, M. Antonelli, R. Baccomi, S. M. Beole et al., *Characterization of analogue Monolithic Active Pixel Sensor test structures implemented in a 65 nm CMOS imaging process*, Nucl. Instrum. Methods Phys. Res. A **1069** (2024) 169896 (cit. on pp. 98, 99, 107, 121).

[150] C. Bespin Valero, *Characterization of the TJ-Monopix2 Depleted Monolithic Active Pixel Sensor for High-Energy Physics Experiments*, Dissertation: University of Bonn, 2024, URL: https://hdl.handle.net/20.500.11811/12562 (cit. on p. 118).

[151] D. Berlea et al., *Depletion depth studies with the MALTA2 sensor, a depleted monolithic active pixel sensor*, Nuclear Instruments and Methods in Physics Research Section A: Accelerators, Spectrometers, Detectors and Associated Equipment **1063** (2024) 169262, ISSN: 0168-9002, URL: https://www.sciencedirect.com/science/article/pii/S0168900224001888 (cit. on p. 118).

[152] O. Feyens,
Grazing Angle Test Beam Studies of the Hybrid-to-Monolithic MAPS Prototype,
Masterarbeit: Vrije Universiteit Brussel, 2025,
URL: https://bib-pubdb1.desy.de/record/638146 (cit. on pp. 118, 119).

[153] Cadence, *Spectre*, Accessed: 30-09-2025, 2025,
URL: https://www.cadence.com/en%5C_US/home/tools/custom-ic-analog-rf-design/circuit-simulation.html (cit. on p. 125).

[154] *ATLAS inner detector*, Technical design report. ATLAS, Geneva: CERN, 1997,
URL: https://cds.cern.ch/record/331063 (cit. on p. 133).

[155] Y. Unno et al., *Specifications and pre-production of n+-in-p large-format strip sensors fabricated in 6-inch silicon wafers, ATLAS18, for the Inner Tracker of the ATLAS Detector for High-Luminosity Large Hadron Collider*,
Journal of Instrumentation **18** (2023) T03008,
URL: https://doi.org/10.1088/1748-0221/18/03/T03008
(cit. on pp. 134, 135, 141).

[156] L. Poley et al.,
The ABC130 barrel module prototyping programme for the ATLAS strip tracker,
Journal of Instrumentation **15** (2020) P09004,
URL: https://doi.org/10.1088/1748-0221/15/09/P09004 (cit. on p. 135).

[157] J. Dandoy et al.,
Quality control testing of the HCC ASIC for the HL-LHC ATLAS ITk strip detector,
Journal of Instrumentation **18** (2023) C02026,
URL: https://doi.org/10.1088/1748-0221/18/02/C02026 (cit. on p. 135).

[158] T. Gosart et al.,
Quality control testing of the AMAC ASIC for the HL-LHC ATLAS ITk Strip Detector,
Journal of Instrumentation **18** (2023) C02013,
URL: https://doi.org/10.1088/1748-0221/18/02/C02013 (cit. on p. 135).

[159] P. Moreira et al., *lpGBT documentation*, 2024,
URL: https://cds.cern.ch/record/2809058 (cit. on p. 136).

[160] L. Olantera et al., *Versatile Link+ Transceiver Production Readiness*,
PoS **TWEPP2019** (2020) 055, URL: https://cds.cern.ch/record/2724957
(cit. on p. 136).

[161] G. Ripamonti et al.,
2.5V step-down DCDCs: a radiation-hard solution for power conversion,
PoS **TWEPP2019** (2020) 071, URL: https://cds.cern.ch/record/2725201
(cit. on p. 136).

[162] F. Faccio, S. Michelis, G. Blanchot, G. Ripamonti and A. Cristiano,
The bPOL12V DCDC converter for HL-LHC trackers: towards production readiness,
PoS **TWEPP2019** (2020) 070, URL: https://cds.cern.ch/record/2725200
(cit. on p. 136).

[163] A. Boebel et al., *The End-of-Substructure (EoS) card for the ATLAS Strip Tracker upgrade — from design to production*, Journal of Instrumentation **19** (2024) C02067, URL: https://doi.org/10.1088/1748-0221/19/02/C02067 (cit. on pp. 137, 140, 141).

[164] L. Bauckhage et al., *Experiences and lessons learned from the End-of-Substructure card production of the ATLAS ITk Strip upgrade*, Journal of Instrumentation **20** (2025) C02020, URL: https://doi.org/10.1088/1748-0221/20/02/C02020 (cit. on p. 137).

[165] L. Bauckhage et al., *Results from End-of-Substructure card production for the ATLAS ITk Strip upgrade using both the lpGBT-v1 and -v2 ASIC*, tech. rep., CERN, 2025, URL: https://cds.cern.ch/record/2949254 (cit. on p. 137).

[166] P. Goettlicher and M. Stanitzki, Private communication, 2026 (cit. on p. 137).

[167] A. Tishelman-Charny et al., *An extreme thermal cycling reliability test of ATLAS ITk Strips barrel modules*, Journal of Instrumentation **19** (2024) P10002, URL: https://doi.org/10.1088/1748-0221/19/10/P10002 (cit. on p. 141).

[168] *CY8CMBR3116-LQXI Data Sheet*, Accessed: 5-12-2025, URL: https://www.infineon.com/part/CY8CMBR3116-LQXI (cit. on pp. 142, 143).

[169] R. Bitter, T. Mohiuddin and M. Nawrocki, *LabVIEW: Advanced programming techniques*, Crc Press, 2006 (cit. on p. 143).

[170] S. Schmitt, Private communication, 2026 (cit. on p. 144).

List of Figures

List of Tables

Acknowledgements

I would like to start expressing my gratitude to Ingrid Gregor and Jochen Dingfelder for agreeing to be the examiners of this work. Thank you also for the warm welcome I found in your groups, which has really helped me feel at home in Bonn and Hamburg over the last five years.

I feel incredibly lucky to have crossed paths with Simon Spannagel six years ago. I don't have words to express how grateful I am to have you as a supervisor, both personally and academically. I would repeat another summer student program, a master's thesis, and even write another PhD under your supervision. Thank you very much for all the opportunities and trust that you have always placed in me.
¡My big thank you to Finn King! It is hard to imagine many parts of this work without your help. Thank you for sitting with me in the lab until everything was working, for the many insightful discussions, and for lighting up the days and nights during test beams.
~~Moreover,~~ I would like to thank Håkan Wennlöf. Thank you so much for all your teaching and for always finding enthusiasm in the problems. We all missed you at DESY.
Thank you, Simon, Finn, and Håkan, for always keeping your office doors open, for carefully reading this thesis, and for following this work so closely — from a parameter in the simulation configuration to dealing with a fire in the accelerator or a broken chip.

This work has greatly benefited from the discussions within the H2M Collaboration, and I would like to thank everyone who contributed to such an interesting project — from the chip design to its testing. In particular, I would like to thank Christian Reckleben, Corentin Lemoine, Dominik Dannheim, Finn King, Michel Campbell, Simon Spannagel, Younes Otarid, and Håkan Wennlöf for following all the H2M results so closely, for their guidance, and for performing simulations that helped explain the measurements. Achieving the results in this work would have been impossible without your weekly input.

Thank you to everyone in the Tangerine project, and beyond, for all the discussions during the Wednesday meetings and for providing invaluable feedback to this work. Thanks, Adriana, Arianna, Daniil, Dohun, Finn, Gianpiero, Håkan, Ingrid, Jona, Judith, Larissa, Lennart, Manuel, Naomi, Nastia, Ono, Paul, Simon, Stephan, Yajun, and Tangy. I truly believe I had the best working group these years!

Thanks a lot to the EoS Team, especially to Harald Ceslik, Luckas Bauckhage, Marcel Stanitzki, Peter Goettlicher, and Stefan Schmitt, for all your patience in teaching me electronics, for your supervision, and for all the opportunities you gave me. Thank you, Stefan, for following all the EoS results in this work so closely, for all the time you spent with me in the lab explaining everything (multiple times), and for always being open to discussions.

I would like to thank the entire DESY-ATLAS group. Many of you I now call friends. Thank you for losing so many bets and making such amazing cakes (except Lukas Bayer, whom I also have to thank for reading parts of this thesis and for the physics discussions), for the *cafesito con chisme de las tres*, Duolingo friend streaks, *Feierabends*, and parties. All the lunches together and social activities make Hamburg a sunnier place.

ESpecial mention to Adriana, Gianpiero, Manuel, and Naomi. Thank you for being an example, the best colleagues I could wish for, and friends. I can't wait to see all the amazing things you'll achieve!

Many thanks to my family and friends. Being so far away is not always easy, but I always feel your love and support. Thank you, Adrián, for being a source of motivation and love.

The measurements leading to these results have been performed at the Test Beam Facility at DESY Hamburg (Germany), a member of the Helmholtz Association (HGF).
The developments presented in this contribution are performed in collaboration with the CERN EP R&D programme on technologies for future experiments.
This project has received funding from the European Union's Horizon 2020 Research and Innovation programme under GA no 101004761.